Delft University of Technology

Scalable Simulation Models for Fractured Porous Media with Complex Geometries

HosseiniMehr, S.Mousa

DOI
10.4233/uuid:7641219e-259f-48a7-8b91-f6691a5e937d

Publication date
2021

Document Version
Final published version

Citation (APA)
HosseiniMehr, S. M. (2021). *Scalable Simulation Models for Fractured Porous Media with Complex Geometries*. [Dissertation (TU Delft), Delft University of Technology]. https://doi.org/10.4233/uuid:7641219e-259f-48a7-8b91-f6691a5e937d

Scalable Simulation Models
for Fractured Porous Media with Complex Geometries

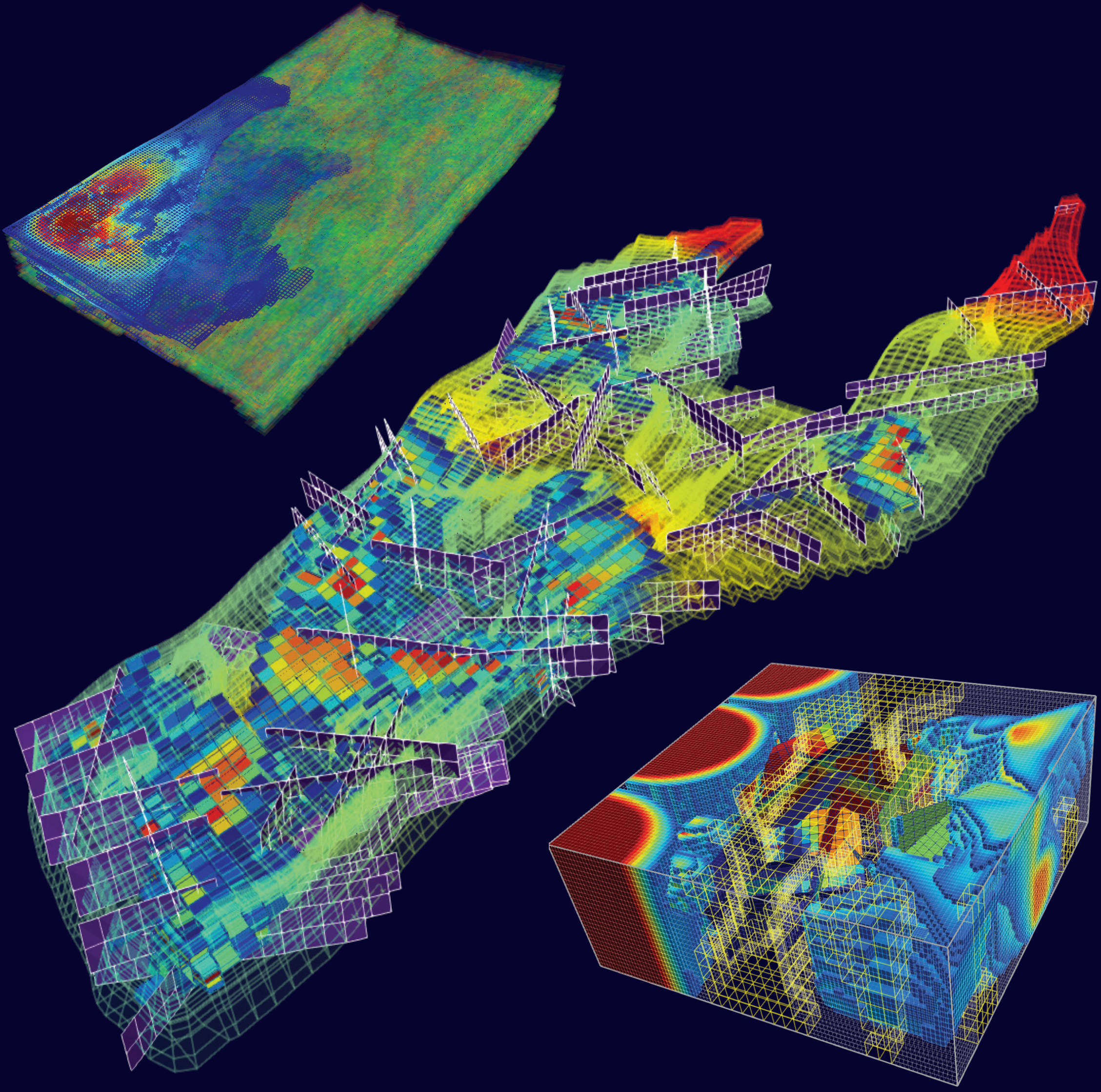

S.Mousa HosseiniMehr

SCALABLE SIMULATION MODELS FOR FRACTURED POROUS MEDIA WITH COMPLEX GEOMETRIES

SCALABLE SIMULATION MODELS FOR FRACTURED POROUS MEDIA WITH COMPLEX GEOMETRIES

Dissertation

for the purpose of obtaining the degree of doctor
at Delft University of Technology,
by the authority of the Rector Magnificus prof.dr.ir. T.H.J.J. van der Hagen,
chair of the Board for Doctorates
to be defended publicly on
Thursday 9th December 2021 at 10:00 o'clock

by

SeyyedMousa HOSSEINIMEHR

Master of Science in Applied Earth Sciences,
Delft University of Technology, the Netherlands

born in Ahvaz, Iran.

This dissertation has been approved by the promotors.

Composition of the doctoral committee:

Rector Magnificus,	chairman
Prof.dr.ir. C. Vuik,	Delft University of Technology, promotor
Dr. H. Hajibeygi,	Delft University of Technology, promotor

Independent members:

Prof.dr.ir. L.J. Sluys,	Delft University of Technology
Prof.dr.ir. J.D. Jansen,	Delft University of Technology
Prof.dr. Y. Efendiev,	Texas A&M University
Prof.dr. S. Geiger,	Heriot-Watt University
Dr. M.S. Al Kobaisi,	Khalifa University, Abu Dhabi
Prof.dr. W.R. Rossen,	Delft University of Technology, reserve member

This research work has been conducted with the support of the Delft Advanced Reservoir Simulation (DARSim) and the Delft Institute of Applied Mathematics (DIAM) groups.

Keywords: Fractured porous media, adaptive mesh refinement, multiscale simulation, dynamic multilevel methods, scalable physics-based nonlinear simulation, corner-point grid geometry, geologically relevant models, geothermal reservoirs

Printed by: Ipskamp Printing (www.ipskampprinting.nl)

Front & Back: Design by the author

ISBN 978-94-6366-481-3

An electronic version of this dissertation is available at
`http://repository.tudelft.nl/`.

To my dear parents,
S.Ahmad HosseiniMehr and Vajiheh Sadeghi

Truth is ever to be found in the simplicity, and not in the multiplicity and confusion of things.

Isaac Newton

CONTENTS

PREFACE

Dear reader,

It makes me glad to see your interest in my PhD dissertation. What you are reading is the result of a four-years project I carried out at TU Delft. Although one cannot illustrate a comprehensive image of such a long journey, I try to highlight the life experiences I have had alongside this wonderful opportunity I was given.

It is said that the future is not something we enter, but rather something we create. When I left Iran and moved to the Netherlands to pursue my MSc studies at TU Delft, I had not imagined what an amazing voyage was awaiting me, standing before my very eyes. The colorful landscapes, beautiful historical sights, and the welcomingness of the Dutch people, soon outcasted my frustrations with the fickle, windy and rainy weather of the country. Having active social engagements and taking a few Dutch language courses provided me with a better connection towards the culture and all the "gezelligheden".

The dynamic and exciting academic atmosphere of the university added to the motivation. But it was the course "reservoir simulation" by Dr. Hadi Hajibeygi that made me find out my passion. It soon became clear that computer programming and modeling, despite no initial background, is the path I wanted to take. Having my MSc thesis under his supervision gave me even better insights. I enjoyed every moment of programming and writing codes from the scratch with all the challenges I faced. After successfully finishing my MSc, I had eager interest in continuing the same path towards PhD. Looking at different research opportunities from various universities, none of them captured my interest. I clearly knew what I wanted, but such a project did not exist. Discussing it with Hadi, he gave me an ambitious suggestion, i.e., if the PhD position you want does not exist, create it yourself! Therefore, I wrote my own PhD research proposal, and it was eventually accepted. My PhD journey started with Dr. Hadi Hajibeygi and Prof.dr.ir Cornelis (Kees) Vuik as my promotors. My excitement and motivation were great drivers which made me publish my first journal paper just a few months later. Beside scientific knowledge and research skills, I also acquired various personal and social skills. Attending and presenting at various international conferences improved my communication and networking skills. Teaching as well as supervising MSc students highlighted the importance of knowledge transfer for me. This PhD research offered me a renewed perspective towards many aspects in my life. The social part of my life was also full of colors. Organizing and participating at various social activities, trips, drinks, and so on. Learning Latin dances (such as salsa and bachata) changed my lifestyle completely. Having met numerous open-hearted and energetic people, from every corner of the globe, enriched my cultural experience, making me blessed to have met my girlfriend as well. After four years, this PhD journey came to an end, leaving behind countless of vivid and unforgettable memories.

After my PhD contract ended, I had the opportunity to spend three months as a high-performance computing (HPC) software engineer intern at Schlumberger, in Abingdon, UK. Despite the pandemic restrictions and working remotely from home, I could explore computer programming on an industrial scale which opened a new window in front of eyes. Learning advanced C++ and GPU programming, I realized how deep my passion for computer programming runs. Entering industry, I eagerly look forward to applying my knowledge and skills in a practical manner, while continuously improving those I have and learning new ones. At the end, this is what life is all about, never stop learning.

Yours Sincerely,

S.Mousa HosseiniMehr
Delft, November 18, 2021

SUMMARY

In various geo-engineering fields, accurate and scalable modeling of fluid and heat transport in the subsurface fractured porous media is important in order to fulfill scientific, economical and societal expectations on successful field development plans. Such models and the predictions they provide, contribute to efficient and safe operations on the production or storage facilities. However, while attempting to provide accurate results, a number of key challenges exist. Over the past decades, the scientific community have been developing various advanced numerical techniques to address these challenges. In this work, a number of scientific contributions have been made to help address specific challenges, by developing scalable numerical methods for fractured porous media, some with complex geometries. The primary aim of these methods is to provide computational efficiency while delivering accurate results on a desired level.

Chapter 1 starts with background information on why these computer models are needed and the key challenges that exist along the way. Moreover, the contribution of the scientific community in various aspects are highlighted. In addition, the numerical methods developed in this work are briefly pointed out in this chapter.

Chapter 2 covers the governing equations as well as the mathematical and physical relations for various flow models in great detail. These equations include capturing the effect of fractures and faults in the subsurface flow as well. Chapter 3 attempts to provide detailed explanation of the discretized equations. The fine-scale simulation approaches as well as the coupling strategies for the governing equations are described. Moreover, the linearization of the non-linear equations is covered as well. Afterwards, the embedded discrete fracture models are thoroughly explained, where the effect of fractures on the patterns of flow are explicitly captured. In chapter 4, the mentioned fracture models are extended and applied to geologically relevant field-scale models. This is an important part of this work as the real field-scale geological formations cannot be represented by the Cartesian grid geometry (orthogonal box-shaped grids), but they are better represented by unstructured grids (such as corner-point grids). Using a number of numerical results, the capabilities of the developed model are showcased. It is also discussed how this model can offer great flexibility in the gridding strategies for field-scale models.

In the above-mentioned chapters, the focus is on the fine-scale approaches in the numerical simulations. However, despite the technological advancements in computer hardware and high performance computation, the large size of the real field-scale domains, makes it impractical for the current computers to provide simulation results using fine-scale numerical methods. From this point onward, the focus shifts towards the multilevel multiscale methods. Chapter 5 covers the static multilevel multiscale methods for simulation of fluid flow in fractured domains, where the domain is subdivided in

coarser grids across multiple levels of coarsening. With the help of the locally computed functions (also known as the basis functions), an approximated solution is obtained for the entire domain, reducing the size of the linear system of equations and providing computational efficiency.

In chapter 6 and 7, the dynamic multilevel method is described in which different parts of the domain are treated and processed at different resolutions and coarsening levels. Due to different physical processes at various scales in the domain, while some parts of the domain can be treated on a lower resolution, certain regions need a higher resolution to capture the physics accurately, which can dynamically change across simulation time. The dynamic multilevel method uses fine-scale high resolution grids only when and where needed, providing a robust and efficient performance while keeping the accuracy at a desired level. Various numerical tests compare the results of the dynamic multilevel method against those of the fine-scale approach. It is shown that accurate results can be obtained while using only a fraction of the high resolution grids. For large-scale domains, such model can offer a significant reduction in the size of the linear systems, providing an optimal scalability.

This dissertation is concluded in chapter 8 and references used in this work are followed afterwards.

I

INTRODUCTION

1

INTRODUCTION

1.1. WORLDWIDE ENERGY DEMAND

A key necessity for advancements in civilization in many aspects (e.g., technology, economy, and life quality) is energy. The worldwide energy demand is on a continuous and steady growth every year [1]. The year 2020 was exceptionally affected by the unprecedented COVID-19 pandemic, and the year 2021 is predicted to be influenced similarly. To this date (25th of February 2021) more than 113 million COVID-19 cases have been reported and 2.5 million individuals have lost their lives. In the light of the extraordinary impact of this pandemic and the corresponding measures on the energy system, the global energy demand dropped significantly [2, 3]. However, it is expected that the post-pandemic energy demand will shortly grow back to pre-pandemic levels (if not higher).

Despite a significant growth in renewable energy production in recent years, the gap in the global energy demands is mostly filled with a considerable increase in the production of hydrocarbon fuels (i.e., oil and gas). Figure 1.1, from the annual statistical review of world energy consumption in 2020 provided by British Petroleum, illustrates the trend of global energy consumption (in Exajoules) and the role of each energy source type on the entire consumption from 1994 till 2019. To achieve efficient and economical energy production from hydrocarbon resources, and to minimize its environmental impact, more advanced and enhanced recovery methods have been used.

Concurrently, in transition towards green and renewable energy in geo-engineering applications, geothermal energy productions, carbon capture and storage (CCS), and hydrogen storage are among the most important industries. Geothermal energy [4, 5] has the benefit of independent energy production regardless of climate-dependent factors (as compared to solar and wind energy sources). Therefore, it can sustainably provide electricity and/or heat for variety of buildings. The prospective outline looks very promising and its demand will grow steadily within the next decades. The contribution of geological formations is not limited to the energy sector, as they can offer a considerable capacity to store greenhouse gases, i.e., CO_2 in an effort to reduce its concentration in the atmosphere and reverse its impact on climate change [6–10]. In addition, hydro-

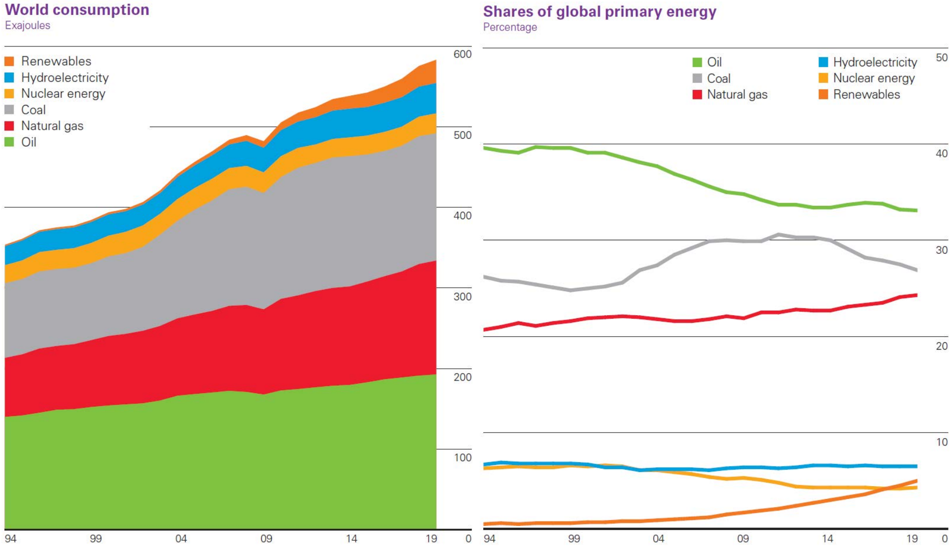

Figure 1.1: Statistic report of the global energy consumption by British Petroleum company. The figure on the left shows the combined global energy consumption in Exajoules from 1994 till 2019 while sub-categorizing the types of energy source. Figure on the right demonstrates the identical data in percentage shares for each of the energy sources.

gen storage has become a fast growing industry that casts a promising solution for future of green and blue energy storage.

1.2. THE NEED FOR COMPUTER MODELS

Regardless of the geo-engineering fields and their application in energy production (e.g., hydrocarbons and geothermal energy) or storage (e.g., CO2 storage and hydrogen storage), a detailed understanding of fluids and heat transport, their physical and chemical interactions together with rock, and their impact on the geological formation is greatly necessary. Accurate scalable modeling of fluid and heat transport in the subsurface porous media is of high importance in order to fulfill scientific, economical and societal expectations on successful field development plans. Such computer models and their resulting predictions contribute to efficient and safe operations on the production or storage facilities with regards to any of the mentioned geo-engineering applications. These predictions provide valuable insights on the optimization of hydrocarbon extractions [11], the energy production outlines and the life-time of geothermal systems [12–15], the practical capacities that can be offered by the underground formations to store CO_2 or hydrogen, and many more. Figure 1.2 shows an example of a computational model (Norne field, more information on section 4.3.6) which is used for field developments plans.

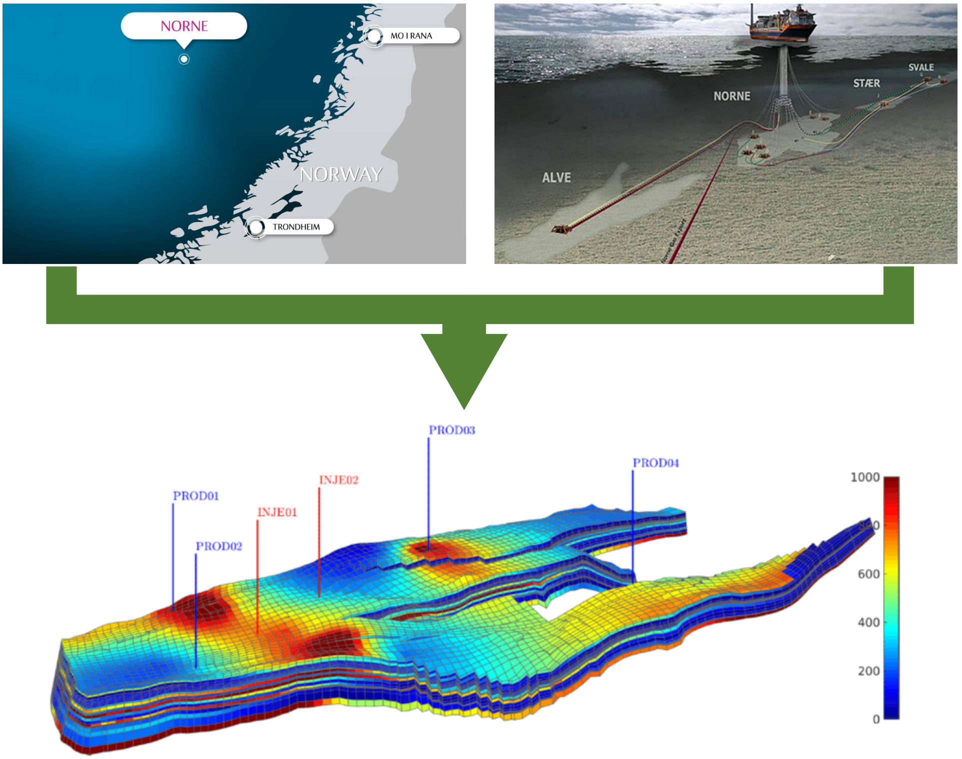

Figure 1.2: Norne oil field located in the Norwegian Sea. This figure illustrates a schematic view of this field and how the Norne computational model looks like. The images are extracted from [16–18].

1.3. CHALLENGES

In many geo-engineering fields, the term porous media refers to geological formations. These formation are often in large scales. While they are located few kilometers deep in the subsurface (crust) and have a thickness of tens (if not hundreds) of meters, their areal extents can easily be in orders of kilometers. The computer models do not have a physical sense of these geological formations as continuum domains. Instead, these continuum domains are subdivided into smaller subdomains called grid cells at fine-scale high resolution. These grid cells must be in size of representative elementary volume (REV) [19] that can reflect the geological and geometrical properties of the subsurface in a desired accuracy. However, this will result in dividing the formations into billions of grid cells. Imposing such high-resolution computational grids on the domain results in significant computational complexity. Despite the significant technological advancements gained on modern computers, it is still impossible to run computer models with such large computational domains using conventional methods.

Moreover, in many subsurface formations, strong spatial heterogeneity contrasts is observed between various physical and chemical properties. These fine-scale heterogeneities affect the flow and transport properties of the rock (i.e., storage capacity and conductivity) in several orders of magnitude. Subsequently, the discretization of the governing partial differential equations or PDEs (see chapter 2) results in ill-conditioned linear systems of equations, creating challenges for numerical solution schemes to solve such heterogeneous systems. In addition, the measurement of the heterogeneous properties several kilometers beneath the subsurface involves a great deal of uncertainty. In order to minimize the impact of such uncertainties, instead of one realization, hundreds (if not thousands) of realizations are created to obtain uncertainty quantification (UQ) and a large number of simulations have to be run. Thus, the complexity of the system can have a huge impact on providing predictions in a reasonable time scale. Furthermore, geological formations are often defined with complex geometry and stratigraphy. Using Cartesian grid geometry, even though it allows for simpler conceptual modeling analyses, can result in oversimplified and inaccurate predictions.

Additionally, the presence of faults and fractures (see section 1.4) has significant effects on fluid and heat flow patterns through the subsurface formations. The heterogeneities in length scales and conductivities caused by these complex networks of fractures and faults can cause extreme challenges in solving the linear systems using numerical methods [20–22]. Therefore, high fidelity representation of the physical phenomena within the heterogeneous fractured reservoirs is crucial [23].

Non-linear behavior of the system due to strong mass-heat coupling results in poor stability and convergence. In case of multi-phase flow (e.g., high-enthalpy systems) these issues become more severe [24]. The geo-mechanical processes (i.e., elastic and plastic deformation) [25–27], reactive transport (e.g., geo-chemical interaction between the substances) [28–30] and compositional changes are other notable challenges that the system might face. These challenges introduce high demands for developing advanced simulation methods that are able to provide efficiency (i.e., applicable to field-scale problems), while maintaining accuracy at the desired level.

To address these challenges, various advanced simulation schemes have been developed that will be briefly covered in the following sections.

1.4. FRACTURE MODELS

Geological formations are often naturally fractured. Figure 1.3 shows examples of real-field outcrops. There are various effects contributing to the formation of these fractures. The tectonic activities and stratigraphic processes are two of the main geo-mechanical causes of fracture generation, which act via influencing the stress-strain field in the subsurface geological formations. The details on how these processes affect the stress-strain field and the formation of fractures are beyond the scope of this work, and thus not explained further.

Depending on the tectonic forces and the lithology, the length scales, the size and the distribution, these fractured formations contain complex geological networks of fractures and faults with a broad range of conductivities. Some reservoirs present a few disconnected fractures while others have very complex fracture networks. Fractures usually have very small apertures (i.e., at the scale of millimeters). Even though their volume is relatively small and they do not contain considerable amount of fluids, they are typically highly conductive (several orders of magnitude more than the rock). In opposite, the faults and fractures that have become sealed due to tectonic activities or physical and chemical interaction between rock and fluid over geological time scales, can act as flow barriers.

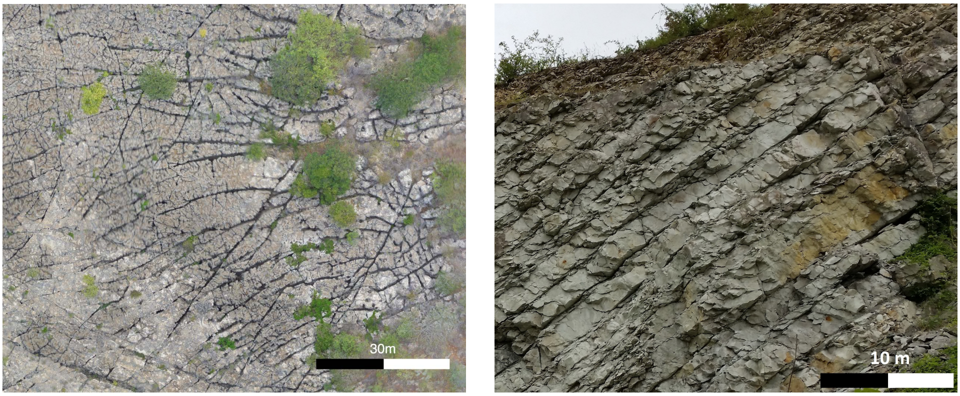

Figure 1.3: The image on the left shows a fracture network in flat-lying carbonates in the Potiguar Basin, Apodi, Rio Grande Do Norte, Brazil. Photo made by K. Bisdom, PhD Candidate, TU Delft. The image on the right illustrates fractures together with inclined layering in the Brochterbeck quarry, Germany. Photo taken by the author.

The significant effect of fractures and faults on fluid and heat flow makes it vital for reservoir simulation and management studies to consider an accurate modeling of fractures in many real scenarios (such as underground water resources, hydrocarbon and geothermal reservoirs, etc.). However, the geometrical complexity of the fractured media together with the large conductivity contrasts between fracture and rock impose a huge challenge to simulators. High computational costs together with low accuracy of the excessively upscaled models have made such simulations incapable of providing satisfactory results for field-scale problems. Consequently, many specialists are working to improve the efficiency of simulations by introducing new techniques and approaches in modeling of flow in fractured media.

Different approaches have been proposed to model the effect of fractures on flow patterns in natural formations. One option, known as fully-resolved approach or DNS (Direct Numerical Simulation), is to explicitly account for fractures by adapting the grid to their geometry and resolution. However, due to the difference of scales (several orders of magnitude) between the size of the domain, fractures' areal extents, and their small aperture sizes, this requires that extremely high resolution grids are employed which is not compatible with the length scales of natural formations. As a consequence, this approach is not practical for field scale simulations.

Alternatively, it is possible to upscale fractures by obtaining averaged and effective properties (e.g., permeability) between fractures (or faults) and the hosting rock (also known as the rock matrix) introducing a porous media representation without fractures but with approximated conductivities. However, such models raise concerns about inaccuracy of the simulation results due to the employed excessively upscaled parameters, especially in the presence of high conductivity contrasts between the matrix and fractures.

Therefore, two distinct methods have been introduced in the fracture modeling approach; the so-called dual permeability model (also known as dual continuum or dual porosity) [31–33] and the discrete fracture model (DFM) [34]. In the former method, the rock matrix plays the role of fluid storage and the fluid only flows inside the fractures. As it is assumed that there is no direct connection between the matrix cells, this model neglects the flow through the porous rock.

DFM considers fractures as a separate system in a lower dimensional domain than that of the rock matrix, and couples them through a transfer function. In 2D domains the fractures are represented by 1D line-segments and in 3D domains each fracture is modeled by a 2D plane-segment. The DFM provides more accurate results. Thus, it has been developed and evolved significantly during the past several years (See, e.g., [35–43], and the references therein). Next, the DFM approaches are being explained in brief.

1.4.1. DISCRETE FRACTURE MODELS (DFM)

Two different DFM approaches have been presented in the literature: the Embedded DFM (EDFM) and the Conforming DFM (CDFM). The main difference between these two techniques resides in the flexibility to the grid geometry. An illustration of these methods is presented in Fig. 1.4.

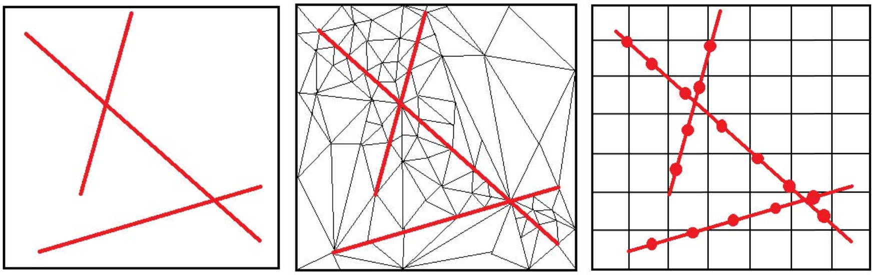

(a) The fractured media (b) CDFM, unstructured matrix grid (c) EDFM, structured matrix grid

Figure 1.4: A schematic sample showing the grid construction of different DFM approaches.

CONFORMING DISCRETE FRACTURE MODEL (CDFM)

In the CDFM, fracture elements are located at the interfaces between the triangular unstructured matrix grid-cells. The effect of fractures is represented by modifying transmissibilities at those interfaces. Therefore, there is an accurate consideration of flux transfer between matrix and fracture [35, 40, 42]. However for highly dense fracture networks the number of matrix grid cells should be very high with very fine triangles close to the fracture intersections, to account for the fractures. In addition, in case of fracture generation and propagation, the matrix grid has to be redefined at step of the simulation which reduces the efficiency of such an approach. All of these complexities can limit the application of CDFM in real-field applications.

EMBEDDED DISCRETE FRACTURE MODEL (EDFM)

In the EDFM, fractures are discretized separately and independently from the matrix on a lower dimensional domain by using non-conforming grids. Once the grid cells are created and the discretization is done, the fractures and matrix are coupled together using Conservative flux transfer terms that calculate the flow of mass and heat between each fracture element and its overlapping neighbors (non-neighboring connectivities). [36, 39, 44, 45]. Having two independent grids allows for modeling of complex fracture networks even with simple grids for the matrix. While the EDFM is applicable to provide acceptable solutions for highly conductive fractures, it leads to very small, yet nonphysical, flux leakages. More importantly, the EDFM cannot accurately represent flow barriers (e.g., sealing fractures and impermeable faults). In order to resolve this limitation, the projection-based EDFM (pEDFM) was introduced [46, 47] where consistent connectivities between matrix and fractures were developed. Therefore, the pEDFM can be applied to fractured porous media with generic range of conductivity contrast between fracture and the hosting rock. However, one needs to note that even with the pEDFM independent gridding, the size of the reservoir and density of the fractures make any fine-scale simulation approach impractical.

1.5. COMPLEX GEOMETRICAL MODELS

To represent the real-field geological formations accurately, instead of using Cartesian grids, more complex and flexible gridding structure are needed as these formations are more conveniently represented by flexible grids [42, 48]. The grid geometry should create a set of discrete cell volumes that approximate the reservoir volume, yet fit the transport process physics, and avoid over complications as much as possible [40]. Unstructured grids allow for many flexibilities, which need to be carefully applied to a computational domain so that the discrete systems do not become over-complex [35, 49]. Without introducing the full flexibility (and at the same time complexity) of the fully unstructured grids, the corner-point grid (CPG) geometry allows for many possibilities in better representation of the geological structures. This has made the CPG geometry attractive in the geoscience industry-grade simulations [50–53].

1.6. MULTISCALE STRATEGIES

As mentioned above, despite employing advanced fracture models such as the pEDFM, the length scale of many geological formations and reservoirs are very large (in orders of kilometers) and the need to run simulations for hundreds (if not thousands) of realization (as a result of intrinsic uncertainties) makes high resolution simulations impractical for field-scale applications.

Conventionally speaking, to reduce the computational costs, upscaling methods [54] have been used. In such techniques, the rock and fluid properties at fine-scale high resolution are mapped to a coarser resolution by obtaining effective averaged properties, which makes simulation affordable computationally. However, in presence of more complex physics, the excessive upscaling of the properties may cause inaccurate and non-satisfactory results. Due to these issues, more advanced algorithms and solvers have to be developed and used to allow for higher resolution grids to be employed.

To address this challenge, the Multiscale Finite-Element (MsFE) [55–57] and the Multiscale Finite-Volume (MsFV) [58–63] methods, and Dynamic Local Grid Refinement

(DLGR) techniques [64–72] and Adaptive Mesh Refinement (AMR) methods [64, 66, 73–76] are two classes of such advanced methods that aim to achieve accurate and efficient simulations by tackling different aspects of the entire complexity map.

The multiscale methods have been developed to solve the elliptic (or parabolic) pressure equation efficiently, in which highly heterogeneous coefficients are taken into account at their fine-scale resolution. First, the full domain is divided into a set of coarser grid cells and a local solution is achieved for each coarse grid cell. At the next stage, the system is solved on a coarse grid resolution. Lastly, the solution obtained at the coarse scale resolution is mapped to fine-scale resolution using the mentioned local solutions while preserving the fine-scale heterogeneities. These local solutions are the basis functions. To improve the accuracy, iterative multiscale techniques have been introduced where it allows a systematic reduction of the error in the multiscale approximation [60, 77, 78]. Moreover, by using an algebraic framework for the multiscale methods, higher computational gains have been put on the focus as well [79–81]. In the algebraic multiscale framework, the mapping between the fine-scale and the coarse-scale resolutions is done by employment of the so-called multiscale restriction and prolongation operators. While the classical multiscale approaches are considered as a great help to decrease the computational cost and at the same time honor accuracy, the computational gain is still not considerable to solve systems on real-field scale with billions of grid cells for which we need more advanced methods to provide a more efficient and faster solution. In order to overcome such issues, it is applicable to extend the concept from only one level into multiple levels of multiscale to increase the efficiency even further [45, 47, 82]. The multilevel multiscale finite volume method (MMsFV) approach uses the same method as in the MsFV approach recursively by giving the coarse grid cells of the 1st multiscale coarsening level to the 2nd multiscale coarsening level and so on (see chapter 5 for more details). Integration of the EDFM models in the MMsFV method allowed to benefit the computational gain of multilevel multiscale methods for simulation of fractured porous media [83]. For porous media containing high heterogeneity contrasts, the MMsFV method suffers the same inaccuracy as in the MsFV approach. Therefore, iterative multiscale can be used to achieve convergence to the fine-scale solution in the MMsFV method as well.

On the other hand, DLGR techniques adapt the grid resolution throughout the time-dependent simulation to employ a high-resolution grid where necessary (i.e., the advancing saturation front), and are, therefore, transport-oriented methods. By extending the DLGR grid refinement strategy and AMR methods, and by taking the advantages of multilevel multiscale techniques, an algebraic dynamic multilevel (ADM) method has been introduced for fully implicit simulation of multiphase fluid flow in non-fractured porous media [45, 47, 84, 85].

1.7. RESEARCH GOALS

Many challenges in the field of simulation of fluid and heat flow in subsurface porous media and various techniques developed to address them were mentioned in the previous sections. These techniques and the developed models by the scientific community provided a multi-dimensional insight to what is needed to obtain advanced models to tackle the challenges. Based on theses challenges and the scientific needs, the aim of this work has been to contribute to the field of computer simulations by developing a scalable model that represents the physical phenomena in the subsurface fractured porous media, honors accuracy and provides significant computational efficiency. The main goal of this work has been to:

- Develop a scalable model using algebraic dynamic multilevel (ADM) method to simulate the coupled mass-heat flow in fractured porous media with complex geometries.

Too achieve this goal, there are two main objectives. The first one is to develop a stand-alone projection-based embedded fracture model (pEDFM) that calculates the geometrical fluxes (geometrical transmissibilities) between fractures and the rock matrix. This model is able to model the fractures (highly conductive flow channels) and faults (impermeable flow barriers) with generic conductivity contrast. In addition, the model works on fully 3D domain and uses either Cartesian geometry or more complex corner-point grid geometry. The second objective is to develop the multilevel multiscale (MMsFV) and the algebraic dynamic multilevel (ADM) methods for fractured porous media with isothermal and non-isothermal flow. These objectives were achieved by setting the following detailed intermediate steps (some have been worked on in parallel) during the project time:

- develop a multilevel multiscale method for fractured porous media;
- develop a 3D projection-based embedded fracture model for Cartesian and corner-point grid geometry;
- develop an algebraic dynamic multilevel method for fully implicit method (FIM) simulations of fluid flow in fractured heterogeneous porous media;
- extend the method developed to more complex physics (i.e., geothermal systems);
- extend the method to use the corner-point grid geometry and thus include more complex geologically relevant domains.

1.8. THESIS OUTLINE

This dissertation consists of eight chapters, including this introduction. At first, in chapter 2, the governing equations for multiphase flow and heat transfer in fractured porous media are presented. The mass conservation (single-phase and multi-phase) and heat conservation (using either pressure-temperature or pressure-enthalpy as the main unknowns) are explained. Inside this chapter, all the phase and rock properties are described in detail as well. Chapter 3, consists of the simulation strategy at fine-scale resolution. The coupling strategies to couple the equations, especially the so-called fully-implicit method (FIM) are explained. Moreover, in this chapter the embedded discrete fracture model (EDFM) and the projection-based EDFM (pEDFM) are presented. The simulation flowcharts are also illustrated. Chapter 4 includes the extension of the fine-scale simulation model and the pEDFM model to include corner-point grid geometries for more geologically relevant applications. In chapter 5 the multilevel multiscale method for single-phase flow in fractured porous media is presented. In chapter 6, the algebraic dynamic multilevel method for multi-phase flow in fractured porous media is presented. Moreover, this chapter compares the employment of multilevel multiscale and homogenization (upscaling) techniques in the ADM method. In chapter 7, the ADM method for low-enthalpy and-high enthalpy fractured geothermal reservoirs is described. In addition, a comparison is made for different thermodynamical formulations. Chapter 8 includes conclusions and future work. At last, the references used in this dissertation are listed.

2

GOVERNING EQUATIONS FOR MASS AND HEAT TRANSPORT IN FRACTURED POROUS MEDIA

In this chapter, at first, the governing equations of isothermal multiphase flow in fractured porous media are given. Thereafter, coupled mass-heat flow in low-enthalpy (single-phase flow) and high-enthalpy (two-phase flow) in fractured geothermal reservoirs will be presented. Moreover, the corresponding correlations between some of the rock and fluid properties will be given. The focus of this chapter is only the governing equations, and the correlations between the primary and dependent variables. The discretization of the equations and the simulation strategy (at fine-scale) will be covered in the next chapter (3).

2.1. MULTIPHASE FLOW IN FRACTURED POROUS MEDIA (ISOTHERMAL)

The mass conservation for phase α in the absence of mass-exchange between phases, capillary, and gravitational effects in porous media with n_{frac} discrete embedded fractures reads

$$\frac{\partial}{\partial t}\left(\phi\rho_\alpha S_\alpha\right)^m - \nabla\cdot\left(\rho_\alpha \boldsymbol{\lambda_\alpha}\cdot\nabla p\right)^m = \rho_\alpha q_\alpha^{m,w} + \sum_{i=1}^{n_{\text{frac}}} \rho_\alpha \mathcal{Q}_\alpha^{m,f_i} \quad , \quad \text{on} \quad \Omega_m \subseteq \Re^n \tag{2.1}$$

for the rock matrix m and

Various parts of this chapter have been extracted from a number of the author's publications.

$$\frac{\partial}{\partial t}\left(\phi\rho_\alpha S_\alpha\right)^{f_i} - \nabla\cdot\left(\rho_\alpha \boldsymbol{\lambda_\alpha}\cdot\nabla p\right)^{f_i} = \rho_\alpha q_\alpha^{f_i,w} + \rho_\alpha \mathcal{Q}_\alpha^{f_i,m} + \sum_{j=1}^{n_{\text{frac}}}\left(\rho_\alpha \mathcal{Q}_\alpha^{f_i,f_j}\right)_{j\neq i} \quad , \qquad \text{on} \quad \Omega_{f_i} \subseteq \Re^{n-1} \quad \forall\, i \in \{1,\ldots,n_{\text{frac}}\} \tag{2.2}$$

for the lower-dimensional fracture f_i. There exist n_α phases. Moreover, the superscripts m, f and w in equations (2.1)-(2.2) indicate the rock matrix, the fractures and the wells, respectively. Here, ϕ is the porosity of the medium. The terms ρ_α, S_α, $\boldsymbol{\lambda_\alpha}$ are the density, saturation, and mobility of phase α, respectively. In addition, $\boldsymbol{\lambda} = \frac{k_{r\alpha}}{\mu_\alpha}\mathbf{K}$ holds, where k_r, μ and $\mathbf{K}$ are the phase relative permeability, the fluid viscosity and the rock absolute permeability tensor, respectively. Also, q_α is the phase source term (i.e., wells). Finally, $\mathcal{Q}_\alpha^{m,f_i}$ and $\mathcal{Q}_\alpha^{f_i,m}$ are the phase flux exchanges between the rock matrix and the i-th fracture, whereas $\mathcal{Q}_\alpha^{f_i,f_j}$ represents the volumetric influx of phase α from j-th fracture to the i-th fracture. Note that the mass conservation law enforces $\iiint\limits_V \mathcal{Q}_\alpha^{m,f_i}\, dV = -\iint\limits_{A_{f_i}} \mathcal{Q}_\alpha^{f_i m}\, dA$ and $\iint\limits_{A_{f_i}} \mathcal{Q}_\alpha^{f_i,f_j}\, dA = -\iint\limits_{A_{f_j}} \mathcal{Q}_\alpha^{f_j,f_i}\, dA$.

The Peaceman well model [86] is used to obtain the well source terms of each phase for the rock matrix as

$$q_\alpha^{m,w} = \frac{PI\cdot\lambda_\alpha^*\cdot(p^w - p^m)}{\Delta V} \tag{2.3}$$

and for the fractures as

$$q_\alpha^{f_i,w} = \frac{PI\cdot\lambda_\alpha^*\cdot(p^w - p^{f_i})}{\Delta A}. \tag{2.4}$$

Here, PI is the well productivity index and λ_α^* is the effective mobility of each phase ($\lambda = \frac{k_{r\alpha}}{\mu_\alpha}K$) between the well and the penetrated grid cell in the medium. ΔV and ΔA are the control volume and control area used in the discrete system for the rock matrix m and the fracture f_i respectively.

The flux exchange terms $\mathcal{Q}_\alpha^{m,f_i}$, $\mathcal{Q}_\alpha^{f_i,m}$ (matrix-fracture connectivities) and $\mathcal{Q}_\alpha^{f_i,f_j}$ (fracture-fracture connectivities) are written as:

$$\begin{aligned} \mathcal{Q}_\alpha^{m,f_i} &= CI^{m,f_i}\cdot\lambda_\alpha^*\cdot(p^{f_i} - p^m) \\ \mathcal{Q}_\alpha^{m,f_i} &= CI^{f_i,m}\cdot\lambda_\alpha^*\cdot(p^m - p^{f_i}) \\ \mathcal{Q}_\alpha^{f_i,f_j} &= CI^{f_i,f_j}\cdot\lambda_\alpha^*\cdot(p^{f_j} - p^{f_i}), \end{aligned} \tag{2.5}$$

where CI denotes the connectivity index between each two non-neighboring elements and is explained in detail in the next chapter (3.61).

Equations (2.1)-(2.2), subject to proper initial and boundary conditions, form a well-posed system for n_α unknowns, once the $\sum\limits_{\alpha=1}^{n_{ph}} S_\alpha = 1$ constraint is employed to eliminate one of the phase saturation unknowns. Here, this system of equations is solved for a two phase flow fluid model with the primary unknowns p and S_1 (in some expressions indicated as S).

2.2. MASS AND HEAT FLOW IN LOW-ENTHALPY FRACTURED POROUS MEDIA

In low-enthalpy geothermal systems, due to more relaxed thermodynamic conditions, it is assumed that the phase exchange (i.e., evaporation of liquid phase into vapor phase and vice versa) does not take place. Therefore, this system is assumed to be single-phase flow. Two sets of equations are described for this system, i.e., the mass balance and the energy balance equations.

2.2.1. MASS BALANCE EQUATION

The mass balance equation for thermal single-phase fluid flow in porous media with n_{frac} discrete fractures is given as

$$\frac{\partial}{\partial t}\left(\phi\rho_{(fl)}\right)^m - \nabla\cdot\left(\rho_{(fl)}\boldsymbol{\lambda}\cdot\nabla p\right)^m = \rho_{(fl)} q^{m,w} + \sum_{i=1}^{n_{\text{frac}}} \rho^*_{(fl)}\, \mathcal{Q}^{m,f_i} \quad , \quad \text{on} \quad \Omega_m \subseteq \Re^n, \tag{2.6}$$

for the rock matrix (m) and

$$\frac{\partial}{\partial t}\left(\phi\rho_{(fl)}\right)^{f_i} - \nabla\cdot\left(\rho_{(fl)}\boldsymbol{\lambda}\cdot\nabla p\right)^{f_i} = \rho_{(fl)} q^{f_i,w} + \rho^*_{(fl)}\, \mathcal{Q}^{f_i,m} + \sum_{j=1}^{n_{\text{frac}}} \left(\rho^*_{(fl)} \mathcal{Q}^{f_i,f_j}\right)_{j\neq i} \quad ,$$
$$\text{on} \quad \Omega_{f_i} \subseteq \Re^{n-1} \quad \forall\, i \in \{1,\dots,n_{\text{frac}}\}, \tag{2.7}$$

for the lower dimensional fracture (f_i). Here, the main unknown is the pressure p. ϕ is the porosity. In addition, $\boldsymbol{\lambda} = \frac{\mathbf{K}}{\mu_{(fl)}}$ is the mobility calculated for the fluid in which $\mu_{(fl)}$ is the fluid viscosity and $\mathbf{K}$ is the rock absolute permeability. Here, $\mathbf{K}$ is a tensor to account for a generic anisotropic case. Superscripts m, f_i and w correspond to matrix, fracture i and well, respectively. Subscripts fl and r denote fluid and rock. $\rho_{(fl)}$ is the density of the fluid. In addition, $q^{m,w}$ and $q^{f_i,w}$ are the source terms (i.e., wells) on matrix m and fracture f_i. Moreover, $\mathcal{Q}^{m,f_i}$ and $\mathcal{Q}^{f_i,m}$ are the flux exchange between the matrix m and the overlapping fracture f_i corresponding to the grid cells where overlap occurs. $\mathcal{Q}^{f_i,f_j}$ is the flux exchange from j-th fracture to the i-th fracture on the intersecting elements. This means that the mentioned flux exchange terms are non-zero only where matrix-fracture overlap or fracture-fracture intersection exists. Due to mass conservation, $\iiint_V \mathcal{Q}^{m,f_i}\, dV = -\iint_{A_{f_i}} \mathcal{Q}^{f_i,m}\, dA$, and $\iint_{A_{f_i}} \mathcal{Q}^{f_i,f_j}\, dA = -\iint_{A_{f_j}} \mathcal{Q}^{f_j,f_i}\, dA$ hold.

The Peaceman well model is used to obtain the well source terms for matrix

$$q^{m,w} = \frac{PI\cdot\lambda^*\cdot(p^w - p^m)}{\Delta V} \tag{2.8}$$

and fractures

$$q^{f_i,w} = \frac{PI\cdot\lambda^*\cdot(p^w - p^{f_i})}{\Delta A}. \tag{2.9}$$

Here, PI is the well productivity index and λ^* is the effective mobility ($\lambda = K/\mu$) between the well and the penetrated grid cell in the medium. ΔV and ΔA are the control volume and control area used in the discrete system for matrix m and fracture f_i respectively. The flux exchange terms $\mathcal{Q}^{m,f_i}$, $\mathcal{Q}^{f_i,m}$ (matrix-fracture connectivities) and $\mathcal{Q}^{f_i,f_j}$ (fracture-fracture connectivities) are written as:

$$\begin{aligned}
\mathcal{Q}^{m,f_i} &= CI^{m,f_i}\cdot\lambda^*\cdot(p^{f_i} - p^m)\\
\mathcal{Q}^{m,f_i} &= CI^{f_i,m}\cdot\lambda^*\cdot(p^m - p^{f_i})\\
\mathcal{Q}^{f_i,f_j} &= CI^{f_i,f_j}\cdot\lambda^*\cdot(p^{f_j} - p^{f_i}).
\end{aligned} \tag{2.10}$$

2.2.2. ENERGY BALANCE EQUATION

Assuming local equilibrium, energy balance on the entire domain reads

$$\begin{aligned}
&\frac{\partial}{\partial t}\left((\rho U)_{eff}\right)^m - \nabla\cdot\left(\rho_{(fl)}H_{(fl)}\boldsymbol{\lambda}\cdot\nabla p\right)^m - \nabla\cdot\left(\Lambda_{eff}\cdot\nabla T\right)^m =\\
&\qquad \rho_{(fl)}H_{(fl)}q^{m,w} + \sum_{i=1}^{n_{\text{frac}}}\rho^*_{(fl)}H^*_{(fl)}\mathcal{Q}^{m,f_i} + \sum_{i=1}^{n_{\text{frac}}}\mathcal{R}^{m,f_i},\\
&\qquad\qquad \text{on}\quad \Omega_m \subseteq \Re^n,
\end{aligned} \tag{2.11}$$

in the rock matrix (m) and

$$\begin{aligned}
&\frac{\partial}{\partial t}\left((\rho U)_{eff}\right)^{f_i} - \nabla\cdot\left(\rho_{(fl)}H_{(fl)}\boldsymbol{\lambda}\cdot\nabla p\right)^{f_i} - \nabla\cdot\left(\Lambda_{eff}\cdot\nabla T\right)^{f_i} =\\
&\rho_{(fl)}H_{(fl)}q^{f_i,w} + \rho^*_{(fl)}H^*_{(fl)}\mathcal{Q}^{f_i,m} + \sum_{j=1}^{n_{\text{frac}}}\left(\rho^*_{(fl)}H^*_{(fl)}\mathcal{Q}^{f_i,f_j}\right)_{j\neq i} + \mathcal{R}^{f_i,m} + \sum_{j=1}^{n_{\text{frac}}}\left(\mathcal{R}^{f_i,f_j}\right)_{j\neq i},\\
&\qquad\qquad \text{on}\quad \Omega_{f_i} \subseteq \Re^{n-1} \quad \forall\, i \in \{1,\dots,n_{\text{frac}}\},
\end{aligned} \tag{2.12}$$

in the lower dimensional discrete fracture (f_i). Here, beside pressure p, the second main unknown is T as the temperature in both fluid and the solid rock. $(\rho U)_{eff}$ is the effective property defined as

$$(\rho U)_{eff} = \phi\rho_{(fl)}U_{(fl)} + (1-\phi)\rho_r U_r, \tag{2.13}$$

where U_f and U_r denote the specific internal energy in fluid and rock, respectively. Distinctly, $(\rho U)^m_{eff} = \phi^m\rho_{(fl)}U_{(fl)} + (1-\phi^m)\rho_r U_r$ and $(\rho U)^{f_i}_{eff} = \phi^{f_i}\rho_{(fl)}U_{(fl)} + (1-\phi^{f_i})\rho_r U_r$. Moreover, $H_{(fl)}$ is the specific fluid enthalpy. The three mentioned terms can be expressed as non-linear functions of pressure and temperature. Λ_{eff} is the effective thermal conductivity of the saturated rock defined as

$$\Lambda_{eff} = \phi \Lambda_{(fl)} + (1-\phi)\Lambda_r. \tag{2.14}$$

Here, $\Lambda_{(fl)}$ and Λ_r are the thermal conductivities in fluid and rock, respectively. The subscripts fl and r indicate fluid and solid rock. Note that, $\Lambda^m_{eff} = \phi^m \Lambda_{(fl)} + (1-\phi^m)\Lambda_r$ and $\Lambda^{f_i}_{eff} = \phi^{f_i} \Lambda_{(fl)} + (1-\phi^{f_i})\Lambda_r$. Lastly, $\mathscr{R}^{m,f_i}$ and $\mathscr{R}^{f_i m,}$ are the conductive heat flux exchange between the matrix m and the overlapping fracture f_i. $\mathscr{R}^{f_i,f_j}$ denotes the conductive heat flux exchange from j-th fracture to the i-th fracture where the intersection occurs. Similar to mass flux exchange, the conductive flux exchange terms are non-zero only for the existing matrix-fracture overlaps or fracture-fracture intersections. $\iiint\limits_V \mathscr{R}^{m,f_i} \, dV = -\iint\limits_{A_{f_i}} \mathscr{R}^{f_i,m} \, dA$, and $\iint\limits_{A_{f_i}} \mathscr{R}^{f_i,f_j} \, dA = -\iint\limits_{A_{f_j}} \mathscr{Q}^{f_j,f_i} \, dA$ hold as well to honor the conservation of energy.

To obtain the conductive heat flux exchanges, i.e., $\mathscr{R}^{m,f_i}$, $\mathscr{R}^{f_i,m}$ (matrix-fracture connectivities) and $\mathscr{R}^{f_i,f_j}$ (fracture-fracture connectivities), the embedded discrete scheme is used, i.e.,

$$\begin{aligned}
\mathscr{R}^{m,f_i} &= CI^{m,f_i} \cdot \Lambda^*_{eff} \cdot (T^{f_i} - T^m) \\
\mathscr{R}^{m,f_i} &= CI^{f_i,m} \cdot \Lambda^*_{eff} \cdot (T^m - T^{f_i}) \\
\mathscr{R}^{f_i,f_j} &= CI^{f_i,f_j} \cdot \Lambda^*_{eff} \cdot (T^{f_j} - T^{f_i}),
\end{aligned} \tag{2.15}$$

where Λ^*_{eff} is obtained as harmonically-averaged property between the two non-neighboring elements. The connectivity index CI is identical to those used in prior equations. Note that the effects of both capillarity and gravity are neglected in all the equations.

2.3. MASS AND HEAT FLOW IN HIGH-ENTHALPY FRACTURED POROUS MEDIA

In the previous section, the governing equations for the low-enthalpy single-phase flow model were described. However, in high-enthalpy systems, due to more intense thermodynamic conditions, phase exchange can occur. In these systems, the water is considered as the dominant fluid. The evaporation of liquid water, and on the other hand, the condensation of vapor water occur due to the exposure of the fluid to sudden temperature and pressure changes. Therefore, a more general multi-phase formulation is taken into account. Yet, two series of mass conservation and energy conservation laws are considered. The subsets of these equations for each phase are added together and form one set of equations for the entire system, namely, one mass balance equation and one energy balance equation for all the phases.

2.3.1. MASS BALANCE EQUATIONS

The equation for the conservation of mass in a pure water system assuming multi-phase flow conditions, i.e. single component water present in two possible phases, is written as [87, 88]

$$\frac{\partial}{\partial t}\left(\phi \sum_{\alpha=1}^{n_{ph}} \rho_\alpha S_\alpha\right)^{m} - \nabla\cdot\left(\sum_{\alpha=1}^{n_{ph}} \left(\rho_\alpha \boldsymbol{\lambda_\alpha}\cdot\nabla p\right)\right)^{m} = \sum_{i=1}^{n_{\text{frac}}} \rho_\alpha q_\alpha^{m,w} + \sum_{\alpha=1}^{n_{ph}}\sum_{i=1}^{n_{\text{frac}}} \rho_\alpha \mathscr{Q}_\alpha^{m,f_i}, \quad \text{on} \quad \Omega_m \subseteq \Re^n, \tag{2.16}$$

for the rock matrix (m) and

$$\frac{\partial}{\partial t}\left(\phi \sum_{\alpha=1}^{n_{ph}} \rho_\alpha S_\alpha\right)^{f_i} - \nabla\cdot\left(\sum_{\alpha=1}^{n_{ph}} \left(\rho_\alpha \boldsymbol{\lambda_\alpha}\cdot\nabla p\right)\right)^{f_i} = \sum_{i=1}^{n_{\text{frac}}} \rho_\alpha q_\alpha^{f_i,w} + \sum_{\alpha=1}^{n_{ph}} \rho_\alpha \mathscr{Q}_\alpha^{f_i,m} + \sum_{\alpha=1}^{n_{ph}}\sum_{j=1}^{n_{\text{frac}}} \left(\rho_\alpha \mathscr{Q}_\alpha^{f_i,f_j}\right)_{j\neq i}, \quad \text{on} \quad \Omega_{f_i} \subseteq \Re^{n-1}, \tag{2.17}$$

for the explicit (discrete) fracture (f_i). In these equations, n_{ph} is the number of phases. For the purpose of this work, we have only two phases in a single component system (i.e., water and steam). Similar to the previous equations ((2.1)-(2.12)), the superscripts m, f_i and w refer to the rock matrix, the i-th fracture and the wells, respectively. ϕ is the medium porosity. λ_α is the phase mobility, comprising both fluid and rock properties as $\boldsymbol{\lambda_\alpha} = \frac{k_{r,\alpha}}{\mu_\alpha}\mathbf{K}$, where $k_{r,\alpha}$ and μ_α are the fluid relative permeability and the fluid viscosity of phase α. $\mathbf{K}$ is the absolute permeability of the rock and can be written as a tensor in presence of anisotropy. Moreover, ρ_α is the fluid density and S_α is the saturation of phase α. In these equations p is the fluid pressure and one of the primary unknowns. q_α is the source term (i.e., wells) for phase α. The summation of the saturation of all the phases equal the unity, i.e., $\sum_{\alpha=1}^{n_{ph}} S_\alpha = 1$.

Similar to the previous sections (e.g., isothermal multiphase flow), $\mathscr{Q}_\alpha^{m,f_i}$ and $\mathscr{Q}_\alpha^{f_i,m}$ are the phase flux exchanged between the rock matrix m and the fracture f_i, and $\mathscr{Q}_\alpha^{f_i,f_j}$ represents the influx of phase α from the fracture f_j to the fracture f_i. Mass conservation ensures that $\iiint_V \mathscr{Q}_\alpha^{m,f_i}\, dV = -\iint_{A_{f_i}} \mathscr{Q}_\alpha^{f_i,m}\, dA$ and $\iint_{A_{f_i}} \mathscr{Q}_\alpha^{f_i,f_j}\, dA = -\iint_{A_{f_j}} \mathscr{Q}_\alpha^{f_j,f_i}\, dA$.

The equations to calculate the volumetric well fluxes and the volumetric flux exchanges between matrix and fractures used in this section are identical to previous sections. The well fluxes are obtained via Peaceman well model [86] both for the rock matrix and the fractures:

$$q_\alpha^{m,w} = \frac{PI\cdot\lambda_\alpha^{*}\cdot(p^w - p^m)}{\Delta V} \tag{2.3, revisited}$$

$$q_\alpha^{f_i,w} = \frac{PI\cdot\lambda_\alpha^{*}\cdot(p^w - p^{f_i})}{\Delta A}. \tag{2.4, revisited}$$

The volumetric flux exchanges between the matrix and fractures are similarly calculated:

$$\begin{aligned}\mathcal{Q}_\alpha^{m,f_i} &= CI^{m,f_i}\cdot\lambda_\alpha^*\cdot(p^{f_i}-p^m)\\ \mathcal{Q}_\alpha^{m,f_i} &= CI^{f_i,m}\cdot\lambda_\alpha^*\cdot(p^m-p^{f_i})\\ \mathcal{Q}_\alpha^{f_i,f_j} &= CI^{f_i,f_j}\cdot\lambda_\alpha^*\cdot(p^{f_j}-p^{f_i}),\end{aligned} \tag{2.5, revisited}$$

As the connectivity indices (i.e., CI), obtained on all the overlaps between the rock matrix and the fractures, are calculated purely geometrically, they are identical for all the equations in this chapter.

2.3.2. ENERGY BALANCE EQUATIONS

The energy balance equation in the single component water and two phase system with the assumption of local equilibrium on the domain reads

$$\frac{\partial}{\partial t}\left((\rho U)_{eff}\right)^m - \nabla\cdot\left(\sum_{\alpha=1}^{n_{ph}}\left(\rho_\alpha h_\alpha \boldsymbol{\lambda}_{\boldsymbol{\alpha}}\cdot\nabla p\right)\right)^m - \nabla\cdot\left(\Lambda_{eff}\cdot\nabla T\right)^m = \sum_{i=1}^{n_{\text{frac}}}\rho_\alpha h_\alpha q_\alpha^{m,w} + \sum_{\alpha=1}^{n_{ph}}\sum_{i=1}^{n_{\text{frac}}}\rho_\alpha h_\alpha \mathcal{Q}_\alpha^{m,f_i} + \sum_{i=1}^{n_{\text{frac}}}\mathcal{R}^{m,f_i}, \quad \text{on} \quad \Omega_m \subseteq \Re^n, \tag{2.18}$$

on the rock matrix (m) and

$$\frac{\partial}{\partial t}\left((\rho U)_{eff}\right)^{f_i} - \nabla\cdot\left(\sum_{\alpha=1}^{n_{ph}}\left(\rho_\alpha h_\alpha \boldsymbol{\lambda}_{\boldsymbol{\alpha}}\cdot\nabla p\right)\right)^{f_i} - \nabla\cdot\left(\Lambda_{eff}\cdot\nabla T\right)^{f_i} = \sum_{i=1}^{n_{\text{frac}}}\rho_\alpha h_\alpha q_\alpha^{f_i,w} + \sum_{\alpha=1}^{n_{ph}}\rho_\alpha h_\alpha \mathcal{Q}_\alpha^{f_i,m} + \sum_{\alpha=1}^{n_{ph}}\sum_{i=1}^{n_{\text{frac}}}\left(\rho_\alpha h_\alpha \mathcal{Q}_\alpha^{f_i,f_j}\right)_{j\neq i} + \mathcal{R}^{f_i,m} + \sum_{i=1}^{n_{\text{frac}}}\left(\mathcal{R}^{f_i,f_j}\right)_{j\neq i}, \quad \text{on} \quad \Omega_{f_i} \subseteq \Re^{n-1}, \tag{2.19}$$

on the lower dimensional fracture (f_i). In these set of equations, in addition to the previously defined parameters, h_α is the fluid enthalpy of phase α. $(\rho U)_{eff}$ is the effective internal energy per unit of mass and is obtained by

$$(\rho U)_{eff} = \phi\sum_{\alpha=1}^{n_{ph}}\rho_\alpha S_\alpha U_\alpha + (1-\phi)\rho_r U_r, \tag{2.20}$$

where U_α and U_r are the specific internal energy in fluid (for each phase) and rock respectively. Moreover, Λ_{eff} is the effective thermal conductivity defined as

$$\Lambda_{eff} = \phi\sum_{\alpha=1}^{n_{ph}} S_\alpha\Lambda_\alpha + (1-\phi)\Lambda_r. \tag{2.21}$$

Here, Λ_α and Λ_r are the thermal conductivities of phase α and the rock, respectively. One can note that $\Lambda^m_{eff} = \phi^m \sum_{\alpha=1}^{n_{ph}} S_\alpha \Lambda_\alpha + (1-\phi^m)\,\Lambda_r$ and $\Lambda^{f_i}_{eff} = \phi^{f_i} \sum_{\alpha=1}^{n_{ph}} S_\alpha \Lambda_\alpha + (1-\phi^{f_i})\,\Lambda_r$. In addition, $\mathscr{R}^{m,f_i}$, $\mathscr{R}^{f_i,m,}$ and $\mathscr{R}^{f_i,f_j}$ are the conductive heat flux exchanges between the rock matrix and the overlapping fractures, defined identical as in eq. 2.15:

$$\begin{aligned}
\mathscr{R}^{m,f_i} &= CI^{m,f_i} \cdot \Lambda^*_{eff} \cdot (T^{f_i} - T^m) \\
\mathscr{R}^{m,f_i} &= CI^{f_i,m} \cdot \Lambda^*_{eff} \cdot (T^m - T^{f_i}) \\
\mathscr{R}^{f_i,f_j} &= CI^{f_i,f_j} \cdot \Lambda^*_{eff} \cdot (T^{f_j} - T^{f_i}),
\end{aligned} \qquad (2.15\text{, revisited})$$

where, similarly to previous section, $\iiint_V \mathscr{R}^{m,f_i}\, dV = -\iint_{A_{f_i}} \mathscr{R}^{f_i,m}\, dA$, and $\iint_{A_{f_i}} \mathscr{R}^{f_i,f_j}\, dA = -\iint_{A_{f_j}} \mathscr{Q}^{f_j,f_i}\, dA$ hold as well.

2.3.3. CHOICE OF PRIMARY VARIABLES

Following Gibb's phase rule [89], defining two independent primary variables is required to fully define the thermodynamic state of a system consisting of single-component water present in either the liquid or the vapor phase (reference). To this end, two main non-linear formulations exist:

- 1) the natural formulation based on pressure (p), temperature (T) and saturation (S) [90], and
- 2) the molar formulation based on pressure (p) and total enthalpy (H) [87].

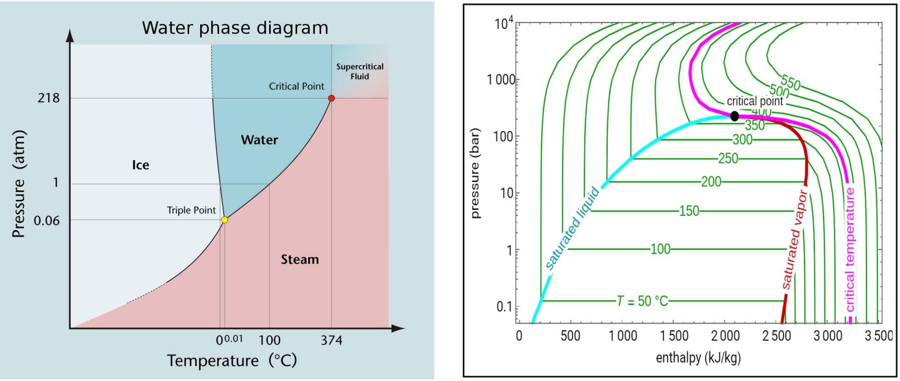

(a) Pressure-Temperature diagram

(b) Pressure-Enthalpy diagram

Figure 2.1: The phase diagrams of pure water. The left plot shows the pressure-temperature (P-T) diagram [91] and the plot on the right illustrates the pressure-enthalpy (p-H) diagram [92]. A point on the line between the water and steam on the P-T diagram corresponds to a horizontal line on the p-H diagram, which connects the saturated liquid curve to the saturated vapor curve.

Use of the natural formulation poses difficulties when defining the thermodynamic state of the system under two-phase conditions. In a pressure-temperature phase diagram (figure 2.1, left), the two-phase region is defined by the vaporization curve as pressure and temperature are dependent under two-phase conditions, i.e. $p = p_{\text{sat}}(T)$. This means that the secondary variables are now only dependent on pressure, and an additional variable, i.e. saturation, is required in order to describe the thermodynamic state of the system [93]. In the two-phase region, the primary variables may be switched to pressure and saturation in order to solve the two-phase system.

Using the molar formulation, the thermodynamic state of the system is uniquely defined under both single- and two-phase conditions as pressure and enthalpy remain independent in the two-phase region, and singularities in the constitutive equations at the critical point are avoided [94]. In a pressure-enthalpy phase diagram (figure 2.1, right), the two-phase region is defined by an area bounded by the bubble- and dew-point curves. This means that the thermodynamic state of the system under two-phase conditions can be determined directly by comparing the total (or mixture) enthalpy (H) of the system to the saturated phase enthalpies [87, 88]. This is illustrated as the following:

$$\text{Phase state} = \begin{cases} \text{Single-phase compressed water,} & \text{if} \quad h_w(p) \geq \quad H \\ \text{Two-phase mixture (water-steam),} & \text{if} \quad h_w(p) < \quad H < h_s(p) \\ \text{Single-phase superheated steam,} & \text{if} \qquad\qquad\quad H \geq h_s(p) \end{cases} \tag{2.22}$$

The saturation of both water and steam can be calculated directly from the mixture enthalpy (H) using:

$$S_w = \frac{\rho_s (h_s - H)}{H\left(\rho_w - \rho_s\right) - \left(h_w \rho_w - h_s \rho_s\right)} \tag{2.23}$$

As the thermodynamic properties are often described as functions of pressure and temperature [93], the natural formulation may be preferred for simulations under single-phase conditions. The molar formulation requires the use of implicit relations in order to describe the properties as functions of pressure and enthalpy, which can affect the accuracy.

Both pressure and temperature (and saturation) are written explicitly in the mass and energy balance equations in (2.16-2.17) and (2.18-2.19). Although enthalpy is also explicitly written in the energy balance equation, it is actually the phase enthalpy (h_α) that this variable is referring to. Application of the molar formulation requires solving the energy balance equation for the total (or mixture) enthalpy (H) instead [87]. In the single-phase region(s) the phase enthalpy is equal to the total enthalpy so that there is no apparent issue using the molar formulation. However, in the two-phase region, both phase- and total enthalpy are two different entities entirely. In order to express the energy balance equation in terms of total enthalpy, the internal energy is re-written according to

$$U = H - PV, \tag{2.24}$$

which states that a change in internal energy in the system is equal to the amount of energy transferred to or from the system, i.e. enthalpy (H), and an associated change in volume at constant pressure (PV) [95]. Here, the PV term represents the work done by compression of the system resulting from a constant external pressure and therefore refers to the effects of matrix compressibility. In terms of the internal energy of the rock (U_r), the work done by compression of the rock itself can be neglected as the rock is assumed non-deformable, i.e., $U_r = H_r$. However, in order to neglect such work, one must assume the absence of poro-seismicity or any geo-mechanical processes (as it has not been taken into account during this PhD project). As the matrix compressibility also affects the fluid volume, neglecting the work done by compression of the system is not that straightforward in terms of the internal energy of the fluid phase (U_α). However, Faust and Mercer [87] state that the compressible work of the fluid volume as a result of an external pressure is negligible, except for fluid volumes of low liquid-phase saturation, i.e., $U_l = H = h_l$ in the compressed water region. This assumption is supported by the knowledge that the vapor phase (i.e. super-heated steam) is highly compressible, especially compared to the low compressibility of the liquid phase. Note that $H = U + PV$, so that the work done by compression of the fluid as a result of the fluid pressure itself is taken into account. This allows re-writing the energy balance equation in terms of the required total enthalpy (H) as

$$\frac{\partial}{\partial t}\left(\left(1-\phi\right)\rho_r H_r + \phi\rho_t H\right) - \nabla\cdot\left(\rho_l h_l \lambda_l \cdot \nabla p\right) - \nabla\cdot\left(\Lambda_{eff}\cdot\nabla T\right) = \rho_l h_l q_l \tag{2.25}$$

for the single-phase compressed water region in which $H = h_l$. In the two-phase region, the total enthalpy H is defined as

$$H = \frac{\rho_l S_l h_l + \rho_v S_v h_v}{\rho_t}, \quad \text{with} \rho_t = \rho_l S_l + \rho_v S_v \tag{2.26}$$

where the subscripts l and v refer to the liquid and vapor phases, respectively. In addition, Faust and Mercer (1979) [87] propose expanding the temperature gradient in the conductive flux in order to re-write the energy balance equation in terms of the total enthalpy H. This approach is illustrated by

$$\nabla\cdot\left(\Lambda_{eff}\cdot\nabla T\right) = \nabla\cdot\left(\Lambda_{eff}\left(\frac{\partial T}{\partial p}\right)_H \cdot\nabla p + \Lambda_{eff}\left(\frac{\partial T}{\partial H}\right)_p \cdot\nabla H\right) \tag{2.27}$$

and applicable as temperature is treated as a function of both pressure and enthalpy. Note that the derivative of temperature with respect to pressure at constant enthalpy is equal to the Joule-Thomson coefficient [94].

Considering the molar formulation, the modified extended energy conservation equation now reads

$$\begin{aligned}\frac{\partial}{\partial t}\left(\rho H\right)^m_t - \nabla\cdot\left(\rho_{(fl)} h_{(fl)} \lambda_{(fl)} \cdot\nabla p\right)^m - \nabla\cdot\left(\Lambda_{eff}\left(\frac{\partial T}{\partial p}\right)_H \cdot\nabla p + \Lambda_{eff}\left(\frac{\partial T}{\partial H}\right)_p \cdot\nabla H\right)^m = \\ \rho_{(fl)} h_{(fl)} q^{m,w}_{(fl)} + \sum_{i=1}^{n_{frac}} \rho^*_{(fl)} h^*_{(fl)} \mathcal{Q}^{m,f_i} + \sum_{i=1}^{n_{frac}} \mathcal{R}^{m,f_i}\end{aligned} \tag{2.28}$$

for the rock matrix (m), and

$$\frac{\partial}{\partial t}(\rho H)_t^{f_i} - \nabla\cdot\left(\rho_{(fl)} h_{(fl)} \lambda_{(fl)} \cdot \nabla p\right)^{f_i} - \nabla\cdot\left(\Lambda_{eff}\left(\frac{\partial T}{\partial p}\right)_H \cdot \nabla p + \Lambda_{eff}\left(\frac{\partial T}{\partial H}\right)_p \cdot \nabla H\right)^{f_i} = \\ \rho_{(fl)} h_{(fl)} q_{(fl)}^{f_i,w} + \rho^*_{(fl)} h^*_{(fl)} \mathscr{Q}^{f_i,m} + \sum_{j=1}^{n_{frac}} \left(\rho^*_{(fl)} h^*_{(fl)} \mathscr{Q}^{f_i,f_j}\right)_{j\neq i} + \mathscr{R}^{m,f_i} + \sum_{i=1}^{n_{frac}} \left(\mathscr{R}^{m,f_i}\right)_{j\neq i} \tag{2.29}$$

for the fracture (f_i). Note that equations (2.28) and (2.29) are written in terms of the total accumulation of enthalpy in the system, which is defined as $(\rho H)_t^\beta = (1-\phi^\beta)\rho_r H_r + \phi^\beta \rho_{(fl)} H_{(fl)}$ on an arbitrary domain β.

2.3.4. CONSTITUTIVE EQUATIONS AND CORRELATIONS

The mass and energy conservation equations presented in the previous section require additional constitutive equations in order to describe the model problem. The thermodynamic properties of pure water and steam are expressed by these constitutive equations, which, in turn, are functions of the primary variables. These correlations form the so-called fluid model, which is presented in this section for both the natural and molar variable formulations. The natural formulation employs correlations developed by [96] and the molar formulation employs correlations developed by [97]. All variables are presented in SI units.

Both formulations apply the same correlations for the porosity ϕ and rock internal energy U_r. These correlations are given by

$$\phi(p) = \phi_0 \times \exp\left(c_r\left(p - p_0\right)\right) \tag{2.30}$$

in which c_r, ϕ_0 and p_0 are the rock compressibility, initial reservoir porosity and initial reservoir pressure, respectively, and

$$U_r(T) = C_p \times T \tag{2.31}$$

where C_p is the rock specific heat capacity. Note that $U_r = H_r$ is assumed, as described in the previous section.

NATURAL FORMULATION

The density of the liquid phase in [kg/m^3] is treated as a function of pressure and temperature and is given by

$$\rho_l(p,T) = \rho_{l,s}(T)\left[1 + c_f(T)\left(p - p_{\text{sat}}\right)\right] \tag{2.32}$$

where the saturation pressure p_{sat} has a constant value of 10^5 [Pa], and the density of the liquid phase at saturation conditions $\rho_{l,s}$ and fluid compressibility c_f are obtained from empirical correlations as

$$\rho_{l,s}(T) = \begin{cases} -0.0032T^2 + 1.7508T + 757.5, & \text{for} \quad T \leq 623.15\,[\mathrm{K}] \\ -0.5214T^2 + 652.73T - 203714, & \text{for} \quad T \geq 623.15\,[\mathrm{K}] \end{cases} \tag{2.33}$$

$$c_f(T) = \left(0.0839T^2 + 652.73T - 203714\right) \times 10^{-12}, \quad \text{for} \quad 273\,[\mathrm{K}] < T < 647\,[\mathrm{K}] \tag{2.34}$$

The liquid phase enthalpy in [J/kg] is treated as a function of pressure and temperature and is given by

$$h_l(p,T) = U_{l,s} + C_{p,l}(T - T_{\mathrm{sat}}) + \frac{p}{\rho_l} \tag{2.35}$$

where the saturation temperature T_{sat} has a constant value of 373 [K], the specific heat capacity of the liquid phase $C_{p,l}$ is constant and has a value of 4200 $\left[\frac{\mathrm{J}}{\mathrm{kg.K}}\right]$ and the liquid phase internal energy at saturation conditions $U_{l,s}$ has a constant value of 420000[J/kg].

The viscosity of the liquid phase in [Pa.s] is treated as a function of temperature and is given by

$$\mu_l(T) = 2.414 \times 10^{-5} \times 10^{\left(\frac{247.8}{T-140}\right)} \tag{2.36}$$

Molar formulation

The correlations used to express the dependent variables in terms of pressure and enthalpy (i.e. molar formulation) are limited to the following range of validity

$$\begin{cases} p: 1 - 175\,[\mathrm{bar}] \\ H: 209 - 3175\,[\mathrm{kJ/kg}] \\ T: 274.15 - 573.15\,[\mathrm{K}] \end{cases} \tag{2.37}$$

The pressure and enthalpy as input to the following correlations are in 10^{-6} [bar] and $10^{-7}\left[\frac{\mathrm{kJ}}{\mathrm{kg}}\right]$, respectively.

The liquid and vapor phase densities in [kg/m^3] are treated as functions of pressure and enthalpy and are given by

$$\begin{aligned}\rho_l(p,H) = (&1.00207 + 4.42607 \times 10^{-11}p - 5.47456 \times 10^{-12}H + 5.02875 \times 10^{-21}Hp \\ &- 1.24791 \times 10^{-21}H^2) \times 10^3\end{aligned} \tag{2.38}$$

$$\begin{aligned}\rho_v(p,H) = (&-2.26162 \times 10^{-5} + 4.38441 \times 10^{-9}p - 1.79088 \times 10^{-19}pH \\ &+ 3.69276 \times 10^{-36}p^4 + 5.17644 \times 10^{-41}pH^3) \times 10^3\end{aligned} \tag{2.39}$$

The saturated liquid and vapor phase enthalpies in [J/kg] are treated as functions of pressure and are given by

$$h_l(p) = (7.30984 \times 10^{9} + 1.29239 \times 10^{2} p - 1.00333 \times 10^{-6} p^{2} + 3.9881 \times 10^{-15} p^{3} - 9.90697 \times 10^{15} p^{-1} + 1.29267 \times 10^{22} p^{-2} - 6.28359 \times 10^{27} p^{-3}) \times 10^{-7} \tag{2.40}$$

$$h_v(p) = (2.82282 \times 10^{10} - 3.91952 \times 10^{5} p^{-1} + 2.54342 \times 10^{21} p^{-2} - 9.38879 \times 10^{-8} p^{2}) \times 10^{-7} \tag{2.41}$$

Temperature in [K] is treated as a function of pressure and enthalpy in the single-phase regions. The temperature in the compressed water region is given by

$$T(p,H) = 273.15 - 2.41231 + 2.5622 \times 10^{-8} H - 9.31415 \times 10^{-17} p^{2} - 2.2568 \times 10^{-19} H^{2} \tag{2.42}$$

and in the superheated steam region by

$$T(p,H) = 273.15 - 374.669 + 4.79921 \times 10^{-6} p - 6.33606 \times 10^{-15} p^{2} + 7.39386 \times 10^{-19} H^{2} - 3.3372 \times 10^{34} H^{-2} p^{-2} + 3.57154 \times 10^{19} p^{-3} - 1.1725 \times 10^{-37} H^{3} p - 2.26861 \times 10^{43} H^{-4} \tag{2.43}$$

Note that in the two-phase region, the saturated liquid phase enthalpy is used in the equation instead.

The liquid and vapor phase viscosities in [Pa.s] are treated as functions of temperature and are given by

$$\mu_l(T) = \left(241.4 \times 10^{\left(\frac{247.8}{T-273.15+133.15}\right)}\right) \times 10^{-4} \tag{2.44}$$

$$\mu_l(T) = (0.407(T - 273.15) + 80.4) \times 10^{-4} \tag{2.45}$$

In order to set the initial and injection properties identically between both formulations, the enthalpy is computed from temperature using

$$h_l(p,T) = \frac{-B + \sqrt{B^{2} - 4D\left(A + Cp^{2} - (T - 273.15)\right)}}{2D} \tag{2.46}$$

where the constants $A = -2.41231$, $B = 2.5622 \times 10^{-8}$, $C = -9.31415 \times 10^{-17}$ and $D = -2.2568 \times 10^{-19}$ are used. Note that this equation is only valid in the compressed water region, and therefore it is assumed that only the liquid phase is present in the injection well.

The water saturation is computed using equation (2.23) presented in this chapter. This equation yields the pressure-enthalpy phase diagram as illustrated in figure 2.2.

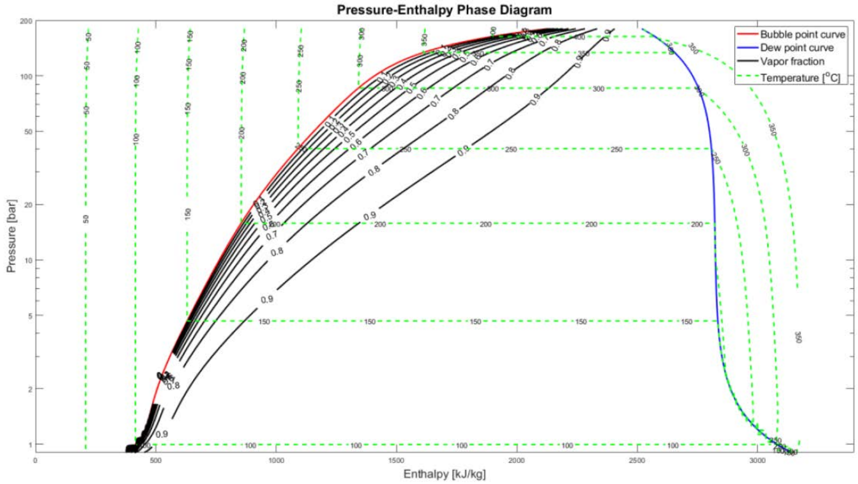

Figure 2.2: The pressure-enthalpy phase diagram of pure water with vapor fraction intermediate lines (in black solid curves inside the two-phase region).

There exists considerable uncertainty regarding a proper correlation for the relative permeability of the two phases in geothermal systems. Watanabe et al. (2017) [98] apply the Corey functions for relative permeability, whereas Faust and Mercer (1977) [97] propose a variation on the Corey functions in which vaporization dominates condensation (a drainage displacement process). Verma functions are also often applied for porous rocks. They are especially applicable to water-steam two-phase flows as they are derived based on the enhancement of steam relative permeability due to phase transformation [98]. Nield and Bejan (2006) [99] state that “experience has shown that the main qualitative features of convection flows are not sensitive to the precise form of the relative permeability versus saturation relationship” and therefore suggest the application of a linear relationship. In an effort not to increase the non-linearity presented by the fluid model any further, a linear relation for the relative permeability is chosen at this point such that

$$k_{r,\alpha}(S_\alpha) = S_\alpha \tag{2.47}$$

for a given phase α.

In the next chapter, the fine-scale simulation strategy including the fine-scale discretization, the coupling approaches and the linearization of the nonlinear equations will be explained. Moreover, both the classic and the projection-based embedded discrete fracture models (EDFM and pEDFM) will be described.

II

FINE-SCALE STRATEGIES

3

DISCRETIZATION AND SIMULATION STRATEGY AT FINE-SCALE

The system of equations presented in the previous chapter (2) for all the formulations covered in this work (i.e., isothermal multiphase flow, low-enthalpy and high-enthalpy geothermal flow) are in the continuous domains and are all nonlinear. However, they do not have analytical solutions and they are mostly solved numerically, and the computer models developed to solve them are thus numerical methods. Therefore, these continuous equations need to be re-written in discrete form. This process is called discretization. The most common approach for the spatial discretization in the realm of fluid flow modeling in porous media is the so-called finite volume method (FVM). Beside the simplicity that it provides, this approach is crucial, especially because it ensures mass conservation [100]. Moreover, the convective terms in the mass and energy conservation equations are discretized with an upwind two-point flux approximation (TPFA) in space. Regarding temporal discretization, both implicit and explicit time integration schemes have been proposed in the literature. However, in this work, the equations are discretized in time with a backward (implicit) Euler scheme. In addition, the solution strategy to couple the sets of the equations in all the fluid models in this work is the so-called fully-implicit approach (FIM) which will be briefly explained later in this chapter.

During the discretization stage, the nonlinear equations need to be linearized using a linearization scheme. This is an integral part of the discretization as a linear system of equations is the input to the linear solver in the simulation model. At this stage, the equations are written in residual forms and the linearization of the nonlinear terms in all the residuals is done using Newton-Raphson method [100, 101], which will be covered further in this chapter.

The discretization of all the equations presented in this chapter includes the explicit representation of the fractures using the embedded discrete fracture models and extra terms will be added to the system of equations. After explaining the discretization, cou-

---

Various parts of this chapter have been extracted from a number of the author's publications.

pling strategy and linearization of these equations, the embedded discrete fracture models will be described in this chapter.

3.1. DISCRETIZATION OF THE CONTINUOUS EQUATIONS

The discretization of the nonlinear equations is done using the finite volume method (FVM). The equations are discretized with a two-point-flux-approximation (TPFA) finite-volume scheme in space and a backward (implicit) Euler scheme in time. This will be explained section by section following the equations presented in the previous chapter. Independent structured grids are generated for a three-dimensional (3D) porous medium and the 2D fracture planes. An illustration is presented in figure 3.1.

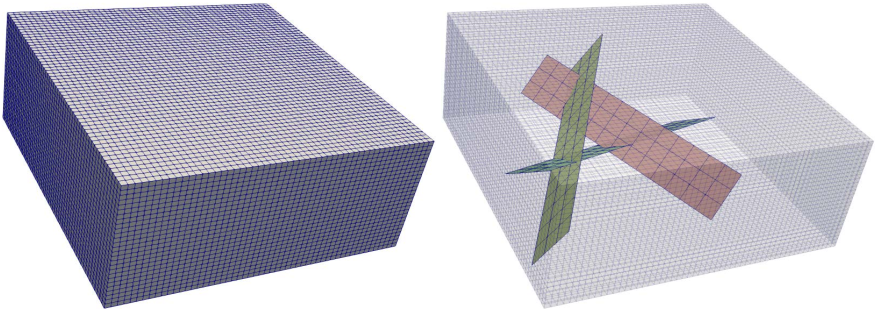

(a) matrix grid (b) fracture grids

Figure 3.1: The independent matrix 3D grid and the fractures 2D grids are shown. Note that each domain has its own grid and that any fracture orientation can be considered.

3.1.1. MULTIPHASE FLOW IN FRACTURED POROUS MEDIA (ISOTHERMAL)

The coupled system of non-linear equations (2.1)-(2.2) is discretized by calculating the fluxes. The advective TPFA flux of phase α between the control volumes i and j reads

$$F_{\alpha,ij} = \rho^*_\alpha \frac{k^*_{r_\alpha}}{\mu^*_\alpha} T_{ij}(p_i - p_j). \tag{3.1}$$

Here, $T_{ij} = \frac{A_{ij}}{d_{ij}} K^H_{ij}$ is the transmissibility between the cells i and j. A_{ij} is the interface area between these two cells, d_{ij} is the distance between the cells centers and K^H_{ij} is the harmonic average of the two permeabilities. The terms indicated with the superscript $*$ are evaluated using a phase potential upwind scheme. Following the EDFM and the pEDFM [44–46] approaches, the fluxes between a rock matrix cell i and a fracture cell j are modeled as

$$\mathscr{F}^{m,f}_{\alpha,ij} = -\mathscr{F}^{f,m}_{\alpha,ij} = -\rho^*_\alpha \frac{k^*_{r_\alpha}}{\mu^*_\alpha} T^{m,f}_{ij} (p^m_i - p^f_j), \tag{3.2}$$

Similarly, the flux exchange between intersecting fracture elements i (belonging to fracture f_i) and j (belonging to fracture f_j) is modeled as

$$\mathscr{F}^{f_i,f_j}_{\alpha,ij} = -\mathscr{F}^{f_j,f_i}_{\alpha,ij} = -\rho^*_\alpha \frac{k^*_{r_\alpha}}{\mu^*_\alpha} T^{f_i,f_j}_{ij}\left(p^{f_i}_i - p^{f_j}_j\right). \tag{3.3}$$

The transmissibilities $T^{m,f}_{ij}$ and T^{f_i,f_j}_{ij} are explained further in section of the fracture models (see section 3.3).

Thus, at each time-step the following system of equations is solved

$$\left(\frac{(\phi\rho_\alpha S_\alpha)^{n+1}_i - (\phi\rho_\alpha S_\alpha)^n_i}{\Delta t}\right)^m + \left(\sum_{j=1}^{N_n} F_{\alpha,ij}\right)^m + \sum_{k=1}^{n_{\text{frac}}}\left(\sum_{j=1}^{N_{f_k}} \mathscr{F}^{m,f_k}_{\alpha,ij}\right) = \rho_\alpha q^{m,w}_{\alpha,i}, \quad \forall\, i \in \{1,\ldots,N_m\} \tag{3.4}$$

in the rock matrix and

$$\left(\frac{(\phi\rho_\alpha S_\alpha)^{n+1}_i - (\phi\rho_\alpha S_\alpha)^n_i}{\Delta t}\right)^{f_h} + \left(\sum_{j=1}^{N_n} F_{\alpha,ij}\right)^{f_h} + \sum_{j=1}^{N_m} \mathscr{F}^{f_h,m}_{\alpha,ij} + \sum_{k=1}^{n_{\text{frac}}}\left(\sum_{j=1}^{N_{f_k}} \mathscr{F}^{f_h,f_k}_{\alpha,ij}\right) = \rho_\alpha q^{f_h,w}_{\alpha,i}, \quad \forall\, i \in \{1,\ldots,N_{f_h}\} \tag{3.5}$$

in each fracture f_h. Here, N_m and N_{f_k} are the number of grid cells in the rock matrix m and and the fracture f_k respectively. N_n indicates the number of the neighboring cells (2 in 1D, 4 in 2D, 6 in 3D).

3.1.2. Mass and heat flow in low-enthalpy fractured porous media

The coupled system of non-linear equations described in section 2.2 ,i.e., equations (2.6)-(2.12) with two main unknowns (i.e., p, T) is discretized similarly by calculating the TPFA mass and heat fluxes.

The mass flux exchange between each two neighboring control volumes i and j (inside one medium) using TPFA scheme can be written as

$$F_{ij} = \frac{\rho^*_{(fl)}}{\mu^*} T_{ij}(p_i - p_j), \tag{3.6}$$

where $T_{ij} = \frac{A_{ij}}{d_{ij}} K^H_{ij}$ denotes the transmissibility between grid cells i and j. A_{ij} is the interface area between the two grid cells, d_{ij} is the distance between their cell centers and K^H_{ij} is the harmonic average of the permeabilities set at the interface of grid cells i and j. The properties with superscript $*$ are obtained using the upwind scheme. Note that density ρ and viscosity μ are functions of pressure and temperature.

The mass flux between each two non-neighboring grid cells i and j (either matrix-fracture or fracture-fracture connectivities) is obtained using the EDFM/pEDFM formulations. The flux between a rock matrix (denoted as m) cell i and a fracture (denoted as f) cell j is defined as

$$\mathscr{F}_{ij}^{m,f} = -\mathscr{F}_{ij}^{f,m} = -\frac{\rho^*_{(fl)}}{\mu^*} T_{ij}^{m,f}(p_i^m - p_j^f), \tag{3.7}$$

Similar to mass flux between matrix and fracture, the mass flux between two non-neighboring and intersecting fracture elements i (on fracture f_i) and j (on fracture f_j) is given as

$$\mathscr{F}_{ij}^{f_i,f_j} = -\mathscr{F}_{ij}^{f_i,f_j} = -\frac{\rho^*_{(fl)}}{\mu^*} T_{ij}^{f_i,f_j}(p_i^f - p_j^g), \tag{3.8}$$

where the transmissibilities $T_{ij}^{m,f}$ and $T_{ij}^{f_i,f_j}$ are calculated and described in the next section (fracture models, 3.3).

The convective heat flux exchange between the neighboring control volumes i and j reads

$$\breve{F}_{ij} = \frac{\rho^*_{(fl)} H^*_{(fl)}}{\mu^*} T_{ij}(p_i - p_j). \tag{3.9}$$

Here, $H^*_{(fl)}$ is the enthalpy of fluid determined at the interface between grid cells i and j. One can conclude that $\breve{F}_{ij} = H^*_{(fl)} F_{ij}$.

Similarly, the convective heat flux exchange between the non-neighboring elements can be obtained via multiplication of their mass flux exchange ($\mathscr{F}_{ij}$) by the effective enthalpy ($H^*_{(fl)}$) determined at the intersection of the two overlapping elements. Namely, $\breve{\mathscr{F}}_{ij} = H^*_{(fl)} \mathscr{F}_{ij}$.

The conductive heat flux exchange between each two neighboring cells i and j is written as

$$G_{ij} = \mathbb{T}_{cond,ij}(T_i - T_j). \tag{3.10}$$

where, $\mathbb{T}_{cond,ij} = \frac{A_{ij}}{d_{ij}}(\Lambda_{eff})^H_{ij}$ is the conductive heat transmissibility between the grid cells i and j. The terms A_{ij}, d_{ij} and $(\Lambda_{eff})^H_{ij}$ are the interface area, the distance from the cell centers and the harmonic average of the effective conductivity set at the interface between grid cells i and j respectively.

The conductive heat flux exchange between the non-neighboring elements i and j is obtained as

$$\mathscr{G}_{ij}^{m,f} = -\mathscr{G}_{ij}^{f,m} = -\mathbb{T}_{cond,ij}^{m,f}(T_i^m - T_j^f), \tag{3.11}$$

for matrix-fracture connectivities and

$$\mathscr{G}_{ij}^{f_i,f_j} = -\mathscr{G}_{ij}^{f_i,f_j} = -\mathbb{T}_{cond,ij}^{f_i,f_j}(T_i^f - T_j^g). \tag{3.12}$$

for fracture-fracture connectivities. The conductive heat transmissibilities for matrix-fracture ($\mathbb{T}_{cond,ij}^{m,f}$) and fracture-fracture ($\mathbb{T}_{cond,ij}^{f_i,f_j}$) connectivities are calculated following the same formulations of the EDFM/pEDFM which are covered later in this chapter.

At every time-step the fine-scale discrete mass balance equation reads

$$\left(\frac{(\phi\rho_{(fl)})_i^{n+1}-(\phi\rho_{(fl)})_i^{n}}{\Delta t}\right)^{m}+\left(\sum_{j=1}^{N_n}F_{ij}\right)^{m}+\sum_{k=1}^{n_{\text{frac}}}\left(\sum_{j=1}^{N_{f_k}}\mathscr{F}_{ij}^{m,f_k}\right)=\left(\rho_{(fl)}q^{m,w}\right)_i, \quad \forall\, i\in\{1,\dots,N_m\} \tag{3.13}$$

for element i in the rock matrix m and

$$\left(\frac{(\phi\rho_{(fl)})_i^{n+1}-(\phi\rho_{(fl)})_i^{n}}{\Delta t}\right)^{f_h}+\left(\sum_{j=1}^{N_n}F_{ij}\right)^{f_h}+\sum_{j=1}^{N_{f_k}}\mathscr{F}_{ij}^{f_h,m}+\sum_{k=1}^{n_{\text{frac}}}\left(\sum_{j=1}^{N_{f_k}}\mathscr{F}_{ij}^{f_h,f_k}\right)=\left(\rho_{(fl)}q^{f_h,w}\right)_i, \quad \forall\, i\in\{1,\dots,N_{f_h}\} \tag{3.14}$$

for element i in the fracture f_h. N_m and N_{f_k} denote the number of elements in the rock matrix m and the fracture f_k respectively. N_n is the number of neighboring grid cells.

Similarly, the fine-scale discrete form of the energy balance equation at each time-step is written as:

$$\begin{aligned}&\left(\frac{((\rho U)_{eff})_i^{n+1}-((\rho U)_{eff})_i^{n}}{\Delta t}\right)^{m}+\left(\sum_{j=1}^{N_n}\breve{F}_{ij}\right)^{m}+\sum_{k=1}^{n_{\text{frac}}}\left(\sum_{j=1}^{N_{f_k}}\breve{\mathscr{F}}_{ij}^{m,f_k}\right)\\&\quad+\left(\sum_{j=1}^{N_n}\breve{G}_{ij}\right)^{m}+\sum_{k=1}^{n_{\text{frac}}}\left(\sum_{j=1}^{N_{f_k}}\breve{\mathscr{G}}_{ij}^{m,f_k}\right)=\left(\rho_{(fl)}H_{(fl)}q^{m,w}\right)_i, \quad \forall\, i\in\{1,\dots,N_m\}\end{aligned} \tag{3.15}$$

for element i in the rock matrix m and

$$\begin{aligned}&\left(\frac{((\rho U)_{eff})_i^{n+1}-((\rho U)_{eff})_i^{n}}{\Delta t}\right)^{f_h}+\left(\sum_{j=1}^{N_n}\breve{F}_{ij}\right)^{f_h}+\sum_{j=1}^{N_m}\breve{\mathscr{F}}_{ij}^{f_h,m}+\sum_{k=1}^{n_{\text{frac}}}\left(\sum_{j=1}^{N_{f_k}}\breve{\mathscr{F}}_{ij}^{f_h,f_k}\right)\\&+\left(\sum_{j=1}^{N_n}\breve{G}_{ij}\right)^{f_h}+\sum_{j=1}^{N_m}\breve{\mathscr{G}}_{ij}^{f_h,m}+\sum_{k=1}^{n_{\text{frac}}}\left(\sum_{j=1}^{N_{f_k}}\breve{\mathscr{G}}_{ij}^{f_h,f_k}\right)=\left(\rho_{(fl)}H_{(fl)}q^{f_h,w}\right)_i, \quad \forall\, i\in\{1,\dots,N_{f_h}\}\end{aligned} \tag{3.16}$$

for element i in the fracture f_h.

3.1.3. MASS AND HEAT FLOW IN HIGH-ENTHALPY FRACTURED POROUS MEDIA

The system of equations (2.16)-(2.19) from section 2.3 is discretized with similar discretization schemes as in previously mentioned formulations. However, as discussed in section 2.3.3, there exist two different choices for selection of the primary variables, i.e., either pressure and temperature (p, T), or pressure and total enthalpy (p, H). In this section, pressure and total enthalpy (p, H) are chosen as the primary unknowns.

First, the discrete mass fluxes need to be calculated. The mass flux of phase α between each two neighboring control volumes i and j (inside one medium) using the TPFA scheme can be written as

$$F_{\alpha,ij} = \rho^*_\alpha \frac{k^*_{r_\alpha}}{\mu^*_\alpha} T_{ij}(p_i - p_j), \tag{3.17}$$

where $T_{ij} = \frac{A_{ij}}{d_{ij}} K^H_{ij}$ is the geological or rock transmissibility between cells i and j. A_{ij} is the interface area between cells i and j, d_{ij} is the distance between the cells centers and K^H_{ij} is the harmonic average of the two permeabilities. The EDFM/pEDFM fluxes between a matrix cell i and a fracture cell j are modeled as

$$\mathscr{F}^{m,f}_{\alpha,ij} = -\mathscr{F}^{f,m}_{\alpha,ij} = -\rho^*_\alpha \frac{k^*_{r_\alpha}}{\mu^*_\alpha} T^{m,f}_{ij}(p^m_i - p^f_j), \tag{3.18}$$

Correspondingly, the flux exchange between the intersecting fracture elements i (belonging to fracture f_i) and j (belonging to fracture f_j) is written as

$$\mathscr{F}^{f_i,f_j}_{\alpha,ij} = -\mathscr{F}^{f_j,f_i}_{\alpha,ij} = -\rho^*_\alpha \frac{k^*_{r_\alpha}}{\mu^*_\alpha} T^{f_i,f_j}_{ij}(p^{f_i}_i - p^{f_j}_j). \tag{3.19}$$

The transmissibilities $T^{m,f}_{ij}$ and T^{f_i,f_j}_{ij} are calculated identical to their counterparts in the previous formulations.

Next, the convective and conductive heat fluxes are calculated. The convective heat flux exchange between the neighboring control volumes i and j for each phase α reads

$$\check{F}_{\alpha,ij} = \frac{\rho^*_\alpha h^*_\alpha}{\mu^*_\alpha} T_{ij}(p_i - p_j). \tag{3.20}$$

Here, h^*_α is the enthalpy of phase α in fluid determined at the interface between grid cells i and j. Conclusively, $\check{F}_{\alpha,ij} = h^*_\alpha F_{\alpha,ij}$. The convective heat flux exchange between the non-neighboring elements can be obtained via multiplication of their mass flux exchange $(\mathscr{F}_{\alpha,ij})$ by the effective phase enthalpy (h^*_α) determined at the intersection of two overlapping elements, i.e., $\check{\mathscr{F}}_{\alpha,ij} = h^*_\alpha \mathscr{F}_{\alpha,ij}$.

The conductive heat flux between the two neighboring cells i and j (belonging to one medium) is written as

$$G_{ij} = \mathbb{T}_{cond,ij}(T_i - T_j). \tag{3.21}$$

where, $\mathbb{T}_{cond,ij} = \frac{A_{ij}}{d_{ij}} (\Lambda_{eff})^H_{ij}$ is the transmissibility between grid cells i and j. A_{ij}, d_{ij} and $(\Lambda_{eff})^H_{ij}$ are the interface area, the distance from the cell centers and the harmonic average of the effective conductivity at the interface between grid cells i and j respectively. Please note that the effective conductivity is calculated via equation (2.21). The conductive heat flux exchange between non-neighboring elements i and j is obtained as

$$\mathscr{G}_{ij}^{m,f} = -\mathscr{G}_{ij}^{f,m} = -\mathbb{T}_{cond,ij}^{m,f}(T_i^m - T_j^f). \tag{3.22}$$

for matrix-fracture connectivities and

$$\mathscr{G}_{ij}^{f_i,f_j} = -\mathscr{G}_{ij}^{f_i,f_j} = -\mathbb{T}_{cond,ij}^{f_i,f_j}(T_i^f - T_j^g). \tag{3.23}$$

for fracture-fracture connectivities. The conductive heat transmissibilities for matrix-fracture ($\mathbb{T}_{cond,ij}^{m,f}$) and fracture-fracture ($\mathbb{T}_{cond,ij}^{f_i,f_j}$) connectivities are explained later in this chapter.

At each time-step the fine-scale discrete mass balance equation is written as

$$\left(\frac{\left(\phi\sum_{\alpha=1}^{n_{ph}}\rho_\alpha S_\alpha\right)_i^{n+1} - \left(\phi\sum_{\alpha=1}^{n_{ph}}\rho_\alpha S_\alpha\right)_i^{n}}{\Delta t}\right)^m + \left(\sum_{\alpha=1}^{n_{ph}}\left(\sum_{j=1}^{N_n} F_{\alpha,ij}\right)\right)^m + \sum_{\alpha=1}^{n_{ph}}\left(\sum_{k=1}^{n_{\text{frac}}}\left(\sum_{j=1}^{N_{f_k}}\mathscr{F}_{\alpha,ij}^{m,f_k}\right)\right) = \left(\sum_{\alpha=1}^{n_{ph}}\rho_\alpha q_\alpha^{m,w}\right)_i, \quad \forall\, i \in \{1,\dots,N_m\} \tag{3.24}$$

for element i in the rock matrix m and

$$\left(\frac{\left(\phi\sum_{\alpha=1}^{n_{ph}}\rho_\alpha S_\alpha\right)_i^{n+1} - \left(\phi\sum_{\alpha=1}^{n_{ph}}\rho_\alpha S_\alpha\right)_i^{n}}{\Delta t}\right)^{f_h} + \left(\sum_{\alpha=1}^{n_{ph}}\left(\sum_{j=1}^{N_n} F_{\alpha,ij}\right)\right)^{f_h} + \sum_{\alpha=1}^{n_{ph}}\left(\sum_{j=1}^{N_{f_k}}\mathscr{F}_{\alpha,ij}^{f_h,m}\right) + \sum_{\alpha=1}^{n_{ph}}\left(\sum_{k=1}^{n_{\text{frac}}}\left(\sum_{j=1}^{N_{f_k}}\mathscr{F}_{\alpha,ij}^{f_h,f_k}\right)\right) = \left(\sum_{\alpha=1}^{n_{ph}}\rho_\alpha q_\alpha^{f_h,w}\right)_i, \quad \forall\, i \in \{1,\dots,N_{f_h}\} \tag{3.25}$$

for element i in the fracture f_h. On a similar pattern, the fine-scale discrete form of the energy balance equation at each time-step is written as:

$$\left(\frac{((\rho U)_{eff})_i^{n+1} - ((\rho U)_{eff})_i^{n}}{\Delta t}\right)^m + \left(\sum_{\alpha=1}^{n_{ph}}\left(\sum_{j=1}^{N_n}\breve{F}_{\alpha,ij}\right)\right)^m + \sum_{\alpha=1}^{n_{ph}}\left(\sum_{k=1}^{n_{\text{frac}}}\left(\sum_{j=1}^{N_{f_k}}\breve{\mathscr{F}}_{\alpha,ij}^{m,f_k}\right)\right) + \left(\sum_{j=1}^{N_n}\breve{G}_{ij}\right)^m + \sum_{k=1}^{n_{\text{frac}}}\left(\sum_{j=1}^{N_{f_k}}\breve{\mathscr{G}}_{ij}^{m,f_k}\right) = \left(\sum_{\alpha=1}^{n_{ph}}\rho_\alpha h_\alpha q_\alpha^{m,w}\right)_i, \quad \forall\, i \in \{1,\dots,N_m\} \tag{3.26}$$

for element i in the matrix m and

$$\left(\frac{\left((\rho U)_{eff}\right)_i^{n+1}-\left((\rho U)_{eff}\right)_i^{n}}{\Delta t}\right)^{f_h}+\left(\sum_{\alpha=1}^{n_{ph}}\left(\sum_{j=1}^{N_n}\breve{F}_{\alpha,ij}\right)\right)^{f_h}+\sum_{\alpha=1}^{n_{ph}}\left(\sum_{j=1}^{N_m}\breve{\mathscr{F}}_{\alpha,ij}^{f_h,m}\right)$$
$$+\sum_{\alpha=1}^{n_{ph}}\left(\sum_{k=1}^{n_{\text{frac}}}\left(\sum_{j=1}^{N_{f_k}}\breve{\mathscr{F}}_{\alpha,ij}^{f_h,f_k}\right)\right)+\left(\sum_{j=1}^{N_n}\breve{G}_{ij}\right)^{f_h}+\sum_{j=1}^{N_m}\breve{\mathscr{G}}_{ij}^{f_h,m}+\sum_{k=1}^{n_{\text{frac}}}\left(\sum_{j=1}^{N_{f_k}}\breve{\mathscr{G}}_{ij}^{f_h,f_k}\right)=$$
$$\left(\sum_{\alpha=1}^{n_{ph}}\rho_\alpha h_\alpha q_\alpha^{f_h,w}\right)_i,\quad \forall\, i\in\{1,\dots,N_m\} \tag{3.27}$$

for element i in the fracture f_h.

3.2. COUPLING AND LINEARIZATION OF THE NONLINEAR EQUATIONS

To solve the sets of the equations together, various coupling strategies have been proposed. Two main category of solution strategies exist: a fully-coupled (or fully implicit) approach (FIM) in which all equations are solved simultaneously and a sequential strategy in which the problem is split into a parabolic (or elliptic) part and a hyperbolic one. The fully-implicit and the sequential solution strategies are briefly reviewed here.

In sequential simulation approaches, the system of equations is solved at each time step in two solution steps. First, the component balance equations (either with a volume- or a mass-based approach) are linearly combined to form the pressure equation. This pressure equation is solved first, where only pressure dependent terms are implicitly treated. Phase velocity or the Darcy velocity of phase α is obtained via

$$\boldsymbol{u}=-\boldsymbol{\lambda}\cdot\left(\nabla p-\rho g\nabla h\right). \tag{3.28}$$

Please note that for the sake of the simplicity the effect of gravity is neglected and therefore the equation above ((3.28)) is rewritten as:

$$\boldsymbol{u}=-\boldsymbol{\lambda}\cdot\nabla p. \tag{3.29}$$

Then, the phase velocities u_α are computed and the total velocity is calculated as

$$\boldsymbol{u}_t=\sum_{\alpha=1}^{n_{ph}}\boldsymbol{u}_\alpha. \tag{3.30}$$

The next step is to solve the mass balance equations using the fact that $\sum_{\alpha=1}^{n_{ph}}S_\alpha=1$ which results in removing one of the phase saturation unknowns [100, 102, 103]. Note that all the transport dependent terms are fixed when the pressure equation is being solved, and all the pressure dependent terms are fixed when the saturation transport equations are being solved. Operating such a split-in during the solution process allows to employ the most suitable solution method for each equation. In particular, the pressure equation is parabolic (elliptic for the incompressible case) whereas the transport one is hyperbolic. The simplest approach would be the "implicit pressure implicit saturation" (IMPES) [100], which employs an implicit time integration scheme to solve the pressure equation and an explicit one to solve the transport. However, IMPES suffers from severe restrictions in the allowable time-step size [104] and it is usually preferable to employ an implicit time integration also for the transport equation. It is known that the stability of such an approach is limited to the cases where the coupling between the two equations, i.e., flow (pressure) and transport (saturation), are not strong. Therefore, applicability of this approach for cases with strong capillary and compositional effects can lead to solution instabilities [104]. For this reason the sequential fully-implicit (SFI) strategy was introduced. In SFI simulation iterations are added between the pressure and the transport equations until convergence is reached. This strategy was first developed for immiscible multiphase flow and then extended to multi-component multiphase flow for both black-oil [105, 106] and general compositional models [107–109]. Figure 3.2 on the left (a) and middle (b) shows schematic representations of sequential and fully-implicit simulation approaches.

In presence of strong coupling terms between flow and transport equations (e.g., capillarity, gravity, phase exchange), sequential strategies may not be efficient [104]. For such cases, fully implicit (FIM) systems are generally more stable than sequential strategies [102, 110]. In the fully-implicit method [101], the multiple sets of equations are fully coupled together and then the coupled system of discretized equations is solved for all unknowns simultaneously and implicitly.

Let us imagine two sets of discretized equations exist (i.e., eq_1 and eq_2) with two primary unknowns (i.e., x_1 and x_2) defined as:

$$\begin{aligned} eq_1 &: Z_1(x_1, x_2) = \text{rhs}_1 \\ eq_2 &: Z_2(x_1, x_2) = \text{rhs}_2 \end{aligned}$$

These equations are rewritten in their residual forms by subtracting the left-hand-side of the equations from their corresponding right-hand-side (residual = rhs − lhs):

$$\begin{aligned} r_1(x_1, x_2) &= \text{rhs}_1 - Z_1(x_1, x_2) = 0 \\ r_2(x_1, x_2) &= \text{rhs}_2 - Z_2(x_1, x_2) = 0 \end{aligned}$$

Here, r_1 and r_2 are the residual vectors corresponding to eq_1 and eq_2. Additionally, x_1 , x_2 are the vectors of the unknowns. Usually, the residual is a non-linear function of the unknowns, thus a global linearization method is employed [100, 101]. Typically, the Newton-Raphson method is used to linearize the residuals of the equations. At every time step (n) the residuals (r_1^n and r_2^n) are calculated based on the primary and secondary variables. The aim is to find the value of the primary unknowns at the next time-step ($n+1$) as such that the residuals at the next time-step (r_1^{n+1} and r_2^{n+1}) are zero. However this can be unreachable due to the complexities and various reasons (e.g., numerical round-off errors). Therefore, an intermediate iteration loop is defined. At every iteration step ν, the residuals (r_1^ν and r_2^ν) are calculated based on the value of the primary and secondary variable within the current iteration step. The residuals at the next iteration step $\nu+1$, namely $r_1^{\nu+1}$ and $r_2^{\nu+1}$ are defined as

$$
\begin{aligned}
r_1^{\nu+1} &\approx r_1^{\nu} + \frac{\partial r_1}{\partial x_1}\bigg|^{\nu} \delta x_1^{\nu+1} + \frac{\partial r_1}{\partial x_2}\bigg|^{\nu} \delta x_2^{\nu+1} = 0 \\
r_2^{\nu+1} &\approx r_2^{\nu} + \frac{\partial r_2}{\partial x_1}\bigg|^{\nu} \delta x_1^{\nu+1} + \frac{\partial r_2}{\partial x_2}\bigg|^{\nu} \delta x_2^{\nu+1} = 0
\end{aligned}
\tag{3.31}
$$

Here, $\frac{\partial r}{\partial x_1}, \frac{\partial r}{\partial x_2}\Big|^{\nu}$ are the derivative of the residuals with respect to the primary variables at iteration step ν, and $\delta x_1^{\nu+1}$ and $\delta x_2^{\nu+1}$ are the vectors of the update of the unknowns at iteration step $\nu+1$. In the equations above (3.31), the aim is to find the unknowns $\delta x_1^{\nu+1}$ and $\delta x_2^{\nu+1}$ that satisfy $r_1^{\nu+1} = 0$ and $r_2^{\nu+1} = 0$. One can rewrite these equations as

$$
\begin{aligned}
\frac{\partial r_1}{\partial x_1}\bigg|^{\nu} \delta x_1^{\nu+1} + \frac{\partial r_1}{\partial x_2}\bigg|^{\nu} \delta x_2^{\nu+1} = -r_1^{\nu} \\
\frac{\partial r_2}{\partial x_1}\bigg|^{\nu} \delta x_1^{\nu+1} + \frac{\partial r_2}{\partial x_2}\bigg|^{\nu} \delta x_2^{\nu+1} = -r_2^{\nu}
\end{aligned}
\tag{3.32}
$$

Therefore, at each iteration step, a sparse large linearized system of equations is solved. This system equation can be shown as:

$$
\underbrace{\begin{pmatrix} J_{eq_1,x_1} & J_{eq_1,x_2} \\ J_{eq_2,x_1} & J_{eq_2,x_2} \end{pmatrix}^{\nu}}_{\mathbf{J}^{\nu}} \underbrace{\begin{pmatrix} \delta x_1 \\ \delta x_2 \end{pmatrix}^{\nu+1}}_{\delta x^{\nu+1}} = - \underbrace{\begin{pmatrix} r_1 \\ r_2 \end{pmatrix}^{\nu}}_{r^{\nu}}
\tag{3.33}
$$

This linearized system of equations can be written in simpler form as:

$$
\mathbf{J}^{\nu} \delta x^{\nu+1} = -r^{\nu}. \tag{3.34}
$$

In this system, $\mathbf{J}^{\nu}$ is the Jacobian matrix including all derivatives. Each block J_{eq_i,x_j} contains the derivatives of the equation eq_i with respect to the unknown x_j, i.e., $J_{eq_i,x_j} = \partial r_i / \partial x_j$. By solving the linearized system (3.33), the vector of the update of the unknowns is obtained. The values of the primary unknowns and the secondary variables are then updated. With the updated properties, residuals can be recomputed. In order to achieve a converged solution, the following conditions have to be assured:

$$
\begin{aligned}
&\left(\frac{||r_1^{\nu+1}||_2}{||r_1^0||_2} < \epsilon_{(r_1)} \;\vee\; \frac{||r_1^{\nu+1}||_2}{||\mathrm{rhs}_1||_2} < \epsilon_{(r_1)} \right) \;\wedge \\
&\left(\frac{||r_2^{\nu+1}||_2}{||r_2^0||_2} < \epsilon_{(r_2)} \;\vee\; \frac{||r_2^{\nu+1}||_2}{||\mathrm{rhs}_2||_2} < \epsilon_{(r_2)} \right) \;\wedge \\
&\left(\frac{||\delta x_1||_2}{||x_1||_2} < \epsilon_{(x_1)} \;\wedge\; \frac{||\delta x_2||_2}{||x_2||_2} < \epsilon_{(x_2)} \right)
\end{aligned}
\tag{3.35}
$$

Here, each threshold (ϵ_x) is a user-defined tolerance set initially as input at the beginning of the simulation. Notations $||r||_2$ and $||x||_2$ are the second norm of the vectors of the residuals and the update of the unknowns. The superscript 0 denotes the value of its corresponding vector at the initial state of the iteration step. Please note that in some systems the condition $\frac{||r^{\nu+1}||_2}{||\text{rhs}||_2} < \epsilon_{(r)}$ can result in a better convergence when compared to $\frac{||r^{\nu+1}||_2}{||r^0||_2} < \epsilon_{(r)}$ and vice versa. Therefore both conditions are checked and either of them can implicate the convergence signal.

In figure 3.2 on the right (c), the schematic of the fully-implicit (FIM) simulation flowchart is illustrated.

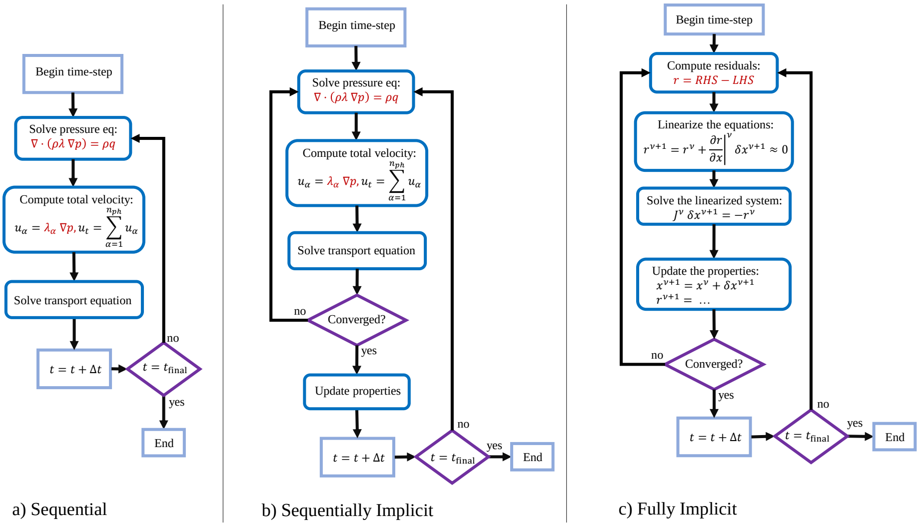

a) Sequential

b) Sequentially Implicit

c) Fully Implicit

Figure 3.2: Schematic of sequentially-coupled (a), sequentially implicit (b) and fully-implicit (c) simulation flowcharts.

3.2.1. MULTIPHASE FLOW IN FRACTURED POROUS MEDIA (ISOTHERMAL)

Equations (3.4)-(3.5) can be written in residual form as

$$\left(r_{\alpha,i}^{n+1}\right)^m = \rho_\alpha q_{\alpha,i}^{m,w} - \left(\frac{(\phi\rho_\alpha S_\alpha)_i^{n+1} - (\phi\rho_\alpha S_\alpha)_i^n}{\Delta t}\right)^m - \left(\sum_{j=1}^{N_n} F_{\alpha,ij}\right)^m - \sum_{k=1}^{n_{\text{frac}}}\left(\sum_{j=1}^{N_{f_k}} \mathscr{F}_{\alpha,ij}^{m,f_k}\right), \quad \forall\, i \in \{1,\dots,N_m\} \tag{3.36}$$

for the rock matrix, and

$$\left(r_{\alpha,i}^{n+1}\right)^{f_h} = \rho_\alpha q_{\alpha,i}^{f_h,w} - \left(\frac{(\phi\rho_\alpha S_\alpha)_i^{n+1} - (\phi\rho_\alpha S_\alpha)_i^{n}}{\Delta t}\right)^{f_h} - \left(\sum_{j=1}^{N_n} F_{\alpha,ij}\right)^{f_h} - \sum_{j=1}^{N_m} \mathscr{F}_{\alpha,ij}^{f_h,m} - \sum_{k=1}^{n_{\text{frac}}} \left(\sum_{j=1}^{N_{f_k}} \mathscr{F}_{\alpha,ij}^{f_h,f_k}\right), \quad \forall\, i \in \{1,...,N_{f_h}\} \tag{3.37}$$

for fracture f_h. Let us define $r^n = [(r^m)^n, (r^{f_1})^n ... (r^{f_{n_{\text{frac}}}})^n]^T$ where $(r^k)^n$ is the residual vector of medium k at time-step n. Similarly, p^n and S^n indicate the vectors of pressure and saturation unknowns (of all media). The residual r^{n+1} is a non-linear function of the primary unknowns p^{n+1} and S^{n+1}. Thus, at each time-step a Newton-Raphson method is employed to solve the non-linear system iteratively, i.e.

$$r_\alpha^{\nu+1} = r_\alpha^{\nu} + \frac{\partial r_\alpha}{\partial p}\bigg|^{\nu} \delta p^{\nu+1} + \frac{\partial r_\alpha}{\partial S}\bigg|^{\nu} \delta S^{\nu+1} = 0 \tag{3.38}$$

where the superscript ν is the iteration index. Consequently, at each Newton's iteration a linear-system $\mathbf{J}^\nu \delta x^{\nu+1} = -r^\nu$ is solved. Here, $\mathbf{J}^\nu$ is the Jacobian matrix with $\delta x^{\nu+1} = [\delta p, \delta S]^T$.

Therefore, assuming two phases (the indices 1 and 2 representing the equations of the first and the second phases respectively), the linear system of equations can be written as

$$\underbrace{\begin{pmatrix} \begin{pmatrix} J_{1,p}^{m,m} & J_{1,p}^{m,f} \\ J_{1,p}^{f,m} & J_{1,p}^{f,f} \end{pmatrix} & \begin{pmatrix} J_{1,S}^{m,m} & J_{1,S}^{m,f} \\ J_{1,S}^{f,m} & J_{1,S}^{f,f} \end{pmatrix} \\ \begin{pmatrix} J_{2,p}^{m,m} & J_{2,p}^{m,f} \\ J_{2,p}^{f,m} & J_{2,p}^{f,f} \end{pmatrix} & \begin{pmatrix} J_{2,S}^{m,m} & J_{2,S}^{m,f} \\ J_{2,S}^{f,m} & J_{2,S}^{f,f} \end{pmatrix} \end{pmatrix}^{\nu}}_{\mathbf{J}^\nu} \underbrace{\begin{pmatrix} \delta p^m \\ \delta p^f \\ \delta S^m \\ \delta S^f \end{pmatrix}^{\nu+1}}_{\delta x^{\nu+1}} = - \underbrace{\begin{pmatrix} r_1^m \\ r_1^f \\ r_2^m \\ r_2^f \end{pmatrix}^{\nu}}_{r^\nu} \tag{3.39}$$

In this formulation, non-linear convergence is reached when the following conditions are satisfied:

$$\begin{gathered} \left(\frac{||r_1^{\nu+1}||_2}{||r_1^0||_2} < \epsilon_{(r_1)} \ \vee \ \frac{||r_1^{\nu+1}||_2}{||\text{rhs}_1||_2} < \epsilon_{(r_1)}\right) \ \wedge \\ \left(\frac{||r_2^{\nu+1}||_2}{||r_2^0||_2} < \epsilon_{(r_2)} \ \vee \ \frac{||r_2^{\nu+1}||_2}{||\text{rhs}_2||_2} < \epsilon_{(r_2)}\right) \ \wedge \\ \left(\frac{||\delta p||_2}{||p||_2} < \epsilon_{(p)} \ \wedge \ \frac{||\delta S||_2}{||S||_2} < \epsilon_{(S)}\right) \end{gathered} \tag{3.40}$$

Here, $\epsilon_{(r_1)}$, $\epsilon_{(r_2)}$, $\epsilon_{(p)}$ and $\epsilon_{(S)}$, are the user-defined tolerances.

3.2.2. MASS AND HEAT FLOW IN LOW-ENTHALPY FRACTURED POROUS MEDIA

The mass conservation equations for low-enthalpy mass-heat flow (3.4)-(3.5) can be written in residual form as:

$$\left(r^{n+1}_{MB,i}\right)^m = \left(\rho_{(fl)} q^{m,w}\right)_i - \left(\frac{(\phi\rho_{(fl)})^{n+1}_i - (\phi\rho_{(fl)})^n_i}{\Delta t}\right)^m - \left(\sum_{j=1}^{N_n} F_{ij}\right)^m - \sum_{k=1}^{n_{\text{frac}}}\left(\sum_{j=1}^{N_{f_k}} \mathscr{F}^{m,f_k}_{ij}\right), \quad \forall\, i \in \{1,\ldots,N_m\} \tag{3.41}$$

for the rock matrix, and

$$\left(r^{n+1}_{MB,i}\right)^{f_h} = \left(\rho_{(fl)} q^{f_h,w}\right)_i - \left(\frac{(\phi\rho_{(fl)})^{n+1}_i - (\phi\rho_{(fl)})^n_i}{\Delta t}\right)^{f_h} - \left(\sum_{j=1}^{N_n} F_{ij}\right)^{f_h} - \sum_{j=1}^{N_{f_k}} \mathscr{F}^{f_h,m}_{ij} - \sum_{k=1}^{n_{\text{frac}}}\left(\sum_{j=1}^{N_{f_k}} \mathscr{F}^{f_h,f_k}_{ij}\right), \quad \forall\, i \in \{1,\ldots,N_{f_h}\} \tag{3.42}$$

for the fracture f_h. Similarly, the residual form of the energy conservation equations are written as:

$$\left(r^{n+1}_{EB,i}\right)^m = \left(\rho_{(fl)} H_{(fl)} q^{m,w}\right)_i - \left(\frac{((\rho U)_{eff})^{n+1}_i - ((\rho U)_{eff})^n_i}{\Delta t}\right)^m - \left(\sum_{j=1}^{N_n} \breve{F}_{ij}\right)^m - \sum_{k=1}^{n_{\text{frac}}}\left(\sum_{j=1}^{N_{f_k}} \breve{\mathscr{F}}^{m,f_k}_{ij}\right) - \left(\sum_{j=1}^{N_n} \breve{G}_{ij}\right)^m - \sum_{k=1}^{n_{\text{frac}}}\left(\sum_{j=1}^{N_{f_k}} \breve{\mathscr{G}}^{m,f_k}_{ij}\right), \quad \forall\, i \in \{1,\ldots,N_m\} \tag{3.43}$$

for element i in the rock matrix m and

$$\left(r^{n+1}_{EB,i}\right)^{f_h} = \left(\rho_{(fl)} H_{(fl)} q^{f_h,w}\right)_i - \left(\frac{((\rho U)_{eff})^{n+1}_i - ((\rho U)_{eff})^n_i}{\Delta t}\right)^{f_h} - \left(\sum_{j=1}^{N_n} \breve{F}_{ij}\right)^{f_h} - \sum_{j=1}^{N_m} \breve{\mathscr{F}}^{f_h,m}_{ij} - \sum_{k=1}^{n_{\text{frac}}}\left(\sum_{j=1}^{N_{f_k}} \breve{\mathscr{F}}^{f_h,f_k}_{ij}\right) - \left(\sum_{j=1}^{N_n} \breve{G}_{ij}\right)^{f_h} - \sum_{j=1}^{N_m} \breve{\mathscr{G}}^{f_h,m}_{ij} - \sum_{k=1}^{n_{\text{frac}}}\left(\sum_{j=1}^{N_{f_k}} \breve{\mathscr{G}}^{f_h,f_k}_{ij}\right), \quad \forall\, i \in \{1,\ldots,N_{f_h}\} \tag{3.44}$$

for element i in the fracture f_h. The full vector of the mass balance and energy balance residuals are defined as

$$r^n_{MB} = [(r^m)^n_{MB}, (r^{f_1})^n_{MB} \ldots (r^{f_{n_{\text{frac}}}})^n_{MB}]^T \quad \text{and} \tag{3.45}$$

$$r^n_{EB} = [(r^m)^n_{EB}, (r^{f_1})^n_{EB} \ldots (r^{f_{n_{\text{frac}}}})^n_{EB}]^T, \tag{3.46}$$

where $(r^k)^n_{MB}$ and $(r^k)^n_{EB}$ are the residual vectors of medium k at time-step n. p^n and T^n indicate the vectors of the pressure and temperature unknowns (of all media). The residual r^{n+1} is a non-linear function of the primary unknowns p^{n+1} and T^{n+1}. Thus, at each time-step a Newton-Raphson method is employed to solve the non-linear system iteratively, i.e.,

$$
\begin{aligned}
r^{\nu+1}_{MB} &= r^{\nu}_{MB} + \frac{\partial r_{MB}}{\partial p}\bigg|^{\nu} \delta p^{\nu+1} + \frac{\partial r_{MB}}{\partial T}\bigg|^{\nu} \delta T^{\nu+1} = 0 \\
r^{\nu+1}_{EB} &= r^{\nu}_{EB} + \frac{\partial r_{EB}}{\partial p}\bigg|^{\nu} \delta p^{\nu+1} + \frac{\partial r_{EB}}{\partial T}\bigg|^{\nu} \delta T^{\nu+1} = 0
\end{aligned}
\tag{3.47}
$$

where the superscripts ν and $\nu+1$ are the current and next iteration indices. At each Newton's iteration step, the linear-system $\mathbf{J}^{\nu}\delta x^{\nu+1} = -r^{\nu}$ is solved. Here, $\mathbf{J}^{\nu}$ is the Jacobian matrix with $\delta x^{\nu+1} = [\delta p, \delta T]^T$. Therefore, one can write the linear system of the equations as:

$$
\underbrace{\begin{pmatrix}
\begin{pmatrix} J^{m,m}_{MB,p} & J^{m,f}_{MB,p} \\ J^{f,m}_{MB,p} & J^{f,f}_{MB,p} \end{pmatrix} & \begin{pmatrix} J^{m,m}_{MB,T} & J^{m,f}_{MB,T} \\ J^{f,m}_{MB,T} & J^{f,f}_{MB,T} \end{pmatrix} \\
\begin{pmatrix} J^{m,m}_{EB,p} & J^{m,f}_{EB,p} \\ J^{f,m}_{EB,p} & J^{f,f}_{EB,p} \end{pmatrix} & \begin{pmatrix} J^{m,m}_{EB,T} & J^{m,f}_{EB,T} \\ J^{f,m}_{EB,T} & J^{f,f}_{EB,T} \end{pmatrix}
\end{pmatrix}^{\nu}}_{\mathbf{J}^{\nu}}
\underbrace{\begin{pmatrix} \delta p^m \\ \delta p^f \\ \delta T^m \\ \delta T^f \end{pmatrix}^{\nu+1}}_{\delta x^{\nu+1}}
= -\underbrace{\begin{pmatrix} r^m_{MB} \\ r^f_{MB} \\ r^m_{EB} \\ r^f_{EB} \end{pmatrix}^{\nu}}_{r^{\nu}}
\tag{3.48}
$$

To reach convergence, the following conditions must be met:

$$
\begin{aligned}
&\left(\frac{||r^{\nu+1}_{MB}||_2}{||r^0_{MB}||_2} < \epsilon_{(r_{MB})} \;\vee\; \frac{||r^{\nu+1}_{MB}||_2}{||\mathrm{rhs}_{MB}||_2} < \epsilon_{(r_{MB})}\right) \wedge \\
&\left(\frac{||r^{\nu+1}_{EB}||_2}{||r^0_{EB}||_2} < \epsilon_{(r_{EB})} \;\vee\; \frac{||r^{\nu+1}_{EB}||_2}{||\mathrm{rhs}_{EB}||_2} < \epsilon_{(r_{EB})}\right) \wedge \\
&\left(\frac{||\delta p||_2}{||p||_2} < \epsilon_{(p)} \;\wedge\; \frac{||\delta T||_2}{||T||_2} < \epsilon_{(T)}\right)
\end{aligned}
\tag{3.49}
$$

Here, $\epsilon_{(r_{MB})}$, $\epsilon_{(r_{EB})}$, $\epsilon_{(p)}$ and $\epsilon_{(T)}$, are the user-defined tolerances. The details of the reason to choose these conditions are previously explained in this section (see Eq. 3.35 and the explanation followed after).

3.2.3. MASS AND HEAT FLOW IN HIGH-ENTHALPY FRACTURED POROUS MEDIA

As mentioned in the discretization section for high-enthalpy formulation, the sets of equations consists of a pair of one set of mass balance equations and one set of energy balance equations. The properties of both phases are summed up in every term in these equations and there is no separate mass or energy balance equation per fluid phase. The mass balance equations (3.24)-(3.25) are rewritten in their residual form as

$$\left(r_{MB,i}^{n+1}\right)^{m} = \left(\sum_{\alpha=1}^{n_{ph}} \rho_\alpha q_\alpha^{m,w}\right)_i - \left(\frac{\left(\phi \sum_{\alpha=1}^{n_{ph}} \rho_\alpha S_\alpha\right)_i^{n+1} - \left(\phi \sum_{\alpha=1}^{n_{ph}} \rho_\alpha S_\alpha\right)_i^{n}}{\Delta t}\right)^{m} - \left(\sum_{\alpha=1}^{n_{ph}}\left(\sum_{j=1}^{N_n} F_{\alpha,ij}\right)\right)^{m} - \sum_{\alpha=1}^{n_{ph}}\left(\sum_{k=1}^{n_{\text{frac}}}\left(\sum_{j=1}^{N_{f_k}} \mathscr{F}_{\alpha,ij}^{m,f_k}\right)\right), \quad \forall\, i \in \{1,\dots,N_m\} \tag{3.50}$$

for element i in the rock matrix m and

$$\left(r_{MB,i}^{n+1}\right)^{f_h} = \left(\sum_{\alpha=1}^{n_{ph}} \rho_\alpha q_\alpha^{f_h,w}\right)_i - \left(\frac{\left(\phi \sum_{\alpha=1}^{n_{ph}} \rho_\alpha S_\alpha\right)_i^{n+1} - \left(\phi \sum_{\alpha=1}^{n_{ph}} \rho_\alpha S_\alpha\right)_i^{n}}{\Delta t}\right)^{f_h} - \left(\sum_{\alpha=1}^{n_{ph}}\left(\sum_{j=1}^{N_n} F_{\alpha,ij}\right)\right)^{f_h} - \sum_{\alpha=1}^{n_{ph}}\left(\sum_{j=1}^{N_{f_k}} \mathscr{F}_{\alpha,ij}^{f_h,m}\right) - \sum_{\alpha=1}^{n_{ph}}\left(\sum_{k=1}^{n_{\text{frac}}}\left(\sum_{j=1}^{N_{f_k}} \mathscr{F}_{\alpha,ij}^{f_h,f_k}\right)\right), \quad \forall\, i \in \{1,\dots,N_{f_h}\} \tag{3.51}$$

for element i in the fracture f_h. Additionally, the energy balance equations are also rewritten as

$$\left(r_{EB,i}^{n+1}\right)^{m} = \left(\sum_{\alpha=1}^{n_{ph}} \rho_\alpha h_\alpha q_\alpha^{m,w}\right)_i - \left(\frac{\left((\rho U)_{eff}\right)_i^{n+1} - \left((\rho U)_{eff}\right)_i^{n}}{\Delta t}\right)^{m} - \left(\sum_{\alpha=1}^{n_{ph}}\left(\sum_{j=1}^{N_n} \breve{F}_{\alpha,ij}\right)\right)^{m} - \sum_{\alpha=1}^{n_{ph}}\left(\sum_{k=1}^{n_{\text{frac}}}\left(\sum_{j=1}^{N_{f_k}} \breve{\mathscr{F}}_{\alpha,ij}^{m,f_k}\right)\right) - \left(\sum_{j=1}^{N_n} \breve{G}_{ij}\right)^{m} - \sum_{k=1}^{n_{\text{frac}}}\left(\sum_{j=1}^{N_{f_k}} \breve{\mathscr{G}}_{ij}^{m,f_k}\right), \quad \forall\, i \in \{1,\dots,N_m\} \tag{3.52}$$

for element i in the rock matrix m and

$$\left(r_{EB,i}^{n+1}\right)^{f_h} = \left(\sum_{\alpha=1}^{n_{ph}} \rho_\alpha h_\alpha q_\alpha^{f_h,w}\right)_i - \left(\frac{\left((\rho U)_{eff}\right)_i^{n+1} - \left((\rho U)_{eff}\right)_i^{n}}{\Delta t}\right)^{f_h} - \left(\sum_{\alpha=1}^{n_{ph}}\left(\sum_{j=1}^{N_n} \breve{F}_{\alpha,ij}\right)\right)^{f_h} - \sum_{\alpha=1}^{n_{ph}}\left(\sum_{j=1}^{N_m} \breve{\mathscr{F}}_{\alpha,ij}^{f_h,m}\right) - \sum_{\alpha=1}^{n_{ph}}\left(\sum_{k=1}^{n_{\text{frac}}}\left(\sum_{j=1}^{N_{f_k}} \breve{\mathscr{F}}_{\alpha,ij}^{f_h,f_k}\right)\right) - \left(\sum_{j=1}^{N_n} \breve{G}_{ij}\right)^{f_h} - \sum_{j=1}^{N_m} \breve{\mathscr{G}}_{ij}^{f_h,m} - \sum_{k=1}^{n_{\text{frac}}}\left(\sum_{j=1}^{N_{f_k}} \breve{\mathscr{G}}_{ij}^{f_h,f_k}\right), \quad \forall\, i \in \{1,\dots,N_m\} \tag{3.53}$$

for element i in the fracture f_h. Similar to the low-enthalpy formulation, the full vector of the mass balance and energy balance residuals can be written as

$$r^n_{MB} = [(r^m)^n_{MB}, (r^{f_1})^n_{MB} ... (r^{f_{n_{\text{frac}}}})^n_{MB}]^T \quad \text{and} \tag{3.54}$$

$$r^n_{EB} = [(r^m)^n_{EB}, (r^{f_1})^n_{EB} ... (r^{f_{n_{\text{frac}}}})^n_{EB}]^T, \tag{3.55}$$

where $(r^k)^n_{MB}$ and $(r^k)^n_{EB}$ are the residual vectors of medium k at time-step n. p^n and H^n are the vectors of the pressure and total enthalpy unknowns (primary unknowns). as the residual r^{n+1} is a non-linear function of the primary unknowns (here, p^{n+1} and H^{n+1}), a Newton-Raphson method is employed to solve the non-linear system iteratively, namely

$$\begin{aligned} r^{\nu+1}_{MB} &= r^{\nu}_{MB} + \frac{\partial r_{MB}}{\partial p}\bigg|^{\nu} \delta p^{\nu+1} + \frac{\partial r_{MB}}{\partial H}\bigg|^{\nu} \delta H^{\nu+1} = 0 \\ r^{\nu+1}_{EB} &= r^{\nu}_{EB} + \frac{\partial r_{EB}}{\partial p}\bigg|^{\nu} \delta p^{\nu+1} + \frac{\partial r_{EB}}{\partial H}\bigg|^{\nu} \delta H^{\nu+1} = 0 \end{aligned} \tag{3.56}$$

with ν and $\nu+1$ superscripts being the current and next iteration indices. At every Newton's iteration step, the linear-system $\mathbf{J}^{\nu}\delta x^{\nu+1} = -r^{\nu}$ is solved. In this expression, $\mathbf{J}^{\nu}$ is the Jacobian matrix with $\delta x^{\nu+1} = [\delta p, \delta H]^T$. Therefore, the linear system of the equations can be illustrated as:

$$\underbrace{\begin{pmatrix} \begin{pmatrix} J^{m,m}_{MB,p} & J^{m,f}_{MB,p} \\ J^{f,m}_{MB,p} & J^{f,f}_{MB,p} \end{pmatrix} & \begin{pmatrix} J^{m,m}_{MB,H} & J^{m,f}_{MB,H} \\ J^{f,m}_{MB,H} & J^{f,f}_{MB,H} \end{pmatrix} \\ \begin{pmatrix} J^{m,m}_{EB,p} & J^{m,f}_{EB,p} \\ J^{f,m}_{EB,p} & J^{f,f}_{EB,p} \end{pmatrix} & \begin{pmatrix} J^{m,m}_{EB,H} & J^{m,f}_{EB,H} \\ J^{f,m}_{EB,H} & J^{f,f}_{EB,H} \end{pmatrix} \end{pmatrix}^{\nu}}_{\mathbf{J}^{\nu}} \underbrace{\begin{pmatrix} \delta p^m \\ \delta p^f \\ \delta H^m \\ \delta H^f \end{pmatrix}^{\nu+1}}_{\delta x^{\nu+1}} = -\underbrace{\begin{pmatrix} r^m_{MB} \\ r^f_{MB} \\ r^m_{EB} \\ r^f_{EB} \end{pmatrix}^{\nu}}_{r^{\nu}} \tag{3.57}$$

The convergence at each iteration loop is reached by satisfying the following conditions:

$$\begin{gathered} \left(\frac{||r^{\nu+1}_{MB}||_2}{||r^0_{MB}||_2} < \epsilon_{(r_{MB})} \;\vee\; \frac{||r^{\nu+1}_{MB}||_2}{||\text{rhs}_{MB}||_2} < \epsilon_{(r_{MB})}\right) \;\wedge \\ \left(\frac{||r^{\nu+1}_{EB}||_2}{||r^0_{EB}||_2} < \epsilon_{(r_{EB})} \;\vee\; \frac{||r^{\nu+1}_{EB}||_2}{||\text{rhs}_{EB}||_2} < \epsilon_{(r_{EB})}\right) \;\wedge \\ \left(\frac{||\delta p||_2}{||p||_2} < \epsilon_{(p)} \;\wedge\; \frac{||\delta H||_2}{||H||_2} < \epsilon_{(T)}\right) \end{gathered} \tag{3.58}$$

The tolerances $\epsilon_{(r_{MB})}$, $\epsilon_{(r_{EB})}$, $\epsilon_{(p)}$ and $\epsilon_{(H)}$, are defined by user in the input. Please see Eq. 3.35 earlier in this section for more details about the choice of the convergence conditions.

3.3. FRACTURE MODELS

The significance of fractures and the need to model them accurately has been previously discussed in section 1.4 in detail. As it was mentioned earlier, there are multiple approaches with regards to modeling the fractures. In this section, we focus on explicit representation of fractures in fractured domains via embedded discretization of fractures. In the following part, the embedded discrete fracture model (EDFM) and the projection-based embedded discrete fracture model (pEDFM) are described.

3.3.1. EMBEDDED DISCRETE FRACTURE MODEL (EDFM)

As mentioned earlier in section 1.4, the non-conforming embedded discrete method benefits from the independent representation of fractures and the hosting rock in the formation (mostly referred to as the rock matrix). In the EDFM approach (as apposed to the CDFM methods, or DFM for short), the fractures are explicitly represented as separate lower dimensional control volumes. Therefore the rock matrix and the fractures have independent gridding structures which provides significant flexibility. Especially, in case of deformation of the rock matrix, and closure or propagation of the fractures, the modification of the gridding structure is significantly simpler. Please note that in the embedded discrete methods, the focus is on those fractures that are large enough (bigger than the scale of the rock matrix control volumes), and the small-scale fractures (below the rock matrix grid resolution) are often homogenized with the rock matrix altering the rock properties such as porosity and permeability. This approach is called hierarchical fracture modeling which avoids the complexities arising from the discretization and dynamic nature of the fracture geometries, especially in presence of dense fracture networks of various scales [37, 44, 111].

In the EDFM method, at first, the computational grids are imposed on the rock matrix and each fracture independently. Figure 3.3 shows a 2D schematic on how the rock matrix and fractures treated during the gridding.

As it can be noticed, in the previous sections of this chapter and the previous chapter, all the mass/energy conservation equations are defined both for the rock matrix and the fractures explicitly. The flux exchanges between the rock matrix control volumes and the fracture elements are defined via the equations 3.2,3.3,3.7,3.8,3.11,3.12,3.18,3.19,3.22,3.23. In these equations, $T_{ij}^{m,f}, T_{ij}^{f_i,f_j}, \mathbb{T}_{cond,ij}^{m,f}, \mathbb{T}_{cond,ij}^{f_i,f_j}$ are the geometrical transmissibilities defined between each two corresponding media.

The geometrical transmissibility in the mass flux between cell i belonging to the rock matrix m and the element j belonging to the fracture f_i reads:

$$T_{ij}^{m,f} = K_{ij}^{H} \times CI_{ij}, \tag{3.59}$$

where, K_{ij}^{H} is the harmonically averaged permeability between the overlapping rock matrix and fracture elements. Please note that the convective heat fluxes employ the identical geometrical transmissibility used in the mass fluxes due to the fact that $\breve{\mathscr{F}}_{ij} = H^{*}_{(fl)} \mathscr{F}_{ij}$ (3.20). Moreover, the geometrical transmissibility used in the conductive heat flux between these two elements is written as:

$$\mathbb{T}_{cond,ij}^{m,f} = (\Lambda_{eff})_{ij}^{H} \times CI_{ij}, \tag{3.60}$$

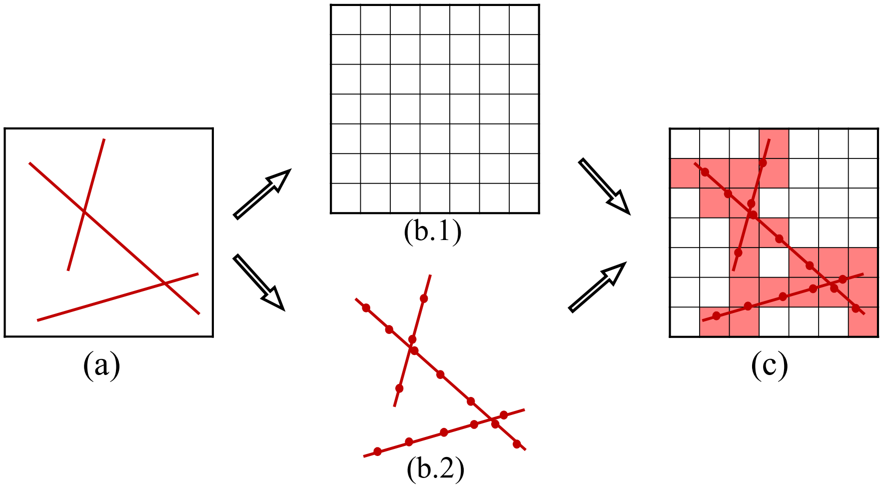

Figure 3.3: Schematic of EDFM gridding. The fractured media (a) is independently split into the rock matrix grid system (b.1) and the fracture network grid (b.2). Also the rock matrix and fracture grids are showed on top of each other (c) with overlapped matrix cells highlighted with color.

where, $(\Lambda_{eff})^H_{ij}$ is the harmonically averaged heat conductivity between the rock matrix control volume and the overlapping fracture element.

In the equations above, the CI_{ij} is the so-called connectivity index between the two elements. The EDFM and pEDFM approaches model the matrix-fracture connectivity index as:

$$CI_{ij} = \frac{A^{m,f}_{ij}}{\langle d \rangle_{ij}}, \tag{3.61}$$

where $A^{m,f}_{ij}$ is the area fraction of the fracture cell j overlapping with the rock matrix cell i (see figure 3.4, on the left) and $\langle d \rangle_{ij}$ is the average distance between these cells [44].

The geometrical transmissibilities in the mass flux and the conductive heat flux between element i in the fracture f_i and the element j in the fracture f_j read:

$$T^{f_i,f_j}_{ij} = K^H_{ij} \frac{CI^{f_i}_{iI_{ij}} \times CI^{f_j}_{jI_{ij}}}{CI^{f_i}_{iI_{ij}} + CI^{f_j}_{jI_{ij}}}, \quad \text{and} \tag{3.62}$$

$$\mathbb{T}^{f_i,f_j}_{cond,ij} = (\Lambda_{eff})^H_{ij} \frac{CI^{f_i}_{iI_{ij}} \times CI^{f_j}_{jI_{ij}}}{CI^{f_i}_{iI_{ij}} + CI^{f_j}_{jI_{ij}}} \tag{3.63}$$

respectively. The transmissibilities T^{f_i,f_j}_{ij} and $\mathbb{T}^{f_i,f_j}_{cond,ij}$ between the two non-neighboring fracture cells are obtained via a lower dimensional connectivity index formulation. Mind

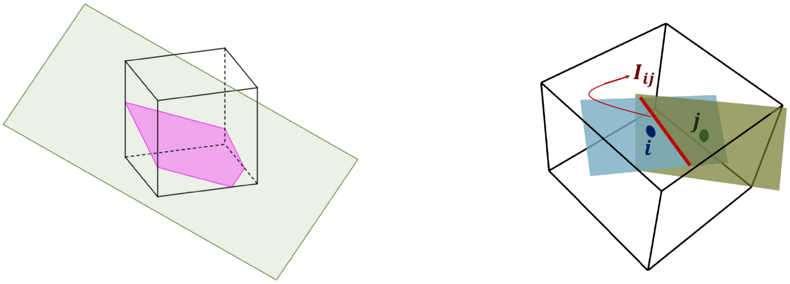

Figure 3.4: Figure on the left: An illustration of a 2D fracture plane overlapping a matrix cell. In this example, the overlapping section forms an irregular polygon. Figure on the right: A visualization of two intersecting fracture planes (left) and discrete elements of different intersecting fractures (right), with the intersection lines shown in red.

that the intersection of 2D fracture planes is a line-segment and for 1D fracture line-segments, it is a point. Figure 3.4 (on the right) shows a visualization example of intersection between two non-neighboring 2D fracture elements. The intersection forms a line segment I_{ij} (shown in red color) with the average distances from the intersection segment of $\langle d \rangle_{iI_{ij}}^{f_i} \neq \langle d \rangle_{jI_{ij}}^{f_j}$. This is the reason why these transmissibilities are computed using an harmonic-average formulation as shown above.

3.3.2. VALIDATION OF THE EDFM

In this section, the EDFM method is validated through a simple 2D test-case and the numerical results of this test-case are presented. Moreover, the accuracy of the EDFM method used in this test-case is compared against a reference solution from the fully-resolved direct numerical simulation (DNS for short). For this purpose let us consider a 2D homogeneous domain of 9 [m] × 9 [m] as shown in figure 3.5. A cross-shaped fracture network is present in the middle of the domain. Each fracture segment is 5[m] long, with a permeability value of 10^9 times higher than that of the rock matrix ($K_m = 2.5 \cdot 10^{-13}$ [m]^2 and $K_f = 1.3 \cdot 10^{-4}$ [m]^2). The fracture aperture is $4 \cdot 10^{-2}$[m]. Two incompressible fluid phases are considered. The reservoir has an initial saturation $S_{1,init} = 0.1$. No-flow boundary conditions are considered at the top and bottom boundaries whereas the left and right boundaries have fixed pressures of $2.0 \cdot 10^7$[Pa] and $1.0 \cdot 10^7$[Pa], respectively. Phase 1 is injected from the left boundary whereas production occurs at the right. These simulations are run using our in-house simulation software called **DARSim** in which all the software developments of this work is done and made available open source at https://gitlab.com/DARSim.

The reference solution (referred to as DNS) is obtained by imposing a 225 × 225 grid that allows to fully resolve the flow inside the fracture. The EDFM simulations are performed with three different matrix grid resolutions of 15 × 15, 25 × 25, and 45 × 45. The grid-cells inside the fractures are chosen to have similar dimensions as the matrix cells. The time-step size is 10^{-4} [days] for all simulations. The pressure and saturation maps after 0.0235 [days] are shown in figure 3.6.

Figures 3.7a and 3.7b present the pressure and saturation errors as functions of the

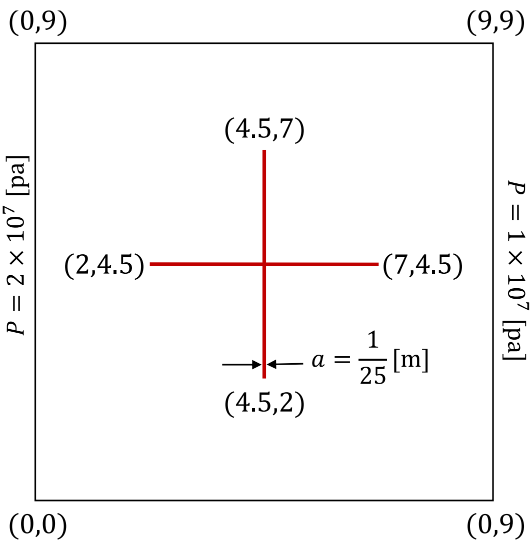

Figure 3.5: Visualization of the 2D domain with a cross-shaped fracture network at the center.

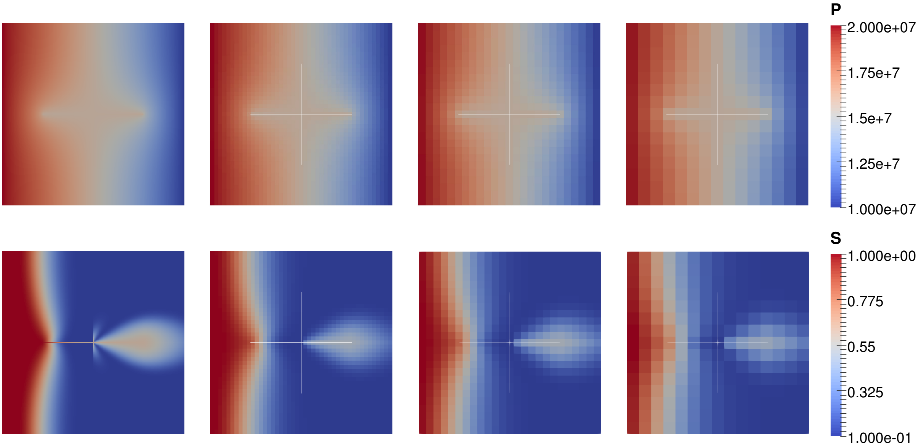

Figure 3.6: Comparison of the fully resolved DNS (left column) using 225 × 225 cells and the EDFM results with different grid resolutions (left to right: 45 × 45, 25 × 25, 15 × 15) after 0.0235 [days]. The pressure results are shown on the top row, while the saturation maps are illustrated on the bottom row.

simulation time. Given a variable x (i.e, pressure or saturation), the error, e_x, is calculated as

$$e_x = \frac{||x_{\text{DNS}} - x_{\text{EDFM}}||_2}{||x_{\text{DNS}}||_2}. \tag{3.64}$$

As can be seen from the error plots, it is noticeable that errors decrease upon refinement of the EDFM solution grid. Moreover, the growth of error in both pressure and

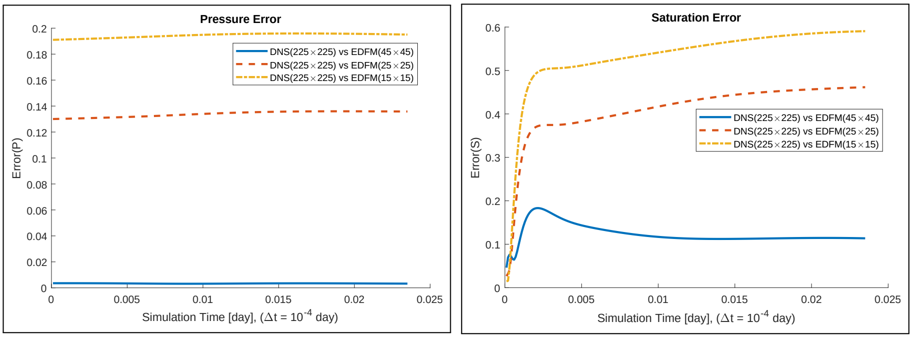

(a) Pressure Error (b) Saturation Error

Figure 3.7: Pressure and saturation errors of EDFM simulations with respect to the reference solution (DNS).

saturation plots reduces over simulation time. There is a sudden increase of saturation error as the saturation front passes through the fractures.

While the EDFM is acceptable to provide accurate solutions for highly conductive fractures, it cannot accurately represent the flow barriers (e.g., sealing fractures and impermeable faults). This is due to the fact that the extra connectivities introduced by the flux exchanges between the rock matrix and the fractures act as parallel connections (in parallel to the classical connections between the neighboring cells within a medium). In presence of highly conductive fractures, the extra connectivities act as highly conductive flow channels dominating the fluid flow compared to the rest of the domain. Therefore, in such cases, the parallel connectivities do not pose any problem and inaccurate results. However, in case of flow barriers, one should expect blockage of the flow, yet the EDFM parallel connectivities result in non-physical flow leakages. In order to solve this issue, the projection-embedded fracture model (pEDFM) was introduced [46, 47]. In the next section, the pEDFM is explained and it will be shown how the parallel connectivities are removed.

3.3.3. PROJECTION-BASED EMBEDDED DISCRETE FRACTURE MODEL (PEDFM)

To correct for the EDFM limitations on the fractures with generic conductivity due the to parallel transmissibilities, the matrix-matrix, fracture-matrix and fracture-fracture connectivities are modified in the overlapping regions. The mentioned modifications eliminate the parallel transmissibilities, such that the pEDFM is applicable to any conductivity contrast between the rock matrix and the fractures. Initially, all connectivities between the two neighboring matrix cells that are disconnected due to the overlapping fractures are detected. Due to the geometrical algorithm devised during the development of this method, a continuous projection path (visible in figure 3.8 as solid lines in light blue color) is automatically obtained on the interfaces as such it disconnects the neighboring connections letting the flux occur only on one route (i.e., through matrix-fracture-matrix).

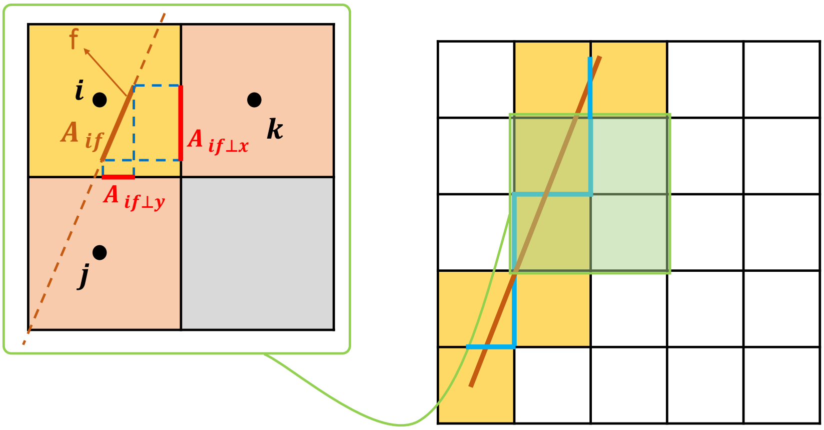

Figure 3.8: The pEDFM Illustration for a 2D domain with structured grid and a 1D overlapping fracture. The overlapped matrix cells are highlighted in yellow color. With the classical EDFM method, these cells are connected to each overlapping fracture element via the connectivity index in the matrix-fracture flux exchange. The pEDFM introduces extra non-neighboring connections between fracture elements and matrix cells highlighted in orange.

Let the fracture element f overlap the rock matrix grid cell i (as shown in figure 3.8) with an area fraction A_{if}. A set of projections is defined on the interface between the overlapped matrix grid cell i and its neighboring grid cells (in orange) that are affected by the crossing (i.e., j and k). Please note that in a 3D case, there will be three projections. For each dimension (i.e., x, y and z) the projection area fractions are obtained via:

$$A_{if\perp x_e} = A_{if} \times \cos(\gamma), \quad x_e \in \{x, y, z\}, \tag{3.65}$$

where γ is the angle between the fracture element and the interface connecting the matrix grid cell i and the neighboring grid cell in the corresponding dimension (shown in figure 3.8 on the zoomed-in section and highlighted in red color as $A_{if\perp x}$ and $A_{if\perp y}$). New transmissibilities are defined to connect the fracture element f to each non-neighboring matrix grid cells (i.e., j and k in the 2D example shown in figure 3.8):

$$T_{i_e f} = \frac{A_{if\perp x_e}}{\langle d \rangle_{i_e f}} \lambda_{i_e f}, \quad x_e \in \{x, y, z\}, \tag{3.66}$$

where, $\langle d \rangle_{i_e f}$ is the average distance between the fracture element f and the rock matrix grid cell i_e. $\lambda_{i_e f}$ is the effective fluid mobility between these cells. As a result of the new transmissibilities, the connectivity between the matrix grid cell i and its corresponding neighboring cells is modified:

$$T_{i i_e} = \frac{A_{i i_e} - A_{if\perp x_e}}{\Delta x_e} \lambda_{i_e f}, \quad \mathfrak{X} \in \{x, y, z\}. \tag{3.67}$$

For the sake of the simplicity of the implementation, the modified transmissibilities are obtained by multiplication of coefficient α as a fraction of the projected cross-section area, and the cross-section area of the corresponding interface. Please note that for all overlapping fracture elements (except for the boundaries of the fractures), the projection will cover the whole interface. Therefore, α is 1.0 for most of the cases, resulting in zero transmissibility between the matrix grid cells (i.e., $T_{ii_e} = 0$), thus removing the parallel transmissibilities. This approach is also similarly used to model horizontal or inclined wells in some widely known simulators (e.g., Eclipse).

3.3.4. VALIDATION OF PEDFM

In this section, the pEDFM method is validated through a simplified 2D test-case and the numerical results of this test-case are shown. The accuracy of the pEDFM method in this test-case is compared against both the reference solution from the fully-resolved direct numerical simulation (DNS) and simulation results from the EDFM approach. In order to attempt this comparison, a 2D homogeneous domain of 3 [m] × 3 [m] is considered (see Fig. 3.9). Two fractures intersect in the middle of the domain forming a cross shape. Both fractures are 1.5[m] long with aperture of 8×10^{-3} [m]. In terms of fractures conductivity, two scenarios are taken into account. In the first scenario, the fractures are $a_f = 10^8$ times more permeable than the rock matrix ($K_m = 10^{-14}$ [m^2] and $K_f = 10^{-6}$ [m^2]) and in the second scenario, the fractures are 10^8 times less permeable than the rock matrix ($K_m = 10^{-14}$ [m^2] and $K_f = 10^{-22}$ [m^2]). The initial pressure and temperature of the reservoir are $p_0 = 1.5 \times 10^7$ [Pa] and $T_0 = 400$[K] respectively. Cold water with pressure $p_{\text{inj}} = 2 \times 10^7$ [Pa] and temperature $T_{\text{inj}} = 400$[K] is injected from the left boundary and hot water is produced from the right boundary with pressure $p_{\text{prod}} = 10^7$ [Pa]. No-flow boundary conditions applies to the top and bottom boundaries. Table 3.1 shows the input parameters of this test case.

Table 3.1: Input parameters of the pEDFM validation test-case for fluid and rock properties.

Property	value
Rock thermal conductivity (Λ_r)	4 [W/m.K]
Fluid thermal conductivity (Λ_f)	negligible
Rock density (ρ_r)	2750 [kg/m^3]
Fluid specific heat (C_{p_f})	4200 [J/kg.K]
Rock specific heat (C_{p_r})	790 [J/kg.K]
Matrix porosity (ϕ)	0.2
Matrix permeability	10^{-14} [m^2]
High-perm fractures permeability	10^{-6} [m^2]
Low-perm fractures permeability	10^{-22} [m^2]
Fractures aperture	8×10^{-3} [m]

To obtain the reference solution (denoted as DNS), a 375 × 375 grid resolution is imposed on the domain. This allows for fully resolving the flow inside the fracture. In this case fractures are defined as channels along the middle row and column of the discretized domain. The EDFM and the pEDFM simulations are run with four different matrix gridding resolutions of 75 × 75, 45 × 45 and 25 × 25. At all runs, the aperture of all the fractures is identical and set to be $a_f = 8 \times 10^{-3}$[m] which is approximately equal to the matrix grid cell size of DNS discretization. The size of grid cells inside the fractures have similar dimensions as the rock matrix grid cells. In cases with highly conductive fractures, the simulation is run for 6 [hours] and in the cases with low-permeability fractures, the simulation is run for 12 [hours]. The results are provided at 50 isochronal intervals.

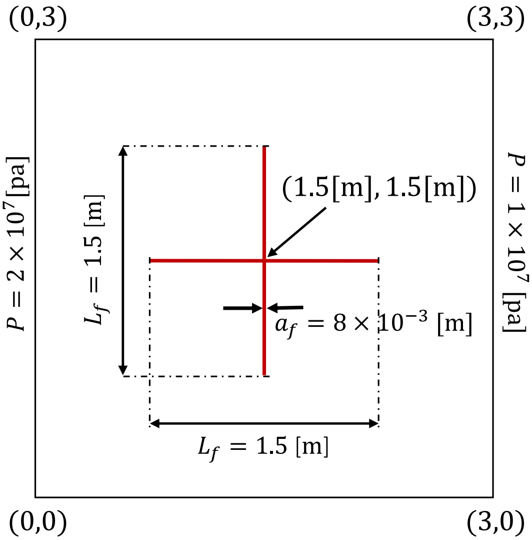

Figure 3.9: The pEDFM validation: Visualization of the geometry of the test case; a 2D domain with a cross-shaped fracture network at the center.

In the first scenario, the fractures are considered to be highly conductive (see table 3.1 for more details). The results of the simulations as plots of pressure and temperature solutions are shown in the figures 3.10 and 3.11.

The plots in figure 3.12 present the pressure and the temperature errors as functions of the simulation time. The error of variable x (i.e, pressure or temperature), denoted as e_x, is calculated via

$$e_x = \frac{||x_{\text{DNS}} - x_{\text{EDFM/pEDFM}}||_2}{||x_{\text{DNS}}||_2}. \tag{3.68}$$

At the center of the domain where the fractures intersect, a difference in the temperature distribution between the DNS, EDFM and pEDFM methods can be observed. Please note that the difference arises from the discretization approaches. In DNS method, fractures are actually channels with aperture of one grid cell. As a result, those matrix grid cells are flooded with the cold fluid. This is not the case for the EDFM and the pEDFM approaches.

In the second scenario, both fractures are set to be 10^8 times less permeable than the rock matrix. Figures 3.13 and 3.14 show the simulation results of this scenario as pressure and temperature solutions respectively.

Figure 3.15 shows the pressure and the temperature errors versus the simulation time for the second scenario. As the EDFM is incapable of capturing the low permeable frac-

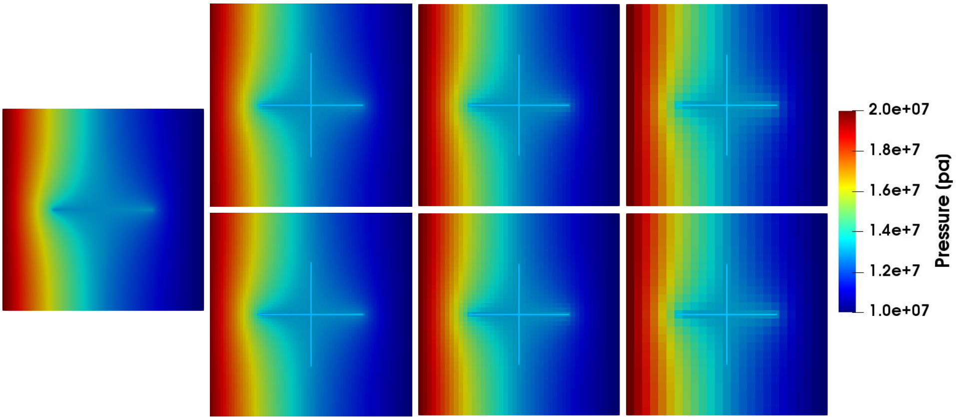

Figure 3.10: The pEDFM validation using highly conductive fractures: comparison of the pressure solution between the fully resolved DNS (single plot at left column) using 375 × 375 grid cells, the pEDFM results (top row) and the EDFM results (bottom row). Both the pEDFM and the EDFM are run with different grid resolutions (left to right: 75 × 75, 45 × 45 and 25 × 25) at the 25th time interval (i.e., $t = 3$ [hours]).

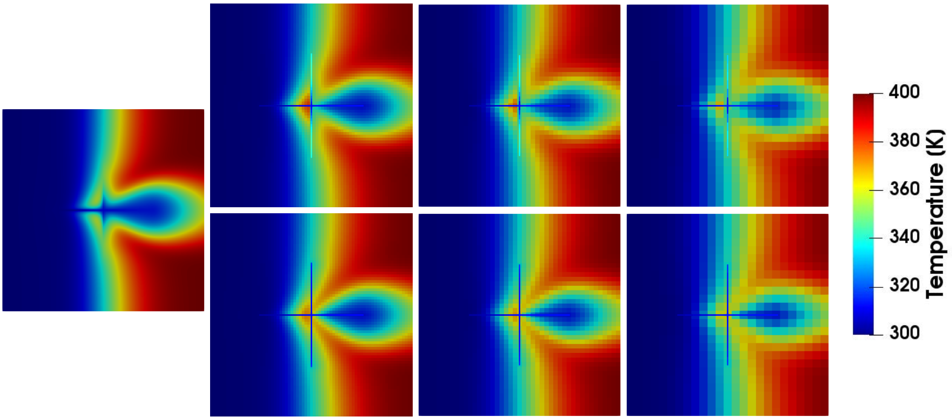

Figure 3.11: The pEDFM validation using highly conductive fractures: comparison of the temperature solutions between the fully resolved DNS, the pEDFM and the EDFM. Similar to previous figure, the single plot at left column shows DNS solution, top row shows the pEDFM results and bottom row shows the EDFM results.

tures and the results are not accurate and representative, the errors are only shown for the pEDFM.

Fine-scale simulation for a simple 2D domain allowed to investigate the pEDFM and the EDFM accuracy, both compared to the direct numerical solution (DNS). Both highly conductive and impermeable fractures were considered. It was shown that in the presence of highly conductive fractures, the pEDFM and the EDFM performed accurately, though the EDFM still allows for small non-physical leakage. In addition, the EDFM failed to capture the low conductive fractures, while the pEDFM shows a good representation of the DNS with satisfactory accuracy.

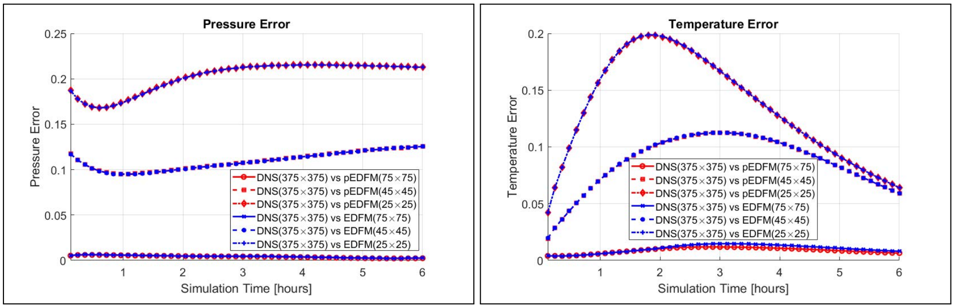

(a) Pressure Error

(b) Temperature Error

Figure 3.12: The pEDFM validation using highly conductive fractures: Pressure and Temperature errors of pEDFM and EDFM simulations with respect to the reference solution (DNS).

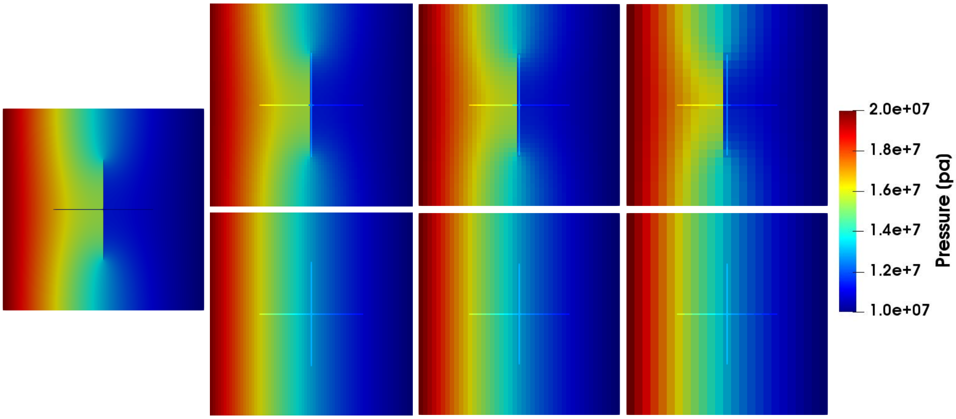

Figure 3.13: The pEDFM validation using impermeable fractures: comparison of the pressure solution between the fully resolved DNS (single plot at left column) using 375 × 375 grid cells, the pEDFM results (top row) and the EDFM results (bottom row). Both the pEDFM and the EDFM are run with different grid resolutions (left to right: 75 × 75, 45 × 45 and 25 × 25) at the 25th time interval (i.e., $t = 6$ [hours]).

While the results suggest accuracy gains by using the pEDFM on Cartesian grids, one should consider that the geological formations and the field-scale models cannot be accurately represented by discretization on Cartesian grids. More complex and flexible gridding structure is needed to be used for field-scale models. A most-commonly used gridding structure is the so-called corner-point grid (CPG) geometry. In the next chapter, the corner-point grid geometry will be briefly explained. Thereafter, the pEDFM model on the corner-point grid geometry will be introduced and some fractured test-cases will compare the accuracy of the corner-point grid results against the Cartesian grid results. Moreover, the pEDFM model will be used on a few field-scale and geologically relevant models to show its performance as a proof-of-concept.

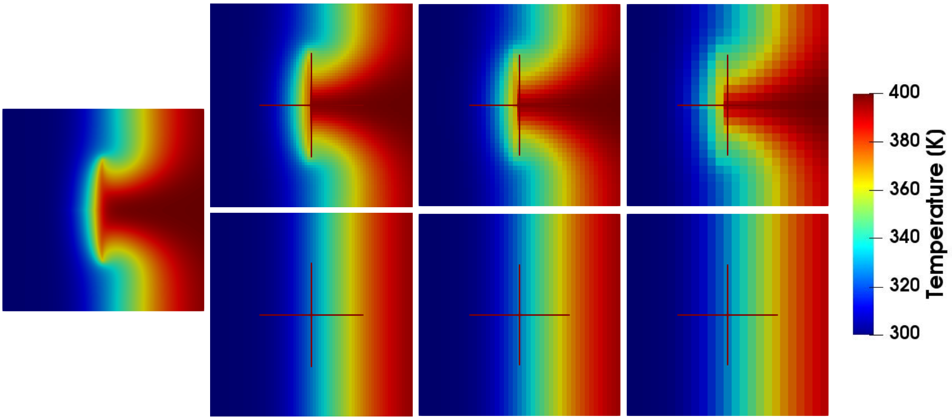

Figure 3.14: The pEDFM validation using impermeable fractures: comparison of the temperature solutions between the fully resolved DNS, pEDFM and EDFM. Similar to previous figure, the single plot at left column shows DNS solution, top row shows the pEDFM results and bottom row shows the EDFM results.

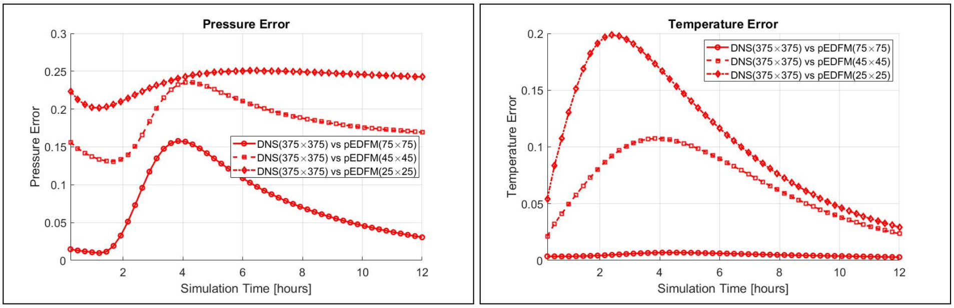

(a) Pressure Error

(b) Temperature Error

Figure 3.15: The pEDFM validation using impermeable fractures: the pressure and the temperature errors of the pEDFM compared to the reference solution (DNS).

4

pEDFM ON CORNER-POINT GRID GEOMETRY

In the previous chapter, the fine-scale discretization of the governing equations for different fluid models was fully covered in detail. The mass and heat (convection and conduction) fluxes between each set of neighboring grid cells in each medium were calculated. Moreover, these fluxes were obtained between the non-neighboring connections (i.e., between the rock matrix and the overlapping fractures, and between the intersecting fracture elements themselves). The discretized equations were written in residual form. Using the Newton-Raphson linearization schemes, the nonlinear terms of the equations were linearized and the linear system of equations were formed, where the vectors of the update of the unknowns were obtained by solving the linearized system inside an iteration loop at each time-step.

At the final section of the previous chapter, we described the fracture models, namely, the embedded discrete fracture model (EDFM) and the projection-based EDFM (pEDFM) approaches. Using two simple test-cases, the validation of these methods were presented. Both methods were able to acceptably represent direct numerical simulation (DNS) results in presence of highly conductive fractures. However, it could be seen that the pEDFM could provide more accuracy when dealing with flow barriers or sealing/impermeable fractures/faults, while the usage of the EDFM resulted in non-physical solutions.

As discussed at the end of the previous chapter, geological formations can hardly be represented by Cartesian grids, as this grid geometry is not an acceptable gridding system when dealing with real field-scale and geologically-relevant domains, although these simplified grids allow for many conceptual modeling analyses. Realistic formations, are more conveniently represented by flexible grids [42, 48]. The grid geometry should create a set of discrete cell volumes that approximate the reservoir volume, yet fit the transport process physics, and avoid over complications as much as possible [40].

Various parts of this chapter have been published by the author in the Journal of Advances in Water Resources.

Therefore, a more complex and flexible gridding system is needed to be employed by simulation models. Unstructured grids allow for many flexibilities, which need to be carefully applied to a computational domain so that the discrete systems do not become unnecessarily complex [35, 49]. Without introducing the full flexibility (and at the same time complexity) of the fully unstructured grids, the so-called corner-point grid (CPG) geometry is a viable option, as it allows for many possibilities in better representation of geological structures. This has made it one of the most commonly used gridding systems and quite attractive in the field of geo-sciences and industry-grade simulation models. [50–53].

In this chapter, the corner-point grid (CPG) geometry is described. Via a number of test-cases with box-shaped domains, the accuracy of the corner-point grid results are compared against the results obtained by the Cartesian grid geometry. Afterwards, the pEDFM model will be presented for the corner-point grid geometry. The pEDFM is employed in order to explicitly and consistently represent fractures and to provide independent gridding of the rock matrix and the fractures regardless of the complex geometrical shapes of such domains. Here, the applicability of the pEDFM implementation [46, 47] has been extended to a fully generic 3D geometry where it allows for inclusion of fractures (or flow barriers) with any orientation on the corner-point grid geometry. This is crucial for practical field-scale applications. In addition to geometrical flexibility, the matrix-matrix and fracture-matrix connectivities are re-adjusted to account for the projection of the fracture planes on the interfaces. It will be shown how these connectivity indices are obtained in the new geometrical system. This allows for consistent modeling of the fractures with a generic range of conductivities. At last, a few geologically relevant models will be used as test-cases to show the performance of the pEDFM model on the corner-point grid geometry as a proof-of-concept.

4.1. CORNER-POINT GRID GEOMETRY

A corner-point grid (CPG) is defined with a set of straight pillars outlined by their endpoints over a Cartesian 2D mesh in the lateral direction [53]. On every pillar, a constant number of nodes (corner-points) is set, and each cell in the grid is set between 4 neighboring pillars and two neighboring points on each pillar. Every cell can be identified by integer coordinates (i, j, k); where the k coordinate runs along the pillars, and i and j coordinates span along each layer. The cells are ordered naturally with the i-index (x-axis) cycling fastest, then the j-index (y-axis), and finally the k-index (negative of z-direction).

For establishing vertical and inclined faulting more accurately, it is advantageous to define the position of the grid cell by its corner point locations and displace them along the pillars that have been aligned with faults surfaces. Similarly, for modeling erosion surfaces and pinch-outs of geological layers, the corner point format allows points to collapse along the coordinate lines. The corner points can collapse along all four lines of a pillar so that a cell completely disappears in the presence of erosion surfaces. If the collapse is present in some pillars, the degenerate hexahedral cells may have less than six faces. This procedure creates non-matching geometries and non-neighboring connections in the underlying i-j-k topology [53].

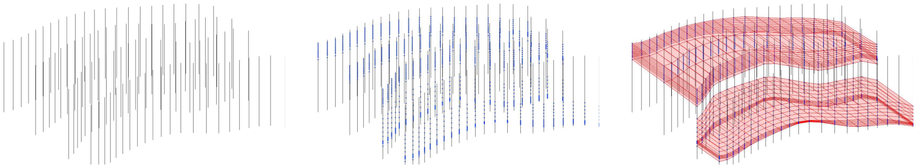

Figure 4.1: Construction of a corner-point grid: Starting from the coordinate lines defining pillars (left), the corner-points are added to them (middle). A stack of cells is created for each set of four lines defining a pillar and at last the full grid is obtained.

4.1.1. TWO-POINT FLUX APPROXIMATION IN THE CORNER-POINT GRID GEOMETRY

In order to only highlight the calculation of the two-point flux approximation in the corner-point grid geometry and avoid complexities in presenting fully detailed governing equations, a simplified linear elliptic equation is used which serves as a model pressure equation for incompressible fluids, i.e.,

$$\nabla \cdot \boldsymbol{u} = f, \tag{4.1}$$

where f is the source/sink term (wells), and u is the Darcy velocity, defined as

$$\boldsymbol{u} = -\mathbf{K}\nabla p. \tag{4.2}$$

Finite volume discrete systems can be obtained by rewriting the equation in integral form, on discrete cell Ω_i, as

$$\int_{\partial\Omega_i} \boldsymbol{u}\cdot\boldsymbol{n}\, dS = -\int_{\Omega_i} q\, d\boldsymbol{x}. \tag{4.3}$$

The flux between the two neighboring cells i and k can be then written as

$$\boldsymbol{u}_{i,k} = \int_{\Gamma_{i,k}} \boldsymbol{u}\cdot\boldsymbol{n}\, dS. \tag{4.4}$$

The faces $\Gamma_{i,k}$ are denominated half face as they are linked with a grid cell Ω_i and a normal vector $\boldsymbol{n}_{i,k}$. It is assumed that the grid is matching to another one so that each interior half-face will have a twin half-face $\Gamma_{k,i}$ that also has an identical area $A_{i,k} = A_{k,i}$ but opposite normal vector $\boldsymbol{n}_{i,k} = -\boldsymbol{n}_{k,i}$. The integral over the cell face is approximated by the midpoint rule, and Darcy's law, i.e.,

$$\boldsymbol{u}_{i,k} \approx A_{i,k}\left(\mathbf{K}\nabla p\right)\left(\boldsymbol{x}_{i,k}\right)\cdot\boldsymbol{n}_{i,k} \tag{4.5}$$

where $\boldsymbol{x}_{i,k}$ indicates the centroid of $\Gamma_{i,k}$.

The one-sided finite difference is used to determine the pressure gradient as the difference between the pressure $\pi_{i,k}$ at the face centroid and the pressure at some point inside the cell. The reconstructed pressure value at the cell center is equal to the average pressure p_i inside the cell, thus,

$$\boldsymbol{u}_{i,k} \approx A_{i,k}\mathbf{K_i}\frac{(p_i - \pi_{i,k})\boldsymbol{c}_{k,i}}{\mid \boldsymbol{c}_{k,i} \mid^2} \cdot \boldsymbol{n}_{i,k} \;\Rightarrow \boldsymbol{u}_{i,k} \approx T_{i,k}(p_i - \pi_{i,k}). \tag{4.6}$$

The vectors $\boldsymbol{c}_{k,i}$ are defined from the cell centroids to the face centroids. Face normal vectors are assumed to have a length equal to the corresponding face areas $A_{i,k} \cdot \boldsymbol{n}_{i,k}$, i.e.,

$$T_{i,k} = A_{i,k}\mathbf{K_i}\frac{\boldsymbol{c}_{k,i} \cdot \boldsymbol{n}_{i,k}}{\mid \boldsymbol{c}_{k,i} \mid^2} \tag{4.7}$$

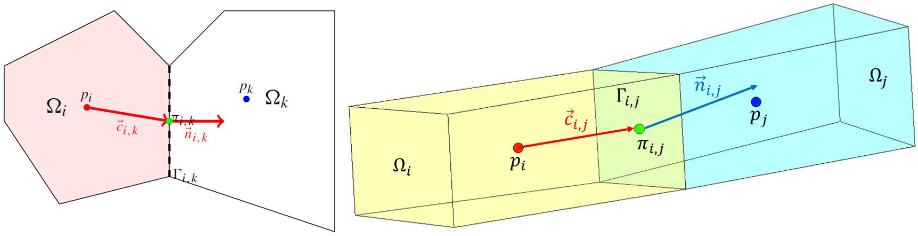

Figure 4.2: Two cells used to define the two-point discretization on general 2D polygon cells (see figure on the left) and 3D polyhedral cells (see figure on the right).

The one-sided transmissibilities $T_{i,k}$ are related to a single cell and provide a two-point relation between the flux across a cell face and the pressure difference between the cell and the face centroids. The proper name for these one-sided transmissibilities is half-transmissibilities as they are associated with a half-face [35, 112].

Finally, the continuity of the fluxes across all the faces, $\boldsymbol{u}_{i,k} = -\boldsymbol{u}_{k,i}$, as well as the continuity of face pressures $\pi_{i,k} = \pi_{k,i} = \pi_{ik}$ are set. This leads to

$$T_{i,k}^{-1}\, \boldsymbol{u}_{ik} = p_i - \pi_{ik} \tag{4.8}$$

$$-\,T_{k,i}^{-1}\, \boldsymbol{u}_{ik} = p_k - \pi_{ik}. \tag{4.9}$$

The interface pressure π_{ik} is then eliminated and the two-point flux approximation (TPFA) scheme is defined as

$$\boldsymbol{u}_{ik} = \left[T_{i,k}^{-1} + T_{k,i}^{-1}\right]^{-1} (p_i - p_k) = T_{ik}\,(p_i - p_k). \tag{4.10}$$

Here, T_{ik} is the transmissibility associated with the connection between the two cells. The TPFA scheme uses two "points", the cell average pressures p_i and p_k, to approximate the flux across the interface $\Gamma_{i,k}$ between cells Ω_i and Ω_k. The TPFA scheme in a compact form obtains a set of cell averages that meet the following system of equations

$$\sum_k T_{ik}\,(p_i - p_k) = q_i\,, \quad \forall \Omega_i \subset \Omega. \tag{4.11}$$

4.2. pEDFM CONNECTIVITIES

As stated in the section of the discretization of governing equations, sets of flux exchange terms are defined between the matrix and the explicit fractures. Inside each term, the connectivity index ($CI_{ij} = \frac{A_{ij}}{\langle d \rangle_{ij}}$) is considered. In the corner-point grid geometry, to calculate the area fraction (A_{ij}) of each overlapping fracture element inside the corresponding matrix grid cell, various geometrical functions are defined which can obtain the intersection between a tetragon (the 2D planar fracture grid cell in 3D geometry) and a hexahedron (the matrix grid cell in the corner-point grid geometry). Once the intersection is obtained and the area fraction is calculated, the average distance ($\langle d \rangle_{ij}$) between the two overlapping elements is calculated as well. Figures 4.3 and 4.4 illustrate the geometry of CPG-based pEDFM grids. Note that the fractures can have any orientations in 3D, and arbitrary crossing lines with other fractures.

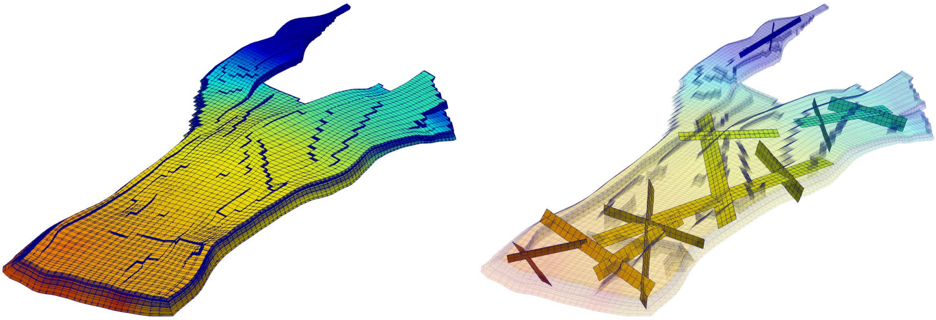
(a) matrix grid

(b) fracture grids

Figure 4.3: An example of a fractured domain on the corner-point grid geometry. The domain presented in the left image is the well-known Norne oil-field which is a representative of the real-field geometry [53]. The figure on the right is a realization of a fracture network inside the domain that was exclusively designed by the author. Note that each sub domain (the rock matrix, and the individual fractures) entail independent grid resolutions, and can have independent complexities (e.g. 3D orientation).

To develop the pEDFM for the CPG geometry, first, all the connectivities between each set of neighboring matrix cells that are disconnected due to the overlapping fractures are detected. Due to the geometrical algorithm devised during the development of this method, a continuous projection path (visible in figure 4.5 as solid lines in light-blue color) is automatically obtained on the interfaces. As such it disconnects the neighboring connections letting the flux occur only on one consistent route (i.e., through matrix-fracture-matrix). Let the fracture element f overlap with the rock matrix grid cell Ω_i (see figure 4.5). The area fraction of this overlap is denoted as A_{if}. In this 2D example, two projections are obtained on the interfaces between the matrix grid cell Ω_i and its neighboring grid cells that are affected by the crossing (i.e., Ω_j and Ω_k). Please note that in the 3D dimensional case, there will be three projections. For the interface between the grid cells Ω_i and Ω_j (denoted as $\Gamma_{i,j}$), the projection area fraction $A_{if\perp\Gamma_{i,j}}$ is obtained via

$$A_{if\perp\Gamma_{i,j}} = A_{if} \times \cos(\gamma), \tag{4.12}$$

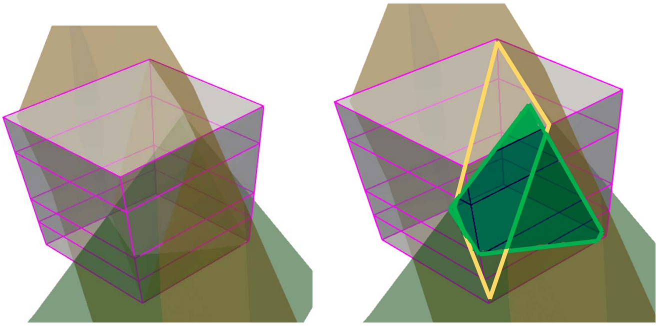

Figure 4.4: The intersection between to fractures and a hexahedron in the corner-point grid geometry is illustrated here. The figure on the right highlights the area fraction of the two separate fracture planes inside the matrix grid cell. The overlapping segment of green fracture forms an irregular pentagon where the yellow fracture has a tetragon as the overlapping segment.

where γ is the angle between the fracture element and $\Gamma_{i,j}$ the interface connecting the matrix grid cell Ω_i and the neighboring grid cell in the corresponding dimension Ω_j. On the zoomed-in section of figure 4.5, this projection area fraction is highlighted in red color. Similarly, the projection area fractions on the interfaces between all the neighboring matrix grid cells that are intersected by fracture elements are calculated based on the same formulation. New transmissibilities are defined to connect the fracture element f to each non-neighboring matrix grid cells (i.e., j and k in the example shown in figure 4.5):

$$T_{i_e f} = \frac{A_{if \perp \Gamma_{i,j}}}{\langle d \rangle_{i_e f}} \lambda_{i_e f}, \tag{4.13}$$

where, $\langle d \rangle_{i_e f}$ is the average distance between the fracture element f and the matrix grid cell i_e. $\lambda_{i_e f}$ is the effective fluid mobility between these cells. As a result of the new transmissibilities, the connectivity between the matrix grid cell i and its corresponding neighboring cells is modified:

$$T_{ii_e} = \frac{A_{ii_e} - A_{if \perp \Gamma_{i,j}}}{\Delta x_e} \lambda_{i_e f}, \quad \mathfrak{X} \in \{x, y, z\}. \tag{4.14}$$

To describe the implementation in a simpler manner, all the transmissibilities are multiplied by a coefficient α as a fraction of the interface cross-sectional area that is covered by the projection. One needs to note that except for the boundaries/edges of the fractures, the projection will cover the whole area of the affected interfaces. Therefore, α is 1.0 for the majority of the cases, resulting in zero transmissibility between the rock matrix grid cells (i.e., $T_{ii_e} = 0$), and removing the parallel transmissibilities [46].

4.3. TEST CASES AND RESULTS

Numerical results of various test cases are presented in this section. The first two test cases compare the pEDFM model on the Cartesian grid geometry with the pEDFM on the corner-point grid geometry The third test case demonstrates the pEDFM result on

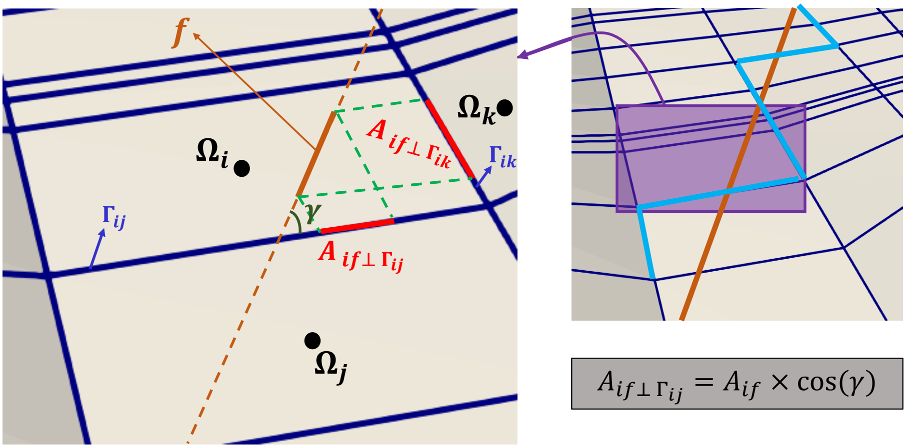

Figure 4.5: The pEDFM Illustration for a rock matrix in the corner-point grid geometry and a 1D overlapping fracture. The overlapped matrix cells are connected to each overlapping fracture element via the connectivity index in the matrix-fracture flux exchange. The pEDFM introduces extra non-neighboring connections between fracture elements and matrix cells. The matrix-matrix connectivities are changed if the fracture plane intersects the line that passes through the cell centers of each two neighboring matrix grid cells.

a non-orthogonal grid model. Thereafter, we move towards a series of geologically relevant fields (all with isothermal multiphase fluid model). Using the pEDFM on the corner-point grid geometry, a number of synthetic (highly conductive) fractures and (impermeable) flow barriers are added to the geologically relevant models. The performance of this method will not be benchmarked as the purpose of these simulation results is to demonstrate the pEDFM on the corner-point grid geometry as a proof-of-concept.

Tables 4.1 and 4.2 show the mutual input parameters that are used for the test cases with isothermal multiphase and geothermal single-phase flow models respectively.

4.3.1. TEST CASE 1: 2D HETEROGENEOUS FRACTURED RESERVOIR (SQUARE)

In this test case, the pEDFM on Cartesian grid versus the corner-point grid geometry is visually compared. For this reason, a box-shaped heterogeneous 100 [m] × 100 [m] domain containing 30 fractures with mixed conductivities is considered. The length of each fracture is different but the size of their aperture is identical and set to $a_f = 5 \cdot 10^{-3}$ [m]. A 136 × 136 grid is imposed on the rock matrix and the fracture network consists of 1024 grid cells (in total 19520 cells). The permeability of the rock matrix ranges from $K_{m_{min}} = 1.2 \times 10^{-15}$ [m^2] to $K_{m_{max}} = 1.2 \times 10^{-12}$ [m^2]. And the permeability of the fracture network has the range of $K_{f_{min}} = 10^{-20}$ [m^2] and $K_{f_{max}} = 10^{-6}$ [m^2]. Two injection wells are located at the bottom left and top left corners with an injection pressure of $p_{\text{inj}} = 2 \times 10^7$ [Pa]. Additionally, there are two production wells at the bottom right and the top right corners with a pressure of $p_{\text{prod}} = 1 \times 10^7$ [Pa]. Table 4.2 demonstrates the input parameters of this test case. Figure 4.6 shows the results of the simulation using both the Cartesian Grid and the corner-point geometry.

Note that in this test case (and the test case 2), the x, y, z coordinates of the grids of

Table 4.1: Input parameters of the fluid and rock properties for isothermal multiphase flow used in some test cases.

Property	value
Matrix porosity (ϕ)	$0.2[-]$
Fractures permeability (min)	10^{-22} [m^2]
Fractures permeability (max)	10^{-6} [m^2]
Fractures aperture	5×10^{-3} [m]
Fluid viscosity (phase 1, μ_1)	0.001 [Pa.S]
Fluid viscosity (phase 2, μ_2)	0.003 [Pa.S]
Fluid density (phase 1, ρ_1)	1000 [kg/m^3]
Fluid density (phase 2, ρ_2)	850 [kg/m^3]
Initial pressure of the reservoir	2×10^7 [Pa]
Initial saturation (phase 1, S_1)	$0.0[-]$
Initial saturation (phase 1, S_2)	$1.0[-]$
Injection Pressure	5×10^7 [Pa]
Production Pressure	1×10^7 [Pa]

Table 4.2: Input parameters of the fluid and rock properties for the geothermal single-phase flow used in some test cases.

Property	value
Rock thermal conductivity (Λ_r)	4 [W/m.K]
Fluid thermal conductivity (Λ_f)	0.591 [W/m.K]
Rock density (ρ_r)	2750 [kg/m^3]
Fluid specific heat (C_{p_f})	4200 [J/kg.K]
Rock specific heat (C_{p_r})	790 [J/kg.K]
Matrix porosity (ϕ)	$0.2[-]$
Fractures permeability (min)	10^{-20} [m^2]
Fractures permeability (max)	10^{-8} [m^2]
Fractures aperture	5×10^{-3} [m]
Initial pressure of the reservoir	1.5×10^7 [Pa]
Initial temperature of the reservoir	400 [K]
Injection Pressure	2×10^7 [Pa]
Injection Temperature	300 [K]
Production Pressure	1×10^7 [Pa]

the Cartesian geometry and the corner-point grid geometry are identical. However, the grids are generated with different geometrical approaches. In one scenario, the grid cells are discretized using the Cartesian grid geometry and the grid cells are indexed in every of the x,y,z directions ($i \in \{1,...,N_x\}$, $j \in \{1,...,N_y\}$, $k \in \{1,...,N_z\}$). For this scenario the pEDFM for the Cartesian grid is used which has already been developed [46]. In the other scenario, the grid cells are generated using the corner-point grid geometry where a list of nodes and a list of all the interfaces and transmissibilities are generated. the pEDFM for the corner-point grid geometry that is developed in this work is used for this scenario. Therefore, the size and positioning of the grid cells in the two scenarios are identical,

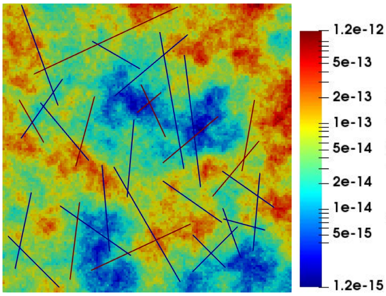

(a) Permeability

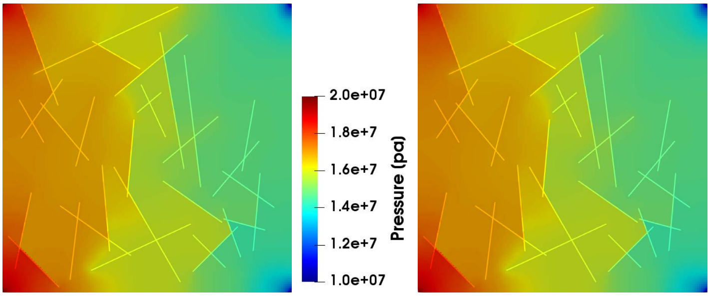

(b) Pressure, Cartesian Grid (c) Pressure, Corner-point Grid

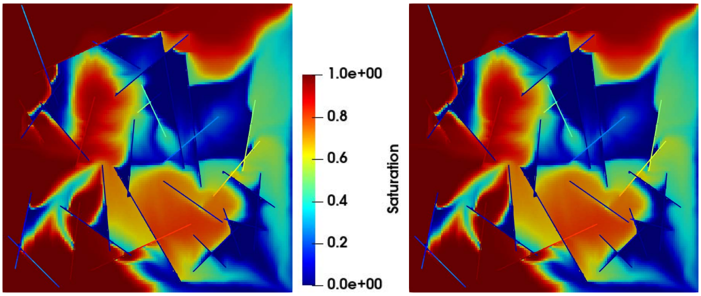

(d) Saturation, Cartesian Grid (e) Saturation, Corner-point Grid

Figure 4.6: Test case 1: 2D Heterogeneous. Figure 4.6a illustrates the permeability map of the system. Figures 4.6b and 4.6c show the pressure solution on a specific time-step for the Cartesian grid and the corner-point grid geometry respectively. The figures on the bottom row (4.6d and 4.6e) visualize the saturation solutions at the same time-step.

though have been generated with different geometrical approaches.

The results of the both scenarios show a match visually. In order to quantify the difference between the results of the two different geometrical approach for the pEDFM, a average relative error (in second norm) is calculated for the pressure and the saturation distributions over the entire simulation time. This relative error for each variable x is calculated as

$$e_x = \frac{|| x_{\text{Cart}} - x_{\text{CPG}} ||_2}{|| x_{\text{Cart}} ||_2}, \tag{4.15}$$

where x is a solution vector (of either of the main unknowns) and the subscripts Cart and CPG indicate Cartesian grid and the corner-point grid geometry. The errors calculated for this test case are $e_p = 1.55 \times 10^{-}5$ and $e_S = 1.60 \times 10^{-}4$.

4.3.2. TEST CASE 2: 3D HOMOGENEOUS FRACTURED RESERVOIR (BOX)

This test case, similar to the test case 1, shows a visual comparison for the pEDFM on the Cartesian grid versus the corner-point grid geometry. A 3D 100 [m] × 100 [m] × 40 [m] domain containing 15 lower dimensional fractures with different geometrical properties is considered. A 50 × 50 × 20 grid is imposed on the rock matrix. The fracture network contains 1005 grid cells (total of 51005 grid cells). The rock matrix has a permeability of $K_m = 10^{-14}\,[\mathrm{m}^2]$. The fracture network consists of both highly conductive fractures with a permeability of $K_f = 10^{-6}\,[\mathrm{m}^2]$ and flow barriers with a permeability of $K_f = 10^{-22}\,[\mathrm{m}^2]$. Two injection wells exist on the left corners with a pressure of $p_{\mathrm{inj}} = 2 \times 10^7$ [Pa]. Similarly, two production wells are located at the right corners with a pressure of $p_{\mathrm{prod}} = 1 \times 10^7$ [Pa]. All wells are vertical and are perforated over the entire thickness of the reservoir.

Two different grids are considered using the CPG geometry: one with orthogonal grids where the coordinates of all the grid cells are identical with those in the Cartesian grid geometry, and one with non-orthogonal grids where the pillars of the grids are slightly tilted. To provide a better insight, the non-orthogonal grid mesh is shown in figure 4.7. As shown, the domain remains a Cartesian box, but the CPG grid is tilted to verify its consistency.

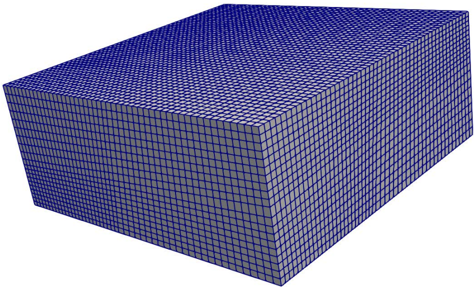

Figure 4.7: Test case 2: The non-orthogonal mesh structure used in this test case. The domain is a 3D Cartesian box, but the grids have tilted pillars in two of the dimensions, creating non-orthogonal grids.

Figure 4.8 illustrates the results of the simulation using both the Cartesian Grid and the two sets of CPG models.

Figure 4.9 shows the errors between the results of the Cartesian grid geometry (as the reference solution) and the two CPG cases (orthogonal and non-orthogonal). Similar to the previous test case, a match is visible between the results of the Cartesian grid and the orthogonal corner-point grid, with errors (calculated via equation 4.15) of $e_p = 1.71 \times 10^{-9}$ and $e_S = 2.47 \times 10^{-8}$. The difference between the solutions of the Cartesian grid and the non-orthogonal corner-point grids are greater as the different grid geometry results in different connectivities ($e_p = 1.03 \times 10^{-2}$ and $e_S = 4.44 \times 10^{-2}$).

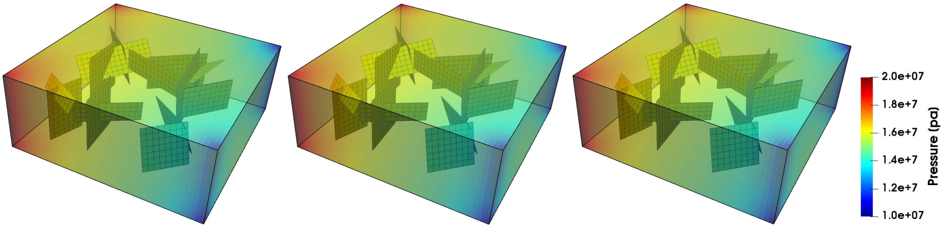

(a) Cartesian Grid (b) Orthogonal CPG (c) Non-orthogonal

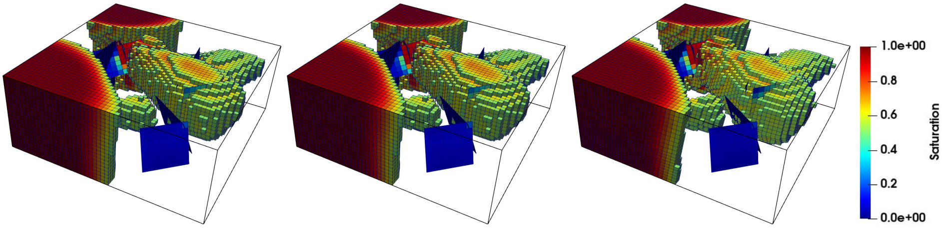

(d) Cartesian Grid (e) Orthogonal CPG (f) Non-orthogonal

Figure 4.8: Test case 2: 3D Homogeneous box. The figures in the upper row show the pressure solutions at a specific time-step for the Cartesian grid and the CPG geometries respectively. The figures on the bottom row illustrate the saturation solutions at the same time-step.

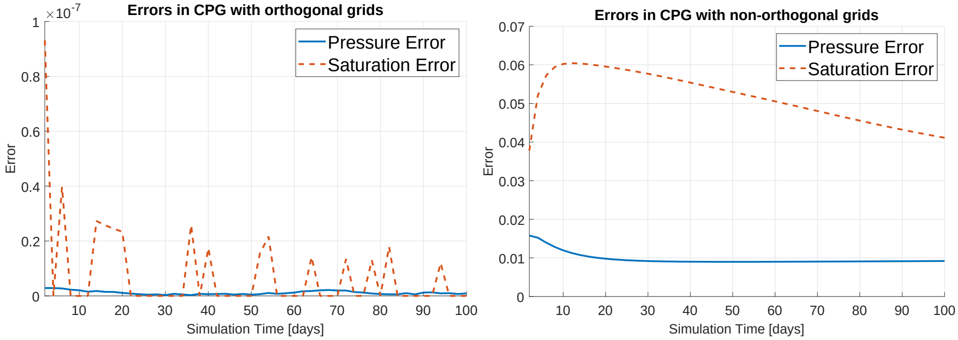

(a) Orthogonal CPG (b) Non-orthogonal CPG

Figure 4.9: Test case 2: The errors (calculated via equation **??**) of the pressure and saturation results between the Cartesian grid geometry (as the reference solution) and the CPG geometries: one with orthogonal grids (figure 4.9a) and one with non-orthogonal grids (figure 4.9b).

4.3.3. TEST CASE 3: 3D RESERVOIR WITH NON-ORTHOGONAL GRIDS

The third test case (figure 4.10) demonstrates the capability of the pEDFM on the reservoir model based on the corner point grids. The grid cells in test case 2 were deformed to create a distorted version of that model. The model allows to test the pEDFM implementation in a non-orthogonal grid system. The same dimensions and gridding from test case 2 are used in this test case. The fracture network consisting of 15 fractures is discretized in 876 grids, and a total of 50876 grid cells are imposed on the entire domain. Some fractures are considered as highly conductive with a permeability of $K_f = 10^{-8}$ [m^2]

while others are given a very low permeability of $K_f = 10^{-20}$ [m^2] and are considered to be flow barriers (shown in figure 4.10a with yellow color for high permeability and blue color for low permeability). The well pattern and the pressure restrictions are also the same as in the previous test case.

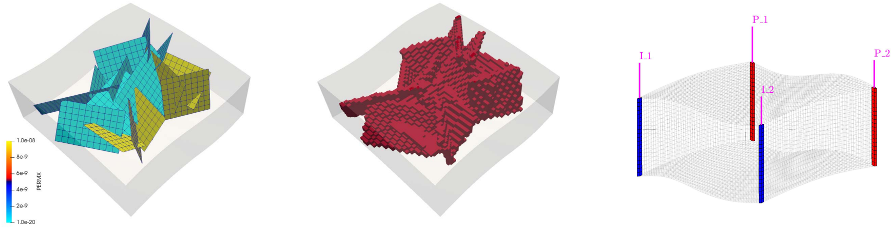

(a) Fractures permeability (scenario 1)

(b) Matrix cells overlapped by fractures

(c) The wells geometry

Figure 4.10: Test case 3: A 3D fractured deformed box with non-orthogonal grid on the corner-point grid geometry. Figures 4.10a shows the permeability of the fractures. Figure 4.10b illustrates the matrix grid cells that are overlapped by the fractures. Figure 4.10c shows the positioning of the injection and production wells.

The pressure and the saturation results are shown in figures 4.11a and 4.11b respectively (at the left side of figure 4.11). As the grid geometry and the gridding system of this test case is not similar to the previous test case, it is not possible to compare the two test cases. The pressure and the saturation distribution of the second scenario (at the same simulation time) can be observed at the right side of figure 4.11. The flow barriers are close to the injection wells, thus restricting the displacement of the injecting phase towards the center of the domain (figure 4.11b). Therefore, a high pressure gradient is visible near the injection wells (figure 4.11a) as the low permeability fractures limit the flux through the domain.

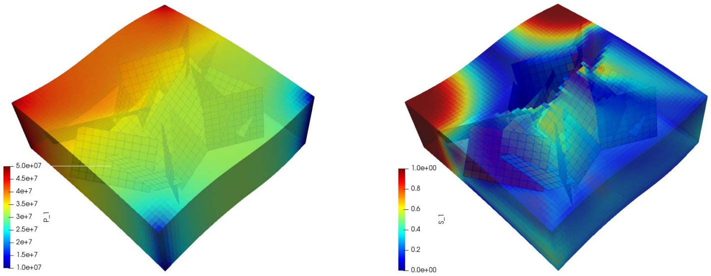

(a) Pressure

(b) Saturation

Figure 4.11: Test case 3: A 3D fractured deformed box with non-orthogonal corner-point grid geometry. Figure 4.11a shows the pressure solution, figure 4.11b illustrates the saturation distribution.

Additionally, to perform a grid resolution sensitivity analysis of the developed model, this test case was used with three different grid resolutions. While keeping all the input parameters identical as the ones that were mentioned above, three different computational grids (using corner-point grid geometry) were imposed on this domain, namely, $80 \times 80 \times 32$, $40 \times 40 \times 16$ and $20 \times 20 \times 8$ for the rock matrix, and 2852, 757 and 173 for the fracture network, respectively. Figure 4.12 shows the saturation distribution of these three different gird resolutions at a simulation time of $t = 100\,[days]$. The results of the two lower grid resolutions (i.e., $20 \times 20 \times 8$ and $40 \times 40 \times 16$) were compared against the results of the highest grid resolution (i.e., $80 \times 80 \times 32$), meaning that the results of the $80 \times 80 \times 32$ grid resolution is used as reference in the calculation of the error. The relative error for pressure and saturation results are given in Figure 4.13. These errors are calculated as:

$$e_x = \frac{||\, x_{\text{HighRes}} - x_{\text{LowRes}} \,||_2}{||\, x_{\text{HighRes}} \,||_2}, \quad x = \{P, S_w\} \tag{4.16}$$

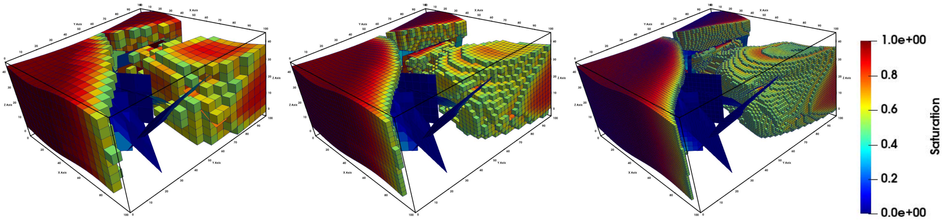

(a) $20 \times 20 \times 8$ (b) $40 \times 40 \times 16$ (c) $80 \times 80 \times 32$

Figure 4.12: Test case 3: Grid resolution sensitivity analysis with three different grid resolutions (with non-orthogonal corner-point grids) imposed on the computational domain. The figures show the saturation distribution at $t = 100[days]$ of simulation time. Only the gird cells with the saturation values of higher than $S_w = 0.5$ are visible.

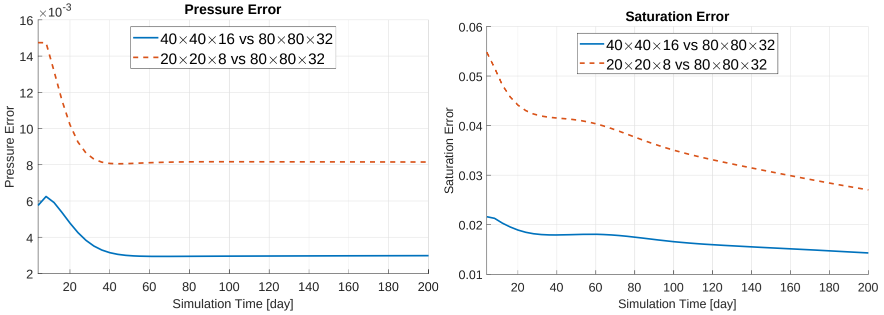

(a) Pressure error (b) Saturation error

Figure 4.13: Test case 3: Grid resolution sensitivity analysis with three different grid resolutions (with non-orthogonal corner-point grids) imposed on the computational domain. These figures illustrate the pressure and saturation errors of the results from different grid resolutions.

4.3.4. TEST CASE 4: THE JOHANSEN FORMATION

The water-bearing Johansen formation was a potential candidate for CO_2 storage in a project promoted by the Norwegian government. The Norwegian continental margin has excellent potential for CO_2 storage options in saline aquifers.

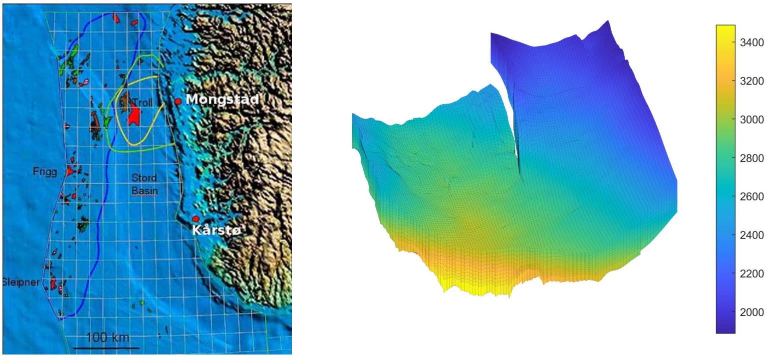

Figure 4.14: Test case 4: The location of the Johansen formation can be observed on the left figure. This formation is located within the green curve in the map, and the yellow curve represents areas where seismic data has been acquired (courtesy of Gassnova). The figure on the right shows the depth map of the Johansen model (NPD5 data set).

The Johansen formation [113] is located in the deeper part of the Sognefjord delta, 40–90[km] offshore Mongstad on Norway's southwestern coast (see figure 4.14). It belongs to the Lower Jurassic Dunlin group and is interpreted as a laterally extensive sandstone, and it is overlaid by the Dunlin shale, and closed from below by the Amundsen shale. A saline aquifer exists in the depth levels ranging from 2200[m] to 3100[m] below sea level. The depth range makes the formation ideal for CO_2 storage due to the pressure regimes existent in the field (providing a thermodynamical situation where CO_2 is in its supercritical phase).

These formations have uniquely different permeabilities, and perform very different roles in the CO_2 sequestration process. The Johansen sandstone has relatively high porosity and permeability, and it is suitable as a container to store CO_2. The overlaying Dunlin shale, with its low permeability, acts as a seal that avoids the CO_2 from leaking to the sea bottom layers.

The Johansen formation has an average thickness of nearly 100[m], and the water-bearing region extends laterally up to 60[km] in the east-west direction and 100[km] in the north-south direction. The aquifer has a good sand quality with average porosities of roughly 25%. This implies that the Johansen formation's theoretical storage capacity can exceed one Gigaton of CO_2 providing the assumption of residual brine saturation of about 20%. The northwestern parts of the Johansen formation are located some 500[m] below the operating Troll field, one of the North Sea's largest hydrocarbon fields.

DATA SET

The MatMoRA project has created five models of the Johansen formation: one full-field model ($149 \times 189 \times 16$ grids), three homogeneous sector models ($100 \times 100 \times n$ for $n = 11, 16, 21$), and one heterogeneous sector model ($100 \times 100 \times 11$) also known as the NPD5 sector. In this work, the last data set (NPD5) has been used. The NPD5 sector can be seen in figure 4.15. In the left side of this figure, the NPD5 sector is highlighted with blue color.

In the discretized computational grids, the Johansen formation is represented by five layers of grid cells. The Amundsen shale below the Johansen formation and the low-permeable Dunlin shale above are characterized by one and five cell layers, respectively. The Johansen formation consists of approximately 80% sandstone and 20% claystone, whereas the Amundsen formation consists of siltstones and shales, and the Dunlin group has high clay and silt content.

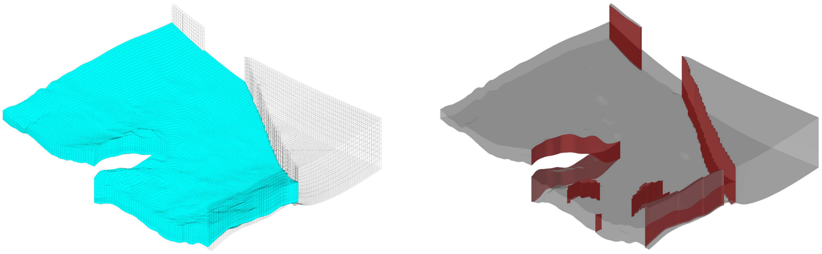

Figure 4.15: Test Case 4: Illustration of the Johansen model (NPD5 data set). The left figure represents the active section of the model or NPD5, highlighted with blue color, and the right figure shows the faults marked with red color.

ROCK PROPERTIES

The Johansen sandstone is a structure with a wedge shaped pinch out in the front part of the model and divided into two sections at the back. Figures 4.16a and 4.16b show the porosity and the permeability maps of the NPD5 sector, where the Dunlin shale above the Johansen and the Amundsen shale below the Johansen formation are excluded. The porosity map shows the cells with porosity values larger than 0.1. The permeability tensor is diagonal, with the vertical permeability equivalent to one-tenth of the horizontal permeability. The permeability is represented on a logarithmic color scale.

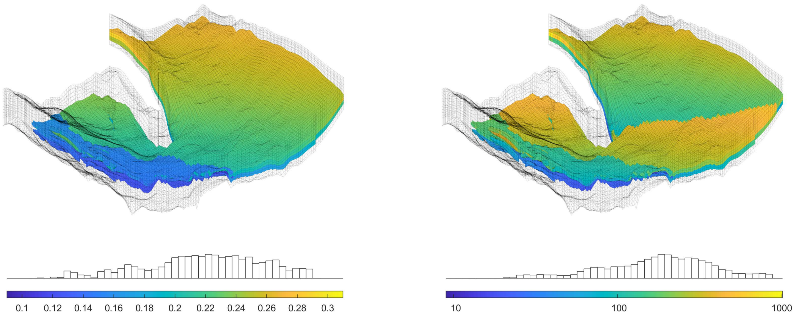

(a) Porosity of the NPD5 sector

(b) Permeability of the NPD5 sector

Figure 4.16: Test Case 4: The porosity and the permeability of the NPD5 sector of the Johansen field.

SIMULATION RESULTS

The “NPD5” sector of the Johansen formation model [53] is used in the following test case. It is a corner-point grid reservoir model that consists of $100 \times 100 \times 11$ grid cells from which 88775 grid cells are active. The rock properties of the Johansen formation available on public data were given as input in the simulation. A network of 121 fractures is embedded in the reservoir geological data set that contains both highly conductive fractures and flow barriers with a permeability of $K_{f_{max}} = 10^{-8}\,[\mathrm{m}^2]$ and $K_{f_{min}} = 10^{-20}\,[\mathrm{m}^2]$ respectively. The model is bounded by two shale formations. Therefore the fractures were placed inside the Johansen formation (layers 6 to 10). The fracture network consists of 3494 grid cells (in total 92269 grid cells for the rock matrix and the fractures). Five injection wells with a pressure of $p_{\mathrm{inj}} = 5 \times 10^7$ [Pa] and four production wells with a pressure of $p_{\mathrm{inj}} = 1 \times 10^7$ [Pa] were placed in the model. Wells are vertical and drilled through the entire thickness of the model. Figure 4.17d illustrates the location of the injection and production wells in this test case.

Two scenarios are considered with two different fracture networks of mixed conductivities. While the geometry of both fracture networks is identical, the permeability values of the fractures from scenario 1 are inverted for scenario 2. This implies that the highly conductive fractures in the fracture network of scenario 1 act as flow barriers in the 2nd scenario and the flow barriers of scenario 1 are modified to be highly conductive fractures in scenario 2. Figures 4.17a and 4.17b display the fracture networks of scenario 1 and scenario 2 respectively. The matrix grid cells overlapped by the fractures are visible in figure 4.17c.

The simulation results of the first scenario are presented in figures 4.18 and 4.19. The injection wells are surrounded by highly conductive fractures that facilitate the flow since the model’s dimensions are considerably large (approximately 50[km] × 50[km]). The pressure distribution in the reservoir is shown in figure 4.18. High pressure values are observed in a large section of the reservoir as there is no restriction for flow from the wells, and two shale formations bound the Johansen sandstone. One can interpret that the high pressure drop observed in some areas is caused by presence of low permeable fractures (or flow barriers) in those regions. The saturation displacement is considerably enhanced by the highly conductive fractures (figure 4.19) located near the injection wells.

The simulation results of the second scenario are presented in figures 4.20 and 4.21. The injection wells are surrounded by low conductive fractures which restrict the flow from the injection wells towards the production wells. The pressure distribution differs considerably when compared to the first scenario. The flow barriers near the wells result in high pressure drops in the vicinity of the injection wells. The saturation displacement (figure 4.21) is lower than that of scenario 1 due to presence of low conductive fractures near the injection wells.

4.3.5. TEST CASE 5: THE BRUGGE MODEL

The Brugge model is an SPE benchmark study conceived as a reference platform to assess different closed-loop reservoir management methods [114]. It is the largest and most complex test case on closed-loop optimization to represent real field management scenarios. The active Brugge field model has 44550 corner-point grid cells, and the main

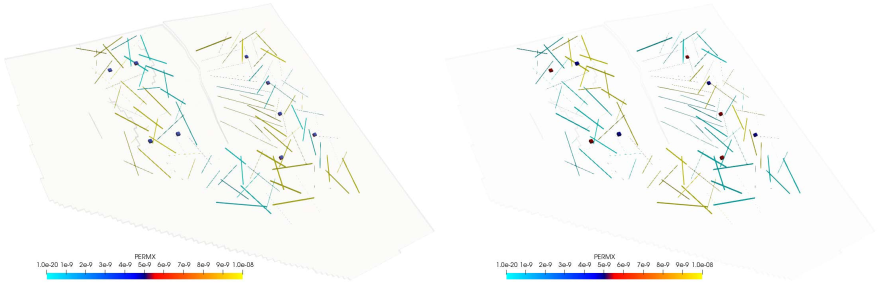

(a) Fractures permeability (scenario 1) (b) Fractures permeability (scenario 2)

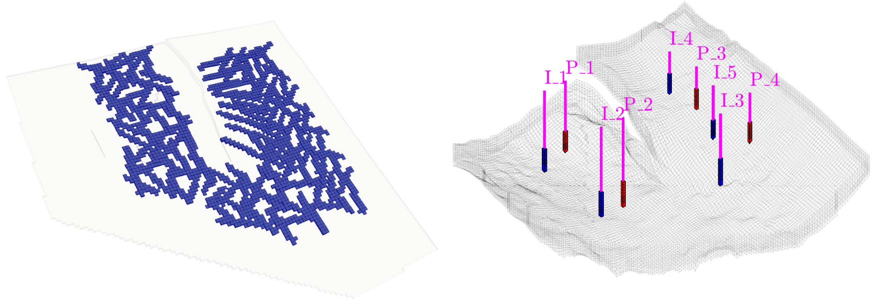

(c) Matrix cells overlapped by fractures (d) Location of injection and production wells

Figure 4.17: Test case 4: The Johansen formation with 9 wells and a set of 121 synthetic fractures (with mixed conductivities). The figures on top show the fracture network with different permeabilities for scenario 1 (top left) and scenario 2 (top right). The figure at bottom left illustrates the highlighted matrix cells that are overlapped by the fracture network. And the figure at bottom right shows the schematics of the injection and production wells.

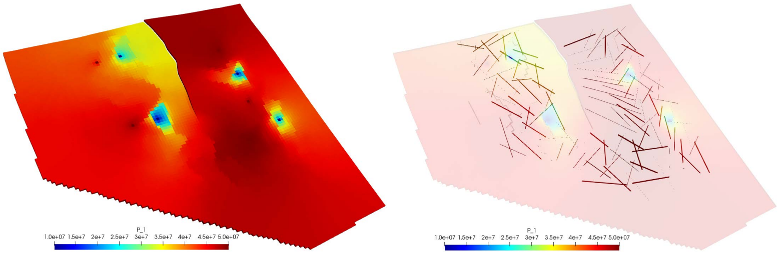

(a) Pressure in the matrix (b) Pressure in the fractures

Figure 4.18: Test case 4: The pressure profile of the Johansen formation for simulation scenario 1. The figure on the left illustrates the pressure distribution in the matrix grid cells. The transparency of this figure is increased to make the fractures visible and to display the pressure profile in the fractures in the figure on the right.

geological features present in the model are a boundary fault and an internal fault. Seven different rock regions with their particular petrophysical properties are distributed in the whole model. Thirty wells are included in the field model's well production pattern: 20 producers and 10 injectors.

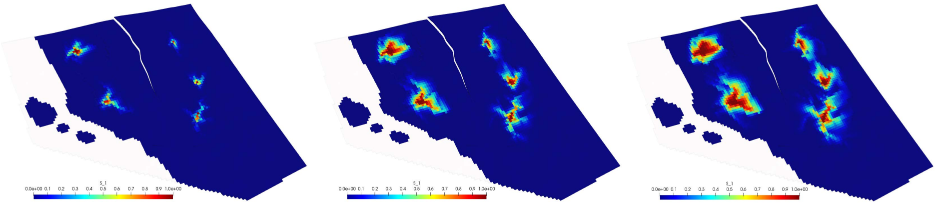

(a) Saturation in the rock matrix after {5000, 20000, 35000}[days]

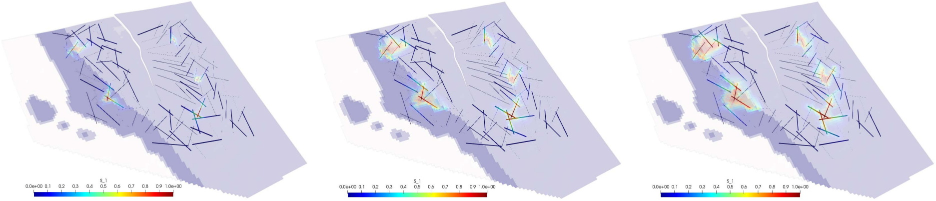

(b) Saturation in the fractures after {5000, 20000, 35000}[days]

Figure 4.19: Test case 4: The saturation profile of the Johansen formation for simulation scenario 1. The figures on the top row show the saturation profile in the matrix grid cells and the figures on the bottom row display the saturation maps in the fractures. From the left column towards the right column, the saturation profiles are displayed for simulations times 5000, 20000 and 35000[days] respectively.

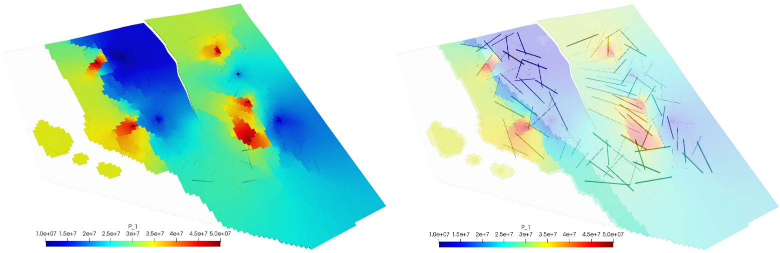

(a) Pressure in the matrix (b) Pressure in the fractures

Figure 4.20: Test case 4: The pressure profile of the Johansen formation for simulation scenario 2. The figure on the left illustrates the pressure distribution in the matrix grid cells. To make the pressure profile of the fractures visible, the transparency of the left side figure is increased and it is presented in the right side figure.

GEOLOGICAL MODEL

The geological structure of the Brugge field contains an east/west elongated half-dome with a boundary fault at its northern edge and an internal fault with a throw at an angle of nearly 20 degrees to the northern fault edge. The dimensions of the field are approximately 10[km] × 3[km]. The original high-resolution model consists of 20 million grid cells, with average cell dimensions of $50[\mathrm{m}] \times 50[\mathrm{m}] \times 0.25[\mathrm{m}]$. In addition to the essential petrophysical properties for reservoir simulation (sedimentary facies, porosity, permeability, net-to-gross, and water saturation), the grid model includes properties measured in real fields (gamma-ray, sonic, bulk density, and neutron porosity). The data was generated at a detailed scale to produce reliable well log data in the thirty wells drilled in the field.

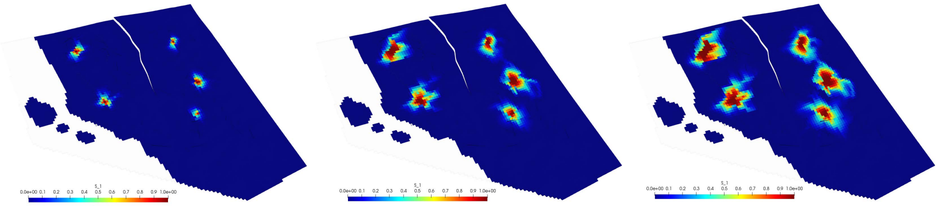

(a) Saturation in the rock matrix after $\{5000, 20000, 35000\}$[days]

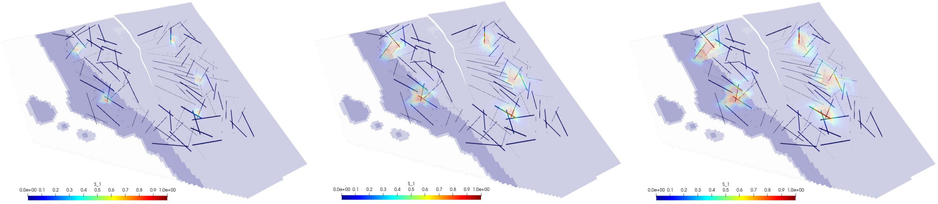

(b) Saturation in the fractures after $\{5000, 20000, 35000\}$[days]

Figure 4.21: Test case 4: The saturation profile of the Johansen formation for simulation scenario 2. The figures on the top row show the saturation profile in the matrix grid cells and the figures on the bottom row display the saturation maps in the fractures. From the left column towards the right column, the saturation profiles are displayed for simulations times 5000, 20000 and 35000[days] respectively.

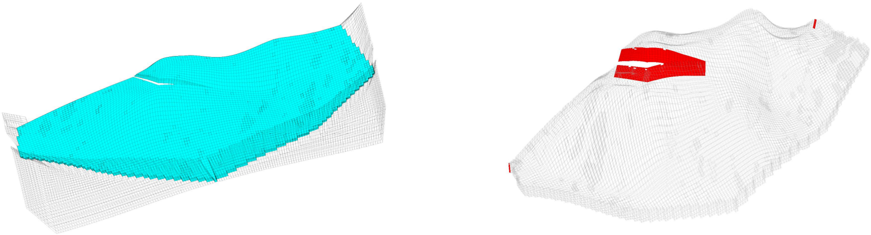

(a) The whole model with active cells

(b) Faults present in the model

Figure 4.22: Test case 5: Illustration of the Brugge model. The left graph represents the active section (colored in blue) of the model, and the right figure shows the faults marked with red color.

The original high-resolution model was upscaled to a 450000 grid cells model, which established the foundation for all additional reservoir simulations of the reference case. A set of 104 realizations, each containing 60000 grid cells, was created from the data that was extracted from the reference case.

ROCK PROPERTIES

Some properties of the realizations, i.e., porosity and permeability maps are visible in figure 4.23.

SIMULATION RESULTS

The following test case from the Brugge model is used to show the pEDFM model's capability on fracture modeling in a synthetic geologically relevant model with the corner-point grid geometry. The reservoir model consists of $138 \times 48 \times 9$ grid cells from which

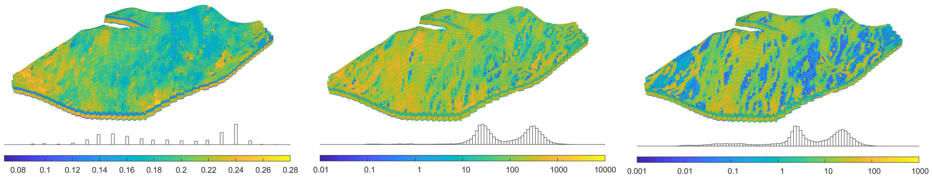

Figure 4.23: Test case 5: Porosity and permeability distributions of the Brugge field. The left graph shows the porosity of the model. The middle and the right figures illustrate the horizontal and vertical permeability, both plotted using a logarithmic color scale.

43474 grid cells are active. Rock properties of the realization available on public data were used in the simulation. A network of 60 fractures is defined in the reservoir domain containing both highly conductive fractures and flow barriers with a permeability of $K_{f_{max}} = 10^{-8}\,[\text{m}^2]$ and $K_{f_{min}} = 10^{-20}\,[\text{m}^2]$ respectively. The fracture network consists of 5384 grid cells (in total 48858 grid cells). The well pattern used in this test case was a modified version of the original well pattern (with 30 wells) [114]. Four injection wells with $p_{\text{inj}} = 5 \times 10^7$ [Pa] and three production wells with a pressure of $p_{\text{prod}} = 1 \times 10^7$ [Pa] were defined in the model. Wells are drilled vertically and perforate through the entire thickness of the reservoir.

Two scenarios are created with two different fracture networks of mixed conductivities. The geometry of both fracture networks is identical but the permeability values of the fractures from scenario 1 are inverted for scenario 2, namely, the highly conductive fractures in the fracture network of scenario 1 act as flow barriers in the 2nd scenario and the flow barriers of scenario 1 are modified to be highly conductive fractures in scenario 2. Figures 4.24a and 4.24b show the fracture networks of scenario 1 and scenario 2 respectively. The matrix grid cells overlapped by the fractures are visible in figure 4.17c.

The pressure and saturation results of scenario 1 are shown in figures 4.25 and 4.26 respectively. The pressure results are only shown for the simulation time 5000[days], but the saturation profiles are presented for three time intervals of 2000, 5000 and 10000[days]. The injection wells are surrounded by highly conductive fractures that act as flow channels. As a result, the saturation of the injecting phase is considerably increased in larger distances from the injection phases and the pressure drop around the injection wells is not high.

The pressure and saturation results of scenario 2 are shown in figures 4.27 and 4.28 respectively. The pressure results are only shown for the simulation time 5000[days], but the saturation profiles are presented for three time intervals of 2000, 5000 and 10000[days]. The injection wells are surrounded by flow barriers that restrict the flow. As a result, a high-pressure zone is formed near the wells since the central area of the reservoir is isolated with the low permeability fractures. This is followed by a sharp pressure gradient. The saturation displacement is small due to the reservoir's low permeability values and the absence of highly conductive fractures near the wells. The saturation displacement is restricted to the area near the injection wells.

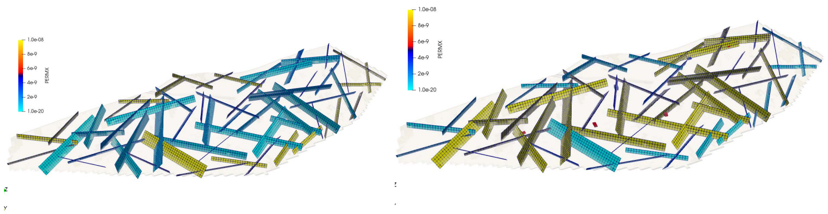

(a) Fractures permeability (scenario 1)

(b) Fractures permeability (scenario 2)

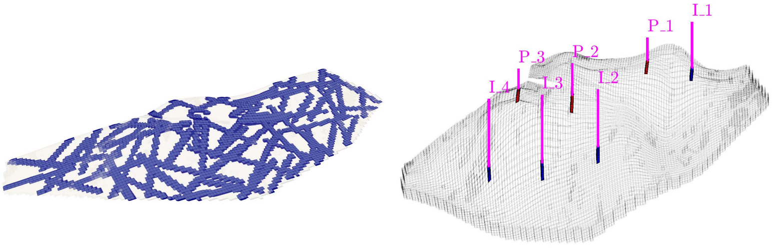

(c) Matrix cells overlapped by fractures

(d) Location of injection and production wells

Figure 4.24: Test case 5: The Brugge model with 7 wells (4 injectors and 3 producers) and a set of 60 synthetic fractures (with mixed conductivities). The figures on top show the fracture network with different permeabilities for scenario 1 (top left) and scenario 2 (top right). The figure at the bottom left illustrates the highlighted matrix cells that are overlapped by the fracture network. And the figure at the bottom right shows the schematics of the injection and production wells.

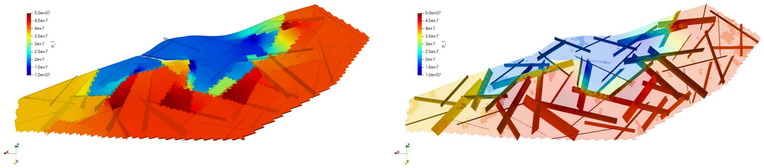

(a) Pressure in the matrix

(b) Pressure in the fractures

Figure 4.25: Test case 5: The pressure profile of the Brugge model for simulation scenario 1. The figure on the left shows the pressure distribution in the matrix grid cells. The transparency of this figure is increased to make the pressure map in the fractures visible. This map is displayed on the right figure. The results are shown for the simulation time 5000[days]

4.3.6. TEST CASES 6 AND 7: THE NORNE FIELD

The Norne field [115] is an oil and gas field situated in the Norwegian Sea around 80 kilometers north of the Heidrun oil field. The field dimensions are approximately 9[km] × 3[km] and the seawater depth in the area is 9[m]. The field is placed in a license awarded in 1986 and incorporates blocks 6608/10 and 6608/11 (see figure 4.29). Equinor is the current field operator. The expected oil recovery factor is more than 60%, which is very high for an offshore sub-sea oil reservoir.

Subsurface data from the Norne field have been published for research and edu-

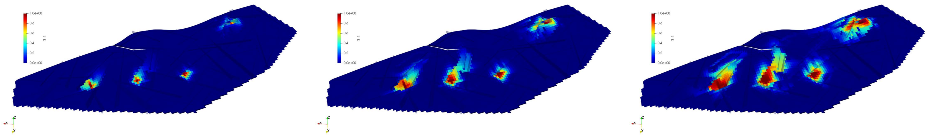

(a) Saturation in the rock matrix after {2000, 5000, 10000} [days]

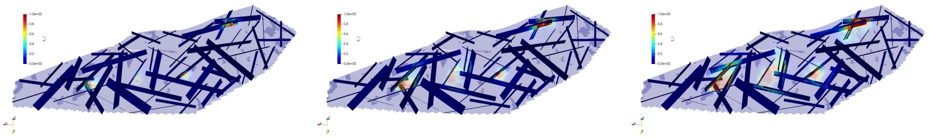

(b) Saturation in the fractures after {2000, 5000, 10000} [days]

Figure 4.26: Test case 5: The saturation profile of the Brugge model for simulation scenario 1. The figures on the top row illustrate the saturation profile in the matrix grid cells and the figures on the bottom row show the saturation maps in the fractures. From the top left column towards the right column, the saturation profiles are displayed for simulations times 2000, 5000 and 10000 [days] respectively.

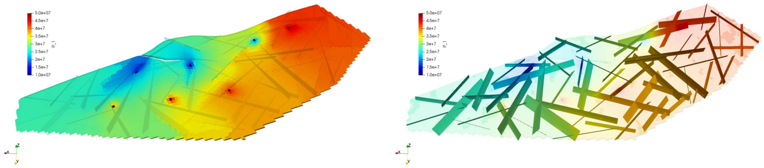

(a) Pressure in the matrix (b) Pressure in the fractures

Figure 4.27: Test case 5: The pressure profile of the Brugge model for simulation scenario 2. The figure on the left shows the pressure distribution in the matrix grid cells. The transparency of this figure is increased to make the pressure map in the fractures visible. This map is displayed on the right figure. The results are shown for simulation time 5000 [days]

cation purposes thanks to NTNU, Equinor, and the partners' initiative. The full simulation model can be obtained through the Open Porous Media (OPM) project (opm-project.org) [116]. The Norne field simulation model was the first benchmark case based on the real field data available to the public. The data is based on the 2004 geological model and consists of $46 \times 112 \times 22$ corner-point grid cells.

RESERVOIR

The production of the Norne field is obtained from a Jurassic sandstone, which lies at a depth of 2500 meters below sea level. The original estimation of recoverable resources was 95.2 million cubic meters for oil, mainly in the Ile and Tofte formations, and 13.01 billion cubic meters for gas in the Garn formation.

PETROPHYSICAL DATA

The field simulation model's petrophysical data consist of porosity, permeability, net-to-gross, and transmissibility multiplier data. Permeability is anisotropic and heterogeneous, with a clear layered structure as expected for a real reservoir field model. The

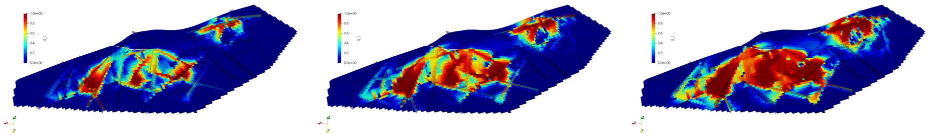

(a) Saturation in the rock matrix after {2000, 5000, 10000} [days]

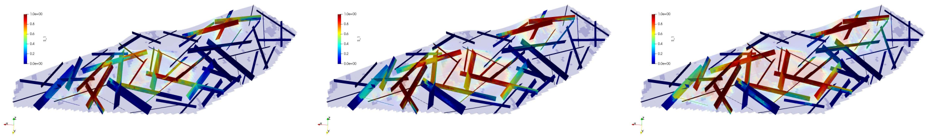

(b) Saturation in the fractures after {2000, 5000, 10000} [days]

Figure 4.28: Test case 5: The saturation profile of the Brugge model for simulation scenario 2. The figures on the top row illustrate the saturation profile in the matrix grid cells and the figures on the bottom row show the saturation maps in the fractures. From the top left column towards the right column, the saturation profiles are displayed for simulations times 2000, 5000 and 10000[days] respectively.

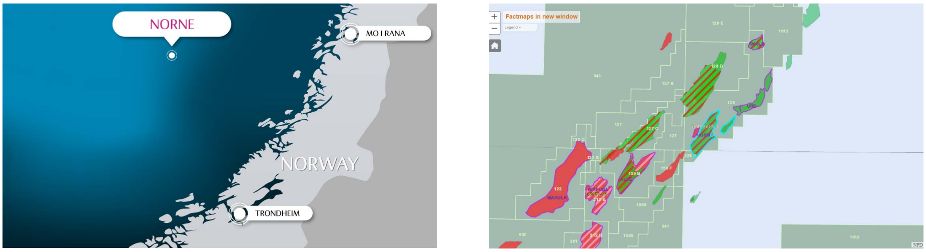

Figure 4.29: Test Case 6 and 7: The location of the Norne Field. The left plot shows the field located in the Norwegian sea (source: Equinor), and the right picture shows the location of the licensed blocks (source: Norwegian Petroleum Directorate).

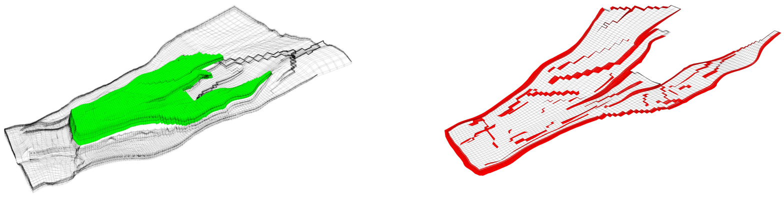

Figure 4.30: Test Case 6&7: Illustration of the Norne field model. The left graph represents the active section (colored in green) of the model, and the right figure shows the faults marked with red color.

vertical communication is decreased in significant regions of the model by the transmissibility multiplier data that is available, resulting in intermediate layers of the reservoir with permeability values close to zero. The porosity values of the field are in the interval between 0.094 and 0.347 (see figure 4.31 on the left). A considerable percentage of impermeable shale is present in some regions in the model.

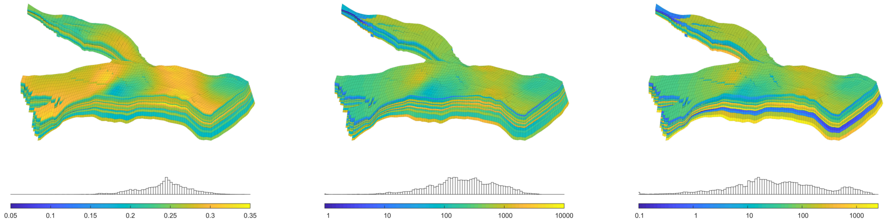

Figure 4.31: Test Case 6 and 7: The porosity and permeability maps for the Norne field. The left graph shows the model's porosity. The middle and the right ones illustrate the horizontal and vertical permeabilities, both plotted using a logarithmic color scale.

SIMULATION RESULTS OF TEST CASE 6: NORNE WITH HIGHLY CONDUCTIVE FRACTURES

This test case demonstrates the performance of the pEDFM model on the Norne field. The corner-point grid data for this and the following test cases was extracted from the input files of the MATLAB Reservoir Simulation Toolbox (MRST) [53].

As explained above, the Norne field is an oil field located around 80 kilometers north of the Heidrun oil field in the Norwegian Sea [53]. As described in the MRST [53], the extent of this oil field is 10 [Km] × 2 [Km] × 100 [m]. The corner-point grid skeleton consists of 46 × 112 × 22 grid cells from which 44915 grid cells are active forming the complex geometrical shape of this oil field. A synthetic network of 15 fractures (designed by the author as a realization) is considered inside this domain. The permeability of the Norne rock matrix in this test case is assumed to be constant at $K_m = 10^{-14}\,[\mathrm{m}^2]$ and the permeability data from the field was not used in this test case. All fractures are highly conductive with a permeability of $K_f = 10^{-8}\,[\mathrm{m}^2]$. Two injection wells with a pressure of $p_{\mathrm{inj}} = 5\times10^7$ [Pa] and two production wells with a pressure of $p_{\mathrm{prod}} = 1\times10^7$ [Pa] are located in the outer skirts of the reservoir as can be seen on figure 4.32a. All wells are vertical and are perforated over the entire thickness of the reservoir. For this test case, the low-enthalpy single-phase geothermal fluid model was used. The input parameters used in this test case are listed in table 4.2.

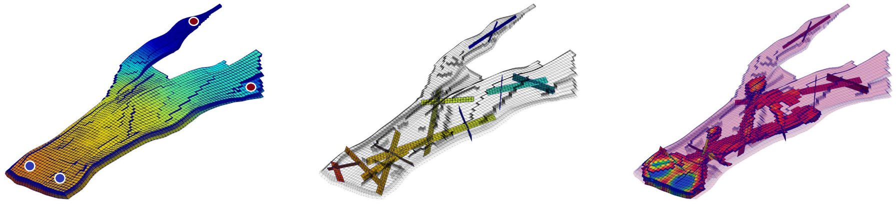
(a) Pressure in the matrix (b) Pressure in the fractures (c) Temperature

Figure 4.32: Test case 6: The Norne oil field. Figures 4.32a and 4.32b show the pressure solutions inside the rock matrix and the embedded fractures. The figure on the right (4.32c) visualizes the temperature solution on the same time-step.

Simulation results of test case 7: Norne with mix-conductive fractures

In this test case, the Norne field model with the skeleton of 46 × 112 × 22 grid cells and a total of 44915 grid cells active matrix grid cells is considered. Unlike in test case 6, the real rock properties of the Norne field were used in this test case. A set of 56 synthetic fractures are created and embedded in the reservoir domain which comprises highly conductive fractures and flow barriers with a permeability of $K_{f_{max}} = 10^{-8}$ [m^2] and $K_{f_{min}} = 10^{-20}$ [m^2] respectively. The fracture network consists of 2165 grid cells. In total there are 48705 grid cells in this test case. Four injection wells with a $p_{\text{inj}} = 5 \times 10^7$ [Pa] and three production wells with a $p_{\text{prod}} = 1 \times 10^7$ [Pa] were placed in the model. The wells are vertical and drilled through the entire thickness of the model.

Similar to the test cases in Johansen (4.3.4) and Brugge (4.3.5) models, two scenarios are considered for the fracture network used in this test case. In both scenarios, the geometrical properties of the fracture networks are identical. However, the permeability values of the highly conductive fractures and flow barriers from scenario 1 are inverted in scenario 2.

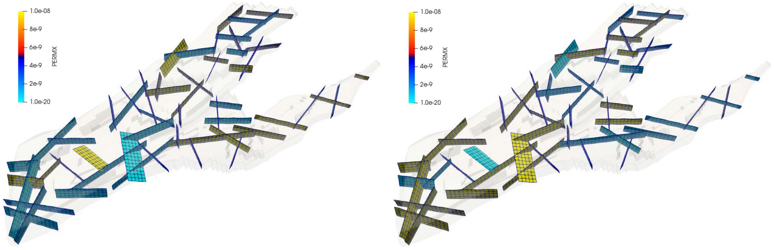

(a) Fractures permeability (scenario 1)   (b) Fractures permeability (scenario 2)

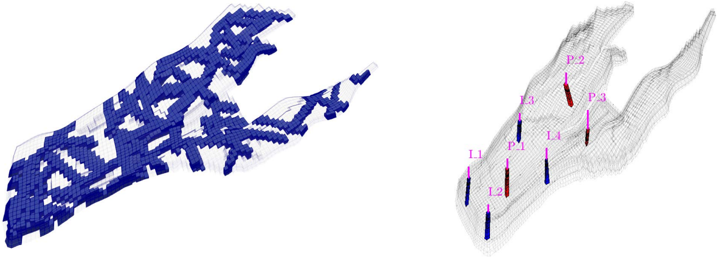

(c) Matrix cells overlapped by fractures   (d) Location of injection and production wells

Figure 4.33: Test case 7: The Norne model with 7 wells (4 injectors and 3 producers) and a set of 56 synthetic fractures (with mixed conductivities). The figures on the top row show the fracture network with different permeabilities for scenario 1 (top left) and scenario 2 (top right). The figure at bottom the left illustrates the highlighted matrix cells that are overlapped by the fracture network. And the figure at the bottom right shows the schematics of the injection and production wells.

The pressure and saturation results of scenario 1 simulation are presented in figures 4.34 and 4.35 respectively. The pressure results are only shown for the simulation time 5000[days], but the saturation profiles are presented for three time intervals of 2000, 5000 and 10000[days]. The injection wells are surrounded by flow barriers that restrict the saturation displacement in the reservoir. The pressure is considerably high in the areas near the wells. These high-pressure areas are an indication that the pEDFM implementation in the corner-point grid geometry is successful in the modeling of the fractures with low conductivities. High pressure drops can be seen at the location of the flow barriers. The increase in saturation is mainly carried out in two parts of the model. These two areas are not isolated from the rest of the model which allows a distribution of the injecting phase through the flow paths.

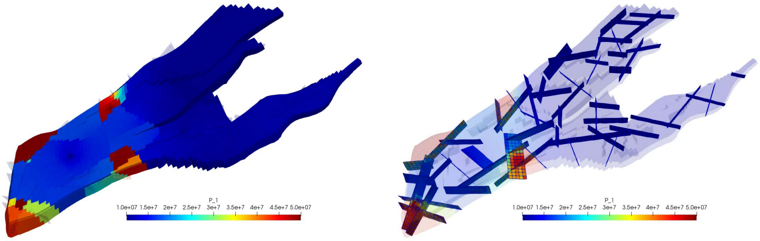

(a) Pressure in the matrix (b) Pressure in the fractures

Figure 4.34: Test case 7: The pressure profile of the Norne model for simulation scenario 1. The figure on the left shows the pressure distribution in the matrix grid cells. The transparency of this figure is increased to make the pressure map in the fractures visible. This map is displayed on the right figure. The results are shown for the simulation time 5000[days]

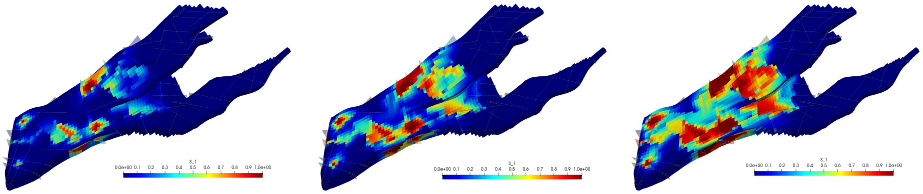

(a) Saturation in the rock matrix after {2000, 5000, 10000}[days]

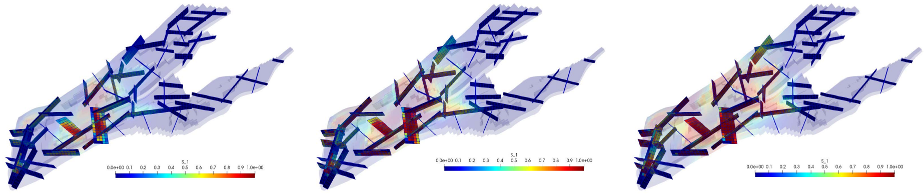

(b) Saturation in the fractures after {2000, 5000, 10000}[days]

Figure 4.35: Test case 7: The saturation distribution of the Norne field for simulation scenario 1. The figures on the top row illustrate the saturation profile in the matrix grid cells and the figures on the bottom row show the saturation maps in the fractures. From the left column towards the right column, the saturation profiles are displayed for simulations times 2000, 5000 and 10000[days] respectively.

The results of scenario 2 are shown in figures **??** and 4.37 respectively. Just like the previous scenario, the pressure results are only shown for the simulation time 5000[days], while the saturation profiles are shown for time intervals of 2000, 5000 and 10000[days]. The injection wells are surrounded by highly conductive fractures that act as flow channels. The pressure is more uniformly distributed. As a result, the effect of high permeable fractures near the injector wells has increased the saturation displacement across larger distances in the domain.

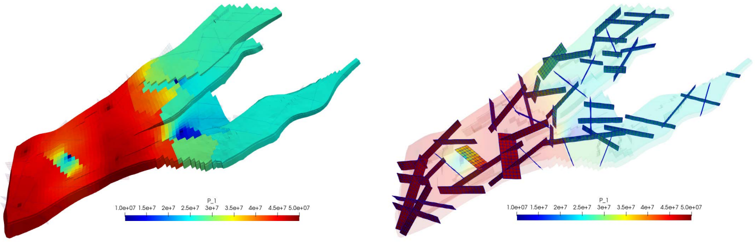

(a) Pressure in the matrix (b) Pressure in the fractures

Figure 4.36: Test case 7: The pressure profile of the Norne model for simulation scenario 2. The figure on the left shows the pressure distribution in the matrix grid cells. The transparency of this figure is increased to make the pressure map in the fractures visible. This map is displayed on the right figure. The results are shown for the simulation time 5000[days]

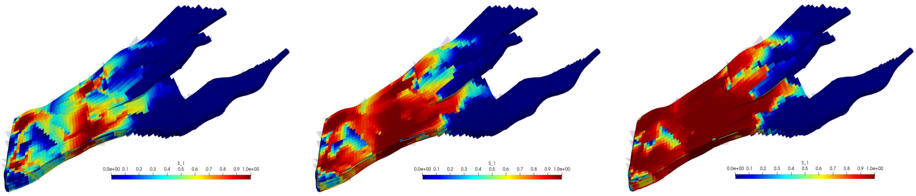

(a) Saturation in the rock matrix after {2000, 5000, 10000}[days]

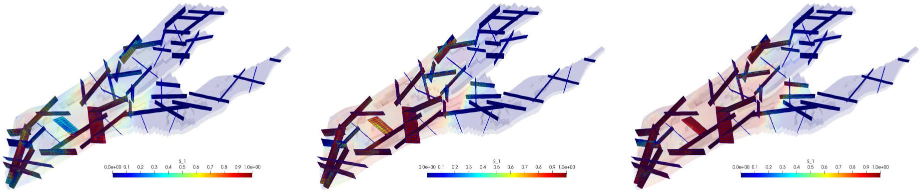

(b) Saturation in the fractures after {2000, 5000, 10000}[days]

Figure 4.37: Test case 7: The saturation distribution of the Norne field for simulation scenario 2. The figures on the top row illustrate the saturation profile in the matrix grid cells and the figures on the bottom row show the saturation maps in the fractures. From the left column towards the right column, the saturation profiles are displayed for simulations times 2000, 5000 and 10000[days] respectively.

4.4. CONCLUSIONS

A projection-based embedded discrete fracture model (pEDFM) for the corner-point grid (CPG) geometry was developed and presented. This method was used with different fluid models, i.e., for fully-implicit simulation of isothermal multiphase fluid flow and low-enthalpy single-phase coupled mass-heat flow in fractured heterogeneous porous media. First, the corner-point grid geometry and its discretization approach were briefly described. Afterwards, the pEDFM model [46, 47] was extended to account for fully 3D fracture geometries on the generic corner-point grid discrete system. Through a few 2D and 3D box-shaped (homogeneous and heterogeneous) test cases, the accuracy of the pEDFM on the corner-point grid geometry was briefly compared against the Cartesian grid geometry. The new method presented similar results of satisfactory accuracy on the corner-point grid geometry when compared to Cartesian grid-geometry. The 3D box-shaped reservoir was then converted into non-orthogonal gridding system to asses the pEDFM method further.

Moreover, numerical results were obtained on a number of geologically-relevant test cases. Different scenarios with various synthetic fracture networks were considered for these test cases. These fine-scale simulations allowed for mix-conductivity fractures. It was shown that pEDFM can capture the physical influence of both highly conductive fractures and flow barriers on the flow patterns. The performance of the pEDFM on the corner-point grid geometry casts a promising solution for increasing the discretization flexibility and enhancing the computational performance while honoring the accuracy. Many geo-models (including ones used in the test cases above) contain millions of grid cells that have complex geometrical alignments to match the positioning of the fractures and faults, causing significant computational complexity and lack of flexibility especially when taking geomechanical deformation into account. The pEDFM model can provide an appropriate opportunity to avoid the complexity of gridding in such models by explicitly representing the discontinuities such as fractures and faults. In presence of elastic and (more importantly) plastic deformations, one could only modify the gridding structure of the affected region in the rock matrix, fully independent of the fractures and faults. This advantage results in significant computational gains especially in the realm of poromechanics.

Advanced methods such as discretization on the corner-point grid and employment of the developed fracture models can deliver substantial computational gains while providing accuracy at a desired level for field-scale models. However, the large size of the geological formations results in imposing such a high number of computational grids on the domain that solving such a large-sized system is beyond the capability of current computers using fine-scale methods. Therefore, more advanced models are in demand to reduce the size of the systems of equations, obtaining an approximate solution in a more computationally efficient manner while avoiding large accuracy sacrifices. In the next chapters of this dissertation, a number of static and dynamic multilevel multiscale methods are described where the main aim of these advanced methods is to create a multilevel multiscale (static or dynamic) representation of the fine-scale system. Various operators provide efficient mapping between different resolutions algebraically. The approximated solutions are achieved with significant computational gains but with minimal accuracy sacrifices.

III

STATIC AND DYNAMIC MULTILEVEL APPROACHES

5

STATIC MULTILEVEL APPROACHES FOR FRACTURED POROUS MEDIA

In the previous chapters, the mathematical and physical concepts of the simulation of mass and heat transport in heterogeneous fractured porous media were briefly covered. The need for such simulations, the challenges that geo-engineering community faces and various proposed solutions to many of those challenges were discussed. Besides the governing equations and the fine-scale discretization of the equations, the simulation strategies for coupling these equations were also explained. To linearize the non-linear equations, the Newton-Raphson iteration scheme is used. After solving the linearized system and updating the properties, the convergence criteria are checked and the solution is obtained after successful convergence at each time-step. To explicitly account for fractures and faults in the domain, the projection-based embedded fracture model (pEDFM) was described. Moreover, the corner-point grid (CPG) geometry was employed for discretization of geologically relevant and field-scale models. To this point, all the mentioned approaches involve fine-scale techniques. However, the size of the field-scale models is yet remarkably large. Discretization of such domains demands imposing high-resolution computational grids. Obtaining simulation solutions on these large scale domains is challenging and results in significant computational complexity. Even with the technological advancements achieved in the field of computer hardware and high performance computation, it is still impossible to run computer models with such large computational domains using conventional methods. Therefore, advanced simulation methods are needed that can provide efficiency (i.e., applicable to field-scale problems) while maintaining accuracy at the desired level.

As was briefly explained in section 1.6, various multiscale and multilevel multiscale methods have been developed by the scientific community to answer the mentioned challenges.

In this chapter, the static multiscale finite volume (MsFV) and the multilevel MsFV (MMsFV) methods for fractured porous media are explained. For the sake of the simplic-

---

Parts of this chapter is taken from the author's M.Sc. dissertation, Delft University of Technology (2016) [83].

ity in the fluid model, isothermal single-phase incompressible flow in fractured porous media is considered. The MsFV method can obtain an efficient solution for the pressure (incompressible flow) equation by solving it at a coarser resolution, while honoring the fine-scale heterogeneities. Even though the MsFV method (with only one coarsening level) is efficient for many scenarios, its applicability is limited to only the use of 2 levels of grids (fine-scale and one level of coarse-scale). For real-field applications, where several millions (or billions) of degrees of freedom exist, the construction of only one level of coarse-grid resolution may not be sufficient to reduce the size of the linear systems significantly. In such domains, the MMsFV method represents an important step forward for the application of multiscale methods where coarse grids with multiple coarsening levels can be imposed on the fine-scale mesh, reducing the size of the linear-system substantially. Combined with explicit fracture models (e.g., the EDFM and the pEDFM), independent coarse grids with different coarsening ratios are employed on the rock matrix and the overlapping fractures, increasing the flexibility and practicality of the MMsFV method for naturally and induced fractured porous media with complex fracture networks. Using a number of 2D fractured test cases, the accuracy of the MsFV and MMsFV methods are assessed and compared against the fine-scale results.

5.1. SINGLE-PHASE INCOMPRESSIBLE FLOW

The mass balance equations of the isothermal multiphase flow in fractured porous media, i.e., (2.1)-(2.2) (see section 2.1), with assumption of incompressible single-phase fluid flow, are reduced to

$$-\nabla\cdot\left(\boldsymbol{\lambda}\cdot\nabla p\right)^{m} = q^{m,w} + \sum_{i=1}^{n_{\text{frac}}} \mathcal{Q}^{m,f_i} \quad , \quad \text{on} \quad \Omega_m \subseteq \Re^{n} \tag{5.1}$$

for the rock matrix m and

$$-\nabla\cdot\left(\boldsymbol{\lambda}\cdot\nabla p\right)^{f_i} = q^{f_i,w} + \mathcal{Q}^{f_i,m} + \sum_{j=1}^{n_{\text{frac}}} \left(\mathcal{Q}^{f_i,f_j}\right)_{j\neq i} \quad , \quad \text{on} \quad \Omega_{f_i} \subseteq \Re^{n-1} \quad \forall\, i \in \{1,\dots,n_{\text{frac}}\} \tag{5.2}$$

for the lower dimensional fracture (f_i). In these equations, $\boldsymbol{\lambda} = \frac{\mathbf{K}}{\mu}$ is the mobility calculated for the fluid in which μ is the fluid viscosity and $\mathbf{K}$ is the rock absolute permeability. Superscripts m, f_i and w correspond to matrix, fracture i and well, respectively. $q^{m,w}$ and $q^{f_i,w}$ are the volumetric source terms (i.e., wells) on the rock matrix m and the fracture f_i. Moreover, $\mathcal{Q}^{m,f_i}$ and $\mathcal{Q}^{f_i,m}$ are the volumetric flux exchanges between the matrix m and the overlapping fracture f_i for the grid cells where overlap occurs, and $\mathcal{Q}^{f_i,f_j}$ is the flux exchange from j-th fracture to the i-th fracture on the intersecting elements. Mass conservation holds in this equation as well, meaning $\iiint\limits_{V} \mathcal{Q}^{m,f_i}\, dV = -\iint\limits_{A_{f_i}} \mathcal{Q}^{f_i,m}\, dA$, and $\iint\limits_{A_{f_i}} \mathcal{Q}^{f_i,f_j}\, dA = -\iint\limits_{A_{f_j}} \mathcal{Q}^{f_j,f_i}\, dA$. Please note that due to the assumption of incompressible single-phase fluid, the density is constant and does not change in space or in time, thus ρ is canceled out from the equation. Therefore, the mass balance equation is written as a volumetric equation with the unit of $[\text{m}^3/\text{s}]$.

According to the Peaceman well model, the volumetric well source terms for the matrix and the fractures are calculated as

$$q^{m,w} = \frac{WI \cdot \lambda^* \cdot (p^w - p^m)}{\Delta V},$$
$$q^{f_i,w} = \frac{WI \cdot \lambda^* \cdot (p^w - p^{f_i})}{\Delta A}.$$

The flux exchanges due to the matrix-fracture and fracture-fracture connectivities, are obtained via

$$\mathcal{Q}^{m,f_i} = CI^{m,f_i} \cdot \lambda^* \cdot (p^{f_i} - p^m)$$
$$\mathcal{Q}^{m,f_i} = CI^{f_i,m} \cdot \lambda^* \cdot (p^m - p^{f_i})$$
$$\mathcal{Q}^{f_i,f_j} = CI^{f_i,f_j} \cdot \lambda^* \cdot (p^{f_j} - p^{f_i}),$$

where CI is the connectivity index between each two non-neighboring elements ((3.61)).

In the equations (5.1)-(5.2), the volumetric flux exchange between each two neighboring control volumes i and j (inside one medium) using the TPFA scheme is given as

$$F_{ij} = \frac{1}{\mu^*} T_{ij}(p_i - p_j), \tag{5.3}$$

where $T_{ij} = \frac{A_{ij}}{d_{ij}} K_{ij}^H$ is the transmissibility between grid cells i and j. A_{ij} is the interface area between the two grid cells, d_{ij} is the distance between their cell centers and K_{ij}^H is the harmonic average of the absolute permeabilities set at the interface of grid cells i and j. The properties with superscript $*$ are obtained using the upwind scheme.

The volumetric flux exchange between a matrix (denoted as m) cell i and a fracture (denoted as f) cell j reads

$$\mathcal{F}_{ij}^{m,f} = -\mathcal{F}_{ij}^{f,m} = -\frac{1}{\mu^*} T_{ij}^{m,f} (p_i^m - p_j^f), \tag{5.4}$$

and the flux between two intersecting (non-neighboring) fracture elements i (on fracture f_i) and j (on fracture f_j) is written as

$$\mathcal{F}_{ij}^{f_i,f_j} = -\mathcal{F}_{ij}^{f_i,f_j} = -\frac{1}{\mu^*} T_{ij}^{f_i,f_j} (p_i^f - p_j^g). \tag{5.5}$$

In the flux terms above, the transmissibilities $T_{ij}^{m,f}$ and $T_{ij}^{f_i,f_j}$ are obtained using identical formulation from the EDFM model in section 3.3.1. The fine-scale discrete mass balance equation for single-phase incompressible flow reads

$$\left(\sum_{j=1}^{N_n} F_{ij} \right)^m + \sum_{k=1}^{n_{\text{frac}}} \left(\sum_{j=1}^{N_{f_k}} \mathcal{F}_{ij}^{m,f_k} \right) = \left(q^{m,w} \right)_i, \quad \forall\, i \in \{1, \dots, N_m\} \tag{5.6}$$

for element i in the rock matrix m and

$$\left(\sum_{j=1}^{N_n} F_{ij}\right)^{f_h} + \sum_{j=1}^{N_{f_k}} \mathscr{F}_{ij}^{f_h,m} + \sum_{k=1}^{n_{\text{frac}}} \left(\sum_{j=1}^{N_{f_k}} \mathscr{F}_{ij}^{f_h,f_k}\right) = \left(q^{f_h,w}\right)_i, \quad \forall\, i \in \{1,\ldots,N_{f_h}\} \tag{5.7}$$

for the element i in the fracture (f_h). Due to the lack of any non-linear term in these time-independent equations, the system of equations is solved as $Ap = q$. Here, A is the coefficient matrix including the transmissibility terms. p is the vector of pressure unknowns and q contains the known terms of the well fluxes. Therefore, one simply can write the system of equations as:

$$\begin{pmatrix} A^{m,m} & A^{m,f} \\ A^{f,m} & A^{f,f} \end{pmatrix} \begin{pmatrix} p^m \\ p^f \end{pmatrix} = \begin{pmatrix} q^m \\ q^f \end{pmatrix} \tag{5.8}$$

In the system of equations above, the $A^{m,m}$ sub-block consists of the connectivities between the neighboring grid cells in the rock matrix. Similarly, $A^{f,f}$ contains the connectivities between the neighboring grid cells within each fracture and also the connectivities between the non-neighboring fracture elements (belonging to two different fractures) due to intersections. The terms inside the $A^{m,f}$ and $A^{f,m}$ sub-blocks are the non-neighboring connectivities between the rock matrix grid cells and the overlapping fracture elements.

The size of this linear system (5.8) at fine-scale resolution can be significantly large in case of field-scale domains. In the next sections, the MsFV and MMsFV methods are employed to reduce the size of the system and provide computational efficiency and at the same time honor the fine-scale heterogeneities.

5.2. MULTISCALE APPROACHES

The multiscale finite volume (MsFV) method [58, 105] and the multiscale finite element (MsFE) [55, 117, 118] methods were developed to solve the elliptic (incompressible) or parabolic (compressible) pressure equations for flow in porous media with higher computational efficiency. These methods are employed as a solver for the pressure equation in simulation models with sequential strategies, (e.g., IMPES [119] or sequential implicit [59]). The computational costs are reduced by solving the pressure equation on a coarser grid resolution compared to the fine-scale discretization of geological properties. These methods represent an alternative to upscaling techniques [54]. Yet, despite the classical upscaling methods, the multiscale methods do not redefine the heterogeneities on a different resolution but only to map the solution between the fine-scale and coarse scale resolutions. In multiscale methods, a coarse-scale system is first constructed for the pressure equation but the fine-scale information is preserved using the local basis functions. Once the pressure is obtained at the coarse scale resolution, the solution is prolonged (or interpolated) back to the original fine-scale resolution. Figure 5.1 shows schematically how different the multiscale approach is compared to the upscaling approach [120].

To enhance the computational performance, algebraic descriptions of multiscale methods have been developed such that the so-called prolongation and restriction oper-

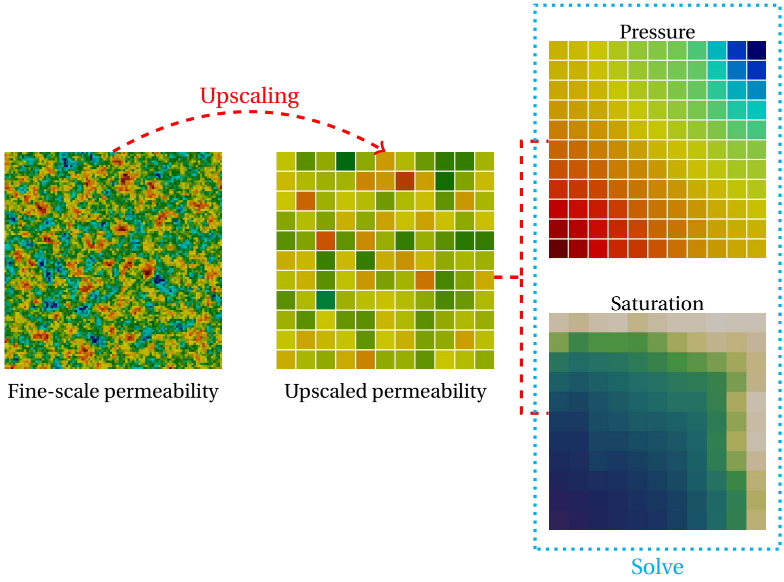

(a) Upscaling approach

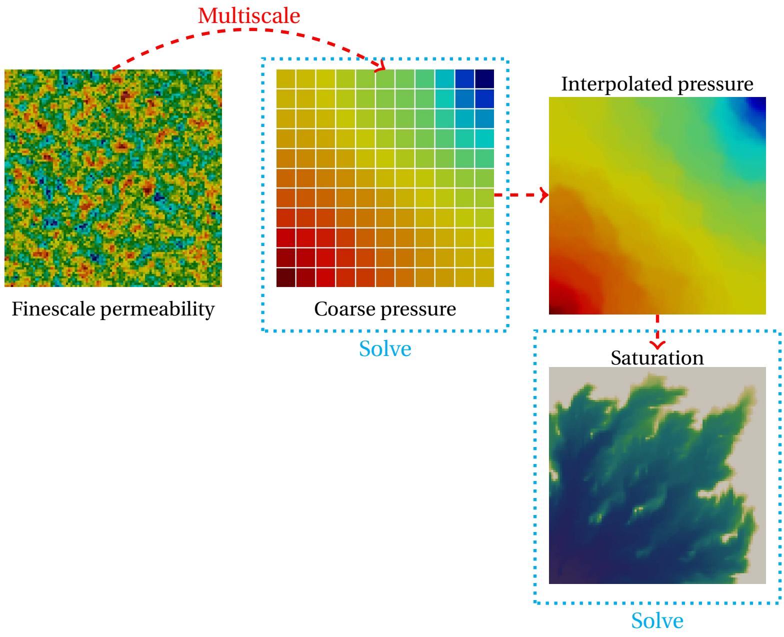

(b) Multiscale approach

Figure 5.1: Visual comparison between the upscaling (a) and the multiscale (b) approaches. In the upscaling approach, the fine-scale rock properties are used to obtain averaged and upscaled properties on a coarse resolution on which governing equations are solved. However, in the multiscale approach, the fine-scale rock properties are used to map the equations to a coarser solution on which a coarse-scale pressure equation is solved. Once a coarse pressure is obtained, the pressure solution is interpolated back to the fine-scale resolution and used to solve the transport equation. This figure is extracted from [120].

ators are used as mapping between the fine-scale coarse scale systems [79, 82, 121–123]. Moreover, to improve the quality of the interpolated pressure solution and improve the convergence, iterative multiscale methods have also been introduced [124]. This approach allows to employ multiscale methods as "physics-based" linear solvers and their performance has been thoroughly studied in the literature [79, 124, 125]. The applicability of multiscale methods to fractured media [44, 81, 126], unstructured grids [63, 127], geomechanical processes [128, 129], and even to real-field applications [130, 131] are among the recent developments. The extensions also include enrichment strategies in presence of strong heterogeneity contrast that improve the multiscale solutions with additional basis functions (enrichment). These extensions were developed both within the finite element and the finite volume frameworks [81, 132–134]. Recently, it has also been shown how to take advantage of multiscale methods within the context of inverse modeling using both analytical [135–137] and stochastic [138, 139] gradient-based optimization algorithms.

Next, the MsFV method for fractured porous media is covered. This is important in order to develop the multilevel multiscale method (MMsFV). Like many advanced computational methods, the MsFV method requires its own computational grids which are imposed on the given fine-scale domain. The MsFV method, in particular, imposes two sets of coarse grids, namely the primal coarse (coarse from now on) and the dual-coarse grids. Next, the construction of these sets of grid cells are explained.

5.2.1. THE MULTISCALE FINITE VOLUME METHOD (MSFV)

In order to describe the multiscale finite volume (MsFV) method for fractured porous media, first the MsFV method is briefly covered. Let the mass balance equation for single-phase incompressible flow (5.1) be rewritten for the rock matrix without presence of the fractures.

$$-\nabla\cdot\left(\boldsymbol{\lambda}\cdot\nabla p\right)=q^{w} \quad , \quad \text{on} \quad \Omega\subseteq\Re^{n} \tag{5.9}$$

where the following boundary conditions are applied to the domain:

$$\begin{cases} -\boldsymbol{\lambda}\cdot\nabla p\cdot\boldsymbol{n}=\bar{u} & \text{on} \quad \Gamma_u \\ p=\bar{p} & \text{on} \quad \Gamma_p, \end{cases} \tag{5.10}$$

with $\Gamma_u\cup\Gamma_p=\partial\Omega$ and $\boldsymbol{n}$ being the unit normal vector associated with $\partial\Omega$. Let the continuum domain be discretized into N_f number of fine-scale grid cells (subscript f denotes the fine-scale resolution). The discretized system of equations from the single-phase flow equation (5.9) can be written in the form:

$$\mathbf{A}_f\, p_f = q_f. \tag{5.11}$$

where, $\mathbf{A}_f$ is an $N_f\times N_f$ matrix and is called the fine-scale pressure coefficient matrix. The MsFV method imposes two overlapping coarse grids. First, on the given fine-scale resolution grid mesh, the primal coarse grid is imposed. The primal coarse cells form a non-overlapping partitioning of the computational domain, with flexible geometry and resolution (i.e., arbitrary coarsening factor in each direction). A selected fine-grid cell in each coarse grid cell is taken as the coarse node (or vertex). The solution at the coarse nodes will be found by solving the coarse-scale system. By connecting the coarse nodes together through a wire-basket pattern, a secondary –i.e., dual– coarse grid is obtained, as shown in figure 5.2 for 1D (on the left) and 2D (on the right) domains. Note that in 2D domain, the fine-scale grid cells can be flagged based on their positions with respect to the dual-coarse grid: vertices (coarse nodes), edges (at the edge of the dual coarse cells), and interiors (inside the dual coarse cells). In a 3D domain however, the fine-scale grid cells are categorized into four flags, namely, vertices (coarse nodes), edges (at the edge of the dual coarse cells), faces (on the faces of the dual coarse cells) and interiors (inside the dual coarse cells). There are two different approaches for construction of the primal and dual coarse grid cells. One approach is to create primal coarse grid cells with identical sizes. In this approach, no coarse node (vertex) is located on the corners of the domain. The top row of figure 5.2 illustrates this approach. Assuming $N_{f,x}$ fine-scale grid cells in x direction (this applies to any of the x, y, z directions), the coarsening ratio in x direction is defined as

$$\gamma_x = \frac{N_{f,x}}{N_{c,x}}, \tag{5.12}$$

where $N_{c,x}$ is the number of coarse grid cells (and conclusively the number of coarse nodes or vertices) in x direction. In this approach the sizes of the dual coarse grid cells vary depending on their location (whether internal or near boundaries of the domain). The second approach allows for putting the coarse nodes on the corners and the boundaries of the domain. In contrary to the first approach, the primal coarse grid cells have different sizes depending on their location but all the dual coarse grids have identical sizes in this method of coarse grid construction. Here, the coarsening ratio in x direction can be obtained as

$$\gamma_x = \frac{N_{f,x} - 1}{N_{c,x}} + 1. \tag{5.13}$$

As an example, in figure 5.2, a ratio of $\gamma = 5$ is considered for both approaches. On the top row, following the first approach, 15 fine-scale grid cells are divided into $N_{c,x} = N_{f,x}/\gamma_x = 15/5 = 3$ primal coarse grid cells. On the bottom row however, with the second method of coarse grid construction, 16 fine-scale grid cells are divided into $N_{c,x} = (N_{f,x} - 1)/\gamma_x + 1 = (16-1)/5 + 1 = 4$ primal coarse grid cells.

Throughout this chapter, both approaches will be used in various examples and test cases. No comparison will be made as each coarse grid construction method requires different fine-scale computational grids.

Using the MsFV method, the fine-scale pressure p_f, is approximated as

$$p_f \approx p' = \sum_{j=1}^{N_d} \left(\sum_{k=1}^{N_{c1}} \Phi^k_{j,c1} p^k_{c1} \right), \tag{5.14}$$

where p^k is the pressure value of the primal coarse control volume k and Φ^k_j is the so-called basis function corresponding to the primal coarse node k with values in $\tilde{\Omega}_j$. The basis functions are acquired by obtaining a numerical solution for a localized problem on each dual coarse domain $\tilde{\Omega}_j$. The right-hand-side of the system of equations for these

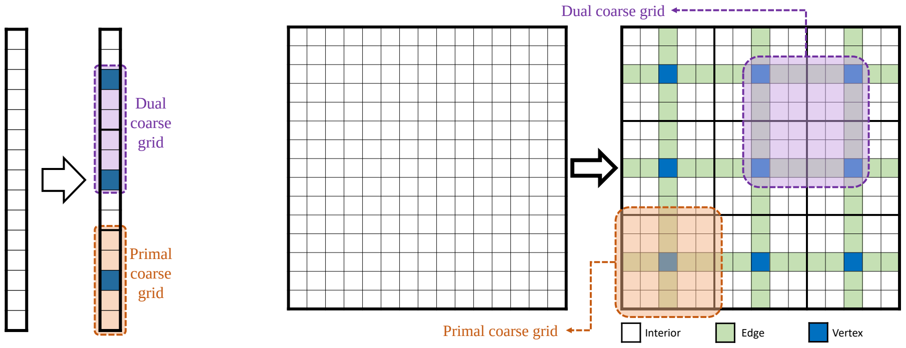

(a) Vertices are not put on the corners. All primal coarse grids have identical size, but dual coarse grids have different sizes.

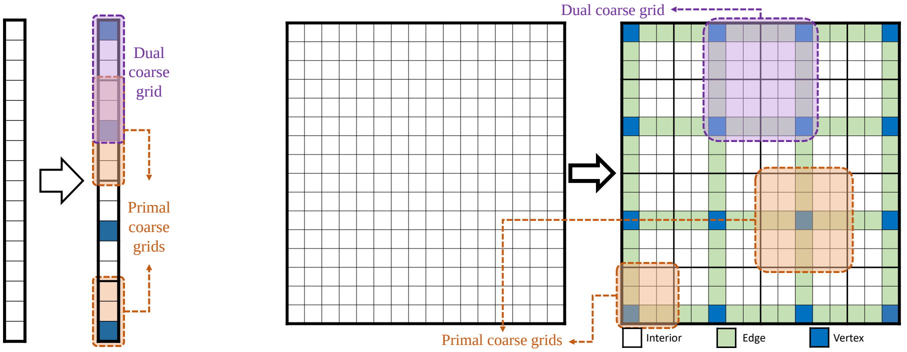

(b) There are vertices on the corners. The primal coarse grids have different sizes, but dual coarse grids have identical sizes.

Figure 5.2: Construction of the primal and dual coarse grid structure in the multiscale approach for 1D (figures on the left) and 2D (figures on the right) domains with two different approaches. On the top row, the domain is subdivided into identical primal coarse grid cells. In this approach, there is no vertex on the corners of the domain and the dual coarse grids can have different sizes depending on their location on the domain. On the bottom row however, coarse nodes (vertices) are located on the corners as well, creating heterogeneous sizes for the primal coarse grid cells, but the dual coarse grid cells have identical sizes. In all the figures in this example, the coarsening ratio in any dimension is $\gamma = 5$. For the first approach, 15 grid cells at fine-scale resolution result in 3 primal coarse grid cells, and for the second approach, 16 fine-scale grid cells are divided into 4 primal coarse grid cells in each direction.

local problems are set to be zero. In order to localize the flow problem, a reduced boundary condition is used on each dual coarse domain, Ω_j. Therefore, the following local problem is solved for each dual coarse cell.

$$\begin{cases} -\nabla\cdot(\boldsymbol{\lambda}\cdot\nabla\Phi_j^k)=0 & \text{on} \quad \tilde{\Omega}_j \\ -\nabla_{||}\cdot\left(\boldsymbol{\lambda}\cdot\nabla\Phi_j^k\right)_{||}=0 & \text{on} \quad \partial\tilde{\Omega}_j \\ \Phi_j^k(x_i)=\delta_{ki} & \forall\, x_i\in\{1,\dots,N_c\}. \end{cases} \tag{5.15}$$

In the equation above, the termδ_{ki} denotes the Kronecker delta, and the subscript $||$ means that only the component parallel to the boundary $\partial\tilde{\Omega}_j$ is taken into account. This refers to solving a problem of reduced dimensions at the boundary of each dual coarse grid cell. Conclusively, in case of a 2D domain, a 1D problem is solved (see figure 5.3). For a 3D domain, this process is done recursively. In other words, at first, 1D problems are locally solved and their results are used as boundary conditions for 2D reduced local problems. Definitively the results of the 2D solutions are used as the boundary conditions for the 3D basis functions.

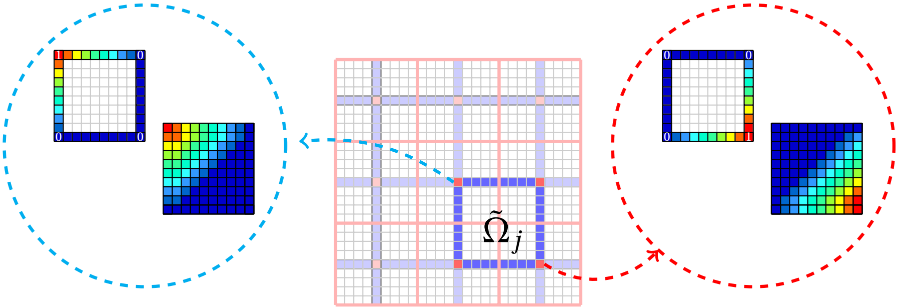

Figure 5.3: Computation of two basis functions from two coarse nodes in a 2D dual coarse domain $\tilde{\Omega}_j$. As shown, the basis function is obtained after solving a 1D reduced problem. The solution of this reduced problem is used as boundary conditions for the computation of the 2D basis function. This figure is taken from [120].

Due to the construction method, the partition of unity holds in the computation of the basis functions, namely,

$$\sum_{k=1}^{N_c}\sum_{j=1}^{N_d}\Phi_j^k = 1. \tag{5.16}$$

Inside a given dual domain, a basis function is computed for each coarse node (4 for 2D and 8 for 3D domains). However, one can merge the basis functions corresponding to one coarse node to obtain one basis function for that coarse node. Therefore, there exist N_c basis functions for N_c coarse nodes in a given domain. Figure 5.4 shows an example of such basis function.

The MsFV system at coarse scale is obtained by substituting equation 5.14 in equation 5.9. Integrating over each primal coarse grid control volume $\breve{\Omega}_k$, the following equation is achieved:

$$-\int_{\breve{\Omega}_k} \nabla\cdot\left(\boldsymbol{\lambda}\cdot\nabla\sum_{j=1}^{N_d}\left(\sum_{k=1}^{N_c}\Phi_j^k p^k\right)\right)d\Omega = \int_{\breve{\Omega}_k} q\,d\Omega \quad \forall\, k=\{1,\ldots,N_c\} \tag{5.17}$$

and applying Gauss theorem results in

$$\sum_{k=1}^{N_c} p^k \sum_{j=1}^{N_d}\int_{\partial\breve{\Omega}_k}\left(-\boldsymbol{\lambda}\cdot\nabla\Phi_j^k\right)\cdot\boldsymbol{n}_k d\Gamma = \int_{\breve{\Omega}_k} q\,d\Omega \quad \forall\, k=\{1,\ldots,N_c\} \tag{5.18}$$

Here, the term $\boldsymbol{n}_k$ indicates the unit normal vector which points outwards of $\partial\Omega_k$. Equation (5.18) shows the mathematical notation of the linear system at coarse scale, i.e.,

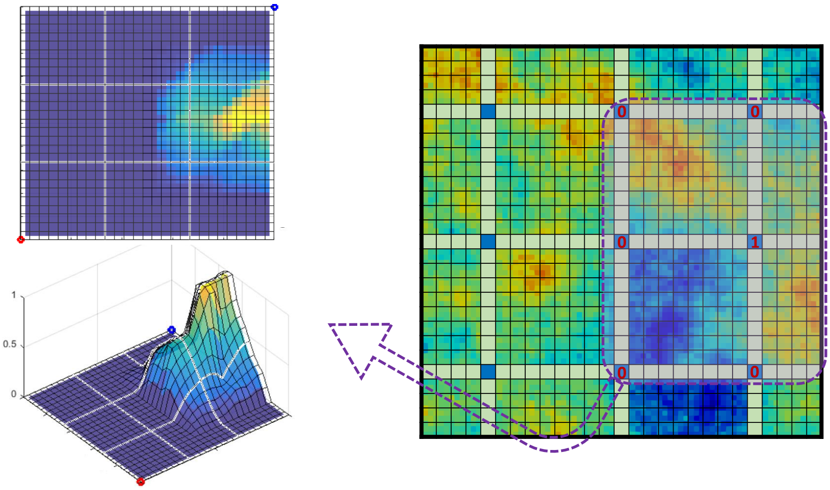

Figure 5.4: An example of a basis function belonging to the middle right coarse node of a 2D heterogeneous domain.

$$\mathbf{A}_c p_c = q_c \tag{5.19}$$

where $\mathbf{A}_c$ is the coefficient matrix at the coarse scale resolution and reads

$$\mathbf{A}_c(l,k) = \sum_{j=1}^{N_d} \int\limits_{\partial\breve{\Omega}_l} \left(-\boldsymbol{\lambda}\cdot\nabla\Phi_j^k\right)\cdot\boldsymbol{n}_k d\Gamma \tag{5.20}$$

and q_c is the right-hand-side of this system and is written as

$$q_c(k) = \int\limits_{\breve{\Omega}_l} q d\Omega. \tag{5.21}$$

The pressure at coarse scale $p_c = [p_1, ..., p_{N_c}]^{\mathsf{T}}$ satisfies the mass balance equation of each coarse grid control volume $\breve{\Omega}_k$. Moreover, the coarse pressure matrix in equation (5.19) has a larger stencil compared with the fine-scale coefficient matrix, as the diagonal fluxes are also taken into account.

The multiscale formulation can be written algebraically in matrix-vector notation by employment of the multiscale operators, i.e., the so-called restriction and prolongation operators. Such a system can be written as

$$\underbrace{(\mathbf{RA}_f\mathbf{P})}_{\mathbf{A}_c} p_c = \underbrace{\mathbf{R}q}_{q_c}. \tag{5.22}$$

Here, $\mathbf{R}$ is the restriction operator which is a $N_c \times N_f$ matrix with values in the k-th row being 1 at column j if cell j belongs to the coarse cell k, and 0 elsewhere, i.e.,

$$\mathbf{R}(k,j)=\begin{cases}1 & \text{if cell } j\in\breve{\Omega}^k,\\ 0 & \text{otherwise.}\end{cases} \tag{5.23}$$

The prolongation operator, $\mathbf{P}$, on the other hand, is a $N_f\times N_c$ matrix and each of its columns k contains the basis function, Φ_k, defined as

$$\Phi^k=\sum_{j=1}^{N_d}\Phi_j^k. \tag{5.24}$$

Alternatively, the multiscale coarse system can be constructed by employing a classical Galerkin-type operator, i.e., $\mathbf{R}_{\mathbf{FE}}=\mathbf{P}^{\mathsf{T}}$, resulting in the MsFE method [55]. This, ensures that the coarse matrix $\mathbf{A}_c$ is symmetric but does not guarantee mass conservation on the primal coarse grid. It has been shown that such an approach is more effective whenever the multiscale is used as an iterative linear solver [79].

Figure 5.5 shows the structure of the prolongation and restriction operators.

$$\mathrm{P}_{(N_f\times N_c)}=\begin{array}{c}\begin{matrix}\Phi_1 & \Phi_2 & \Phi_3 & \Phi_4 & \cdots & \Phi_{N_c-1} & \Phi_{N_c}\\ \downarrow & \downarrow & \downarrow & \downarrow & & \downarrow & \downarrow\end{matrix}\\ \begin{bmatrix}\vert & 0 & 0 & 0 & \cdots & 0 & 0\\ \vert & \vdots & 0 & \vert & \cdots & 0 & 0\\ \vdots & 0 & 0 & \vert & \cdots & 0 & 0\\ \vert & \vert & \vdots & \vert & \cdots & \vdots & 0\\ 0 & \vert & \vert & \vdots & \cdots & \vert & \vdots\\ \vdots & \vdots & \vert & 0 & \cdots & \vert & \vert\\ 0 & 0 & \vdots & 0 & \cdots & \vdots & \vert\\ 0 & 0 & 0 & 0 & \cdots & 0 & \vert\end{bmatrix}\end{array}
\qquad
\mathrm{R}_{(N_c\times N_f)}=\begin{bmatrix}1 & 1 & \cdots & 1 & 0 & \cdots & 0 & 0\\ 0 & \cdots & 1 & 1 & 1 & \cdots & 0 & 0\\ 0 & 0 & \cdots & 1 & 1 & \cdots & 0 & 0\\ 0 & 0 & 1 & \cdots & 1 & 1 & \cdots & 0\\ 0 & 0 & 0 & \cdots & 1 & \cdots & 0 & 0\\ \vdots & \vdots & \vdots & \vdots & \vdots & \vdots & \vdots & \vdots\\ 0 & 0 & 0 & 0 & \cdots & 1 & 1 & 1\end{bmatrix}$$

Figure 5.5: The structure of the prolongation and restriction operators.

To enhance the computational efficiency of the construction of the multiscale operators, algebraic multiscale solver framework was introduced [79]. In this framework, the fine-scale system is first re-ordered using the wire-basket algorithm:

$$\mathbf{A}=\mathbf{G}\mathbf{A}_f\mathbf{G}^{\mathsf{T}}, \tag{5.25}$$

where, $\mathbf{G}$ is an orthogonal permutation matrix containing the topological information about the dual coarse grids. Using this permutation matrix, the linear system is re-ordered, and can be written as

$$\underbrace{\begin{bmatrix}\mathbf{A}_{II} & \mathbf{A}_{IF} & & \\ \mathbf{A}_{FI} & \mathbf{A}_{FF} & \mathbf{A}_{FE} & \\ & \mathbf{A}_{EF} & \mathbf{A}_{EE} & \mathbf{A}_{EV}\\ & & \mathbf{A}_{VE} & \mathbf{A}_{VV}\end{bmatrix}}_{\mathbf{A}}\begin{bmatrix}p_I\\ p_F\\ p_E\\ p_V\end{bmatrix}=\begin{bmatrix}q_I\\ q_F\\ q_E\\ q_V\end{bmatrix}, \tag{5.26}$$

with the subscripts I, F, E and V denoting interior, face, edge and vertex cells respectively.

The localization assumption requires that the blocks $\mathbf{A}_{FI}$ and $\mathbf{A}_{EF}$ are set to zero, which corresponds to the connectivities between the face and the interior cells, and between the face and the edge cells respectively. Therefore, the full multiscale system can be written as

$$\begin{bmatrix} \mathbf{A}_{II} & \mathbf{A}_{IF} & & \\ & \tilde{\mathbf{A}}_{FF} & \mathbf{A}_{FE} & \\ & & \tilde{\mathbf{A}}_{EE} & \mathbf{A}_{EV} \\ & & & \mathbf{A}_{c} \end{bmatrix} \begin{bmatrix} p'_I \\ p'_F \\ p'_E \\ p'_V \end{bmatrix} = \begin{bmatrix} q_I \\ q_F \\ q_E \\ q_c \end{bmatrix}. \tag{5.27}$$

Here, $\tilde{\mathbf{A}}_{FF}$ and $\tilde{\mathbf{A}}_{EE}$ are the face and the edge blocks that have been modified to account for the deleted connectivities. The system of equation (5.27) is upper triangular and can be easily solved by employing a backward substitution algorithm. Consequently, given the coarse solution p'_V the approximate fine-scale solution is obtained as

$$\begin{bmatrix} p'_I \\ p'_F \\ p'_E \\ p'_V \end{bmatrix} = \begin{bmatrix} -\mathbf{A}_{II}^{-1}\left(\mathbf{A}_{IF}\tilde{\mathbf{A}}_{FF}^{-1}(\mathbf{A}_{FE}\tilde{\mathbf{A}}_{EE}^{-1}\mathbf{A}_{EV})\right) \\ \tilde{\mathbf{A}}_{FF}^{-1}(\mathbf{A}_{FE}\tilde{\mathbf{A}}_{EE}^{-1}\mathbf{A}_{EV}) \\ -\tilde{\mathbf{A}}_{EE}^{1}\mathbf{A}_{EV} \\ \mathsf{I}_{VV} \end{bmatrix} p'_V \tag{5.28}$$

Therefore, the multiscale prolongation operator, P is written as

$$\mathsf{P} = \mathsf{G}^{\mathsf{T}} \begin{bmatrix} -\mathbf{A}_{II}^{-1}\left(\mathbf{A}_{IF}\tilde{\mathbf{A}}_{FF}^{-1}(\mathbf{A}_{FE}\tilde{\mathbf{A}}_{EE}^{-1}\mathbf{A}_{EV})\right) \\ \tilde{\mathbf{A}}_{FF}^{-1}(\mathbf{A}_{FE}\tilde{\mathbf{A}}_{EE}^{-1}\mathbf{A}_{EV}) \\ -\tilde{\mathbf{A}}_{EE}^{1}\mathbf{A}_{EV} \\ \mathsf{I}_{VV} \end{bmatrix}. \tag{5.29}$$

5.2.2. THE MSFV METHOD FOR FRACTURED POROUS MEDIA (F-MSFV)

The multiscale coarse grid construction on a fractured domain using embedded discrete fracture models (EDFM or pEDFM) follows a similar approach. The coarse grids are constructed independently for the fine-scale grids of the rock matrix and each individual fracture. For this purpose, the equations (5.1)-(5.2) and the linear system (5.8) are considered. Please note that fractures are represented as lower dimensional objects. Therefore, on a 2D domain where the fractures are represented in 1D, their fine-scale grids are flagged only as vertex or edge. On a 3D domain however, the fractures have vertex, edge or face cells on the coarse grid structure. Figure 5.6 illustrates a 2D example where the coarse grids of the rock matrix and three 1D fractures are constructed independently.

As every fracture contains coarse nodes, there are basis functions associated with the coarse nodes of the fractures as well. The fracture basis functions are obtained using the similar approach of the matrix basis functions computation. However, one should note that the region of the basis function for each medium is now extended to other overlapping media. Conclusively, the matrix basis function are not only affected by presence of the explicit fracture, but they also affect the fractures. These basis functions are called fully-coupled basis functions as they are computed on the local dual coarse domain but with fully coupled manner. This means that for computation of each basis function a

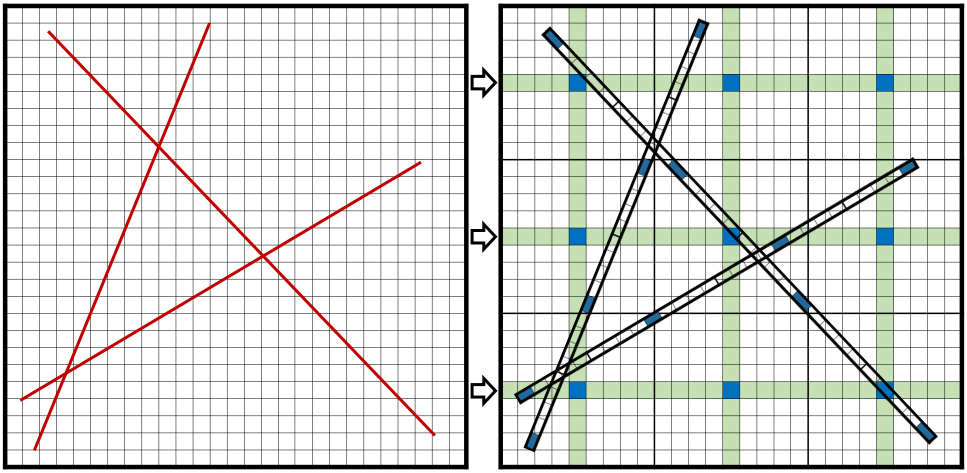

Figure 5.6: An example of the coarse grid construction for a 2D domain with three fractures. As can be seen, the primal and dual coarse grids are constructed independently for the rock matrix and each fracture.

local EDFM/pEDFM problem is solved. An example of the matrix and fracture basis functions are illustrated in figure 5.7.

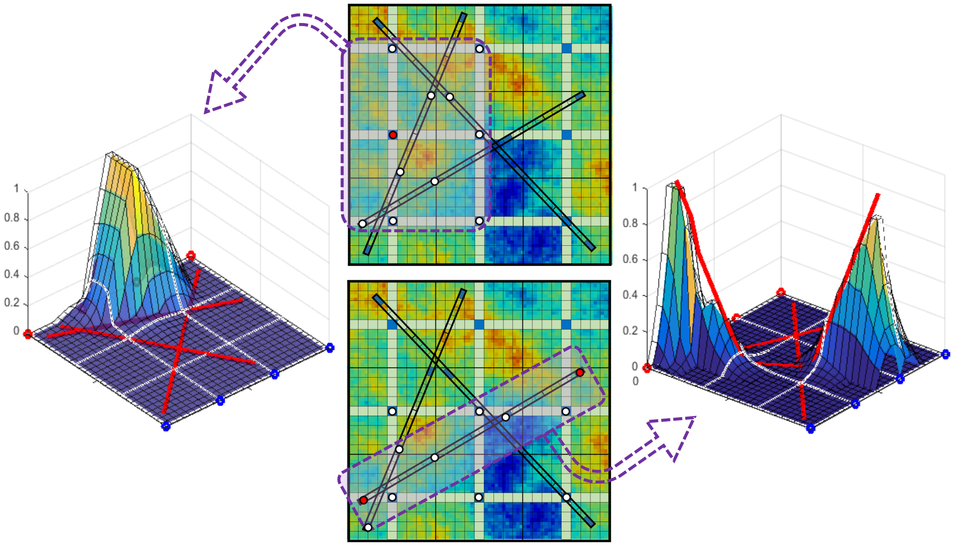

Figure 5.7: An example of a basis function for the rock matrix (the plot on the left) belonging to the middle left coarse node of the matrix, and two basis functions of a fracture (the plot on the right) belonging to two coarse nodes in that fracture. As can be seen, to obtain each basis function for the corresponding coarse node, Dirichlet boundary condition (1.0 and 0.0) values are set not only on the coarse nodes of one medium, but also on the coarse nodes of the overlapping media in the region of the influence of that basis function.

Similar to equation (5.22), the linear system of the F-MsFV method at coarse scale resolution can be written as

$$\underbrace{\underbrace{\begin{pmatrix} \mathbf{R}^m & 0 \\ 0 & \mathbf{R}^f \end{pmatrix}}_{\mathbf{R}} \underbrace{\begin{pmatrix} \mathbf{A}^{m,m} & \mathbf{A}^{m,f} \\ \mathbf{A}^{f,m} & \mathbf{A}^{f,f} \end{pmatrix}}_{\mathbf{A}_{\text{fs}}} \underbrace{\begin{pmatrix} \mathbf{P}^{m,m} & \mathbf{P}^{m,f} \\ \mathbf{P}^{f,m} & \mathbf{P}^{f,f} \end{pmatrix}}_{\mathbf{P}}}_{\mathbf{A}_c} \begin{pmatrix} p_c^m \\ p_c^f \end{pmatrix} = \underbrace{\begin{pmatrix} \mathbf{R}^m & 0 \\ 0 & \mathbf{R}^f \end{pmatrix} \begin{pmatrix} q_{\text{fs}}^m \\ q_{\text{fs}}^f \end{pmatrix}}_{q_c} \tag{5.30}$$

Different coupling strategies have been studied for the calculation of the rock matrix and the fracture basis functions and their influences on each other [81]. In this work, fully coupled basis functions are employed.

5.2.3. EVALUATION OF THE F-MSFV METHOD

In this section, the accuracy of the MsFV method for fractured porous media is evaluated and the F-MsFV results are compared with the fine-scale simulations on a 2D single-phase incompressible system (see Eq. 5.1 and 5.2). The input parameters that are used identical in each test case are available in table 5.1. The pressure error of F-MsFV results with respect to the fine-scale results (denoted as e_p) is calculated using second norm of the pressure vectors as

$$e_p = \frac{||\, p_{\text{FS}} - p_{\text{MS}} \,||_2}{||\, p_{\text{FS}} \,||_2}, \tag{5.31}$$

where, p indicates pressure and the subscripts FS and MS denote the fine-scale and the MsFV method, respectively. Moreover, the multiscale pressure graph consists of an absolute error curve underneath the pressure curve which is simply calculated as $Error = |\, p_{FS} - p_{MS} \,|$. This error is not the normalized error and it is present only to illustrate the absolute differences between the fine-scale and the multiscale pressure through the domain. All results include a residual surface plot in fulfillment of the fine-scale equation. Note that non-zero terms in residual exist at the boundaries of the dual coarse grid cells.

TEST CASE 1: 2D HOMOGENEOUS DOMAIN WITH 2 "+" SHAPED FRACTURES

In this test case, two fractures are located in the center of a homogeneous domain perpendicular to each other (horizontal and vertical). Five injection wells at the left boundary and five production wells at the right boundary form a line drive pattern. A $75 \times 75 = 3600$ grid is imposed on the rock matrix and fractures are discretized into 92 grid cells in total. A coarsening ratio of $\gamma = 15$ is considered for the matrix (in both directions) and the fractures. Figure 5.8 shows the results of this test case.

The fine-scale system is solved with 75×75 matrix cells and 92 fracture elements, whereas the multiscale system is solved by 5×5 matrix coarse grid cells and 8 fracture coarse grid cells (with a significantly reduced number of degrees of freedom or DOF). The white lines in the multiscale pressure plot indicate the boundaries of the primal coarse grids. The plotted graph below the multiscale graph in the right figure is the absolute difference between the fine-scale and the multiscale solutions. The normalized error calculated via equation (5.31) is $e_p = 2.66 \times 10^{-2}$.

Table 5.1: Input parameters of fluid and rock properties of single-phase incompressible flow used in the test cases of the F-MsFV evaluation.

Property	value
Length of the domain in x direction (L_x)	100.0 [m]
Length of the domain in y direction (L_y)	100.0 [m]
Matrix porosity (ϕ)	0.3[−]
Reservoir permeability	10^{-14} [m^2]
Fracture permeability	10^{-8} [m^2]
Fracture aperture	5×10^{-3} [m]
Fluid viscosity (μ)	0.001 [Pa.S]
Fluid density (ρ)	1000 [kg/m^3]
Injection Pressure	3×10^7 [Pa]
Production Pressure	0×10^7 [Pa]

TEST CASE 2: 2D HETEROGENEOUS DOMAIN WITH 2 “X” SHAPED FRACTURES

In this test case, two fractures are located in the center of a heterogeneous domain with an “x” shape. Identical to the previous test case, a line-drive pattern well exists at the left and right boundaries of the domain. A $91 \times 91 = 8281$ computational grid is imposed on the rock matrix and fractures are discretized into 106 grid cells in total. The coarsening ratio is set to $\gamma = 13$ for the matrix (in both directions) and the fractures. The permeability of the rock matrix is heterogeneous with the contrast of $k_{\max}/k_{\min} = 2.2 \times 10^4$. Figure 5.9 shows the results of this test case.

In this test case (2), the fine-scale system is solved with 91×91 grids cells in the rock matrix and 106 elements in the fractures, whereas the multiscale system is solved by 7×7 coarse grid cells in the matrix and 10 coarse grid cells in the fractures. The normalized error calculated using equation (5.31) reads $e_p = 5.58 \times 10^{-2}$.

TEST CASE 3: 2D HETEROGENEOUS DOMAIN WITH 5 FRACTURES

In the following test case, a 2D heterogeneous fractured domain consisting of 5 fractures is discretized on a $99 \times 99 = 9801$ computational grids. A total of 247 grids are imposed on the fracture network. There are five injection wells at the left boundary and five production wells at the right boundary. The coarsening ratio of $\gamma = 11$ is considered. The heterogeneous permeability has a contrast of $k_{max}/k_{min} = 2.0 \times 10^4$. the results of this test case are presented on the figure 5.10.

In this test case (3), the fine-scale system consists of 99×99 matrix cells and 106 fracture elements, a total of 10048 grid cells. However, the multiscale system is solved by 9×9 matrix coarse grid cells and 27 fracture coarse grid cells. The normalized error calculated using equation (5.31) reads $e_p = 7.22 \times 10^{-2}$.

The F-MSFV method resulted in an acceptable approximation of the fine-scale pressure for many challenging test cases. Residual plots confirm that the highest pressure errors exist on the boundaries of the dual coarse domain which is caused by the localization assumption of the reduced problems (solved as boundary conditions for obtaining the basis functions). The MsFV method provides an efficient solution for flow in heterogeneous media, by solving the problem at the coarse scale while honoring heterogeneity

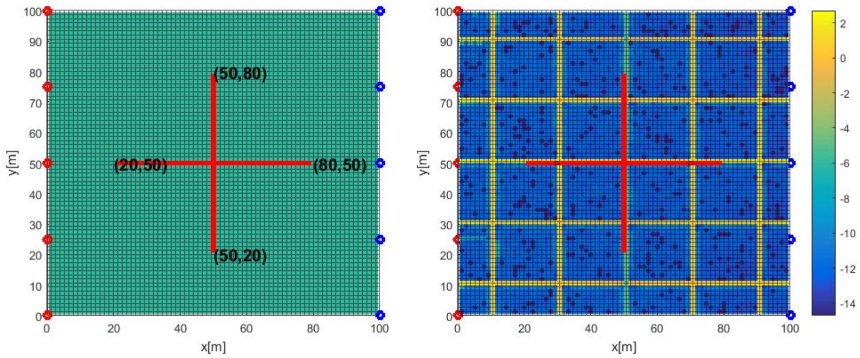

(a) Permeability of the matrix (homogeneous)

(b) Residual (= $Ap-q$)

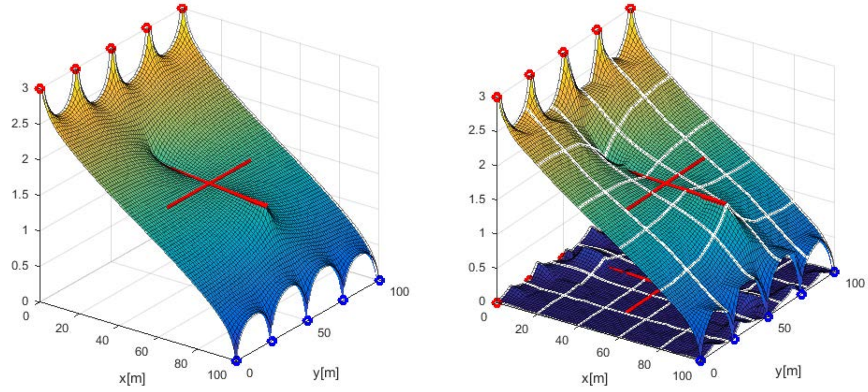

(c) Fine-scale pressure

(d) Multiscale pressure

Figure 5.8: Test case 1: A 2D homogeneous domain with two discrete fractures located in its center perpendicular to each other (horizontal and vertical). Figure 5.8a shows the permeability plot in logarithmic scale with location of the fractures and the wells. Figure 5.8a visualizes the residual of the system of the equation ($Ap-q$) in logarithmic scale indicating non-zero values at dual coarse cell boundaries. The pressure results of the fine-scale and multiscale methods are illustrated on figures 5.8c and 5.8d respectively.

at the original fine-scale resolution. The coarse scale solution is interpolated back to the original fine-scale resolution, which is a unique advantage compared with upscaling methods. But note that the F-MSFV method is yet found sensitive to the coarsening ratio (for both matrix and fracture), and the heterogeneity contrasts. The accuracy of the multiscale solutions can be systematically improved through iterative procedure, which was first developed in [60] and later extended in [81, 125, 140].

One should realize, despite the computational gains that the MsFV method can provide by reducing the size of the fine-scale linear system a few orders of magnitude, the large size of the field-scale domains, even after reduction using multiscale methods, is still beyond the computational capabilities of the current computers. In order to increase the computational efficiency of the multiscale approaches, it is applicable to ex-

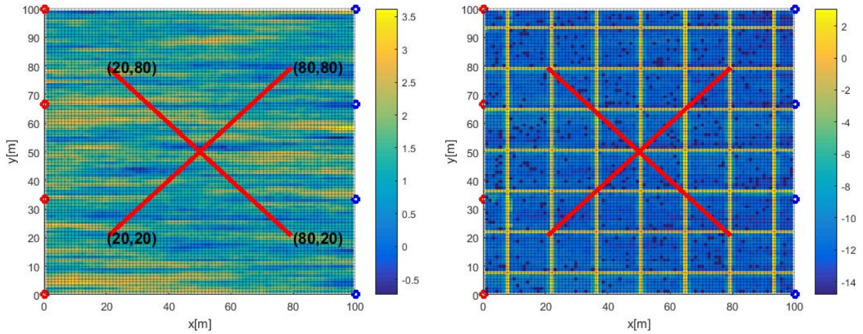

(a) Permeability of the matrix (homogeneous)

(b) Residual ($r = \mathbf{A}p - q$)

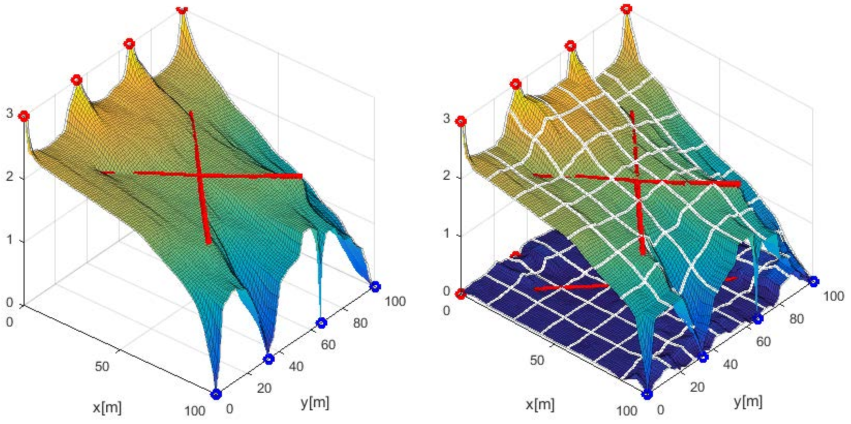

(c) Fine-scale pressure

(d) Multiscale pressure

Figure 5.9: Test case 2: A 2D heterogeneous domain with two discrete fractures located in its center forming an “x” shape. Figure 5.9a shows the heterogeneous permeability plot in logarithmic scale with location of the fractures and the wells. Figure 5.9a visualizes the residual of the system of the equation ($Ap - q$) in logarithmic scale indicating non-zero values at dual coarse cell boundaries. The pressure results of the fine-scale and multiscale methods are illustrated on figures 5.9c and 5.9d respectively.

tend the concept of the MsFV method from only one coarsening level to multiple levels of multiscale [82]. This approach is called the multilevel multiscale finite volume (MMsFV) method. In the next section, the MMsFV method is explained including the extension of this method for fractured porous media using the EDFM approach.

5.3. MULTILEVEL MULTISCALE APPROACHES

In the previous section, the multiscale approaches, especially the MsFV and the F-MsFV methods, were demonstrated. The advantages of such methods including their computational gains while honoring the fine-scale heterogeneities on a desired accuracy were presented. Moreover, the shortcomings and the challenges arising from employing the

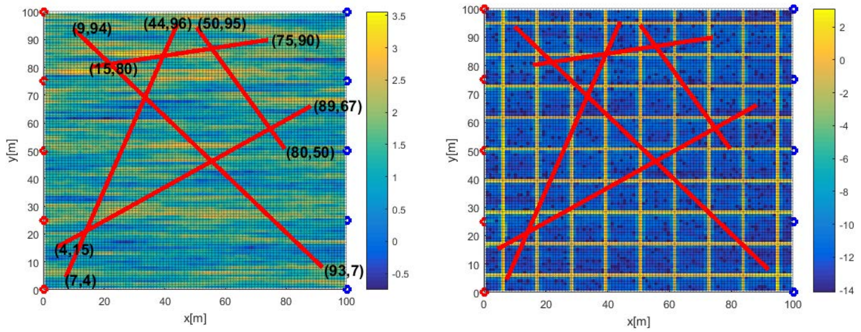

(a) Permeability of the matrix (homogeneous)

(b) Residual (= $Ap - q$)

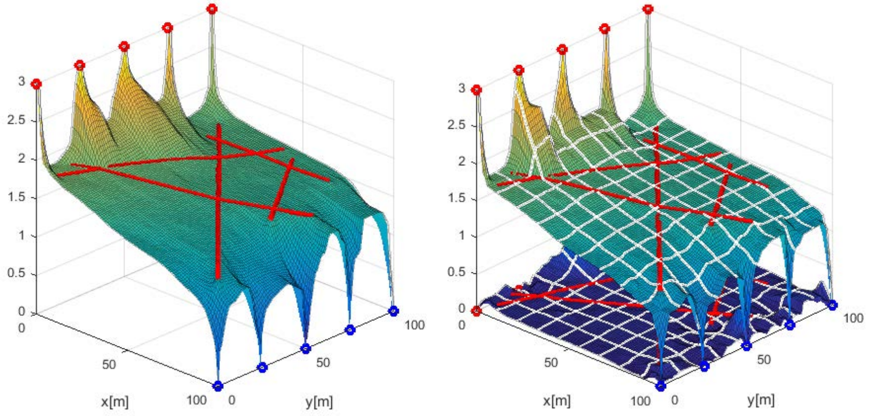

(c) Fine-scale pressure

(d) Multiscale pressure

Figure 5.10: Test case 3: A 2D heterogeneous domain with a network of 5 intersecting fractures. Figure 5.10a shows the heterogeneous permeability plot in a logarithmic scale with location of the fractures and the wells. Figure 5.10a illustrates the residual of the system of the equation ($Ap - q$) in logarithmic scale indicating non-zero values at dual coarse cell boundaries. The pressure results of the fine-scale and multiscale methods are shown on the figures 5.10c and 5.10d respectively.

multiscale methods were briefly discussed. To benefit from the computational efficiency of the multiscale method, one can extend its application to multiple coarsening levels on a recursive manner such that the size of the fine-scale linear system is reduced in many orders of magnitude. The mapping of the linear system from fine-scale resolution to coarse level 1 can be repeated to obtain the a further-reduced linear system at coarse level 2. This process can theoretically be repeated for an arbitrary number of coarsening levels as long as the size of the fine-scale system allows the mapping and remapping procedure.

5.3.1. THE MULTILEVEL MULTISCALE FINITE VOLUME (MMSFV) METHOD

In the description of the MsFV method, equation (5.9) and its corresponding fine-scale linear system (5.11) were considered. For the MMsFV method, the same fine-scale system of equations can be used where the $\mathbf{A}_f$ is a $N_f \times N_f$ coefficient matrix referring to the fine-scale system. At first, a coarse grid structure is imposed on the fine-scale mesh. This is called the coarse grid for coarsening level 1 which is identical to the coarse grid construction of the MsFV method and can be seen in figure 5.2 from the previous section. The coarse grid structure of the coarsening level 1 can act as a fine-scale gridding system for a another coarse grid construction, namely, for coarsening level 2. This results in imposing a set of nested coarse grids on the original fine-scale grid cells on an arbitrary number of coarsening levels, and theoretically there is no limit to the number of coarsening levels as long as these grids can hierarchically be embedded within the fine-scale resolution. Figure 5.11 shows 2 examples of a 2 level multiscale coarse grid construction. On the top figure, at first, a set of primal and dual coarse grids are imposed on the 75×75 fine-scale grid mesh with no vertex on the corners. The coarsening ratio is $\gamma = 5$. This results in a 15×15 coarse grid structure as the first coarsening level. Next, another set of primal and dual coarse grids are imposed on this 15×15 coarse grids, creating 3×3 coarse grid structure at coarsening level 2. For this coarse grid construction approach, the relation between the coarsening ratio and the number of coarse grids in x direction (applicable to any of the x, y, z directions) can be written as

$$\gamma_x = \frac{N_{l-1,x}}{N_{l,x}}, \qquad \text{or} \qquad \gamma_x = \left(\frac{N_{0,x}}{N_{l,x}}\right)^l, \tag{5.32}$$

where γ is the coarsening ratio in x direction. N_0, N_{l-1} and N_l are the number of grid cells at fine-scale, coarsening level $l-1$ and coarsening level l in any direction respectively. Note that for fine-scale, $l = 0$. The figure on the bottom shows a 2 level multiscale coarse grid construction with vertices being put on the corners of the domain as well. In this approach, one can write the relation between the coarsening ratio and the number of coarse grids as

$$\gamma_x = \frac{N_{l-1,x} - 1}{N_{l,x}} + 1, \qquad \text{or} \qquad \gamma_x = \left(\frac{N_{0,x} - 1}{N_{l,x}} + 1\right)^l. \tag{5.33}$$

In the MsFV section, the approximated fine-scale using pressure p_f was obtained via (5.14) which is recalled here as

$$p_f \approx p' = \sum_{j=1}^{N_d} \left(\sum_{k=1}^{N_{c_1}} \Phi_{j,c_1}^k p_{c_1}^k \right).$$

The pressure of the coarse system at coarsening level 1, i.e., p_{c_1} can be approximated using the MMsFV method at coarsening level 2, namely,

$$p_{c_1} = \sum_{j=1}^{N_d} \left(\sum_{k=1}^{N_{c_2}} \Phi_{j,c_2}^k p_{c_2}^k \right). \tag{5.34}$$

Conclusively, for a 2 level multiscale system, the pressure at fine-scale can be approximated as

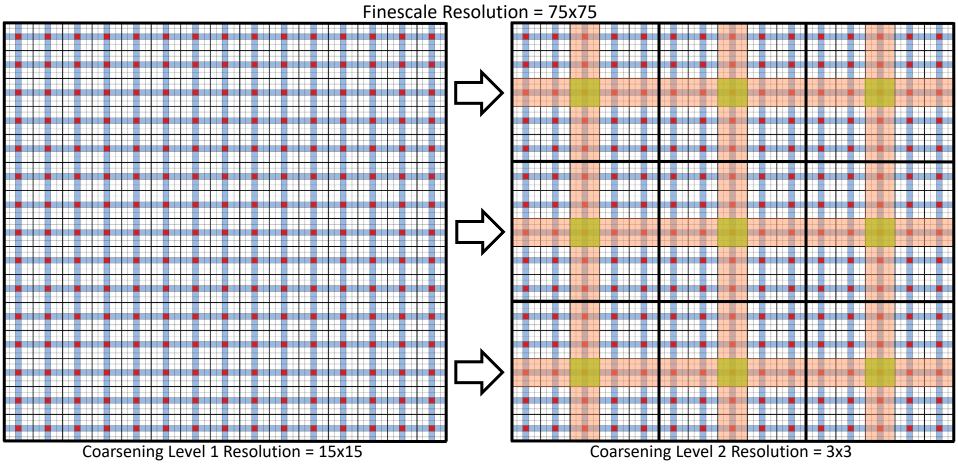

(a) Vertices are not put on the corners.

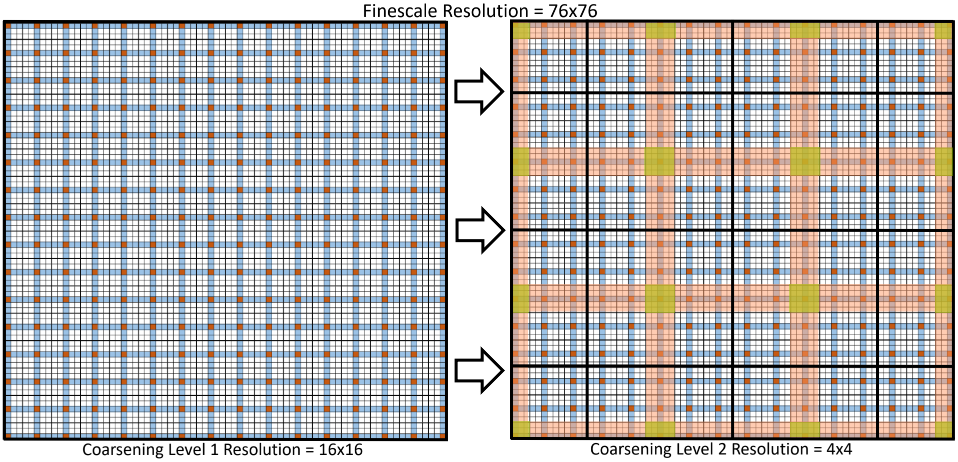

(b) Vertices are put on the corners as well.

Figure 5.11: Construction of primal and dual coarse grid structure in the multilevel multiscale approach for a 2D domain with two different approaches. On the fine-scale grid mesh, first, a set of primal and dual coarse grid cells are imposed with the coarsening ratio of $\gamma = 5$. Next, on this coarse grids level 1, another set of primal and dual coarse grids is constructed. This is a 2 level multiscale coarse grid structure. The difference between the top and bottom figures arises from the two different approaches in the coarse grid construction (whether to put the vertices on the corners or not).

$$p_f \approx p' = \sum_{j=1}^{N_d} \left(\sum_{k=1}^{N_{c_1}} \Phi_{j,c_1}^k \sum_{j=1}^{N_d} \left(\sum_{k=1}^{N_{c_2}} \Phi_{j,c_2}^k p_{c_2}^k \right) \right). \tag{5.35}$$

In theory, this process can be repeated for any arbitrary number of coarsening levels. Figure 5.13 shows an example of the basis functions for two coarsening levels on a 2D

75×75 domain.

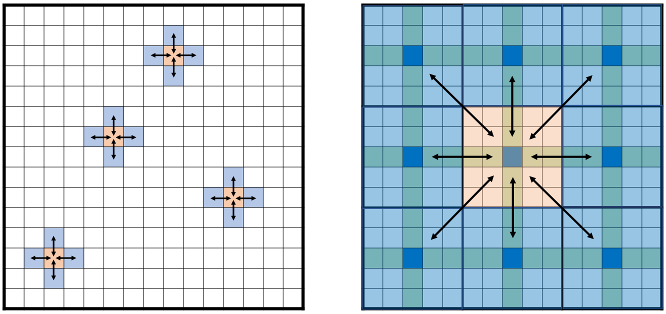

Figure 5.12: The two-point flux approximation (TPFA) fine-scale system (left) considers connectivity of each fine-scale grid cell with only the direct neighbors, whereas the multi-point flux approximation (MPFA) coarse scale system (right) adds the connectivity of each dual coarse grid cell with its diagonal neighbors as well. Computation of the basis functions for the first coarsening level is done using the TPFA scheme. For higher coarsening levels, the coarse system develops an MPFA scheme.

Computation of the basis functions at first coarsening level is done using the two-point flux approximation (TPFA) at fine-scale system, meaning that each grid cell has non-zero transmissibility with only direct neighboring cells (2 connections in 1D, 4 connections in 2D and 6 connections in 3D). In 2D, the edge cells are only connected to the neighboring interiors and edges. Vertices are only connected to the neighboring edges, and interiors have connectivity with the neighboring edges and the interiors (and not with the vertices). Next, the coarse grid system of the first coarsening level is seen as the base for the next coarsening level. This coarse system, in contrary to the fine-scale system, is considered as a multi-point flux approximation (MPFA) based system (since all the direct and diagonal neighbors of a grid cell have non-zero transmissibilities for the calculation of the basis functions inside thr control volumes). In other words, each dual coarse block has connectivity not only with the direct neighboring blocks that have direct connection (left, bottom, right and top in 2D), but also with its diagonal neighbors [141]. Here, the MPFA-based pressure matrix A_p^{l-1}, which stands as the fine-scale system for level $l-1$, is constructed by the multiscale finite-element procedure as

$$\tilde{A}_p^{l-1} = (\mathbf{P}_{l-2}^{l-1})^T \, A_p^{l-2} \, \mathbf{P}_{l-2}^{l-1}. \tag{5.36}$$

Then, $\tilde{A}_p^{l-1}$ is reduced to a TPFA-based system, i.e.,

$$A_p{}^{l-1} = TPFA(\tilde{A}_p^{l-1}), \tag{5.37}$$

where the $TPFA(\bullet)$ extracts the TPFA components of the matrix (hepta-diagonal matrix for 3D Cartesian grids), by considering the transmissibility between cells i and j equal to entry A_{ij} of the original matrix. The algebraic multiscale procedure for the calculation of the basis functions is now performed on this TPFA system at level $l-1$ [81], in order to obtain the basis functions at level l, i.e., $(\mathbf{P}_p)_{l-1}^{l}$. Note that the TPFA reduction of the MPFA multilevel system is done independently for each sub-domain of the rock matrix, and the individual fractures. Figure 5.12 represents the schematic view of the TPFA and the MPFA systems.

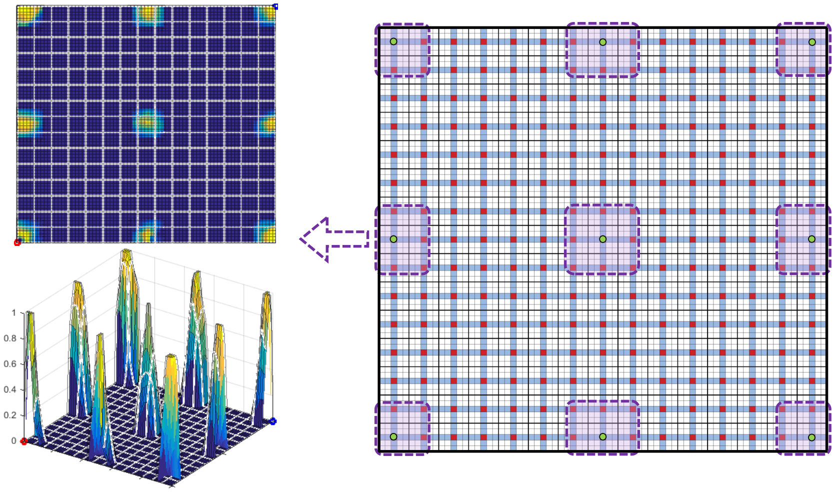

(a) A few basis functions at coarsening level 1.

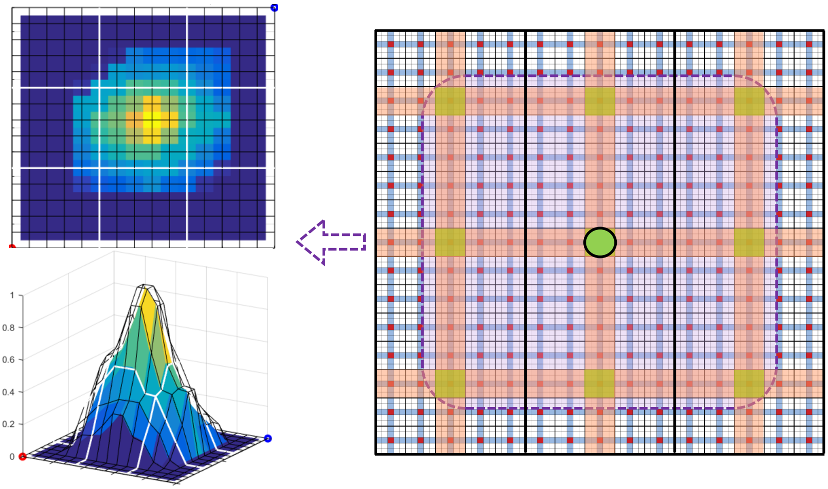

(b) The basis function of the central coarse node at coarsening level 2.

Figure 5.13: Visualization of some basis functions for coarsening level 1 (figure on top) and coarsening level 2 (figure at the bottom) for a 2D domain with 75×75 fine-scale grid cells. Note that the basis functions at coarsening level 2 are used to map the solution between the coarsening levels 1 and 2, while the basis functions of the coarsening level 1 map the solution between the fine-scale and coarsening level 1.

Similar to the MsFV method, the MMsFV method can be formulated in an algebraic manner using multiscale restriction and prolongation operators. These operators are constructed with identical procedure across all coarsening levels. The multilevel multiscale linear system of equations can be written as

$$\underbrace{\mathbf{R}_l^{l-1}\dots\mathbf{R}_1^0\mathbf{A}_f\mathbf{P}_0^1\dots\mathbf{P}_{l-1}^l}_{\mathbf{A}_l}\,p_l = -\underbrace{\mathbf{R}_l^{l-1}\dots\mathbf{R}_1^0 q_f}_{q_l}, \tag{5.38}$$

where $\mathbf{R}_l^{l-1}$ is the restriction operator mapping the system from resolution $l-1$ to resolution l. Similarly, $\mathbf{P}_{l-1}^l$ is the prolongation operator mapping the system from coarsening level l to coarsening level $l-1$. Once the linear system of equations is solved at this multilevel multiscale resolution, the approximated solution at fine-scale resolution p_f is obtained by

$$p_f \approx p' = \mathbf{P}_0^1\dots\mathbf{P}_{l-1}^l\,p_l. \tag{5.39}$$

In the equations above, $\mathbf{A}_l$, p_l and q_l correspond to the components of the linear system at the highest coarsening level l. And $\mathbf{A}_f$, p_f and q_f denote the components at fine-scale resolution (where $l = 0$).

5.3.2. THE MMSFV METHOD FOR FRACTURED POROUS MEDIA (F-MMSFV)

As the MMsFV method can provide higher efficiency for solving the system of equations with large amounts of degrees of freedom in multiple of orders of magnitude, it is important to apply the same technique for fractured porous media. The construction of the hierarchically nested coarse grids structure both for the rock matrix and the embedded fractures is done similar to the MMsFV method (see section above) independently and this is repeated for every coarsening level. Figure 5.14 shows an example of coarse grid construction on a 2D fractured domain with 75 × 75 computational grids imposed on the rock matrix and 75 × 1 grids on each of the three 1D fractures at fine-scale resolution. The coarse grids are constructed for 2 coarsening levels. At the highest coarsening level, the rock matrix contains 3×3 primal coarse grid cells and each fracture has 3 coarse nodes.

The fully coupled basis functions are obtained for the coarse nodes of the rock matrix and the fractures across all coarsening levels. The algebraic description of the F-MMsFV method is identical to that of the MMsFV method. However, the restriction and prolongation operators are extended to encompass the information of the explicit fractures and their basis functions as well as the coupling effects of the two media on each other. Let us recall the algebraic description of the MMsFV (5.38):

$$\underbrace{\mathbf{R}_l^{l-1}\dots\mathbf{R}_1^0\mathbf{A}_f\mathbf{P}_0^1\dots\mathbf{P}_{l-1}^l}_{\mathbf{A}_l}\,p_l = -\underbrace{\mathbf{R}_l^{l-1}\dots\mathbf{R}_1^0 q_f}_{q_l}. \tag{5.38}$$

For a fractured media, the prolongation operator $\mathbf{P}_{l-1}^l$ has a block structure which reads

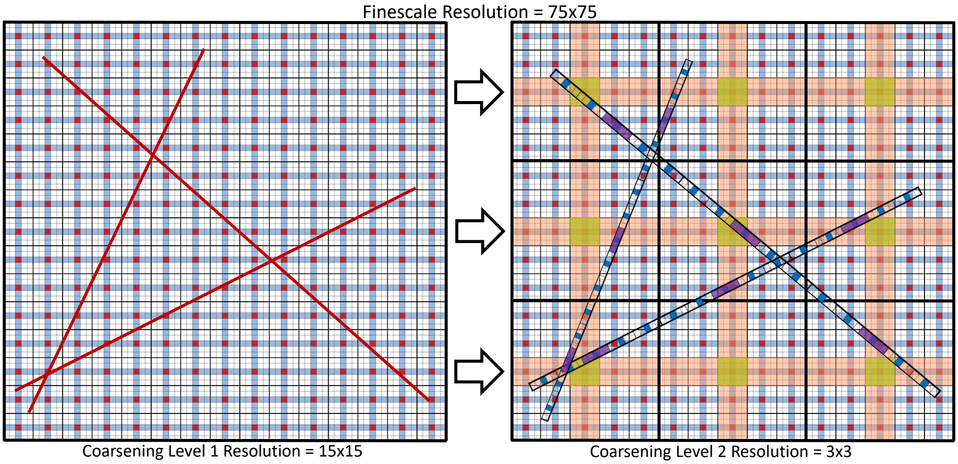

Figure 5.14: An example of the coarse grid construction with 2 coarsening levels for a 2D domain with three fractures.

$$\mathbf{P}_{l-1}^{l} = \begin{pmatrix} \left(\mathbf{P}_{l-1}^{l}\right)^{m,m} & \left(\mathbf{P}_{l-1}^{l}\right)^{m,f} \\ \left(\mathbf{P}_{l-1}^{l}\right)^{f,m} & \left(\mathbf{P}_{l-1}^{l}\right)^{f,f} \end{pmatrix}. \tag{5.40}$$

And the restriction operator $\mathbf{R}_{l}^{l-1}$ is written as

$$\mathbf{R}_{l}^{l-1} = \begin{pmatrix} \left(\mathbf{R}_{l}^{l-1}\right)^{m} & 0 \\ 0 & \left(\mathbf{R}_{l}^{l-1}\right)^{f} \end{pmatrix}. \tag{5.41}$$

An example of a few computed fully coupled basis functions for a fractured domain with three fractures and two coarsening levels using the F-MMsFV method is visualized on figure 5.15.

5.3.3. EVALUATION OF THE F-MMSFV METHOD

In this section, the F-MMsFV method is evaluated and its accuracy is compared against the fine-scale results. For this purpose, the single-phase incompressible system from equations (5.1)-(5.2) is considered on 2D fractured domains. The input parameters that are mutually used in the following test cases are identical to the test cases in the evaluation section of the F-MsFV method and available in table 5.1. Note that, similar to the F-MsFV evaluation, the pressure error of the F-MMsFV results with respect to the fine-scale results (denoted as e_p) is calculated using the second norm of the pressure vectors as

$$e_p = \frac{\| p_{\mathrm{FS}} - p_{\mathrm{MMS}} \|_2}{\| p_{\mathrm{FS}} \|_2}, \tag{5.42}$$

Different test cases are designed to address various possible challenges. The sensitivity of the F-MMsFV method to the number of the coarse levels and the coarsening ratios employed and to the permeability contrast is presented.

TEST CASE 1: 2D HETEROGENEOUS DOMAIN WITH 2 “+” SHAPED FRACTURES

In this test case, two fractures are positioned in the center of a heterogeneous domain perpendicular to each other (horizontal and vertical) forming a “+” shape. Five injection wells at the left boundary and five production wells at the right boundary form a line drive pattern. The test case consists of $100 \times 100 = 10000$ computational grid cells on the rock matrix and 152 elements on the fractures. The coarsening level is 2 and coarsening ratio is $\gamma = 5$ for all media and in all directions. Figure 5.16 shows the results of this test case.

The fine-scale system is solved with 100×100 matrix cells and 152 fracture elements, whereas the multilevel multiscale system is solved by 4×4 matrix coarse grid cells and 8 fracture coarse grid cells at coarsening level 2 with coarsening ratio of $\gamma = 5$ (merely 626 times lower number of degrees of freedom or DOFs). The white and gray lines in the multilevel multiscale pressure plot indicate the boundaries of the primal coarse grids for different coarsening levels. The plotted graph below the multiscale graph in the right figure is the absolute difference between the fine-scale and the multiscale solutions. The normalized error calculated via equation (5.31) is $e_p = 4.40 \times 10^{-2}$.

TEST CASE 2: 2D HOMOGENEOUS DOMAIN WITH 2 DIAGONAL FRACTURES (“X” SHAPED)

In this test case, two diagonal fractures are located in the center, perpendicular to each other, in a 2D homogeneous domain with line drive well pattern consisting of five injectors and five producers. An $81 \times 81 = 6561$ fine-scale grid cells is imposed on the rock matrix and 164 elements on the fractures. Solution sensitivity and error analysis will be studied for different coarsening levels and coarsening ratios in this test case. The following options will be considered:

1. Finescale (reference) solution
2. One coarsening level, with coarsening ratio $\gamma = 3$
3. One coarsening levels, with coarsening ratio $\gamma = 9$
4. One coarsening levels, with coarsening ratio $\gamma = 27$
5. Two coarsening levels, with coarsening ratio $\gamma = 3$
6. Three coarsening levels, with coarsening ratio $\gamma = 3$

Figure 5.17 shows the results of this test case.

In order to understand the effect of different coarsening levels and coarsening ratios on the accuracy of the MsFV and the MMsFV methods compared to fine-scale results, various combinations are considered and their pressure plots together with errors are shown in the figure 5.17. As can be seen, by increasing the number of coarsening levels the error increases. On the other hand, the computational gain increases exponentially as every extra coarsening level results in a γ^2 (for 2D) or γ^3 (in 3D) times reduction in the size of the linear system to be solved using the MMsFV method.

TEST CASE 3: 2D HOMOGENEOUS DOMAIN WITH 5 INTERSECTING FRACTURES

This test case consists of five intersecting fractures in a 2D homogeneous domain with line drive well pattern of five injection wells at left boundary and five production wells at the right boundary. A $75 \times 75 = 5625$ grid cells are imposed on the rock matrix and a total of 380 grid cells on the fracture network. The coarsening level is 2 and coarsening ratio is 5. The results of this test case are presented in figure 5.18.

The fine-scale system is solved with $75 \times 75 = 5625$ grids on the rock matrix and 380 fracture elements. The multilevel multiscale system, however, is solved on a reduced size of the 3×3 coarse grid cells for the rock matrix and 20 coarse grid cells for the fracture network. The coarsening level is 2 and the coarsening ratio is 5. The normalized error for this test case (3) is $e_p = 7.85 \times 10^{-2}$.

TEST CASE 4: 2D HOMOGENEOUS DOMAIN WITH 35 FRACTURES

A 2D fractured 75 [m] × 75 [m] reservoir with 35 fractures is considered. A 375×375 grid is imposed on the rock matrix at fine-scale. Fractures have different lengths but identical apertures of 5×10^{-3} [m]. The fracture network consists of 4420 grid cells (a total of 145045 grid cells) at fine-scale resolution. The matrix permeability is 10^{-14} [m^2] whereas the fracture permeability is 2.08×10^{-6} [m^2]. Two injection wells at the bottom left and the top left corners ($p_{\text{inj}} = 2 \times 10^7$ [Pa]) and two production wells at the bottom right and the top right corners ($p_{\text{prod}} = 1 \times 10^7$ [Pa]) exist. The multilevel multiscale method is run with different number of coarsening levels and coarsening ratios. Here, similar to the previous test cases, the fully-coupled multilevel multiscale basis functions are considered. The settings of each multilevel multiscale run, the pressure error (e_p) and the number of degrees of freedom (DOF) are presented in table 5.2.

	Coarsening levels	Coarsening ratio (γ_m)	Num. of DOF	Error (e_p [%])
Case 1	1	5 × 5	6509	0.11
Case 2	1	25 × 25	1109	0.22
Case 3	2	5 × 5	877	0.27
Case 4	1	125 × 125	893	0.64
Case 5	3	5 × 5	661	0.98

Table 5.2: Test case 4: the multilevel multiscale settings and errors

The surface plots of the pressure distributions obtained with fine-scale simulations and with different multilevel multiscale settings are presented in figure 5.19.

TEST CASE 5: 2D HETEROGENEOUS DOMAIN WITH 35 FRACTURES

A heterogeneous 2D domain of 75 [m] × 75 [m] with a network of 35 fractures (identical to test case 4) is considered. The matrix and the fracture network are discretized into 135 ×

135 and 1665 fine-scale grids, respectively, resulting in 19890 total grid cells. The top right plot on figure 5.20 shows the heterogeneous permeability map for this test case with the minimum and maximum values of 1.3×10^{-16} [m^2] and 9.9×10^{-13} [m^2], respectively. The wells have identical location and constraints as in test case 4. Different coarsening levels and ratios are considered. The pressure error with respect to the reference (i.e., fine-scale solution) for different numbers of degrees of freedom (DOF) are shown in table 5.3.

	Coarsening levels	Coarsening ratio (γ_m)	Num. of DOF	Error (e_p [%])
Case 1	1	3×3	2580	12.8
Case 2	1	9×9	780	12.7
Case 3	2	3×3	410	13.6
Case 4	1	27×27	580	11.0
Case 5	3	3×3	210	12.1

Table 5.3: Test Case 5: the multilevel multiscale settings and errors

The figure 5.20 presents the pressure results of the fine-scale run as well as the multilevel multiscale run at various coarsening levels and coarsening ratios. All the multilevel multiscale runs employ fully-coupled basis functions. As can be seen in Table 5.3, for the corresponding coarsening ratios, the multilevel multiscale and the 1-level multiscale strategies deliver comparable results. Note that no iterations have been employed to improve the multilevel multiscale results.

5.4. DISCUSSIONS AND CONCLUSION

In this chapter, the multiscale (MsFV) and the multilevel multiscale (MMsFV) methods for fractured porous media were presented. To simplify the description of these methods, single-phase incompressible fluid flow model was considered. The coarse grid construction and computation of basis functions for the rock matrix as well as the discrete fractures were discussed on multiple coarsening levels. Moreover, the algebraic description of the multiscale and multilevel multiscale approaches were briefly covered. Using the restriction and prolongation operators, the fine-scale system was mapped to a coarse scale system. After solving the linear system at the coarsest resolution, the solution was then mapped back to the fine-scale resolution using the basis functions, hence providing an approximated solution. Using a number of 2D homogeneous and heterogeneous fractured test cases, the accuracy of these techniques were compared with the fine-scale results as reference solutions. It was seen that the residual of the fine-scale system was non-zero only at the boundaries of the dual coarse grid cells, due to the localization assumption imprinted in the multiscale method. Note that the presented results are all based on the MsFV/MMsFV approach, without employment of an iterative procedure that could have improve the final results. Yet, it can be seen that the multilevel multiscale method for fractured porous media (F-MMsFV) proposed in this chapter provides accurate results compared to the fine-scale solution. The results show that the F-MMsFV method can accurately capture the complex effects of fractures and the rock heterogeneities on arbitrary levels of coarse grids. For test cases with high-permeability contrasts and strong anisotropic permeability tensors, though, one needs to consider an iterative procedure to ensure the quality of the results. Important to emphasize here is that, in test case 3, only small error differences exist between the results of coarsening levels 1, 2 and 3 (using identical coarsening ratio of $\gamma = 3$). On the other hand, the size of the linear system (to be solved) reduces significantly by increasing the number of coarsening levels, providing considerable computational efficiencies which is promising in the case of large-scale simulation models. At last, with the test cases 4 and 5, the capability of the devised multilevel multiscale method for fractured porous media was assessed using a network of 35 highly conductive intersecting fractures. The results and the calculated errors, show a satisfactory accuracy of the F-MMsFV method even in presence of a dense and complex fracture network. Please note that the MMsFV method automatically reduces to the MsFV method if only 1 coarsening level is employed. This gives full flexibility to the user, when real-field applications are being studied.

While multilevel multiscale approach in this chapter offers satisfactory performance compared to fine-scale results, one needs to realize that such an approach solves the entire system at the coarse scale resolution. Even though this provides significant computational efficiency, it can result into high errors in certain regions in the domain especially where the heterogeneity contrasts in the rock matrix as well as presence of complex networks of fractures and faults cause a severely ill-conditioned linear system. Moreover, in the cases of multiphase flow and coupled mass-heat transport with hyperbolic equations, of particular interest is to capture the sharp gradients of the solution (e.g., the saturation and heat fronts) accurately. Therefore, one needs to employ higher resolution in certain parts of the domain which can dynamically change across simulation time-steps. In these scenarios, a dynamic grid resolution is necessary to capture various physical phenomena on a resolution that is required. In the following chapters, an algebraic dynamic multilevel method will be covered and explained in detail, which addresses the multilevel multiscale coexistence of the pressure (elliptic or parabolic) and transport (hyperbolic) unknowns.

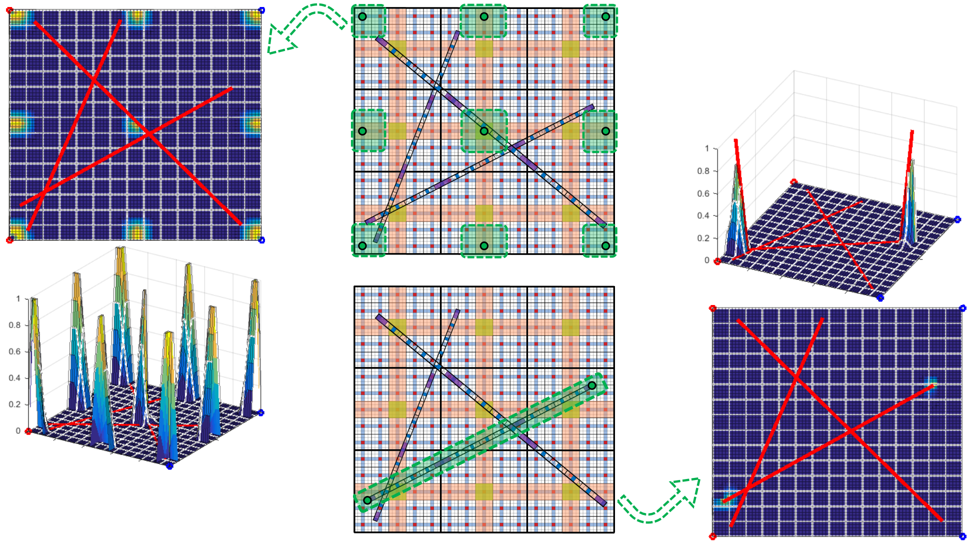

(a) A few basis functions in the rock matrix and the two basis functions at the end points of a fracture, all at coarsening level 1.

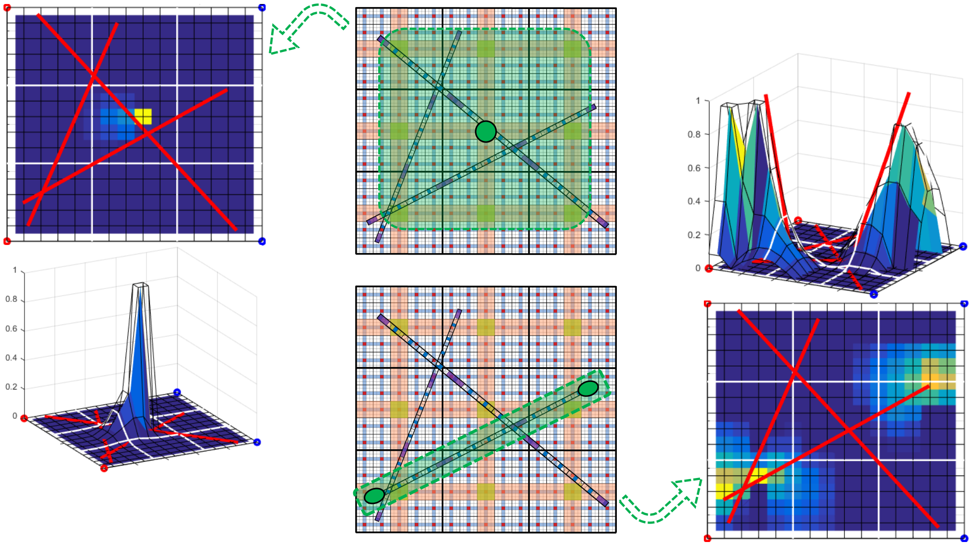

(b) The basis function of the central coarse node in the rock matrix and the two basis functions at the end points of a fracture, both at coarsening level 2.

Figure 5.15: Visualization of some basis functions for coarsening level 1 (figure on top) and coarsening level 2 (figure at the bottom) for a 2D domain with 75 × 75 fine-scale grid cells and three 1D fractures each with 75 grid cells. Note that the basis functions at coarsening level 2 are used to map the solution between the coarsening levels 1 and 2, while the basis functions of the coarsening level 1 map the solution between the fine-scale and coarsening level 1. Note the fully coupled strategy in the computation of the rock matrix and the fracture basis functions at both coarsening levels.

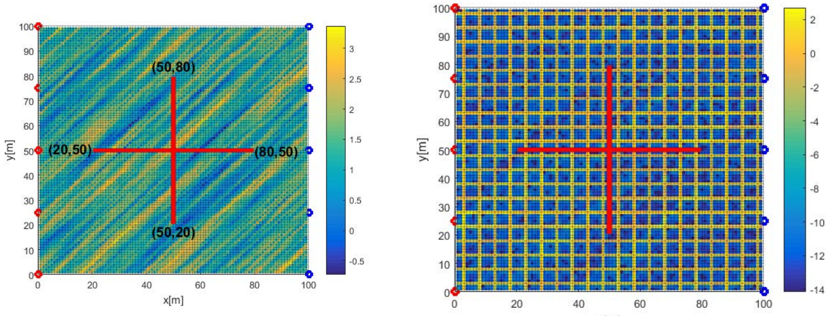

(a) Permeability of the matrix (heterogeneous)

(b) Residual (= $Ap - q$)

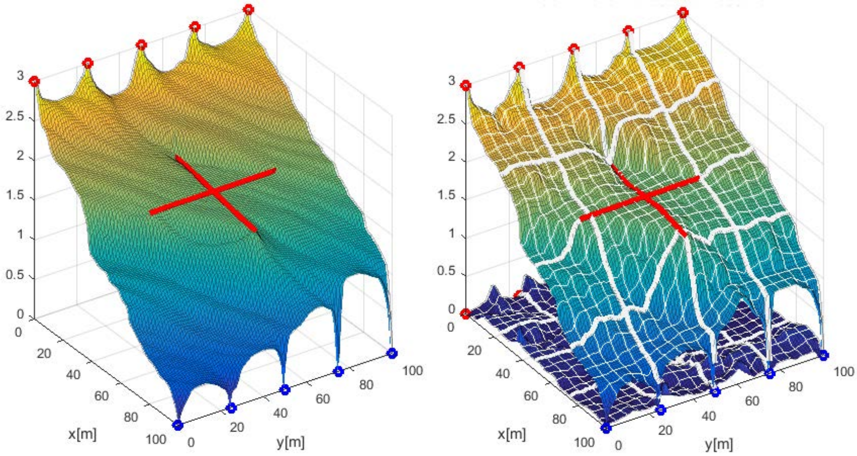

(c) Fine-scale pressure

(d) Multilevel multiscale pressure

Figure 5.16: Test case 1: A 2D heterogeneous domain with two discrete fractures located in its center perpendicular to each other (horizontal and vertical). Figure 5.8a shows the permeability plot in logarithmic scale with location of the fractures and the wells. Figure 5.8a visualizes the residual of the system of the equation $(Ap - q)$ in logarithmic scale indicating non-zero values at dual coarse cell boundaries. The pressure results of the fine-scale and multilevel multiscale methods are illustrated on the figures 5.8c and 5.8d respectively.

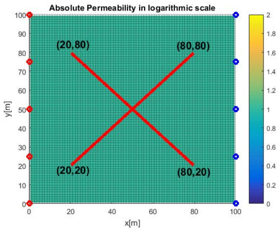

(a) Permeability of the matrix (homogeneous)

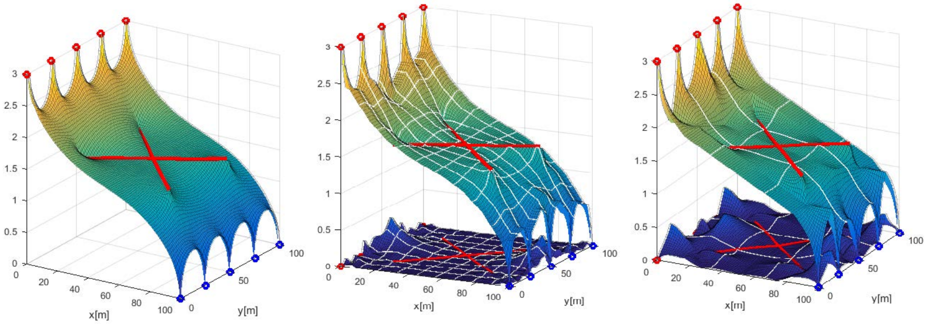

(b) Fine-scale pressure

(c) Coarsening level = 1, coarsening ratio = 9, error $e_p = 2.63 \times 10^{-2}$

(d) Coarsening level = 1, coarsening ratio = 27, error $e_p = 5.84 \times 10^{-2}$

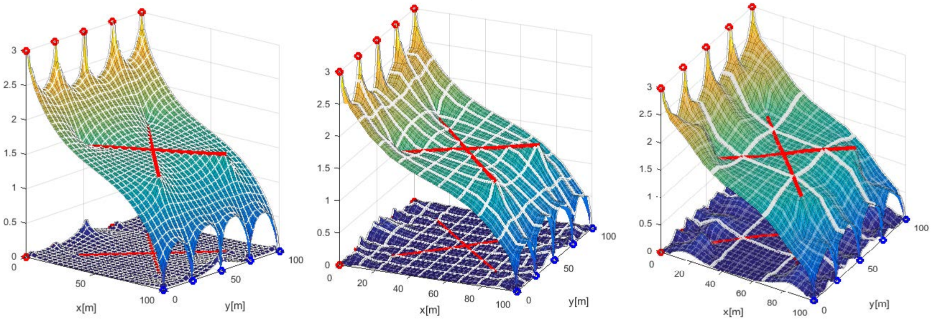

(e) Coarsening level = 1, coarsening ratio = 3, error $e_p = 1.82 \times 10^{-2}$

(f) Coarsening level = 2, coarsening ratio = 3, error $e_p = 3.83 \times 10^{-2}$

(g) Coarsening level = 3, coarsening ratio = 3, error $e_p = 6.71 \times 10^{-2}$

Figure 5.17: Test case 2: A 2D homogeneous domain with two discrete fractures located diagonally in its center perpendicular to each other. Various coarsening levels and coarsening ratios are selected and their corresponding pressure results are plotted. The errors are calculated using (5.42) and fine-scale pressure is used as reference solution.

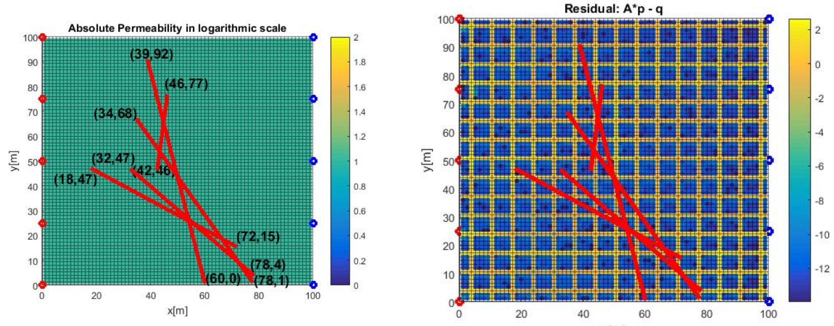

(a) Permeability of the matrix (homogeneous)

(b) Residual (= $Ap - q$)

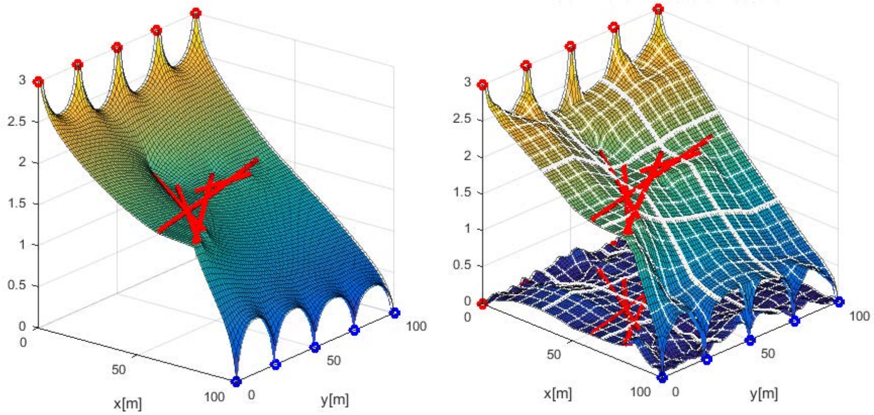

(c) Fine-scale pressure

(d) Multilevel multiscale pressure

Figure 5.18: Test case 3: A 2D homogeneous domain with five discrete fractures located. Figure 5.10a shows the permeability plot in logarithmic scale with location of the fractures and the wells. Figure 5.10a visualizes the residual of the system of the equation ($Ap - q$) in logarithmic scale indicating non-zero values at dual coarse cell boundaries. The pressure results of the fine-scale and multilevel multiscale methods are illustrated on the figures 5.10c and 5.10d respectively.

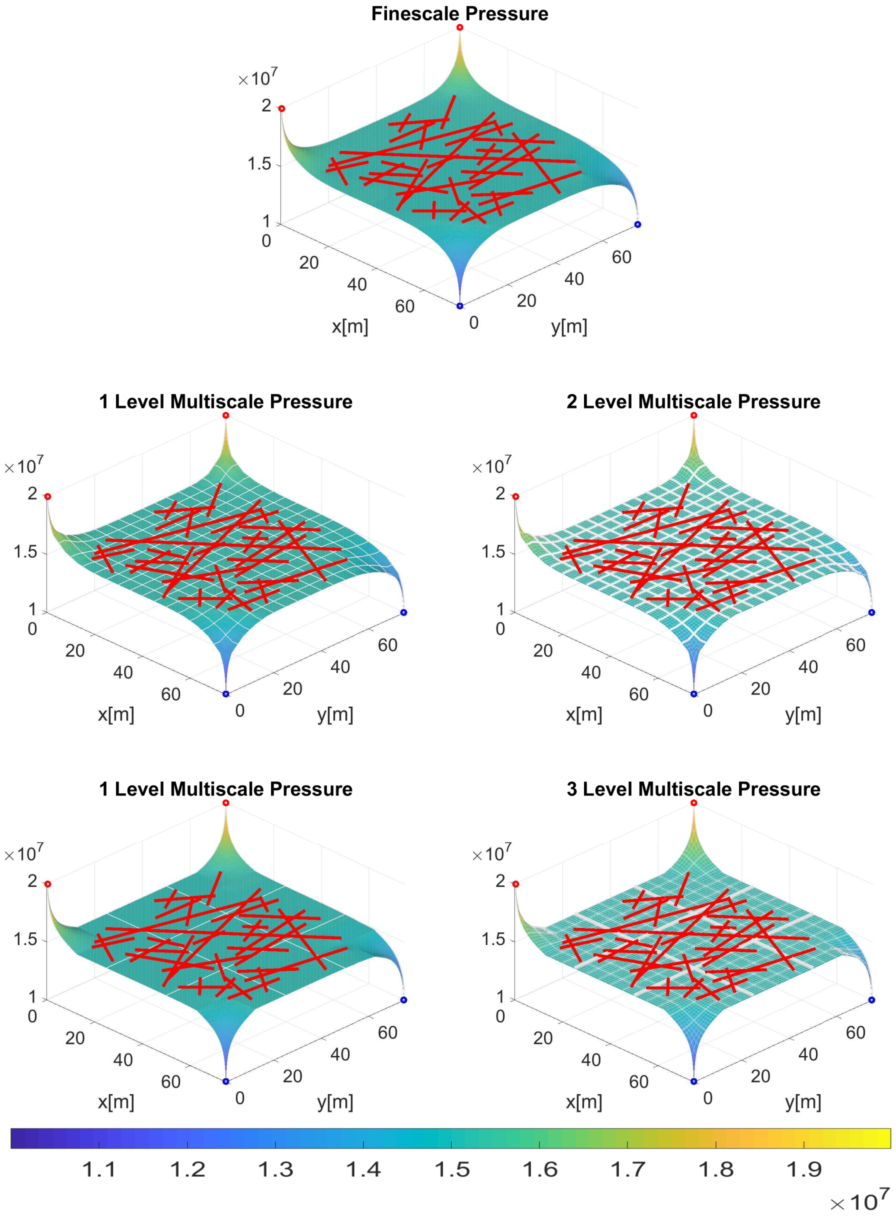

Figure 5.19: Test case 4: comparison of the pressure distributions obtained by the fine-scale simulations and with static multilevel multiscale approach, where the pressure is solved everywhere at the coarsest level. The top plot is the fine-scale solution. The middle row shows the 1 level multiscale solution with $\gamma_m = 25\times 25$ (left) and the 2 level multiscale solution with $\gamma_m = 5\times 5$ (right). Shown in the bottom row is the 1 level multiscale solution with $\gamma_m = 125\times 125$ (left) and the 3 level multiscale solution with $\gamma_m = 5\times 5$ (right). Note that the error norms are presented in table 5.2.

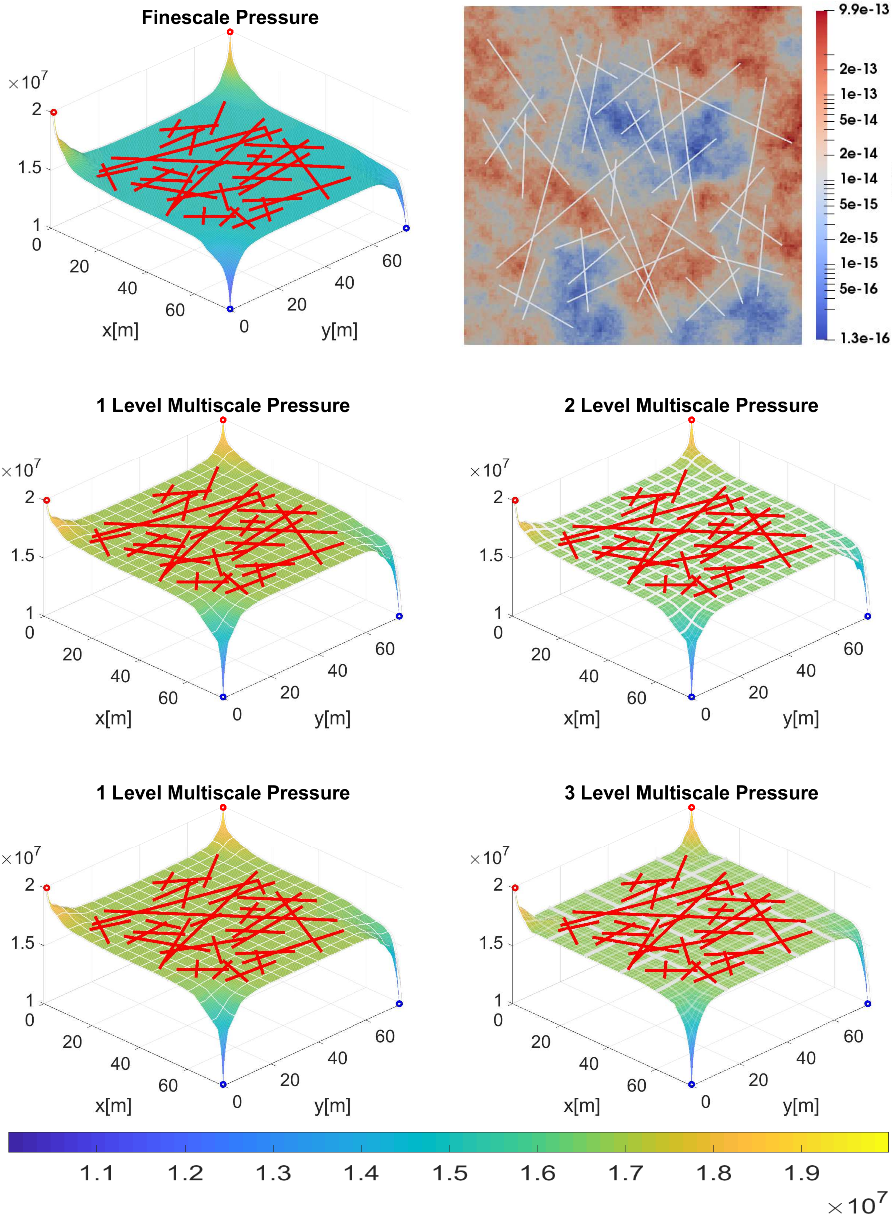

Figure 5.20: Test case 5: comparison of the pressure distributions obtained by the fine-scale simulations with those from the static multilevel multiscale approach. The top left plot is the fine-scale solution. The permeability map is shown in the top right plot. The middle row shows the 1 level multiscale solution with $\gamma_m = 9 \times 9$ (left) and the 2 level multiscale solution with $\gamma_m = 3 \times 3$ (right). The bottom row illustrates the 1 level multiscale solution with $\gamma_m = 27 \times 27$ (left) and the 3 level multiscale solution with $\gamma_m = 3 \times 3$ (right). The errors are shown in table 5.3.

6

ALGEBRAIC DYNAMIC MULTILEVEL (ADM) METHOD FOR ISOTHERMAL MULTIPHASE FLOW IN FRACTURED POROUS MEDIA

In the previous chapter, the static multilevel approaches such as the multiscale finite volume (MsFV) and the multilevel multiscale finite volume (MMsFV) methods were described. The construction of the primal and dual coarse grids both for the rock matrix and the fractures across multiple coarsening levels was explained. Moreover, the calculation of the fully-coupled basis functions was described for each medium at each coarsening level. The multilevel multiscale formulation, obtaining the linear system at coarse scale and the approximation of the fine-scale solution were covered in detail as well. In addition, the algebraic description of the multiscale and multilevel multiscale methods were briefly discussed. Through a number of fractured test cases including heterogeneous ones, the accuracy of the static multiscale and multilevel multiscale finite volume methods was presented. Even though these methods provided acceptable accuracy while reducing the size of the linear system with multiple orders of magnitude (especially with MMsFV method), the accuracy of their results can be hindered in presence of severe heterogeneity contrasts within the rock matrix and presence of complex fracture networks. Moreover, the geometry of the coarse grids affects the final results. Please mind that by using iterative schemes for multiscale approaches, the accurate representation of the fine-scale heterogeneity can significantly be improved.

Despite their benefits, one should note that using multilevel multiscale techniques maps the entire system of equations from fine-scale resolution to the coarsest level. While this results in significant reduction in the size of the linear system providing high

---

Parts of this chapter is the revised version of two of the author's publication in the Journal of Computational Physics, **Vol. 373** (2018) [45], and in the Journal of Advances in Water Resources, **Vol. 143** (2020) [142].

computational gains, the fine-scale heterogeneities and physical phenomena such as saturation or heat fronts in certain regions of the domain need to be captured with higher orders of accuracy compared to the rest of the domain. Therefore, more advanced techniques are needed to address such challenges. Algebraic dynamic multilevel (ADM) methods have been introduced to provide higher flexibility in coarsening levels by combining the dynamic local grid refinement (DLGR) approach with multilevel multiscale techniques. In this chapter, the ADM method is developed for isothermal two-phase immiscible fluid flow in fractured porous media employing the embedded discrete fracture model (EDFM). For more details about the fracture models, please see section 3.3. Using the ADM method, at every simulation time-step, the discretized and linearized system of equations (coupled using the FIM approach) at fine-scale resolution, is mapped to a dynamically defined multilevel multiscale resolution grid (the so-called ADM grid) both for the rock matrix and the fractures independently. Such a dynamic multilevel grid is obtained to employ the fine-scale resolution only when and where it is needed (e.g., at the advancing saturation fronts). The ADM dynamic grid is chosen independently for the rock matrix and fractures, based on a front-tracking criterion that aims to minimize the cost-accuracy trade-off. Mapping the solution across different grid resolutions is performed through sequences of the ADM restriction and prolongation operators. These operators are obtained from the static multilevel multiscale operators assembled on various coarsening levels. The static multilevel multiscale operators are computed only at the beginning of the simulation to increase the computational efficiency of the ADM methods. The finite-volume restriction operators are employed for all unknowns to ensure mass conservation at all levels. On the other hand, regarding the prolongation operators, different interpolation strategies are considered for the two main unknowns (pressure and saturation). Specifically, fully coupled basis functions (see sections 5.2.2 and 5.3.2) are used for the rock matrix and the fractures on all coarsening levels to take into account the effects of the fractures on the flow pattern accurately. The devised multilevel multiscale basis functions are employed as the pressure interpolators. However, piece-wise constant functions are used to interpolate the saturation values, as the grid refinement strategy avoids crossing the scales at the saturation front locations. Once the system of equations is solved at ADM resolution, the solution is mapped back to fine-scale resolution using the ADM prolongation operator, to obtain an approximated solution. Such a development allows for an automatic framework to explicitly or effectively represent a fracture at any coarse level, i.e., through the selection of the location of the coarse nodes. More precisely, if no coarse node for a fracture network inside a dual coarse grid is chosen, the matrix basis functions will automatically homogenize the effect of the fracture at the corresponding coarse scale. However, if coarse nodes are selected inside the fracture network of that dual coarse cell, the fractures will be explicitly represented at the corresponding coarser resolution. The accuracy and the sensitivity of the ADM method to the error criterion and to the pressure basis functions are studied through a set of 2D and 3D test cases. The devised ADM strategy provides a dynamic treatment of highly fractured media, and casts a promising approach for real-field applications.

6.1. THE ADM SIMULATION STRATEGY

For the purpose of describing the ADM simulation strategy in this chapter, an isothermal two-phase fluid flow in heterogeneous fractured reservoirs is considered. The governing equations of this fluid flow model are covered in detail in section 2.1. The discretized equations and the fine-scale linearized system are explained comprehensively in sections 3.1.1 and 3.2.1 respectively.

At each Newton iteration, The ADM method constructs an algebraically reduced system based on equation (3.39) on a multilevel grid which is dynamically defined at the beginning of each time-step. A schematic of the ADM simulation is shown in figure 6.1.

As the first step, the ADM grid needs to be described. Sets of N_m and N_{f_i} nested Cartesian grids are imposed on the matrix and fracture fine-scale grid cells. The level at which the fine-scale computational domain is obtained is referred to as $l = 0$. Let N_m^l be the number of grid cells in the porous matrix and $N_{f_i}^l$ the number of grid cells in fracture i, both at level l. The coarsening ratio, γ^l can therefore be defined as

$$\gamma^l = \left(\gamma_m^l, \gamma_{f1}^l, \cdots, \gamma_{n_{\text{frac}}}^l\right) = \left(\frac{N_m^l}{N_m^{l-1}}, \frac{N_{f_1}^l}{N_{f_1}^{l-1}}, \cdots, \frac{N_{f_{n_{\text{frac}}}}^l}{N_{f_{n_{\text{frac}}}}^{l-1}}\right). \tag{6.1}$$

Note that the count of the coarsening levels and the coarsening ratios for the rock matrix and every individual fracture are independent, which leads to a flexible framework. Therefore, the ADM grid at each time-step is constructed by combining grid cells at different resolutions. The ADM method maps the fine-scale system to the dynamic multilevel grid by applying sequences of restriction (**R**) and prolongation (**P**) operators, which are constructed based on the values computed at the beginning of the simulation (figure 6.1). More precisely, at each iteration, the ADM system reads

$$\underbrace{\hat{\mathbf{R}}_l^{l-1} \dots \hat{\mathbf{R}}_1^0 \mathbf{J_0} \hat{\mathbf{P}}_0^1 \dots \hat{\mathbf{P}}_{l-1}^l}_{\mathbf{J}_{ADM}} \delta\hat{x}_l = -\underbrace{\hat{\mathbf{R}}_l^{l-1} \dots \hat{\mathbf{R}}_1^0 r_0}_{r_{ADM}}, \tag{6.2}$$

where $\hat{\mathbf{R}}_l^{l-1}$ is the restriction operator mapping part of the vector of the solution which is at level $l-1$ ($\delta\hat{x}_{l-1}$) to level l ($\delta\hat{x}_l$). Similarly, $\hat{\mathbf{P}}_{l-1}^l$ is the prolongation operator mapping part of the entire solution vector which is at level l to level $l-1$. Once the ADM system is solved at the dynamic multilevel resolution, the approximated solution at the fine-scale resolution $\delta x_0'$ (the reference fine-scale solution is represented as δx_0) is given by

$$\delta x_0 \approx \delta x_0' = \hat{\mathbf{P}}_0^1 \dots \hat{\mathbf{P}}_{l-1}^l \delta x_l. \tag{6.3}$$

The multilevel multiscale prolongation operator $\mathbf{P}_{l-1}^l$ between each two levels l and $l-1$ is obtained for the entire domain, though at each time step only a fraction of the domain needs to go through this map, which is illustrated by the ADM prolongation operator, i.e., $\hat{\mathbf{P}}_{l-1}^l$ in equation (6.2). The multilevel multiscale prolongation operator $\mathbf{P}_{l-1}^l$ has a block structure which reads

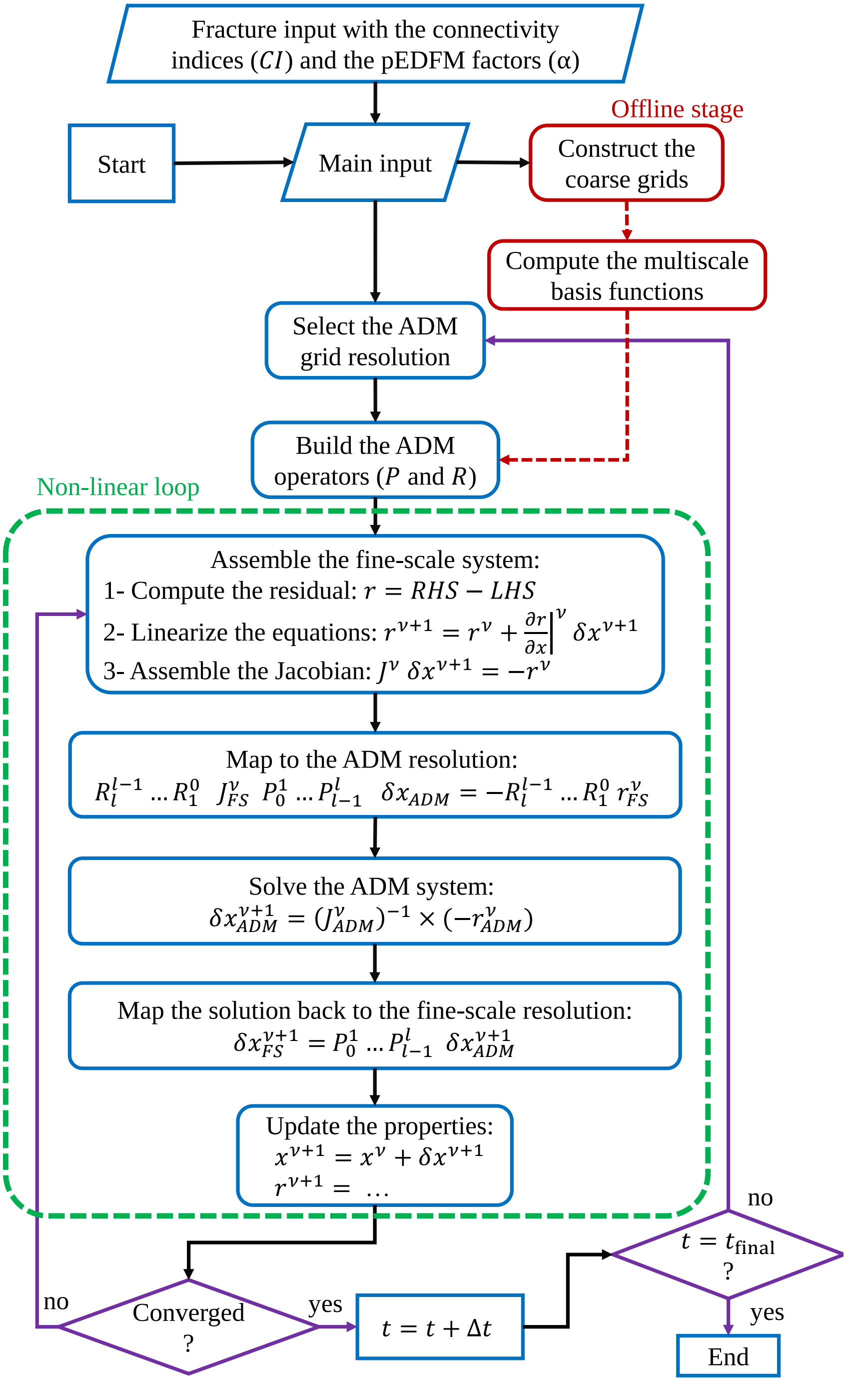

Figure 6.1: Schematic description of the ADM strategy.

$$\mathbf{P}_{l-1}^{l} = \begin{pmatrix} \left((\mathbf{P}_p)_{l-1}^{l}\right)^{m,m} & \left((\mathbf{P}_p)_{l-1}^{l}\right)^{m,f} & 0 & 0 \\ \left((\mathbf{P}_p)_{l-1}^{l}\right)^{f,m} & \left((\mathbf{P}_p)_{l-1}^{l}\right)^{f,f} & 0 & 0 \\ 0 & 0 & \left((\mathbf{P}_S)_{l-1}^{l}\right)^{m,m} & 0 \\ 0 & 0 & 0 & \left((\mathbf{P}_S)_{l-1}^{l}\right)^{f,f} \end{pmatrix}_{N_{l-1}\times N_l} . \tag{6.4}$$

Similarly, the restriction operator reads

$$\mathbf{R}_{l}^{l-1} = \begin{pmatrix} \left(\mathbf{R}_{l}^{l-1}\right)^{m} & 0 & 0 & 0 \\ 0 & \left(\mathbf{R}_{l}^{l-1}\right)^{f} & 0 & 0 \\ 0 & 0 & \left(\mathbf{R}_{l}^{l-1}\right)^{m} & 0 \\ 0 & 0 & 0 & \left(\mathbf{R}_{l}^{l-1}\right)^{f} \end{pmatrix}_{N_l\times N_{l-1}} . \tag{6.5}$$

A finite-volume restriction operator is employed in order to guarantee mass conservation as convergence is reached on the multilevel ADM grid, i.e.,

$$\mathbf{R}_{l}^{l-1}(s,t) = \begin{cases} 1 & \text{if cell } s \text{ is inside coarser cell } t, \\ 0 & \text{otherwise.} \end{cases} \tag{6.6}$$

On the other hand, the pressure and saturation blocks of the prolongation operator, $(\mathbf{P}_p)_{l-1}^{l}$ and $(\mathbf{P}_S)_{l-1}^{l}$ are different [84] as different interpolation rules are used for each variable. In this work $(\mathbf{P}_S)_{l-1}^{l} = \left[\mathbf{R}_{l}^{l-1}\right]^{T}$, where the superscript T indicates the transpose operator. The $(\mathbf{P}_p)_{l-1}^{l}$ blocks, instead, are constructed following a multilevel multiscale procedure for fractured media described in section 5.3.2. The ADM method allows for full flexibility in the choice of the coupling strategies at all multilevel multiscale resolutions. In the mathematical description of the multilevel multiscale prolongation operator above (6.4), the extracted pressure prolongation operators can also be written as

$$(\mathbf{P}_p)_{l-1}^{l} = \left[\left((\mathbf{P}_p)_{l-1}^{l}\right)^{m} \quad \left((\mathbf{P}_p)_{l-1}^{l}\right)^{f}\right] = \begin{bmatrix} \left((\mathbf{P}_p)_{l-1}^{l}\right)^{m,m} & \left((\mathbf{P}_p)_{l-1}^{l}\right)^{m,f} \\ \left((\mathbf{P}_p)_{l-1}^{l}\right)^{f,m} & \left((\mathbf{P}_p)_{l-1}^{l}\right)^{f,f} \end{bmatrix} . \tag{6.7}$$

Here, the blocks $\left((\mathbf{P}_p)_{l-1}^{l}\right)^{m}$ and $\left((\mathbf{P}_p)_{l-1}^{l}\right)^{f}$ contain the basis functions corresponding to the rock matrix and the fracture coarse-scale unknowns. Each one, e.g., $\left((\mathbf{P}_p)_{l-1}^{l}\right)^{m}$, can have non-zero values inside the rock matrix and the fracture sub-domains, depending on the local coupling strategy. More precisely, while the fully-coupled approach leads to non-zero sub-blocks of $\left((\mathbf{P}_p)_{l-1}^{l}\right)^{m,f}$ and $\left((\mathbf{P}_p)_{l-1}^{l}\right)^{f,m}$, the decoupled approach would lead to zero values in these local coupling sub-blocks. Figure 5.15 from section

5.3.2 shows some of the rock matrix and the fracture basis functions at two different coarsening levels for a 2D domain. The description of the multilevel multiscale basis functions is available in the mentioned section in the previous chapter. Moreover, a detailed explanation of the multiscale basis function entries on various coupling strategies can be found in [81].

6.2. SELECTION OF THE GRID RESOLUTION

The fine-scale grid resolution is mapped into the ADM grid resolution using the ADM operators. This dynamic grid resolution is obtained by a user-defined grid selection criterion as a front tracking technique. At each time-step, the ADM grid is constructed by combining grid cells of the previously defined sets of the grids both in the rock matrix and in the fractures at various fine-scale and coarsening levels. Figure 6.2 shows an example of a 3D test case with one fracture plane, for simplicity of the illustration. On top of the fine-scale grid resolution, two coarse levels are employed in the rock matrix along with one coarse level in the fracture. The grid selection method is applied independently in the rock matrix and in the fractures, therefore, different criteria can be set for each medium. Since no well-functions are employed in the dynamic simulations, fine-scale resolution is kept around all the wells at all time.

The grid resolution at time-step $n+1$ is chosen based on the saturation map at time-step n, thus employing an explicit procedure. A semi-implicit gridding strategy [143] could also be used to avoid the misplacement of the grid. The selection of the grid resolution is done using a threshold set as the input parameter for the grid selection criterion. The condition for which the criterion is considered, compares the differences of the values of a main unknown (in this case, the saturation of the injecting phase, phase 1) between neighboring cells and the grid cells in a coarse node (spatial gradient of the unknown) [84]. Let Ω_l^I and Ω_l^J be the set of two neighboring coarse grid cells I and J at coarsening level l. The indices of fine-scale grid cells belonging to the coarse grid cells Ω_l^I and Ω_l^J are indicated by i and j respectively. The saturation differences $\Delta\bar{S}_{IJ}$ are obtained as

$$\Delta\bar{S}_{IJ} = max\big(|S_i - S_j|\big) \quad \forall\, i \in \Omega_l^I \text{ and } \forall\, j \in \Omega_l^J. \tag{6.8}$$

The coarse grid block I is refined from coarsening level l to level $l-1$ if the condition

$$\Delta\bar{S}_{IN} > \text{tol} \tag{6.9}$$

holds. Here, N refers to all the coarse grid cells neighboring the coarse grid cell I (at coarsening level l). Figure 6.3 shows a more detailed example of a 3D domain including one fracture with two coarsening levels over the rock matrix and one coarsening level over the fracture. Please note the independent coarsening strategy and grid selection procedure for the matrix and the fracture. It can be realized that the moving front of the flooding fluid will be captured with higher resolution as it corresponds to a sharper gradients. Moreover, as mentioned above, the grid cells around the wells are always kept at fine-scale resolution to guarantee accurate capture of the source term fluxes.

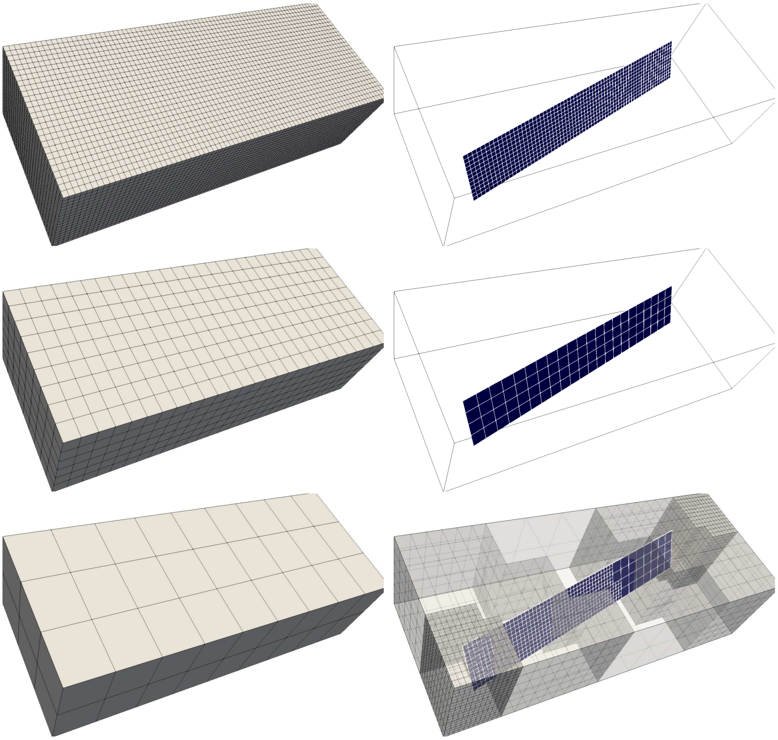

Figure 6.2: Example of the ADM grid selection for a 3D test case with one single planar fracture. Two coarse levels are used in the rock matrix ($l = 1, 2$) and one coarse level is used in the fracture ($l = 1$). The bottom right figure shows an example of a dynamic grid.

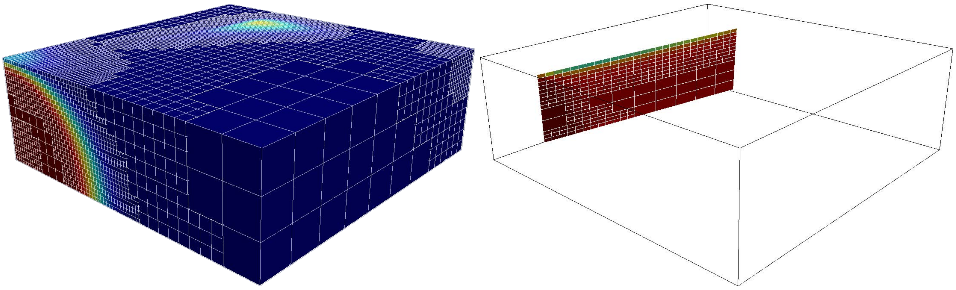

(a) ADM grid on matrix

(b) ADM grid on fracture

Figure 6.3: Example of an ADM grid for a 3D domain with one fracture plane at a specific time-step during the simulation. Two coarsening levels are employed for the rock matrix and one coarsening level is used in the fracture. Here, the moving front of the fluid is captured at the fine-scale resolution.

6.3. ADM METHOD VS. UPSCALING (HOMOGENIZATION)

In general, model order reduction techniques have been developed to reduce the degrees of freedom (DoF) and provide meaningful approximate simulation framework, in the sense that they are fast to be obtained for large-scale computational domains. Note that any advanced method of this type becomes field applicable only when it allows for error reduction to any desired threshold value [144].

Within the model order reduction techniques, two promising developments for next-generation simulators are multiscale [55, 118] and homogenization [145] methods.

These approaches are different in the sense that the multiscale method deals with crossing the solution, e.g. the pressure, across the scales [58, 60, 146, 147], while the latter (homogenization) aims at the development of effective lower-resolution parameters, e.g. permeability or transmissibility, [148–150]. Moreover, multiscale basis functions have been formulated purely algebraically [79], while the same does not hold for homogenized and other parameter-based upscaling, e.g., flow-based upscaling. Specially the integration of homogenized parameters within the fully implicit framework in an algebraic manner has not yet been developed so far. The developments of this work include this achievement too.

Both methods, at the same time, have many similarities. Both find their mapping strategy via local solutions of the original governing equations with local boundary conditions. Multiscale basis functions often times employ reduced-dimensional boundary conditions [63, 125], and the homogenization schemes employ periodic boundary conditions [151–153]. Both methods are effective for global equations within the fully coupled system of local-global unknowns, e.g. global pressure and local saturation. Both have been extended to nonlinear and geologically complex models [45, 154, 155]. Recent developments of these two classes of approaches have introduced a fully-implicit dynamic multilevel simulation framework (ADM) in which heterogeneous detailed geo-models are mapped into adaptive dynamic coarser mesh [72, 85].

The ADM method develops a fully-implicit discrete system for coupled flow and transport equations in which each equation can be represented at a different resolution than the defined fine-scale one. More importantly, the procedure can be done fully algebraically based on an error threshold. In contrast to the rich existing literature on Adaptive Mesh Refinement (AMR) methods [64, 66, 73–76], ADM can be defined as an adaptive mesh coarsening strategy which is automatically applicable to heterogeneous and coupled systems [84].

Irrespective of the choice of the dynamic mesh strategy, it is always a challenge to construct adaptive multiscale entries of the implicit systems.
The ADM method so far has included multiscale basis functions [84]. Following the ADM development, homogenization methods have been also developed for dynamic grids [154, 156]. Of great interest to the scientific community is the investigation of the homogenization-based coarser system entries and a benchmark study of the quality of the two approaches of ADM-multiscale (ADM-MS) and ADM-homogenized (ADM-HO) for coupled implicit multiphase flow scenarios.

In this section, as a unified framework, the ADM method is extended to account for both multiscale and homogenization schemes for multiphase flow simulations. This development makes it possible to allow for different coarse-scale entries for dynamic simulations, and importantly to benchmark the two classes of multiscale and homogenization strategies. Once the effective parameters are computed, all other homogenization procedures are implemented algebraically. This is done by introducing constant unity local basis functions, with the support of the primal (non-overlapping) coarse-scale partitions. The multiscale ADM is implemented fully algebraically since the local basis functions are also solved algebraically over the overlapping (dual) coarse grid domains.

6.3.1. ADM using multiscale (ADM-MS)

In the ADM method using the multiscale approach (ADM-MS), as explained in the previous section, the prolongation operator for the pressure is found based on multiscale basis functions. These local basis functions are computed algebraically [79], based on the pressure equation. In this study, the incompressible flow equation (elliptic pressure equation) is used to construct the multiscale basis functions [125]. An example of a basis function is shown in 6.4 (also see section 5.2.1 and figure 5.4).

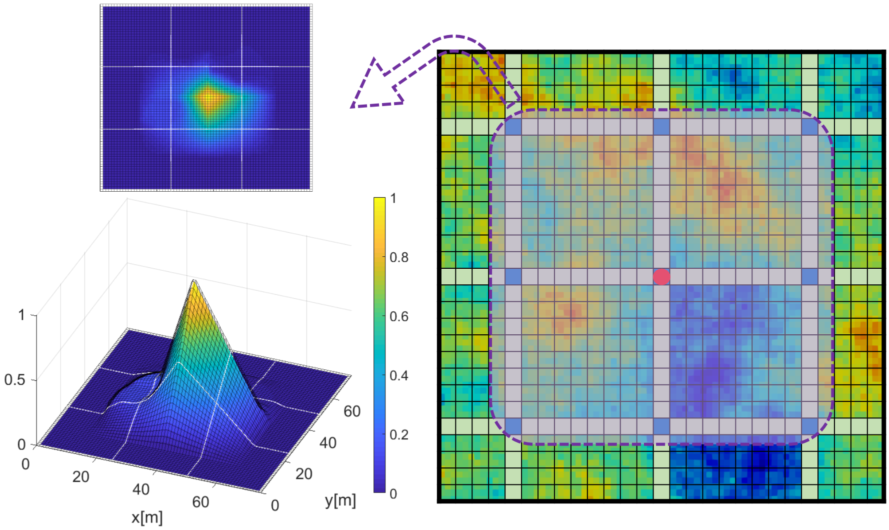

Figure 6.4: An example of a basis function belonging to the middle coarse node of a heterogeneous 2D domain.

6.3.2. ADM using homogenization (ADM-HO)

The homogenization method can be used to construct effective properties at the dynamic multilevel mesh. The effective properties at multilevel mesh are found (similar to in ADM-MS) by solving local flow (pressure) equations based on an incompressible (elliptic) equation.

To develop an ADM-HO system, a scale separation is assumed. Further, by doubling the spatial variable into a fast and a slow one, one assumes that all quantities in the mass balance equation satisfy the *homogenization ansatz* theory, namely that they can be expanded regularly in terms of the scale separation parameter and they are locally periodic w.r.t. the fast variable. The theoretical details can be found in the literature, i.e., [151, 157, 158], and [154, 155, 159–162] where these ideas are used to develop effective numerical simulation schemes.

Given a fine-scale effective permeability K and for each coarsening level l an effective permeability tensor $\mathbf{K}^l$ is computed locally in a pre-process step. First the domain Ω is divided in coarse cells Ω_l that corresponds to a partition of the domain Ω as shown in figure 6.5.

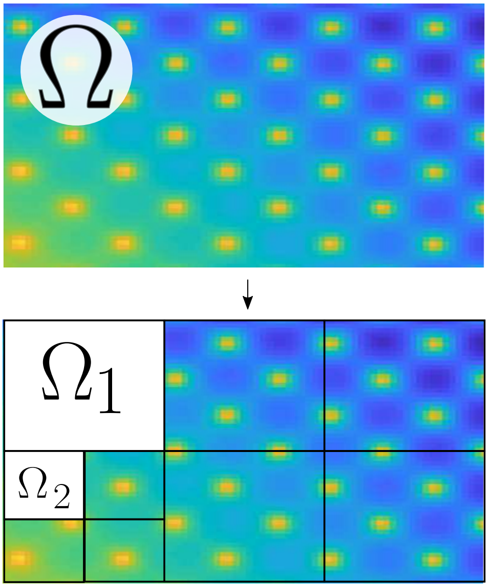

Figure 6.5: Sketch of the coarse partition of Ω.

For each coarse cell Ω_l and at level l the effective permeability is calculated as

$$\mathbf{K}^l_{i,j}\Big|_{\Omega_l} = \int_{\Omega_l} \left(K\left(\mathbf{e}_j + \nabla\omega^j\right)\right)\cdot \mathbf{e}_i \, d\mathbf{y}. \tag{6.10}$$

Here ω^j are the periodic solutions of the *micro-cell* equation, which can be expressed as

$$-\nabla\cdot\left(K\left(\nabla_y\omega^j+\mathbf{e}_j\right)\right)=0, \text{ for all } \mathbf{y}\in\Omega_l. \tag{6.11}$$

Here, $\{\mathbf{e}_j\}_{j=1}^d$ is the canonical basis of dimension d. To guarantee the uniqueness of the solution ω^j, next to its periodicity, one assumes that the average value over the cell Ω_l is 0.

To determine the value of the permeability tensor at each coarse cell Ω_l, two micro-cell problems (6.11) are solved for each spatial direction in 2D. 6.6 provides an illustration of these local solutions for a coarse element.

More details about the homogenization procedure can be found in [142]. Note that the local problems (6.11) capture the rapidly oscillating characteristics within a coarse

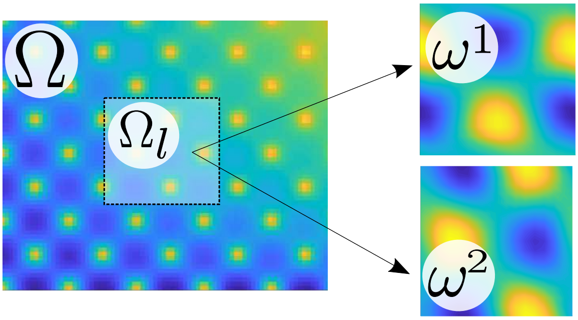

Figure 6.6: Example of the local solutions ω^1 (top right, for x-direction) and ω^2 (bottom right, for y-direction) for a coarse cell inside a 2D domain. The heterogeneous permeability field is also shown for the entire domain (left).

element, completely decoupled from other coarse elements. The homogenized parameters, like multiscale bases, are computed at the beginning of the simulation. Figure 6.7 illustrates the calculation of the effective permeability at different levels.

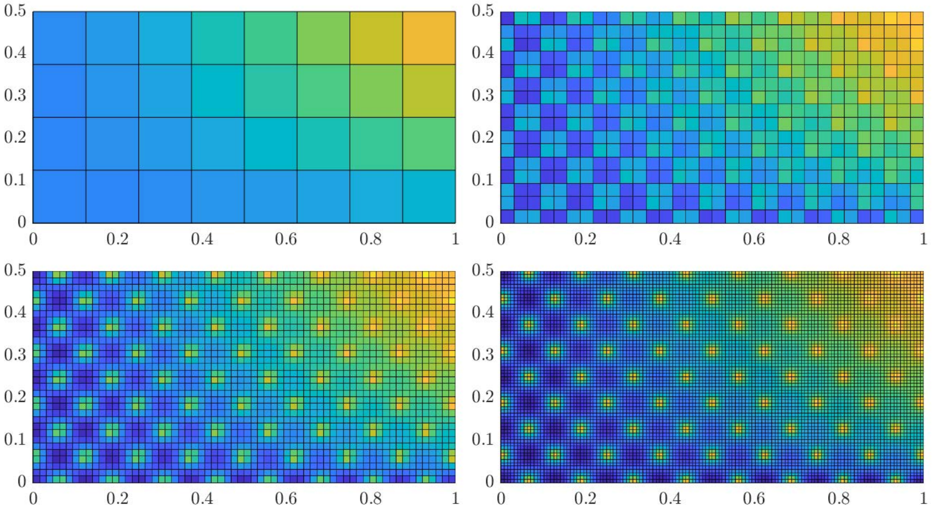

Figure 6.7: Example of four different levels of homogenized permeability values: fine scale (bottom right), coarse level 1 (bottom left), coarse level 2 (top right) and coarse level 3 (top left).

After this pre-process step, the homogenized parameters are used at each level and constant unity functions are employed to interpolate the coarse-scale solutions to the fine-scale ones. This is achieved by setting prolongation operators to unity. Finally, in figure 6.8, the ADM process combining the usage of either the fine-scale permeability or the upscaled permeability via homogenization technique is sketched. More details about the role of the homogenization in the offline stage and the complete algorithm of ADM-MS/ADM-HO can be found in the algorithm chart 1.

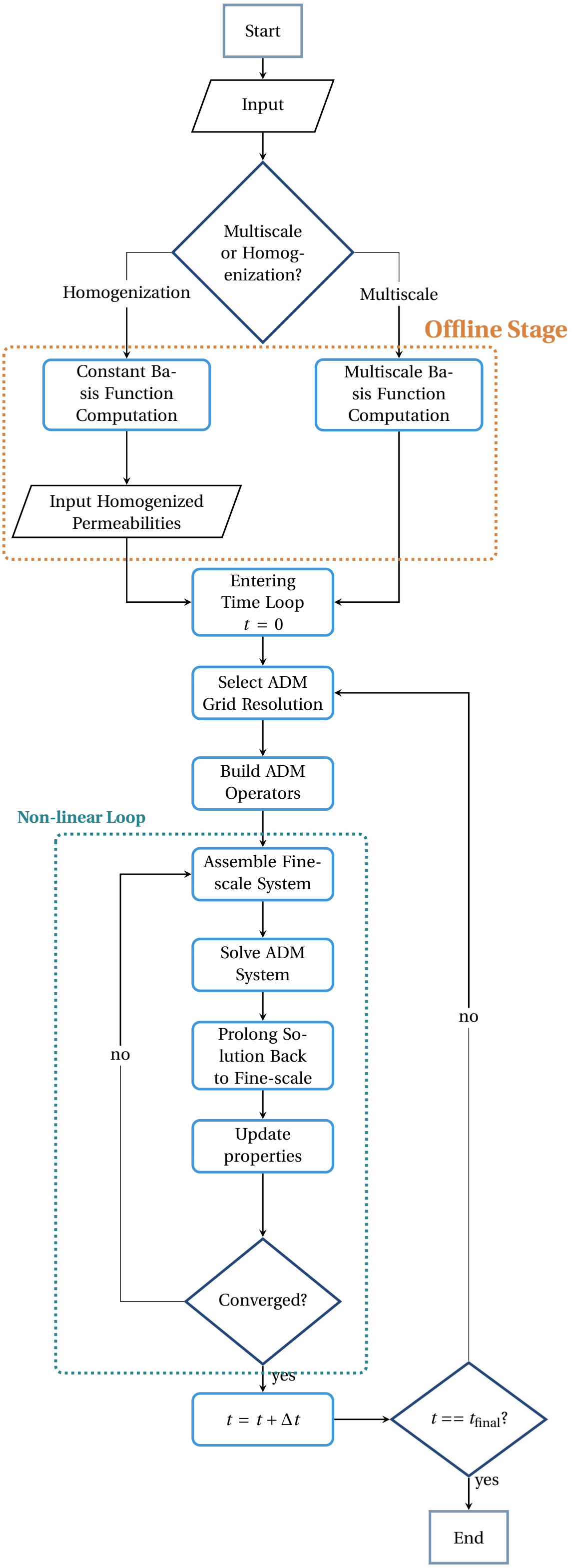

Figure 6.8: Schematic description of ADM method for the combination of the multiscale and homogenization techniques.

Algorithm 1: The ADM algorithm using multi-scale basis functions (ADM-MS) or homogenization (ADM-HO)

```
Given a fine scale $K$ and the number of levels $l$
if Homogenization then
    for $k = 0$ to $l$ do
        Compute the homogenized $\mathbf{K}^k$
    end
end
Compute the constant basis functions
for time step $t^n$ do
    Select ADM grid resolution
    Build ADM operators
    Take $i = 1$ and initialize pressure
    while error $\geq$ tolerance do
        Assemble fine scale system
        Solve the ADM system
        Prolong back to fine scale
        Next iteration $i = i + 1$
    end
    Next time step
end
```

In the section of the numerical results (6.4), the two test cases 6.4.4 and 6.4.5 compare the ADM results using multiscale basis functions and the homogenization technique.

6.4. RESULTS AND THE EVALUATION OF THE ADM METHOD

In this section, the numerical results of the ADM method for fractured porous media are presented. A number of homogeneous and heterogeneous 2D as well as 3D test cases are considered in which the accuracy and sensitivity of the ADM method are investigated. ADM results are compared against the fine-scale simulations, used as a reference. The error of the ADM results (compared to the fine-scale reference solution) is calculated as

$$e_x = \frac{|| x_{\mathrm{FS}} - x_{\mathrm{ADM}} ||_2}{|| x_{\mathrm{FS}} ||_2} \tag{6.12}$$

where, x is either the pressure or the saturation vector (the main unknowns) and the subscripts ADM and FS denote ADM and fine-scale, respectively. In all the test cases, the fluids and the rock are considered to be incompressible, and quadratic relative permeability functions are used.

Afterwards, to benchmark the homogenization and multiscale based solutions for a dynamic mesh on heterogeneous media, two heterogeneous non-periodic permeability fields from the top and bottom layers of the SPE 10th Comparative Solution Project [163] are considered. For both test cases, the computational domain entails 216 × 54 grid cells at fine-scale with $\Delta x = \Delta y = 1$[m]. No-flow condition is imposed on all boundaries. The reservoir initially contains oil and during the simulation water is injected from the injection well. Both fluids are assumed to be incompressible. Injection and production take place by introducing source terms (wells).

Table 6.1 shows the input parameters of the fluid and rock properties used in these test cases.

Table 6.1: Input parameters of the fluid and rock properties.

Property	value
Porosity (ϕ)	0.2
Water density (ρ_w)	1000 [Kg/m^3]
Oil density (ρ_o)	1000 [Kg/m^3]
Water viscosity (μ_w)	10^{-3} [Pa·s]
Oil viscosity (μ_o)	10^{-3} [Pa·s]
Initial pressure (p_0)	10^7 [Pa]
Connate water saturation (S_{wc})	0 [-]
Residual oil saturation (S_{or})	0 [-]
Injection pressure (p_{inj})	2×10^7 [Pa]
Production pressure (p_{prod})	0 [Pa]

Numerical results of the ADM-MS and ADM-HO methods will be compared to those obtained from fine-scale reference permeability simulations. Both ADM methods employ the coarsening ratio of 3×3 with two coarsening levels. This is set due to the size of the domain.

6.4.1. Test case 1: 2D homogeneous fractured reservoir

A 2D fractured 75 [m] × 75 [m] reservoir with 35 fractures is considered. The rock matrix is discretized with a 135×135 fine-scale grid, and 1665 grid cells are imposed on the fractures (total domain grid cells: 19890). The ADM method employs 2 coarse levels with coarsening ratio of 3 in each direction both for the rock matrix and the fractures. Both decoupled and fully-coupled multiscale basis functions are considered as pressure interpolators. The saturation difference between neighboring cells is used as the ADM coarsening criterion with four different threshold values: $\Delta S = \{0.1, 0.3, 0.5, 0.8\}$. Three equidistant injection wells ($p_{\text{inj}} = 2 \times 10^7$ [Pa]) and three equidistant production wells ($p_{\text{prod}} = 1 \times 10^7$ [Pa]) are present at the left and the right boundaries, respectively. The total simulation time is set to 1000 days.

Figures 6.9 and 6.10 show the pressure and the saturation maps at the end of the simulation for the results of the fine-scale simulation and the ADM simulations with 2 different threshold values of $\Delta S = \{0.1, 0.8\}$.

Figures 6.11a,6.11b and 6.11c,6.11d show the ADM pressure and saturation errors (both using decoupled and coupled basis functions) at each time-step for the four values of the coarsening criterion. Figures 6.12a and 6.12b illustrate the amount of active grid cells (as a percentage of the number of the fine-scale grid cells) for each time-steps. Note that the grid cells around the wells are always kept at the fine-scale resolution. Here, 864 grid cells are kept at the fine-scale resolution due to near-well refinement, which is 4.74 percent out of the 8.61 percent of the active grid cells at the first time-step. Figures 6.12c and 6.12d provide the average pressure and saturation errors along with the average per-

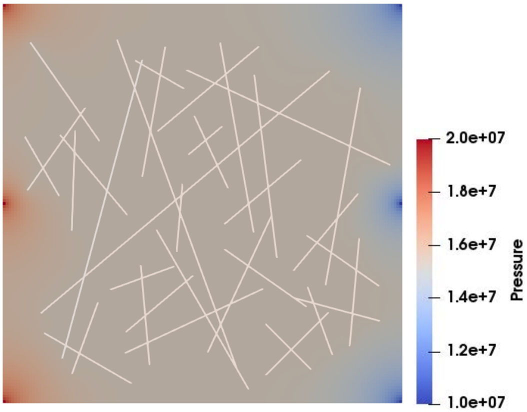

(a) Fine-scale

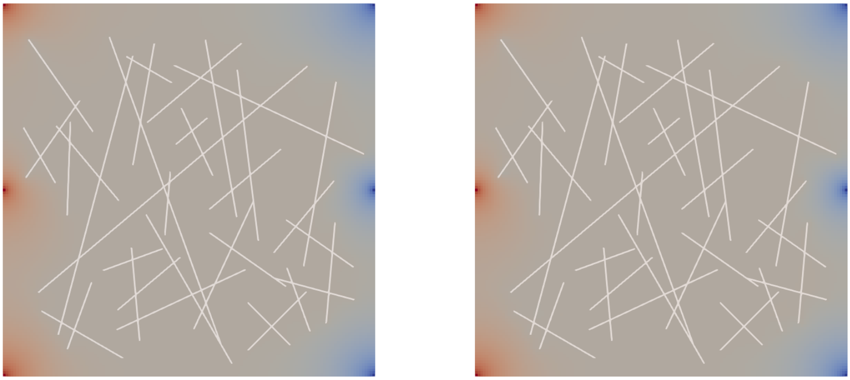

(b) Tol(ΔS) = 0.1, active grid cells = 53.2%, $err_p = 1.88 \times 10^{-4}$

(c) Tol(ΔS) = 0.8, active grid cells = 9.5%, $err_p = 3.25 \times 10^{-3}$

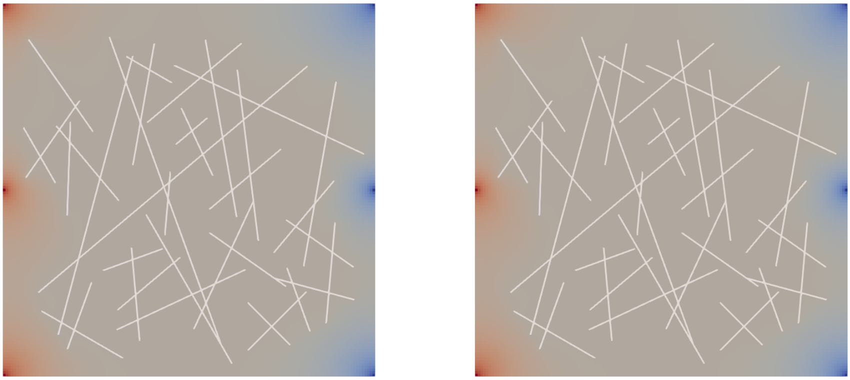

(d) Tol(ΔS) = 0.1, active grid cells = 52.4%, $err_p = 3.49 \times 10^{-4}$

(e) Tol(ΔS) = 0.8, active grid cells = 10.0%, $err_p = 2.28 \times 10^{-3}$

Figure 6.9: Test case 1: The pressure plots. The plot 6.9a shows the fine-scale pressure solution. The plots 6.9b and 6.9c visualize the ADM results with thresholds 0.1 and 0.8 using decoupled basis functions. And ADM solutions with thresholds 0.1 and 0.8 using fully coupled basis functions are illustrated on the plots 6.9d and 6.9e, respectively.

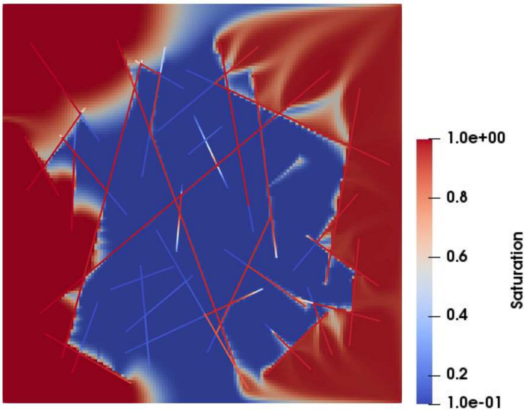

(a) Fine-scale

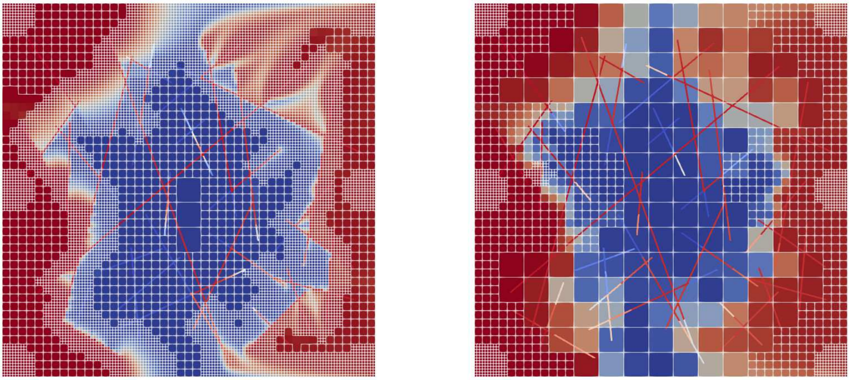

(b) Tol(ΔS) = 0.1, active grid cells = 53.2%, $err_S = 5.76 \times 10^{-2}$

(c) Tol(ΔS) = 0.8, active grid cells = 9.5%, $err_S = 2.92 \times 10^{-1}$

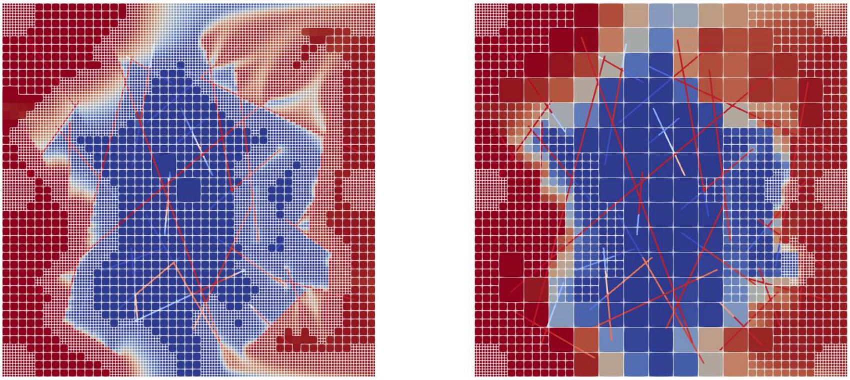

(d) Tol(ΔS) = 0.1, active grid cells = 52.4%, $err_S = 9.14 \times 10^{-2}$

(e) Tol(ΔS) = 0.8, active grid cells = 10.0%, $err_S = 2.29 \times 10^{-1}$

Figure 6.10: Test case 1: The water (injecting phase) saturation results. The plot 6.10a contains the fine-scale saturation result. The plots 6.10b and 6.10c show the ADM results with thresholds 0.1 and 0.8 using the decoupled basis functions. And the ADM solutions with thresholds 0.1 and 0.8 using fully coupled basis functions are illustrated on the plots 6.10d and 6.10e, respectively.

centage of the grid cells employed by the ADM method as functions of the coarsening criterion threshold values.

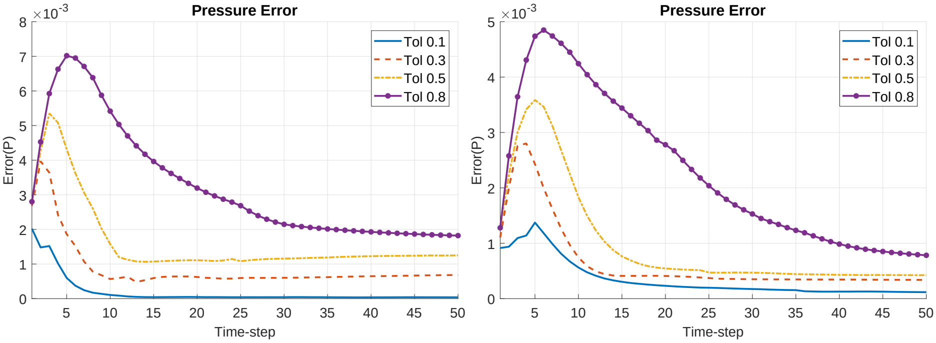

(a) Pressure errors, using the decoupled basis functions (b) Pressure errors, using the fully coupled basis functions

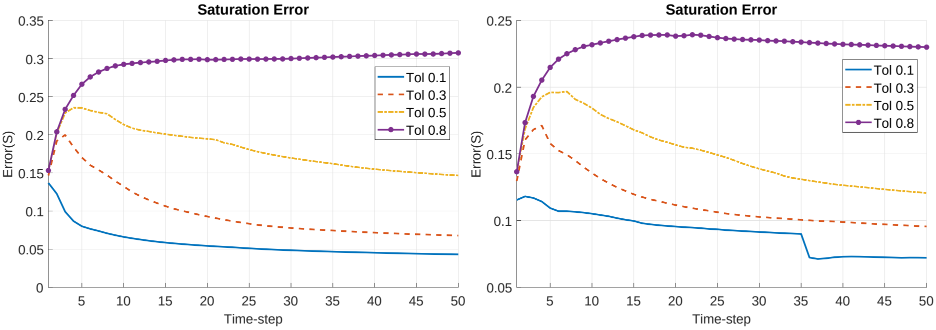

(c) Saturation errors, using the decoupled basis functions (d) Saturation errors, using the fully coupled basis functions

Figure 6.11: Test case 1: The pressure and the saturation errors. Figures 6.11a and 6.11b show the pressure errors for simulations with decoupled and fully coupled basis functions respectively. The data is obtained over simulation time-steps and for four different ADM tolerances. Figures 6.11c and 6.11d illustrated the saturation errors versus the simulation time-steps for both decoupled basis functions and the fully coupled basis functions.

ADM results in this test case show a low sensitivity to the type of the basis functions employed. Note that the fully coupled basis functions are more computationally expensive and provide a denser prolongation operator. However, in case of using static prolongation operators, as the basis functions of all levels are computed only once at the beginning of the simulation, the extra computational costs involved in the calculation of the fully coupled basis functions can be considered negligible. In this test case, the saturation plots (see figure 6.10) highlight a considerable by-pass of injection fluid due to presence of the highly conductive fractures, resulting in an inefficient sweep of the reservoir fluid (second phase) in the middle of the domain.

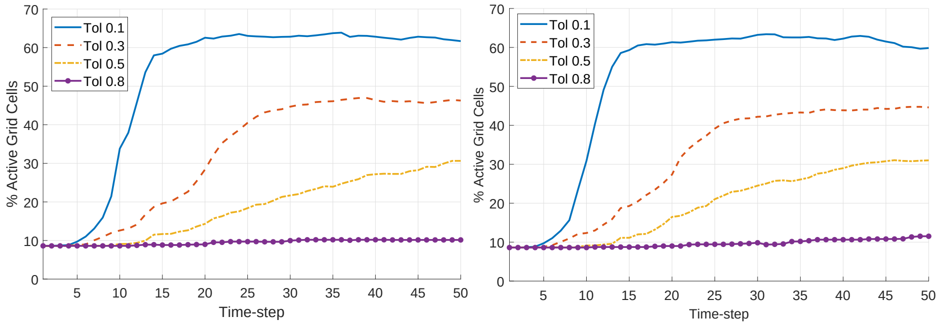

(a) Active grid cells, using the decoupled basis functions (b) Active grid cells, using the fully coupled basis functions

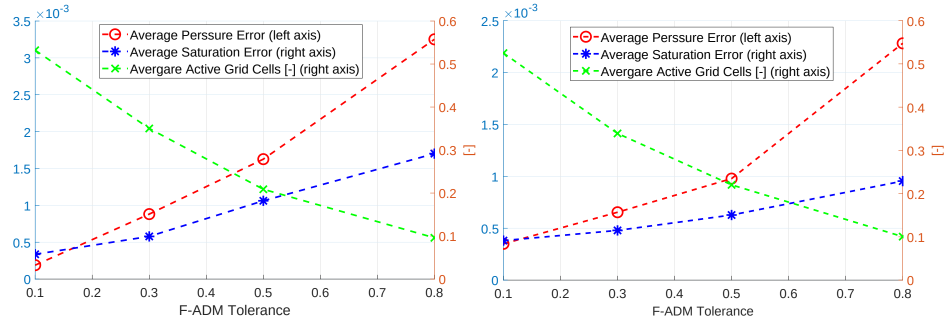

(c) Average values, using the decoupled basis functions (d) Average values, using the fully coupled basis functions

Figure 6.12: Test case 1: The percentage of the active grid cells and the averaged errors. Figures 6.12a and 6.12b demonstrate the percentage of the active grid cells for the two mentioned approaches respectively. The data is obtained over simulation time-steps and for four different ADM tolerances. Figures 6.12c and 6.12d show the average of the pressure error, the saturation error and the percentage of the active grid cells over the whole simulation time for both approaches.

6.4.2. TEST CASE 2: 2D HETEROGENEOUS FRACTURED RESERVOIR

This test case differs from the test case 1 only in the permeability of the rock matrix as it is heterogeneous. The rest of the input parameters and configurations are identical to test case 1. The permeability map has a heterogeneity contrast of 7.7×10^3 with minimum and maximum permeability values of 1.3×10^{-16} [m^2] and 9.9×10^{-13} [m^2], respectively. The well positioning follows the same configuration (line drive with 3 equidistant injectors and producers). Moreover, the coarsening level, the coarsening ratios and the coarsening criteria are identical to the previous test case. As for their similar performance to the decoupled approach, only the results of the simulation using the fully coupled basis functions are presented.

6.4.3. TEST CASE 3: 3D HOMOGENEOUS FRACTURED RESERVOIR

For this test case, a 3D 75 [m] × 75 [m] × 30 [m] homogeneous domain containing 26 fracture planes of different geometrical properties is considered, as shown in figure 6.16. A $99 \times 99 \times 27$ Cartesian grid is imposed on the rock matrix with a total of 264,627 grid cells. Independent 2D grids are imposed on each fracture plane. The grid cells in the fractures have sizes $\Delta\xi$ and $\Delta\eta$ such that $\text{mean}(\Delta\xi, \Delta\eta) = 2 \times \text{mean}(\Delta x_m, \Delta y_m, \Delta z_m)$. Here, $\Delta x_m, \Delta y_m, \Delta z_m$ indicate the sizes of the matrix grid cells in each direction. The total number of grid cells in the fracture network is 2,646 grid cells. The rock matrix permeability is 10^{-14} [m^2] whereas the fracture permeability is 2.08×10^{-6} [m^2]. Three injection wells are present at the bottom left, middle left and the top left boundary, all perforated over the whole thickness of the reservoir ($p_{\text{inj}} = 2 \times 10^7$ [Pa]). Similarly three production wells are located at the right-hand side of the domain ($p_{\text{prod}} = 1 \times 10^7$ [Pa] Pa). The simulation is run for 1000 days.

The ADM method employs 2 levels of coarsening with coarsening ratios $\gamma = 3$ in each direction. Figure 6.17 shows, for instance, the saturation distribution at time-step 15 along with the ADM grid employed at that time-step.

An identical error measures used for the previous test cases are conducted in this test case as well. Figures 6.18a and 6.18b present the pressure and the saturation errors at each time-step for four different threshold values of the coarsening criterion, i.e. 0.1, 0.3, 0.5 and 0.8. The evolution of the number of the active grid cells throughout the ADM simulations is shown in figure 6.18c. Average of all the pressure errors, saturation errors and active grid cells over the whole simulation time versus ΔS thresholds are given in figure 6.18d. In this test case, 23,328 grid cells near the wells are kept at fine-scale resolution that is 8.73 percent out of 10.51 percent of the active grid cells at the first time step. An increase in the grid section threshold (ΔS) correlates with a decrease in size of the ADM system as less active grid cells are used.

6.4.4. TEST CASE 4: ADM-MS AND ADM-HO ON SPE10 TOP LAYER

In this test case, the SPE10 top layer is considered. A 216×54 grid cells mesh at fine-scale is imposed on the 2D domain. The minimum and the maximum values of the heterogeneous permeability map are $K_{min} = 3.0 \times 10^{-18}$[m^2] and $K_{max} = 4.6 \times 10^{-12}$[m^2] respectively. The permeability distribution of the SPE10 top layer is shown in 6.19. One injection well and one production well are placed in the bottom left corner and top right corner of the domain. The simulation time is $t = 1000$ [days] and the results are reported

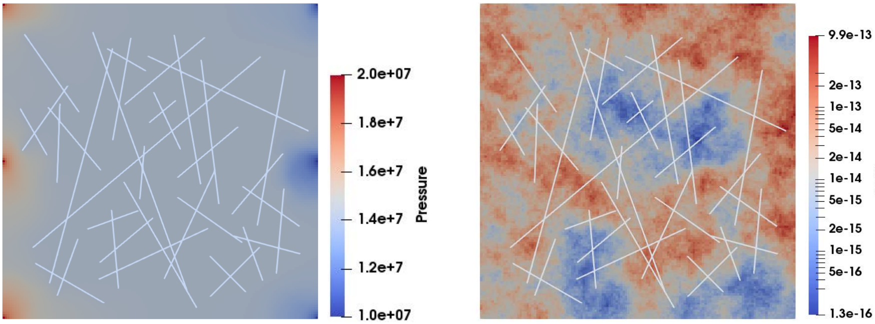

(a) Fine-scale Pressure

(b) Permeability

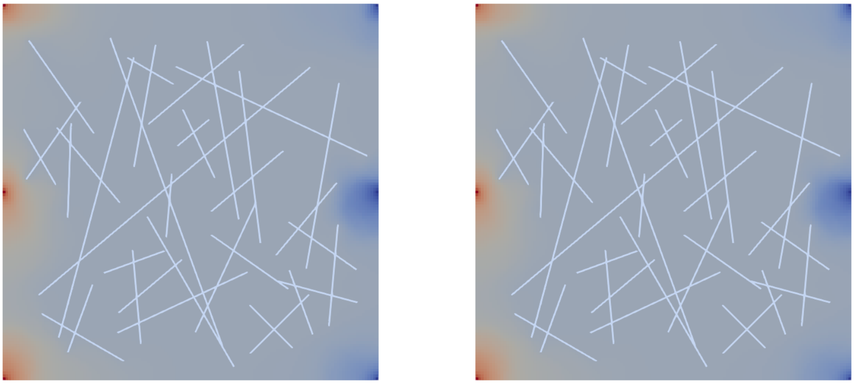

(c) Tol(ΔS) = 0.1, active grid cells = 55.7%, $err_p = 5.30 \times 10^{-5}$

(d) Tol(ΔS) = 0.3, active grid cells = 41.4%, $err_p = 1.96 \times 10^{-4}$

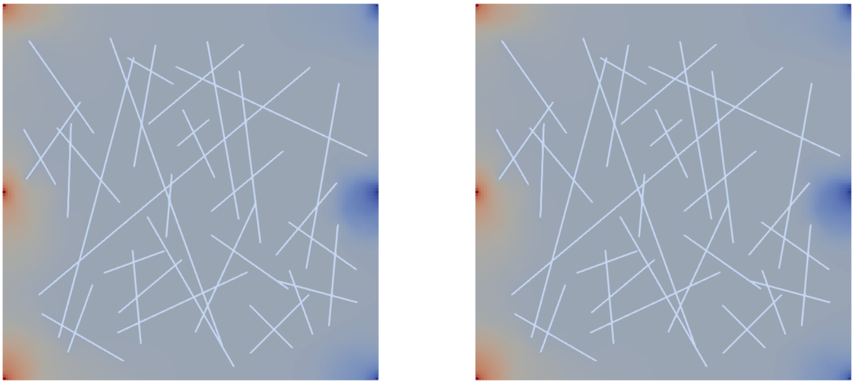

(e) Tol(ΔS) = 0.5, active grid cells = 30.4%, $err_p = 5.86 \times 10^{-4}$

(f) Tol(ΔS) = 0.8, active grid cells = 13.5%, $err_p = 9.42 \times 10^{-4}$

Figure 6.13: Test case 2: The permeability and the pressure plots. The plot 6.13b shows the permeability distribution in the domain. The plot 6.13a is the fine-scale pressure solution. The plots 6.13c, 6.13d, 6.13e and 6.13f visualize the ADM results with thresholds (Tol(ΔS)) of 0.1 and 0.3, 0.5 and 0.8 respectively.

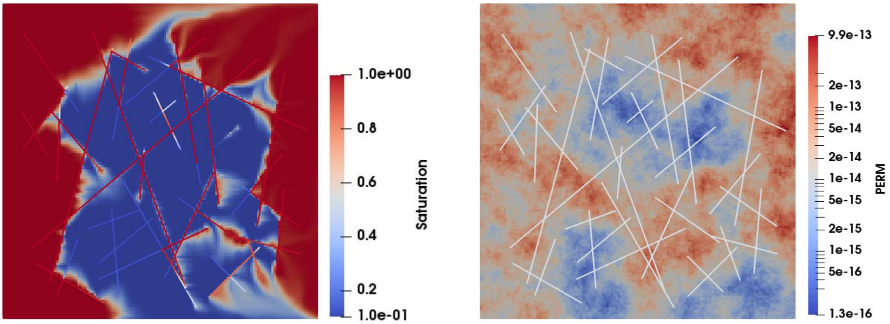

(a) Fine-scale Saturation

(b) Permeability

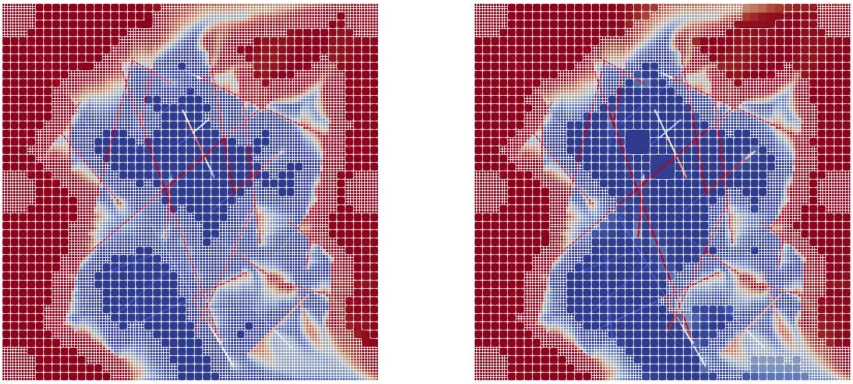

(c) Tol(ΔS) = 0.1, active grid cells = 55.7%, $err_S = 4.30 \times 10^{-2}$

(d) Tol(ΔS) = 0.3, active grid cells = 41.4%, $err_S = 6.24 \times 10^{-2}$

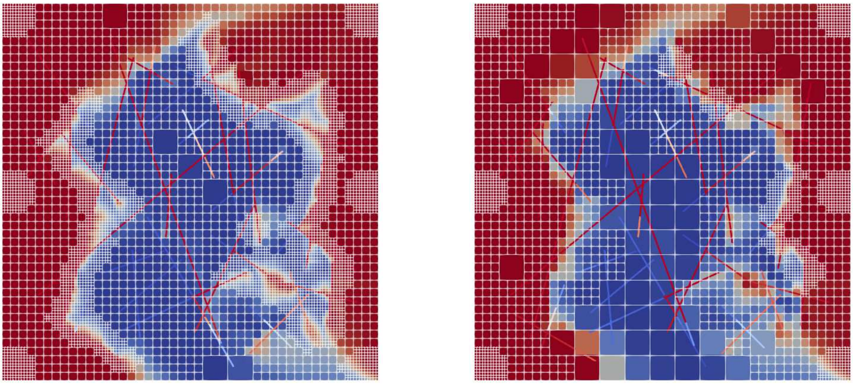

(e) Tol(ΔS) = 0.5, active grid cells = 30.4%, $err_S = 9.54 \times 10^{-2}$

(f) Tol(ΔS) = 0.8, active grid cells = 13.5%, $err_S = 1.93 \times 10^{-1}$

Figure 6.14: Test case 2: The saturation plots. The plot 6.14a shows the fine-scale saturation solution. The plots 6.14c, 6.14d, 6.14e and 6.14f are the ADM results with thresholds (Tol(ΔS)) of 0.1 and 0.3, 0.5 and 0.8 respectively.

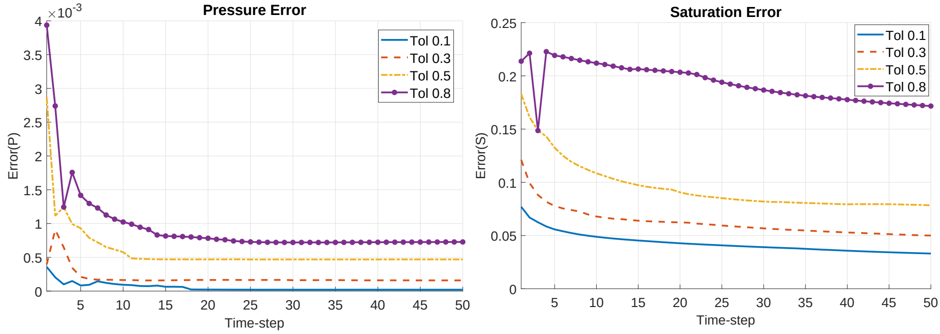

(a) Pressure errors

(b) Saturation errors

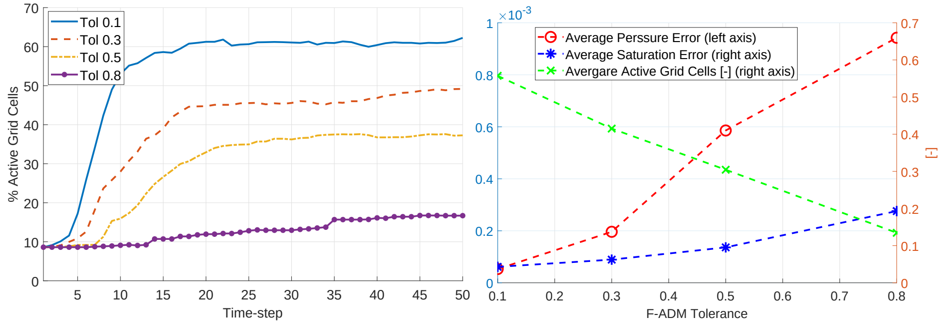

(c) Active grid cells

(d) Average values over the entire simulation time

Figure 6.15: Test case 2: The error history of the ADM pressure and the ADM saturation results versus the simulation time can be seen on figures 6.15a and 6.15b respectively. Figure 6.15c shows the changes in the percentage of active grid cells (compared with the number of fine-scale grid cells) versus simulation time for four different ADM grid selection criteria. All these data is averaged over the entire simulation time and is presented in figure 6.15d versus the ADM grid selection tolerance.

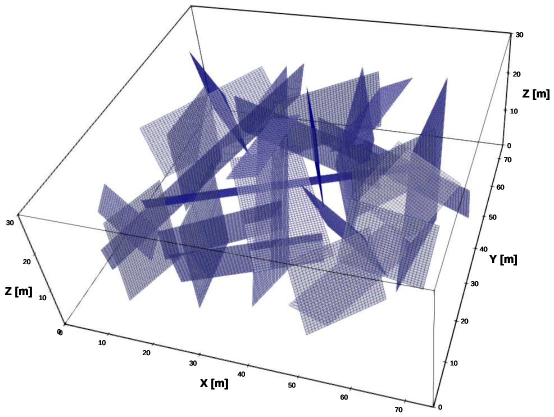

Figure 6.16: Test Case 3: The reservoir geometry and the fracture network.

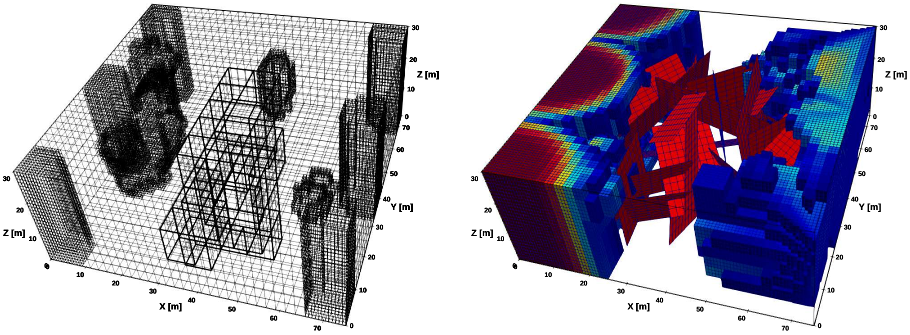

Figure 6.17: Test Case 3: illustration of the ADM mesh at time-step 15 (left) and saturation distribution (right). Only saturation values higher than 0.5 are shown (right).

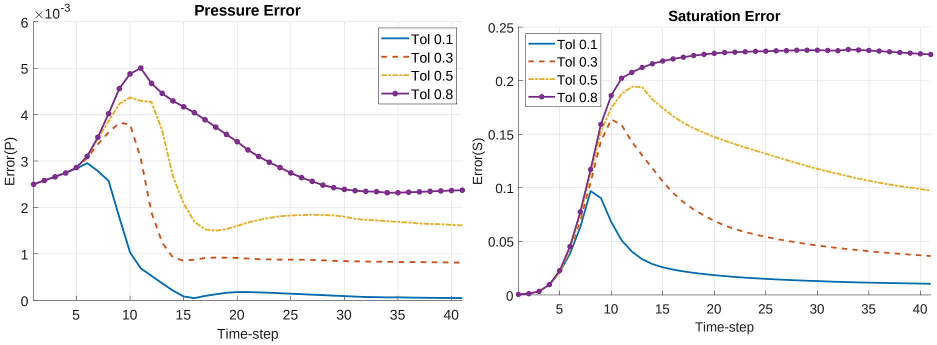

(a) Pressure errors

(b) Saturation errors

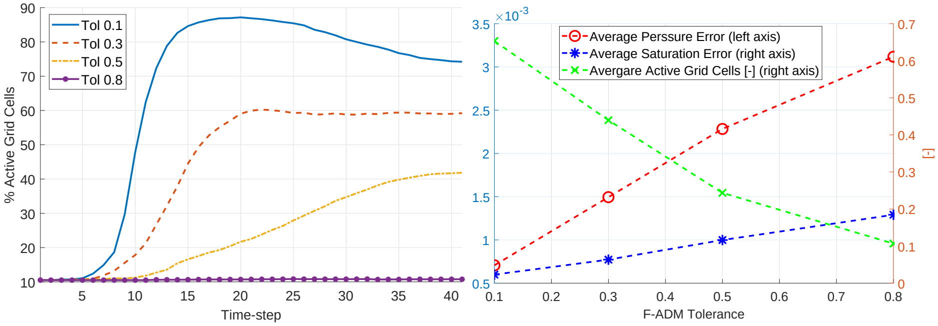

(c) Active grid cells

(d) Average values over the entire simulation time

Figure 6.18: Test case 3: The ADM pressure and the ADM saturation errors versus the simulation time can be viewed in figures 6.18a and 6.18b respectively. Figure 6.18c visualizes the changes in the percentage of active grid cells (compared with the number of fine-scale grid cells) versus simulation time. All the data is then averaged over the entire simulation time and is presented in figure 6.18d versus the ADM grid selection tolerance.

on 100 equidistant time intervals.

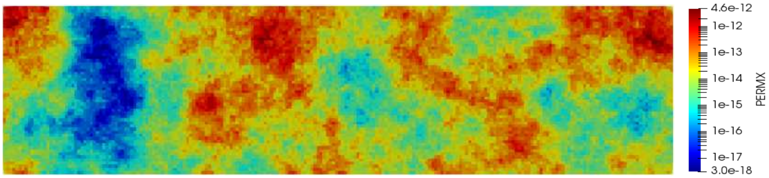

Figure 6.19: Test case 4: Fine-scale permeability (Log_{10} scale) of the SPE10 top layer dataset.

Figure 6.20 shows the homogenized version of the permeability at 2 different coarsening levels. It is noteworthy to mention that the homogenized permeability at both coarse levels preserve the structure of the original fine-scale permeability. The high and low permeable zones remain clearly detectable.

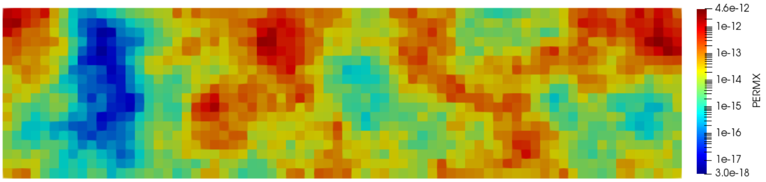

(a) Coarse level 1 with 72 × 18 cells.

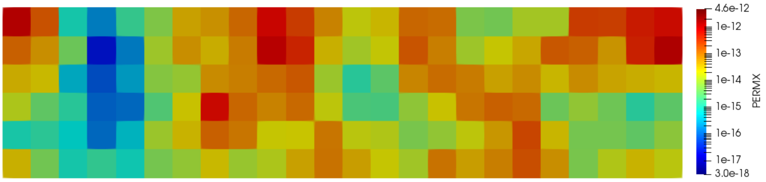

(b) Coarse level 2 with 24 × 6 cells.

Figure 6.20: Test case 4: Homogenized permeability of the top layer of the SPE10 for two coarsening levels coarsening ratio $\gamma_x \times \gamma_y = 3 \times 3$.

The saturation and pressure results of the fine-scale, ADM-MS and ADM-MS methods at the final time step are shown in figure 6.21. Numerical results of ADM-MS and ADM-HO methods are both compared with the fine-scale result as reference solution. In the homogenized approach, by using an effective homogenized parameter for a coarse cell with high and low permeable fine cells higher flow leakage can be seen when compared to fine-scale and multiscale-based approaches. This effect can be seen in figure 6.20, in the saturation results of the ADM-HO method. Moreover, figure 6.22 illustrates the adaptive mesh at 2000 days after injection. Notice that the refinement of the permeability is most dominant at the saturation front, due to the chosen mesh refinement criterion. For this figure, the grid resolution selection threshold value is $\Delta S = 0.3$, i.e., a cell is successively coarsened if ΔS is lower than 0.3.

The pressure and saturation error history maps for the ADM-MS and the ADM-HO

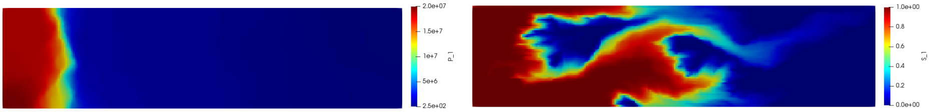

(a) Fine-scale pressure (b) Fine-scale saturation

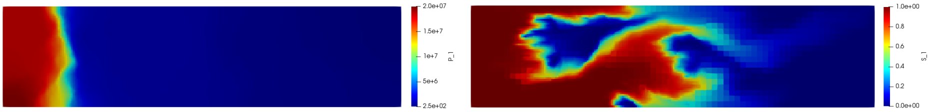

(c) ADM multiscale pressure (d) ADM multiscale saturation

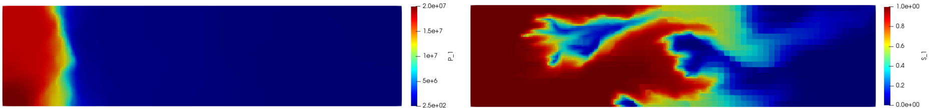

(e) ADM homogenized pressure (f) ADM homogenized saturation

Figure 6.21: Test case 4: Pressure and saturation results of the fine-scale (top row), the multiscale-based ADM method (middle row) and the homogenized-based ADM method.

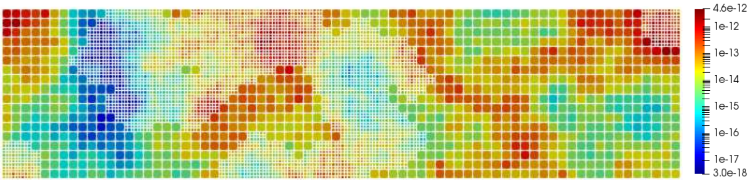

Figure 6.22: Test case 4: Adaptive mesh and homogenized permeability for the SPE10 top layer test case. The threshold value for the front tracking criterion is $\Delta S = 0.3$.

methods are computed and shown in figures 6.23a and 6.23b respectively. These relative errors, are calculated using equation (6.12). Moreover, figure 6.23c illustrates the percentage of the active grid cells (compared to all the fine-scale grid cells) employed during the simulation time. Finally, these quantities are averaged over the entire simulation time and presented in figure 6.23d versus the ADM grid selection criterion for three threshold values of $\Delta S = \{0.1, 0.3, 0.5\}$.

The results indicate that the homogenization-based simulations have higher errors compared with the multiscale-based simulations. They both have similar average usage of active grid cells, with ADM-MS having slightly fewer grid cells. This is shown in figure 6.23c. Note that the grid cells around the wells are kept at the fine-scale resolution permanently. Furthermore, for tighter error tolerance values, the quality of both approaches become comparable.

6.4.5. TEST CASE 5: ADM-MS AND ADM-HO ON SPE10 BOTTOM LAYER

In this test case, the SPE10 bottom layer model is used as the test domain. Similar to the previous test case, a 216×54 grid cells mesh at fine-scale is imposed. The perme-

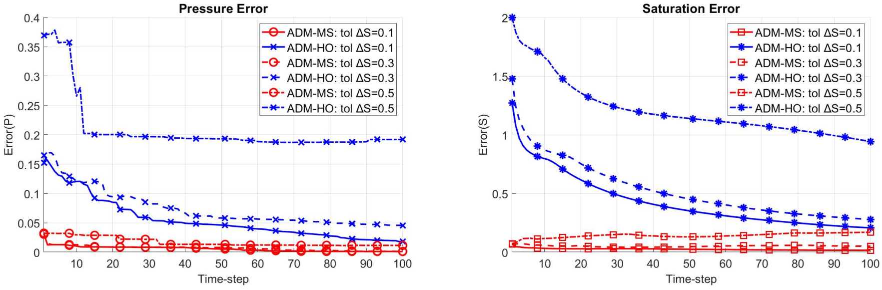

(a) Pressure errors

(b) Saturation errors

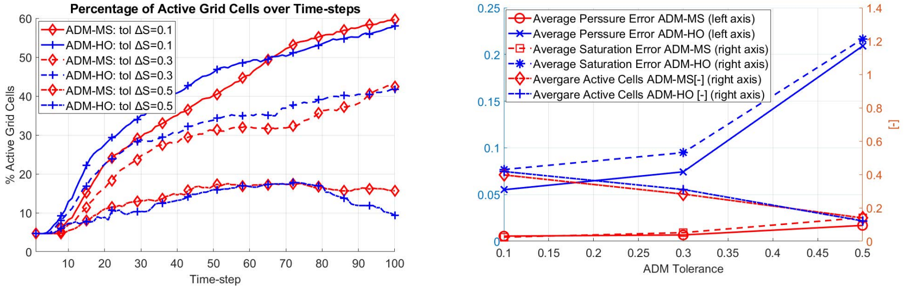

(c) percentage of the active grid cells

(d) Averaged values of the pressure and saturation errors, and the active grid cells

Figure 6.23: Test case 4: the error history maps of the pressure and saturation results of the ADM-MS and ADM-HO methods both compared to fine-scale reference solution are shown in the plots in the top row. Moreover, the history of the active grid cells employed though the simulation time, as well as the averaged values of the three properties (mentioned here) over the entire simulation time are presented in the plots at bottom row.

ability of the SPE10 bottom layer has higher heterogeneity contrast compared to the top layer, with $K_{min} = 2.3 \times 10^{-18}\,[\mathrm{m}^2]$ and $K_{max} = 2.0 \times 10^{-11}\,[\mathrm{m}^2]$. The fluid properties and the injection/production well conditions are identical to the previous test case. However, the simulation time is 20 [days]. The permeability map of this domain at fine-scale resolution is presented in figure 6.24.

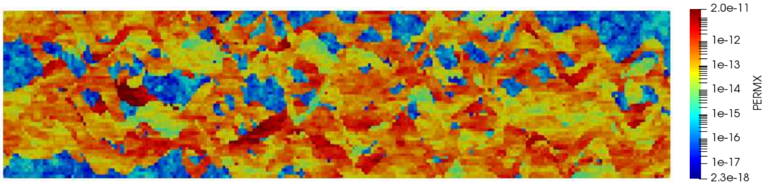

Figure 6.24: Test case 5: Fine-scale permeability (Log_{10} scale) of the SPE10 bottom layer dataset.

The homogenized version of the permeability of the SPE10 bottom layer is shown in figure 6.25 at 2 different coarsening levels. In this case, the channelized patterns of the permeability are less visible. Due to the many high contrast channels, more active cells are employed compared with the SPE10 top layer, as shown in 6.26.

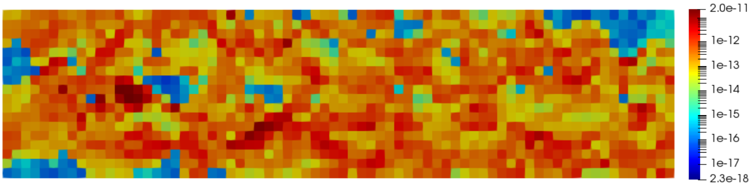

(a) Coarse level 1 with 72 × 18 cells.

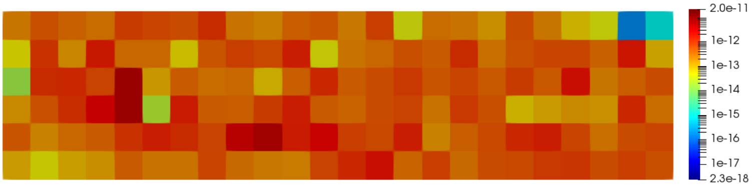

(b) Coarse level 2 with 24 × 6 cells.

Figure 6.25: Test case 5: Homogenized permeability of the bottom layer of the SPE10 for two coarsening levels coarsening ratio $\gamma_x \times \gamma_y = 3 \times 3$.

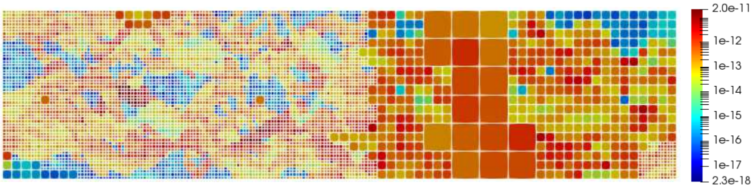

Figure 6.26: Test case 5: Refinement of the permeability of the bottom layer of the SPE10 using ADM-HO after 20 days. The threshold value for the front tracking criterion is $\Delta S = 0.3$.

The saturation and pressure maps at the final time step are shown in figure 6.27 for the fine-scale (top row), the multiscale-based ADM (middle row) and the homogenization-based ADM (bottom row) methods.

The error history plots of the pressure and saturation results of the ADM-MS and the ADM-HO illustrated in figures 6.28a and 6.28b respectively. In addition, figure 6.28c shows the percentage of the active grid cells employed during the simulation time. Figure 6.23d presents the averaged values of the mentioned quantities over the entire simulation time versus the ADM grid selection criterion for three threshold values of $\Delta S = \{0.1, 0.3, 0.5\}$.

The results indicate a noticeable difference in the errors of the ADM-MS and the ADM-HO methods. The pressure error in the ADM-HO method is significantly higher since ADM-HO uses homogenized effective parameters. Instead, the ADM-MS method employs multiscale basis functions. Moreover, as a result of a more accurate pressure, the ADM-MS saturation error is lower than that of the ADM-HO method. The difference in the percentage of the active grid cells used in the two approaches is less noticeable than the difference in the errors. However, the ADM-HO method uses more active grid

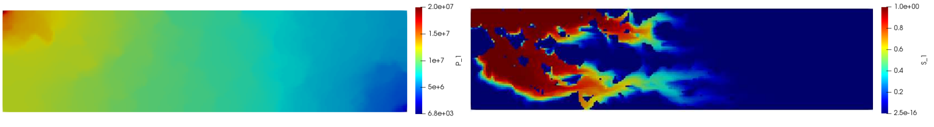

(a) Fine-scale pressure

(b) Fine-scale saturation

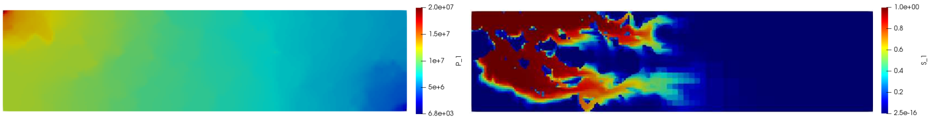

(c) ADM multiscale pressure

(d) ADM multiscale saturation

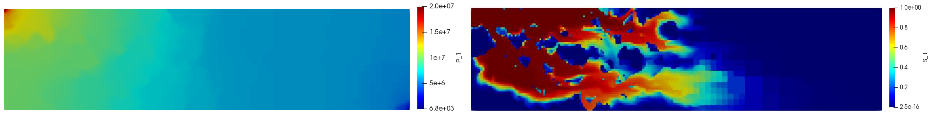

(e) ADM homogenized pressure

(f) ADM homogenized saturation

Figure 6.27: Test case 5: The pressure and saturation results of the fine-scale (top row), the multiscale-based ADM method (middle row) and the homogenized-based ADM method for the SPE10 bottom layer model.

cells, especially in the SPE10 bottom layer test case.

6.5. DISCUSSIONS AND CONCLUSION

In this chapter, an algebraic dynamic multilevel method for fully-implicit simulations of multiphase fluid flow in porous media with embedded discrete fractures, was presented. Built on the embedded discrete fracture model (EDFM), the fine-scale fully implicit system was mapped on to a multilevel dynamic grid, defined independently for the rock matrix and the fractures. This was achieved by development of the sequences of prolongation operators (containing local basis functions) for the fractured media. These local multilevel multiscale basis functions were introduced after selection of the coarse nodes on both the rock matrix and the fracture sub-domains, with flexible matrix-fracture coupling. If at a coarse scale, no coarse nodes are selected on a fracture domain, its effect will be taken into account through the rock matrix basis functions in a homogenized (effective) manner. Selecting the coarse nodes on a fracture however, allows for its explicit representation at that coarse scale. The front-detection strategy is used to employ the fine-scale grids only when and where they are needed, while multilevel multiscale grid is used elsewhere. The use of the multilevel multiscale basis functions guarantees the accuracy of the global (pressure) unknowns where coarse grids are imposed.

Numerical results for both 2D and 3D test cases were presented to validate the ADM method for fractured porous media. Moreover, the sensitivity of the ADM method to the type of the pressure interpolators (i.e., with and without matrix-fracture coupling) and the fraction of the active grid cells chosen indirectly by different threshold values was studied. The results, with different amount of active dynamic grids, show that the ADM method is able to provide accurate results for flow in fractured media by employing only a fraction of the fine-scale grid-cells both in the rock matrix and in the fractures. It is

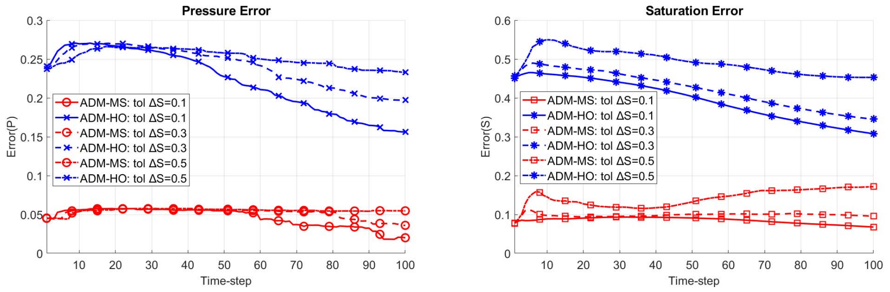

(a) Pressure errors

(b) Saturation errors

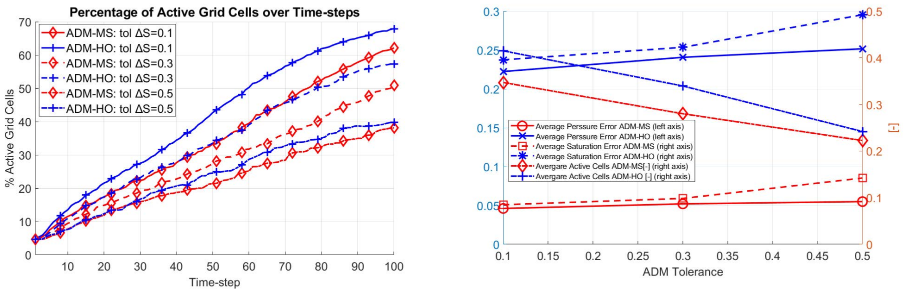

(c) percentage of the active grid cells

(d) Averaged values of the pressure and saturation errors, and the active grid cells

Figure 6.28: Test case 5: The error history maps of the pressure and saturation results of the ADM-MS and ADM-HO methods both compared to fine-scale reference solution for the SPE10 bottom layer are shown in the plots in the top row. Moreover, the history of the active grid cells employed though the simulation time, as well as the averaged values of the three properties (mentioned here) over the entire simulation time are presented in the plots at the bottom row.

expected that the greater the size of the domain, the lower the percentage of the active grid cells compared to the global number of the fine-scale grids. As such, ADM method casts a promising approach for the simulation of multiphase fluid flow in real field-scale fractured porous media.

In addition, homogenization and the multiscale methods have been developed and evolved during the past decade as promising advanced simulation approaches for heterogeneous large-scale systems. In this work, the two methods were investigated, extended into a unified fully-implicit framework, and benchmarked for simulation of multiphase flow in porous media. It was shown that the two methods allow the construction of coarser level systems, and both rely on local solutions to find their corresponding maps. While homogenization methods deliver effective parameters, multiscale methods find interpolation of the solution (pressure) across scales. This is the main difference between the two approaches. For highly heterogeneous test cases it was shown that the two approaches provide accurate solutions, while ADM-MS provided more accurate solutions compared with ADM-HO. The use of the effective parameters for coarse cells with high and low permeable cells can lead to excessive leakage if an effective parameter is used instead of the basis function. Furthermore, it was very important to demonstrate solutions of the ADM-HO for permeability fields with no periodic structure. This illustrated the applicability of homogenization methods for problems with no separation of scales if they are combined with an adaptive mesh strategy (ADM). Moreover, both methods were developed algebraically. Specially by setting a constant unity prolongation operator, it was shown how the ADM-HO method can be developed straightforwardly. This comparison sheds new light on the application of multiscale and homogenization methods for real-field simulation of multiphase flow in porous media.

7

ALGEBRAIC DYNAMIC MULTILEVEL (ADM) METHOD FOR FRACTURED GEOTHERMAL RESERVOIRS

In the previous chapter, the algebraic dynamic multilevel (ADM) method was explained for isothermal multiphase flow in fractured porous media. After describing the governing equations in section 2.1 and discretizing the continuum system as well as linearizing the non-linear equations at fine-scale resolution in sections 3.1.1 and 3.2.1, the linear system of equations was mapped on to a dynamic resolution grid (i.e., the ADM grid) using the ADM restriction and prolongation operators. These operators themselves are assembled using the static multilevel multiscale operators constructed at the beginning of the time-dependent simulation. Once the fine-scale system is mapped to the ADM resolution and the system was solved at this dynamically defined grid resolution, the obtained solution is mapped back to the fine-scale resolution using the ADM prolongation operator, resulting in an approximated solution. The ADM method was tested using various fractured test cases. It could be seen that the ADM method could provide satisfactory results with a user-defined level of accuracy while providing significant computational efficiency by reducing the size of the linear system with multiple orders of magnitude. In addition, the results of the multiscale-based ADM (ADM-MS) and the homogenization-based ADM (ADM-HO) were compared with the fine-scale results (as the reference solution) using test cases that employed the top and the bottom layers of the SPE 10th comparative solution project [163]. It was shown that the multiscale-based ADM was able to capture the fine-scale heterogeneities and adapt to the saturation front more accurately than the homogenization-based ADM.

In many geothermal reservoirs, the presence of complex fracture networks pose significant challenge to accurate fluid flow modeling, especially in formations with low per-

---

Parts of this chapter includes revised version of two of the author's publications in the Journal of Computational Physics: X, **Vol. 7** (2020) [47], and in the Journal of Geothermics.

meabilities where the fluid and heat transport mostly occurs through the fractures. In such scenarios, the ADM method could provide computational benefits without sacrificing the accuracy considerably.

In this chapter, the ADM method is described for low enthalpy (single-phase) and high-enthalpy (multiphase) flow in fractured geothermal reservoirs. The governing equations and the fine-scale discretization of the equations were already covered in chapters 2 and 3 respectively. The choice of the primary unknowns and the relating thermodynamical correlations and theories were also already discussed in section 2.3.3. After describing the ADM methodology for geothermal flow, its performance will be presented through various homogeneous, heterogeneous and fractured domains test cases both for low enthalpy (single-phase flow) and high-enthalpy (multiphase flow) fluid models. Especially, for low enthalpy single-phase flow, the effects resulting from the choice of the primary unknowns (either pressure-temperature or pressure-enthalpy) will be compared with each other.

7.1. ADM SIMULATION STRATEGY FOR THERMAL FLOW

In this section, two different flow models are considered for the fine-scale system, i.e., single-phase flow for the low-enthalpy geothermal systems and multiphase flow for the high-enthalpy geothermal systems. In low-enthalpy conditions where the water is assumed not to phase change (no evaporation of the water under the in-situ thermodynamical conditions), two formulations can be chosen. The first is the natural formulation where the primary unknowns are the pressure (p) and the temperature (T) of the system. The other one is the molar formulation in which the pressure (p) and the total enthalpy (H) are considered as the primary unknowns (please see section 2.3.3 for more details on the choice of the primary unknowns). However, for the high enthalpy systems, only the molar formulation with pressure (p) and the total enthalpy (H) as the primary unknowns is taken into account.

The ADM simulation strategy for geothermal flow follows a similar approach as the one for isothermal multiphase flow described in section 6.1. The flow chart shown in figure 6.1 applies to this approach as well. For both geothermal systems, at each iteration, the ADM system reads

$$\underbrace{\hat{\mathbf{R}}_l^{l-1}\dots\hat{\mathbf{R}}_1^{0}\,\mathbf{J}_0\,\hat{\mathbf{P}}_0^{1}\dots\hat{\mathbf{P}}_{l-1}^{l}}_{\mathbf{J}_{ADM}}\,\delta\hat{x}_l = -\underbrace{\hat{\mathbf{R}}_l^{l-1}\dots\hat{\mathbf{R}}_1^{0}\,r_0}_{r_l}. \qquad (6.2)$$

After solving the linearized system of equations above at ADM resolution, the approximated solution at the fine-scale resolution (i.e., $\delta x_0'$) is obtained as

$$\delta x_0 \approx \delta x_0' = \hat{\mathbf{P}}_0^{1}\dots\hat{\mathbf{P}}_{l-1}^{l}\,\delta x_l. \qquad (6.3)$$

The ADM prolongation and restriction operators used for geothermal flow models are assembled from the multilevel multiscale (MMsFV) operators constructed only at the beginning of the simulation. These ADM operators are obtained similar to the ADM operators for isothermal multiphase flow.

7.1.1. THE ADM OPERATORS

The MMsFV prolongation operator (i.e., $\mathbf{P}_{l-1}^{l}$) for the low-enthalpy single-phase geothermal flow, with consideration of natural formulation (pressure and temperature as the main unknowns), between the coarsening levels l and $l-1$, reads

$$\mathbf{P}_{l-1}^{l} = \begin{pmatrix} \left((\mathbf{P}_p)_{l-1}^{l}\right)^{m,m} & \left((\mathbf{P}_p)_{l-1}^{l}\right)^{m,f} & 0 & 0 \\ \left((\mathbf{P}_p)_{l-1}^{l}\right)^{f,m} & \left((\mathbf{P}_p)_{l-1}^{l}\right)^{f,f} & 0 & 0 \\ 0 & 0 & \left((\mathbf{P}_T)_{l-1}^{l}\right)^{m,m} & 0 \\ 0 & 0 & 0 & \left((\mathbf{P}_T)_{l-1}^{l}\right)^{f,f} \end{pmatrix}_{N_{l-1}\times N_l}. \tag{7.1}$$

Similarly, the MMsFV prolongation operator for low-enthalpy single-phase geothermal flow and high-enthalpy multiphase geothermal flow, both with molar formulation (pressure and total enthalpy as the primary unknowns), is given as

$$\mathbf{P}_{l-1}^{l} = \begin{pmatrix} \left((\mathbf{P}_p)_{l-1}^{l}\right)^{m,m} & \left((\mathbf{P}_p)_{l-1}^{l}\right)^{m,f} & 0 & 0 \\ \left((\mathbf{P}_p)_{l-1}^{l}\right)^{f,m} & \left((\mathbf{P}_p)_{l-1}^{l}\right)^{f,f} & 0 & 0 \\ 0 & 0 & \left((\mathbf{P}_H)_{l-1}^{l}\right)^{m,m} & 0 \\ 0 & 0 & 0 & \left((\mathbf{P}_H)_{l-1}^{l}\right)^{f,f} \end{pmatrix}_{N_{l-1}\times N_l}. \tag{7.2}$$

Please note that the MMsFV restriction operator is identical for both the natural and the molar formulations, and also identical to the MMsFV restriction operator explained in section 6.1, namely,

$$\mathbf{R}_{l}^{l-1} = \begin{pmatrix} \left(\mathbf{R}_{l}^{l-1}\right)^{m} & 0 & 0 & 0 \\ 0 & \left(\mathbf{R}_{l}^{l-1}\right)^{f} & 0 & 0 \\ 0 & 0 & \left(\mathbf{R}_{l}^{l-1}\right)^{m} & 0 \\ 0 & 0 & 0 & \left(\mathbf{R}_{l}^{l-1}\right)^{f} \end{pmatrix}_{N_l\times N_{l-1}}. \tag{6.5}$$

The temperature blocks and the total enthalpy blocks of the prolongation operators are assembled with constant basis functions due to the local nature of these variables. This means that these interpolators can be constructed as the transpose of the restriction operators. In other words, $(\mathbf{P}_T)_{l-1}^{l} = (\mathbf{P}_H)_{l-1}^{l} = \left[\mathbf{R}_{l}^{l-1}\right]^{T}$. However, the pressure blocks of the prolongation operators are calculated (identically in both formulations) using the multilevel multiscale procedure for fractured media (see section 5.3.2). To achieve an efficient writing style, the duplication of the contents for the ADM and the MMsFV methods for these flow models is avoided as much as possible.

7.1.2. SELECTION OF THE GRID RESOLUTION

For the geothermal flow models, the system of equations is mapped between the fine-scale resolution and the ADM grid resolution using the ADM operators. The user-defined grid selection criterion (already explained in section 6.2) is written differently depending on the natural or the molar formulations. For the natural formulation, the front tracking technique captures the temperature gradient to achieve the correct dynamic grid selection. Assuming Ω_l^I and Ω_l^J as the set of two neighboring coarse grid cells I and J at coarsening level l, with indices of fine-scale grid cells belonging to the coarse grid cells Ω_l^I and Ω_l^J written as i and j respectively, the temperature differences $\Delta\bar{T}_{IJ}$ are given by

$$\Delta\bar{T}_{IJ} = max\big(|T_i - T_j|\big) \quad \forall\, i \in \Omega_l^I \text{ and } \forall\, j \in \Omega_l^J. \tag{7.3}$$

The coarse grid block I is refined from coarsening level l to coarsening level $l-1$ if the condition

$$\Delta\bar{T}_{IN} > \text{tol} \tag{7.4}$$

is met. Similarly, for the molar formulation, the front tracking technique captures the gradient of the total enthalpy on the system. Therefore, The total enthalpy differences $\Delta\bar{H}_{IJ}$ are written as

$$\Delta\bar{H}_{IJ} = max\big(|H_i - H_j|\big) \quad \forall\, i \in \Omega_l^I \text{ and } \forall\, j \in \Omega_l^J, \tag{7.5}$$

and the coarse grid block I is refined from resolution level l to level $l-1$ if the condition

$$\Delta\bar{H}_{IN} > \text{tol} \tag{7.6}$$

is met. All other procedures involving the ADM methodology for geothermal flow are identical to those of the ADM method for isothermal multiphase flow. The details of the code development are not covered here.

7.2. NUMERICAL RESULTS AND THE EVALUATION OF THE ADM METHOD

In this section, the algebraic dynamic multilevel (ADM) method for geothermal flow is studied using various test cases. The section of the numerical results is divided into three subsections. In the first subsection, using three homogeneous and heterogeneous fractured test cases (2D and 3D), i.e., test cases 1, 2 and 3, the ADM method for single-phase flow in low-enthalpy geothermal reservoirs is assessed for the natural formulation (pressure p and temperature T as the primary unknowns). In the second subsection, using the next two test cases (test cases 4 and 5), a comparison between the results of the simulations for the molar (pressure p and the total fluid enthalpy H as the main unknowns) and the natural formulations (pressure p and the temperature T as the primary unknown) is presented. Moreover, a comparison of the performance of both formulations is conducted. At last, in the third subsection, through a number of 1D, 2D and 3D fractured test case (test cases 6-8), the performance of the ADM method is demonstrated for the high-enthalpy multiphase flow simulation in fractured geothermal domains with implementation of the molar formulation. The ADM results are compared against the fine-scale results (as the reference solution). The ADM error is calculated as

$$e_x = \frac{\| x_{\text{FS}} - x_{\text{ADM}} \|_2}{\| x_{\text{FS}} \|_2}, \qquad (6.12)$$

with x being a solution vector (of either of the main unknowns) and the subscripts ADM and FS indicating ADM and fine-scale.

7.2.1. SINGLE-PHASE FLOW IN LOW-ENTHALPY FRACTURED GEOTHERMAL SYSTEMS USING NATURAL FORMULATION (P-T)

In this section, three homogeneous and heterogeneous fractured test cases (2D and 3D) are included to assess the ADM method for single-phase mass-heat coupled flow in low enthalpy fractured geothermal reservoirs.

TEST CASE 1: 2D HOMOGENEOUS FRACTURED RESERVOIR

In this test case, the accuracy of the ADM method for mass-heat transport with natural formulation (pressure and temperature as the main unknowns) in a homogeneous domain containing fractures with mixed conductivities is studied. For this purpose, a 2D fractured 100 [m] × 100 [m] domain with 30 fractures is considered. The length of each fracture is different but the size of their aperture is identical and set to $a_f = 5 \cdot 10^{-3}$ [m]. A 136 × 136 grid is imposed on the rock matrix and the fracture network consists of 315 grid cells (in total 18811 cells). The matrix permeability is homogeneous with $K_m = 10^{-14}$ [m^2] and the permeability of the fracture network has the range of $K_{f_{min}} = 10^{-20}$ [m^2] and $K_{f_{max}} = 10^{-7}$ [m^2]. Two injection wells are located at the bottom left and top left corners with injection pressure of $p_{\text{inj}} = 2 \cdot 10^7$ [Pa]. additionally, there are two production wells at the bottom right and the top right corners with pressure of $p_{\text{prod}} = 1 \cdot 10^7$ [Pa]. Table 7.1 demonstrates the input parameters of this test case.

Table 7.1: Input parameters of the fluid and rock properties for test case 1.

Property	value
Rock thermal conductivity (Λ_r)	4 [W/m/K]
Fluid thermal conductivity (Λ_f)	negligible
Rock density (ρ_r)	2750 [kg/m^3]
Fluid specific heat (C_{p_f})	4200 [J/kg.K]
Rock specific heat (C_{p_r})	790 [J/kg.K]
Matrix porosity (ϕ)	0.2
Matrix permeability	10^{-14} [m^2]
fractures permeability (min)	10^{-20} [m^2]
fractures permeability (max)	10^{-7} [m^2]
Fractures aperture	5×10^{-3} [m]

The maximum number of the coarsening level for the rock matrix is $l_m = 2$ and for the fractures is $l_f = 1$. Over the entire computational grids, the coarsening ratio is $\gamma = 3 \times 3$. The ADM simulations are run for three different thresholds of grid resolution selection, namely, $\Delta T = 5, 10, 20\,[\mathrm{K}]$ and the ADM results are compared to the result of the fine-scale simulation as the reference solution. The simulations are run for 1000[days] and the results are printed at 100 isochronal intervals.

Figures 7.1 and 7.2 show the pressure and the temperature solutions of the fine-scale and the ADM simulations. The errors (e_p and e_T) and the percentage of the active grid cells (AGC) are mentioned under the ADM plots.

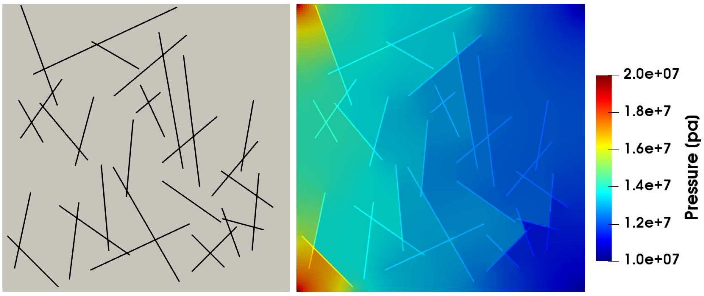

(a) Fracture network geometry (b) Fine-scale pressure

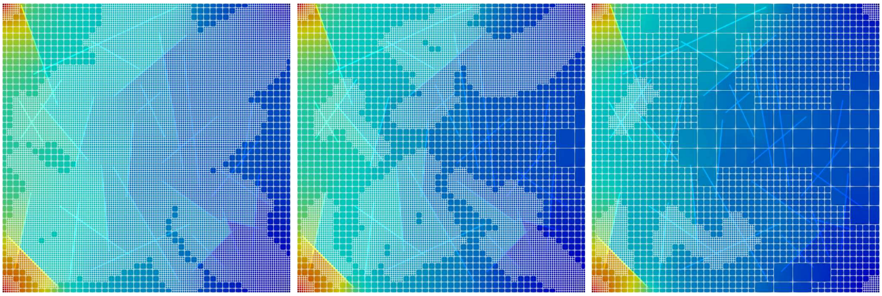

(c) ADM with $\Delta T = 5\,[\mathrm{K}]$
$e_p = 9.0 \times 10^{-3}$, $AGC = 52\%$

(d) ADM with $\Delta T = 10\,[\mathrm{K}]$
$e_p = 1.3 \times 10^{-2}$, $AGC = 20\%$

(e) ADM with $\Delta T = 20\,[\mathrm{K}]$
$e_p = 2.3 \times 10^{-2}$, $AGC = 14\%$

Figure 7.1: Test case 1: pressure plots. Figure 7.1a illustrates the fracture network of this test case. The figure on the top right is the fine-scale solution (7.1b), and the figures on the bottom row show the ADM solution with thresholds of $\Delta T = 5\,[\mathrm{K}]$ (7.1c), $\Delta T = 10\,[\mathrm{K}]$ (7.1d) and $\Delta T = 20\,[\mathrm{K}]$ (7.1e) respectively.

Figure 7.3 provides more details of the error analysis for test case 1. On the top row, the pressure and the temperature errors (figures 7.3a and 7.3b) versus simulation time-steps are shown. Figure 7.3c plots the percentage of the active grid cells used during the simulation. Lastly, averaged errors and averaged active grid cells are plotted over the entire simulation time for all the three thresholds (7.3d).

Please note that the regions around the wells are always kept at fine-scale resolution and as a result (depending on the size of the domain) a noticeable portion of the active grid cells are imposed. In this test case, approximately 5 percent of the total grid cells are kept at the fine-scale resolution due to near-well refinement. Moreover, in this test case, intersection between permeable fractures and impermeable fractures (or flow barriers) occur. In this test case (and the following ones), the impermeable fractures are considered as “non-sealing” flow barriers, meaning that the crossing of the highly permeable fractures causes flow leakage. This effect can be seen in the figure 7.1 where the pressure

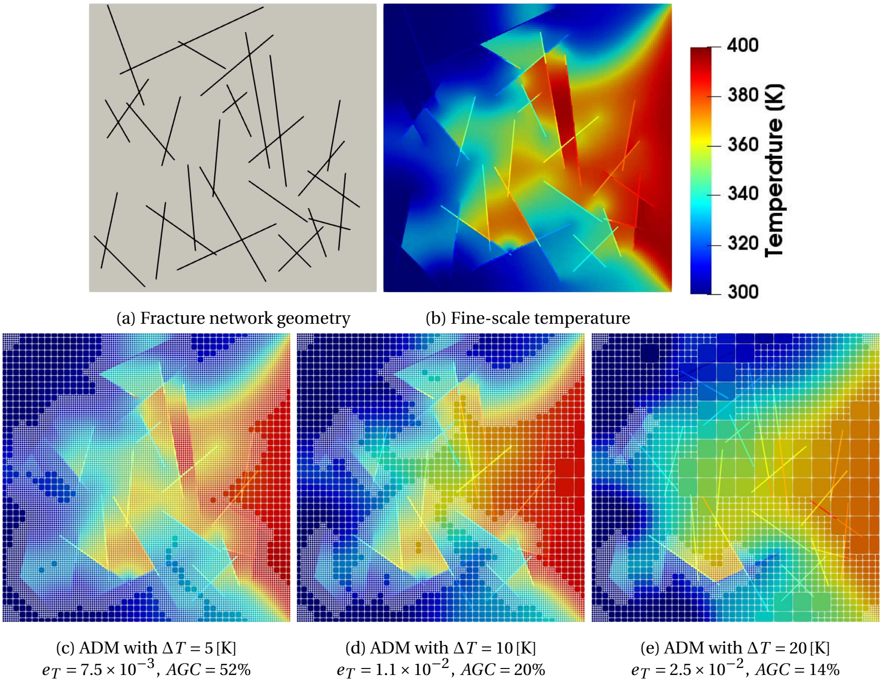

(a) Fracture network geometry
(b) Fine-scale temperature
(c) ADM with $\Delta T = 5\,[\mathrm{K}]$ $e_T = 7.5 \times 10^{-3}$, $AGC = 52\%$
(d) ADM with $\Delta T = 10\,[\mathrm{K}]$ $e_T = 1.1 \times 10^{-2}$, $AGC = 20\%$
(e) ADM with $\Delta T = 20\,[\mathrm{K}]$ $e_T = 2.5 \times 10^{-2}$, $AGC = 14\%$

Figure 7.2: Test case 1: temperature plots. Figure 7.2b on the top right shows the fine-scale temperature solution. The ADM solutions are shown on the figures of the bottom row with thresholds of $\Delta T = 5\,[\mathrm{K}]$ (7.2c), $\Delta T = 10\,[\mathrm{K}]$ (7.2d) and $\Delta T = 20\,[\mathrm{K}]$ (7.2e).

gradient across the permeable fracture stays negligible on both sides of the impermeable fracture. However, please note that in reality, this depend on the geologic history of the fracture patterns. The geological discussion related to this matter is out of the scope of this work.

TEST CASE 2: 2D HETEROGENEOUS FRACTURED RESERVOIR

This test case assesses the ADM performance on a 2D heterogeneous fractured domain. Similar to the previous test case, a 2D domain with dimensions of $100\,[\mathrm{m}] \times 100\,[\mathrm{m}]$ is considered. A network of 30 fractures with identical geometry as in test case 1 exists. The rock matrix is discretized into 136×136 fine-scale grid cells, and 291 grids are imposed on the fracture network (in total 18516 grid cells). The permeability of the matrix ranges from $K_{m_{min}} = 1.2 \times 10^{-15}\,[\mathrm{m}^2]$ to $K_{m_{max}} = 1.2 \times 10^{-12}\,[\mathrm{m}^2]$. All fractures are highly conductive with permeability of $K_f = 10^{-8}\,[\mathrm{m}^2]$. The well pattern used in this test case is identical to test case 1. Moreover, the same coarsening strategy is used in this test case. The input parameters of table 7.1 holds for this test case as well, except for permeability values of the rock matrix and the fractures. The ADM simulations are run for four different grid resolution selection thresholds ($\Delta T = 5, 10, 20, 40\,[\mathrm{K}]$) and their results are compared to the reference solution (fine-scale). The simulation is done for 200[days] and the results are extracted at 100 isochronal intervals.The pressure and the tempera-

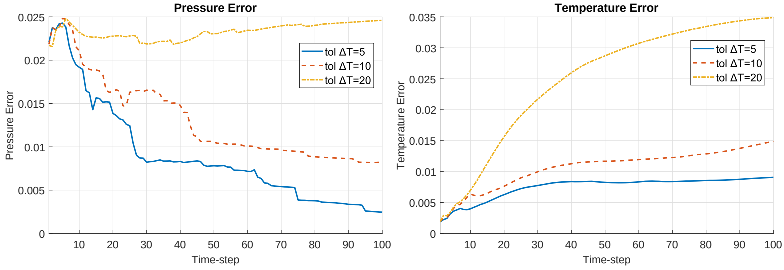

(a) Pressure error

(b) Temperature error

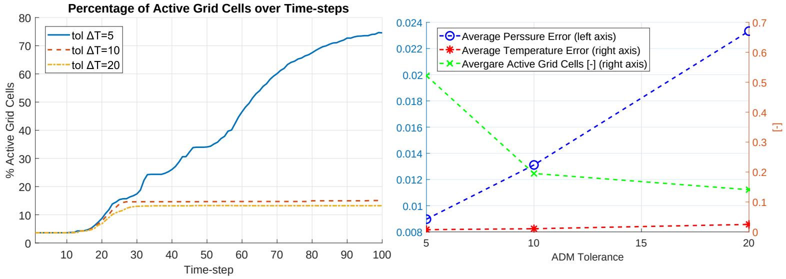

(c) Active grid cells

(d) Average values

Figure 7.3: Test case 1: error analysis. Figures 7.3a and 7.3b show the ADM error of pressure and temperature versus the simulation time-steps. The errors are calculated based on equation (6.12). Figure 7.3c shows the percentage of the active grid cells used during simulation versus the simulation time-steps. Lastly, figure 7.3d demonstrates the averaged values of the mentioned parameters over the entire simulation time for the three thresholds.

ture solutions of fine-scale and the ADM simulations are displayed on figures 7.4 and 7.5 respectively. Similar to the previous test case, the errors (e_p and e_T) and the percentage of the active grid cells (*AGC*) are indicated under the ADM plots.

Figures 7.6 shows the error analysis for test case 2. The pressure and the temperature errors versus simulation time-steps are illustrated on the top row (figures 7.6a and 7.6b). Figure 7.6c shows the percentage of the active grid cells employed during the simulation time. Average errors and average active grid cells over the entire simulation time can be seen for all four ADM thresholds on figure 7.6d.

Test Case 3: 3D homogeneous fractured reservoir

In this test case, a 3D 100 [m] × 100 [m] × 40 [m] containing 15 lower dimensional fractures with different geometrical properties is considered. An 81 × 81 × 27 Cartesian grid is imposed on the rock matrix, and the fracture network is discretized in to 1377 grid cells (summation of 178524 grid cells). The rock matrix has permeability of $K_m = 10^{-14}$ [m^2]. The fracture network consists of both highly conductive fractures with permeability of $K_f = 10^{-6}$ [m^2] and flow barriers with permeability of $K_f = 10^{-22}$ [m^2]. Figure 7.8a shows the structure of the fracture network for this 3D test case. Two injection wells exist at the bottom left and the top left boundaries with a pressure of $p_{\text{inj}} = 5 \times 10^7$ [Pa]. Similarly, two production wells are located at the bottom right and the top right boundaries with a pressure of $p_{\text{prod}} = 1 \times 10^7$ [Pa]. All the wells are vertical and are perforated over the entire

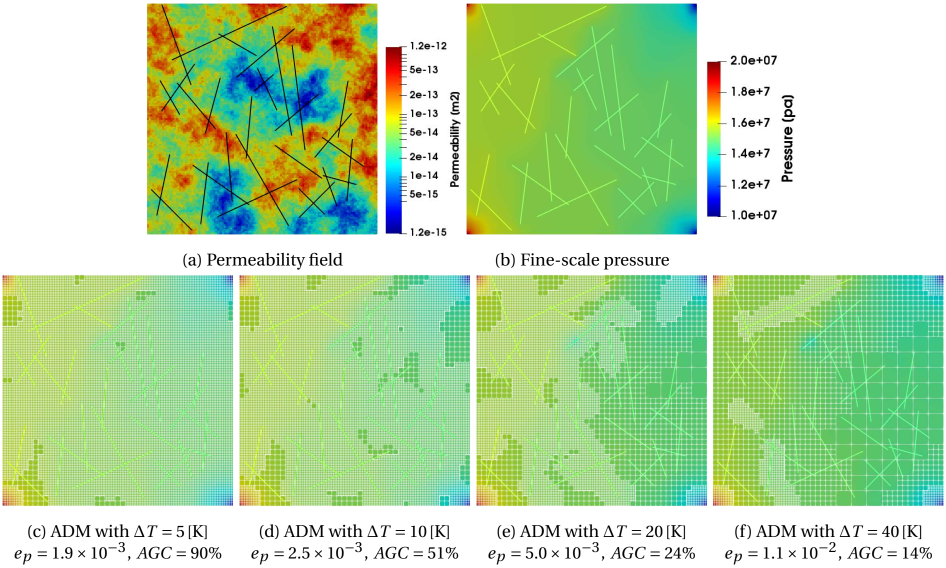

(a) Permeability field

(b) Fine-scale pressure

(c) ADM with $\Delta T = 5$ [K] $e_p = 1.9\times10^{-3}$, $AGC = 90\%$

(d) ADM with $\Delta T = 10$ [K] $e_p = 2.5\times10^{-3}$, $AGC = 51\%$

(e) ADM with $\Delta T = 20$ [K] $e_p = 5.0\times10^{-3}$, $AGC = 24\%$

(f) ADM with $\Delta T = 40$ [K] $e_p = 1.1\times10^{-2}$, $AGC = 14\%$

Figure 7.4: Test case 2: pressure plots for the 2D heterogeneous test case with 30 highly conductive fractures. Shown above, are the permeability map 7.4a, fine-scale solution 7.4b, ADM with thresholds $\Delta T = 5$ [K] 7.4c, $\Delta T = 10$ [K] 7.4d, $\Delta T = 20$ [K] 7.4e and $\Delta T = 40$ [K] 7.4f respectively.

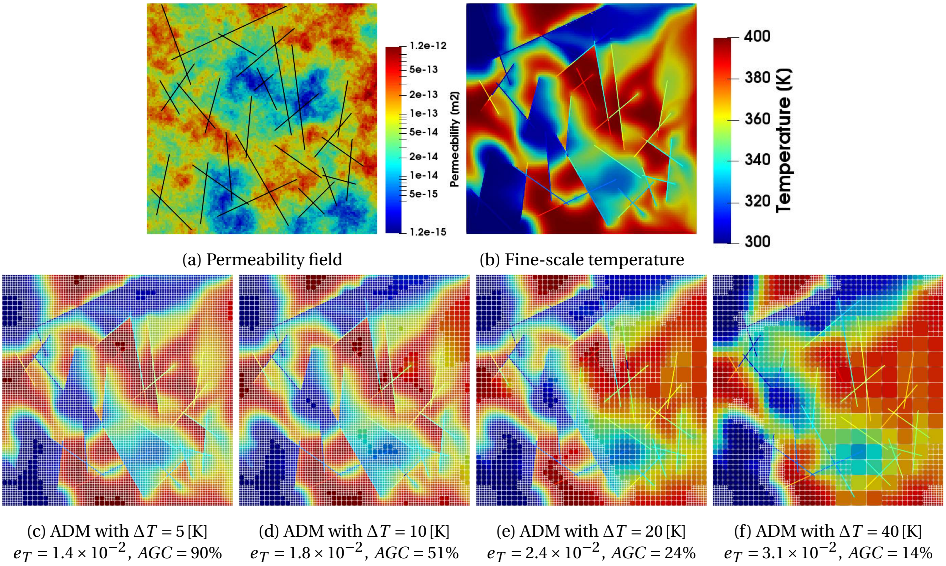

(a) Permeability field

(b) Fine-scale temperature

(c) ADM with $\Delta T = 5$ [K] $e_T = 1.4\times10^{-2}$, $AGC = 90\%$

(d) ADM with $\Delta T = 10$ [K] $e_T = 1.8\times10^{-2}$, $AGC = 51\%$

(e) ADM with $\Delta T = 20$ [K] $e_T = 2.4\times10^{-2}$, $AGC = 24\%$

(f) ADM with $\Delta T = 40$ [K] $e_T = 3.1\times10^{-2}$, $AGC = 14\%$

Figure 7.5: Test case 2: temperature plots for the 2D heterogeneous test case with 30 highly conductive fractures. The permeability map is shown in figure 7.5a. The numerical solution of the temperature is given for the fine-scale run (figure 7.5b), and the ADM runs with thresholds $\Delta T = \{5, 10, 20, 40\}$ [K] (figures 7.5c, 7.5d, 7.5e and 7.5f) respectively.

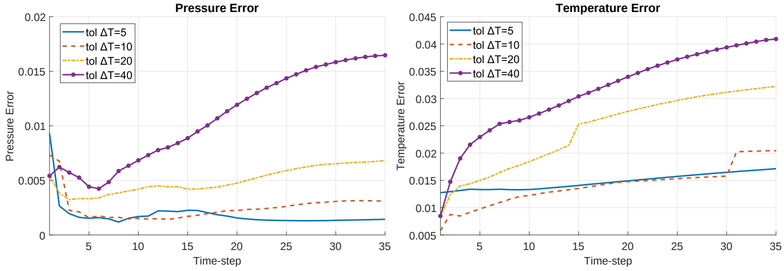

(a) Pressure error

(b) Temperature error

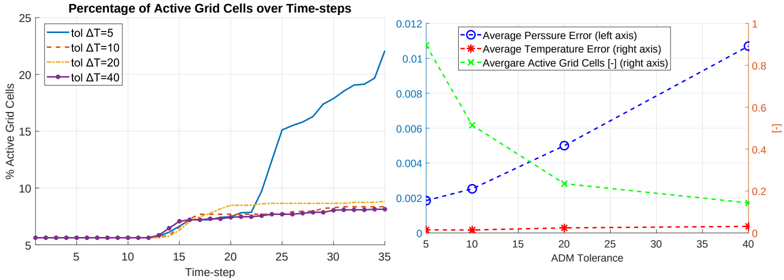

(c) Active grid cells

(d) Average values

Figure 7.6: Test case 2: error analysis. Figures 7.6a and 7.6b demonstrate the ADM error of pressure and temperature results versus the simulation time-steps. The errors are calculated based on equation (6.12). Figure 7.6c shows the percentage of the active grid cells employed versus the simulation time-steps. Lastly, figure 7.6d presents the averaged values of the mentioned parameters over the entire simulation time for the four ADM thresholds mentioned above.

thickness of the reservoir. Simulation is run for 200 days and the results are printed at 100 isochronal intervals.. Two coarsening levels with coarsening ratio of $\gamma_m = 3 \times 3 \times 3$ is considered for matrix and one coarsening level with coarsening ratio of $\gamma_f = 3 \times 3$ for the fractures. Figure 7.7 illustrates how the ADM grids looks like for various coarsening levels and resolutions at a specific simulation time.

The simulations are run for the fine-scale and the ADM with four different thresholds ($\Delta T = \{10, 20, 40, 80\}$ [K]). The results of the ADM are compared to the reference solution (fine-scale). The temperature solutions are shown in figure 7.8.

Figure 7.9 provides the error analysis of this test case.

7.2.2. COMPARISON BETWEEN THE NATURAL FORMULATION (P-T) AND THE MOLAR FORMULATION (P-H)

In this subsection with the next two test cases (test cases 4,5), a comparison is made between the natural formulation (pressure p and temperature T as the main unknowns) and the molar formulation (pressure p and the total enthalpy H as the primary unknowns) for single-phase flow in low-enthalpy geothermal systems. And finally, with test case 6, the ADM method is assessed for multiphase flow in high-enthalpy fractured geothermal reservoirs using the molar formulation. An identical reservoir geometry and production strategy is considered for all the following test cases. The initial reservoir

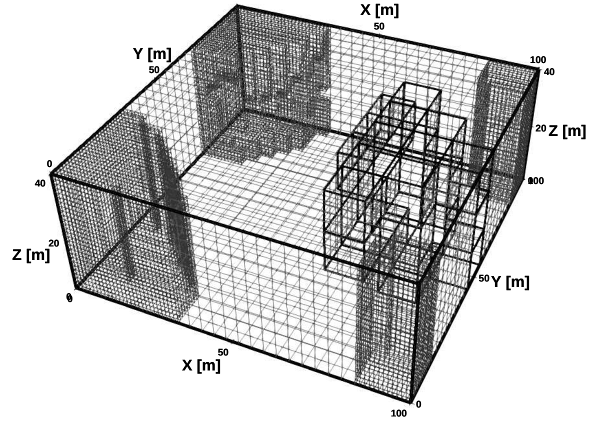

Figure 7.7: Test case 3: Illustration of the ADM grid at time interval 10 ($t = 20$ [dyas]) for $\Delta T = 40$ [K]. Note that the grid cells near the wells are always kept at the fine-scale resolution.

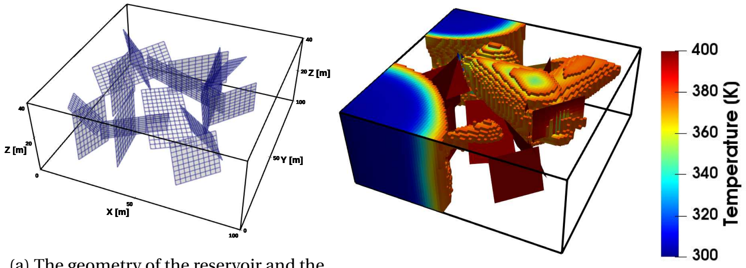

(a) The geometry of the reservoir and the fracture network

(b) Fine-scale temperature

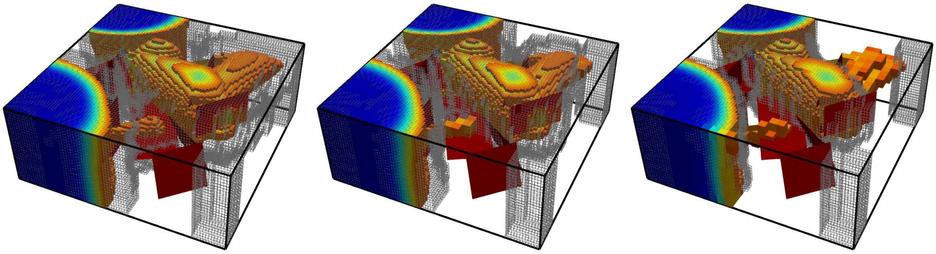

(c) ADM with $\Delta T = 10$ [K] $e_T = 1.6 \times 10^{-3}$, $AGC = 58\%$

(d) ADM with $\Delta T = 20$ [K] $e_T = 2.9 \times 10^{-3}$, $AGC = 54\%$

(e) ADM with $\Delta T = 40$ [K] $e_T = 8.6 \times 10^{-3}$, $AGC = 40\%$

Figure 7.8: Test case 3: Temperature plots. Figure 7.8b on the top right shows the fine-scale solution. The ADM solutions are presented on the figures of the bottom row with thresholds of $\Delta T = 10$ [K] (7.8c), $\Delta T = 20$ [K] (7.8d) and $\Delta T = 40$ [K] (7.8e). For the sake of the visualization, only the grid cells with the temperature values of 300 [K] $< T <$ 350 [K] illustrated. On these plots, the ADM grids belonging to the fine-scale resolution are shown with gray color, but the ADM grids of the coarser levels are hidden for better visualization. The temperature distribution corresponds to the simulation time interval 25 ($t = 50$ [dyas]). The figure on the top left (7.8a) shows the fracture network including the discrete fracture planes.

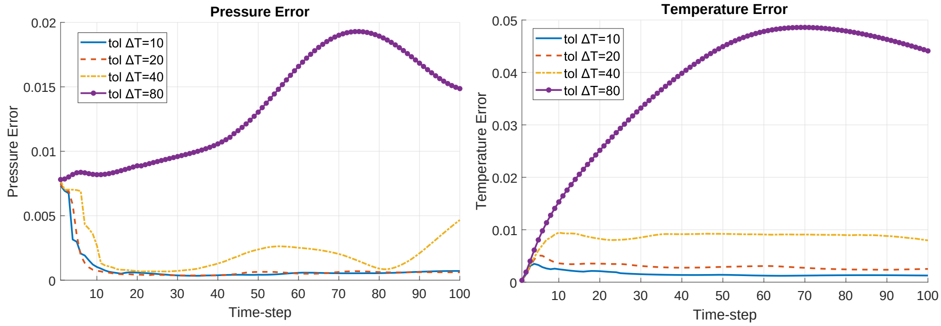

(a) Pressure error

(b) Temperature error

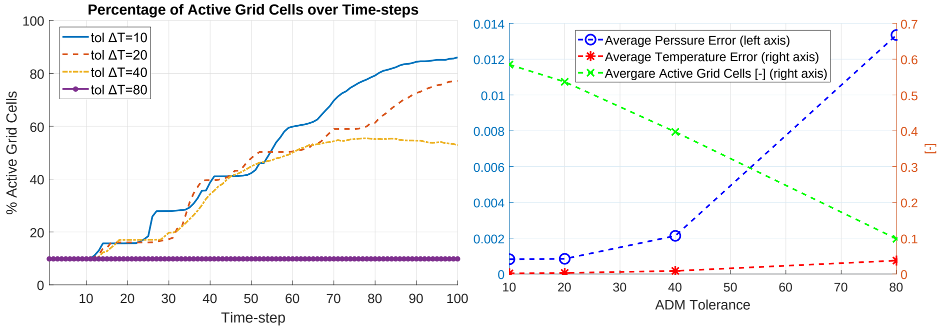

(c) Active grid cells

(d) Average values

Figure 7.9: Test case 3: error analysis. Figures 7.9a and 7.9b present the ADM error of pressure and temperature results versus the simulation time-steps. The errors are calculated based on equation (6.12). Figure 7.9c demonstrates the percentage of the active grid cells employed versus the simulation time-steps. Lastly, figure 7.9d presents the averaged values of the mentioned parameters over the entire simulation time for the four ADM thresholds mentioned above.

pressure is identical for all the simulations. Figure 7.10 shows a schematic overview of the reservoir geometry and production strategy. A subdivision is made in terms of the geological realization of the reservoir. The initial reservoir temperature, rock matrix properties and permeability map are chosen such that the two models represent the geothermal fields of Middenmeer in the Netherlands and Soultz-sous-Forêts in France [164], but only in terms of the mentioned properties. Other properties such as formation type, geological history, etc. have not been taken into account. Therefore, to avoid misunderstanding, from now on, the model with the Soultz-sous-Forêts properties will be referred to as "field A", and the model with the Middenmeer properties will be denoted as "field B". Please note that the geothermal fluid is assumed to be pure water for both geothermal fields. Table 7.2 shows the rock matrix properties of both geothermal fields. The rest of the input parameters used mutually in all the following test cases are presented in table 7.3.

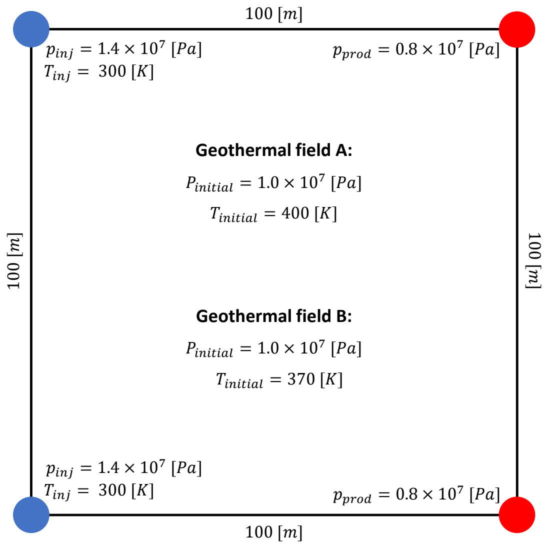

Figure 7.10: Schematic overview of the reservoir geometry and production strategy applied in test cases 4 and 5. Two injection wells are located on the left corners of the domain with injection pressure of $p_{\text{inj}} = 1.4 \times 10^7$ [Pa] and injection temperature of $T = 300$[K]. Two production wells are located on the right corners of the domain with production pressure of $p_{\text{prod}} = 0.8 \times 10^7$ [Pa]. The initial pressure and temperature of the reservoirs are indicated for both geothermal fields under consideration.

In order to compare the results between the molar and natural formulations, a so-called formulation error e_f is defined that represents the relative difference between the numerical solutions obtained from both formulations. The formulation error is calculated as

$$e_f = \frac{\| x_{(p-H)} - x_{(p-T)} \|_2}{\| x_{(p-T)} \|_2}, \tag{7.7}$$

Table 7.2: Input parameters of the rock properties for the geothermal fields A and B.

Property	value for field A	value for field B
Porosity (ϕ)	0.2	0.2
Rock density (ρ_r)	2600 [Kg/m^3]	2600 [Kg/m^3]
Specific heat capacity (C_p)	850 [J/Kg/K]	830 [J/Kg/K]
Thermal conductivity (Λ)	2.9 [W/m/K]	2.9 [W/m/K]

Table 7.3: The rest of the input parameters mutually used in the test cases 4,5 and 6.

Property	value
Injection temperature (T_{inj})	300 [K]
Injection pressure (p_{inj})	1.4×10^7 [Pa]
Production pressure (p_{prod})	0.8×10^7 [Pa]
Simulation time [days]	2000[days]
Maximum size of the time-step	30[days]
Maximum number of iterations	10 [-]
Tolerances for convergence	10^{-4} [-]
ADM coarsening levels (l)	2
ADM coarsening ratios (γ)	3×3 [-]
ADM grid resolution selection tolerance	$\Delta T = 20$ [K]

where $|| \ x_{(p-H)} \ ||$ and $|| \ x_{(p-T)} \ ||$ are the second error norms of a given variable x using the molar and natural formulation, respectively.

The first test case (test case 4) is the geothermal field A with assumption of homogeneous permeability. The second test case (test case 5) is the geothermal field B with heterogeneous permeability field. For both of the first two cases, two realizations are taken into account, one with a network of 15 fractures and one with 30 fractures. Both fracture networks have mix-conductive fractures, some highly conductive with permeability of $K_{f,max} = 10^{-8}$ [m^2] and flow barriers with permeability of $K_{f,min} = 10^{-20}$ [m^2]. The geometry of the fracture networks are available in figure 7.12. Figure 7.11 shows the permeability of both geothermal fields.

TEST CASE 4: GEOTHERMAL FIELD A

In this test case, the geothermal field A with assumption of homogeneous permeability is considered. Figure 7.11a shows the permeability map. The properties of this field can be found in table 7.2. As mentioned, two realizations are taken into account, one with 15 fractures and one with a fracture network consisting of 30 fractures. Figure 7.12 illustrates the geometry of the fracture networks.

REALIZATION 1

The first realization of the geothermal field A, is fractured with a network of 15 fractures with both highly conductive and impermeable ones (see figure 7.12a). Figure 7.13 shows the results of multiple runs with both formulations (natural and molar) on fine-scale and ADM. The relative error indicating the difference between the two formulations is available in figure 7.14.

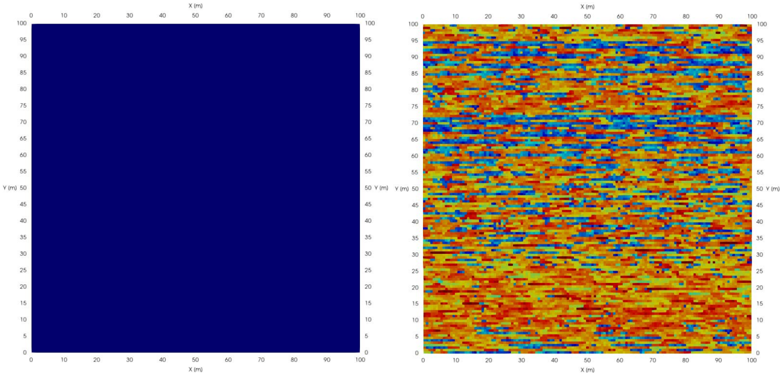

(a) Permeability of the geothermal field A

(b) Permeability of the geothermal field B

Figure 7.11: Test cases 4 and 5: Permeability maps. For geothermal field A, a homogeneous permeability with $K_m = 10^{-14}$ [m^2] is considered (figure 7.11a), and for field B, a heterogeneous permeability map extracted from the SPE10 bottom layer model is assumed (7.11b).

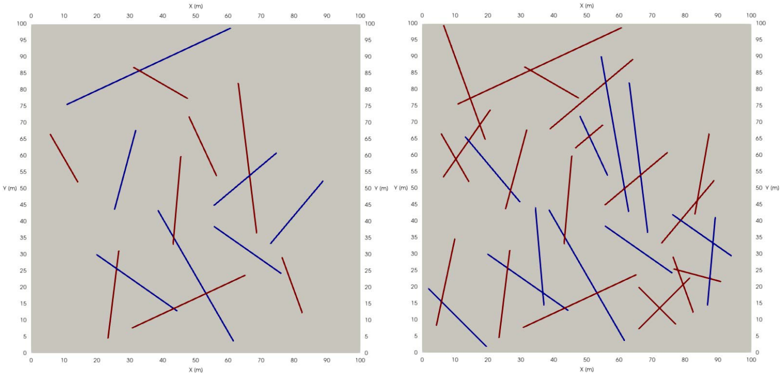

(a) The fracture network with 15 fractures

(b) The fracture network with 30 fractures

Figure 7.12: Test cases 4 and 5: The fracture networks used for test cases 4, 5 and 6.

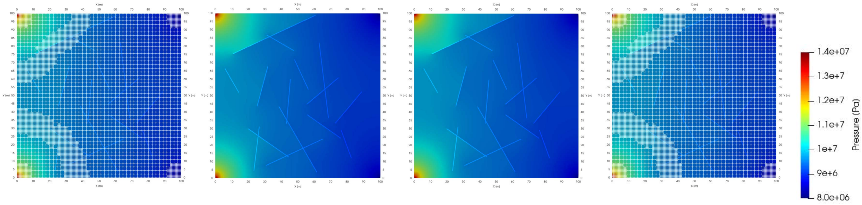

(a) ADM, natural formulation (b) Fine-scale, natural formulation (c) Fine-scale, molar formulation (d) ADM, molar formulation

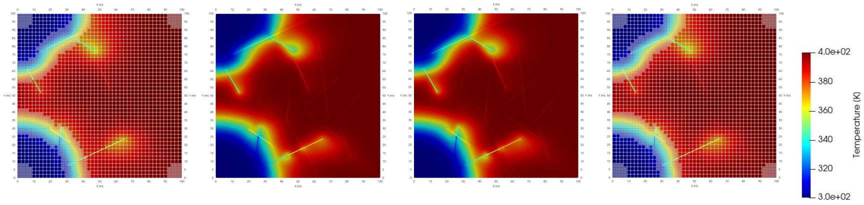

(e) ADM, natural formulation (f) Fine-scale, natural formulation (g) Fine-scale, molar formulation (h) ADM, molar formulation

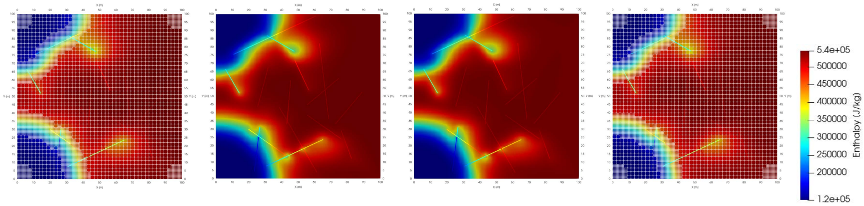

(i) ADM, natural formulation (j) Fine-scale, natural formulation (k) Fine-scale, molar formulation (l) ADM, molar formulation

Figure 7.13: Test case 4: Realization 1. The pressure (top row), temperature (middle row) and the total enthalpy (bottom row) results of the fine-scale and ADM simulations, both for the natural and the molar formulation.

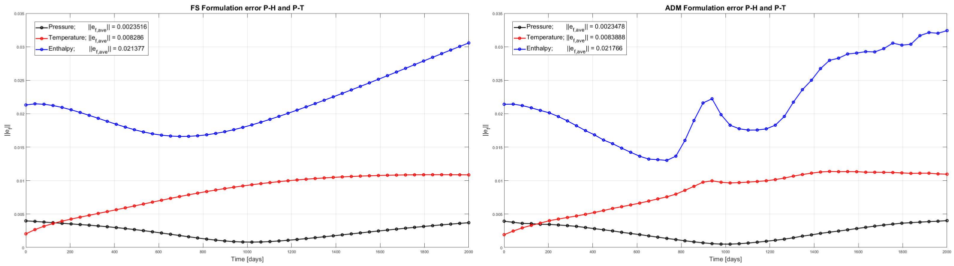

(a) The formulation error for fine-scale (b) The formulation error for ADM

Figure 7.14: Test case 4: Realization 1. The formulation error is calculated as a relative error (in second norm) between the natural formulation and the molar formulation. This error is calculated separately for the fine-scale and the ADM results and based on the equation (7.7).

REALIZATION 2

In the second realization of geothermal field A, the domain consists of 30 fractures (including highly conductive fractures and flow barriers; see figure 7.12b). Figure 7.15 contains the results of the multiple runs with both formulations (natural and molar) on fine-scale and ADM. The relative error indicating the difference between the two formulations can be found in figure 7.16.

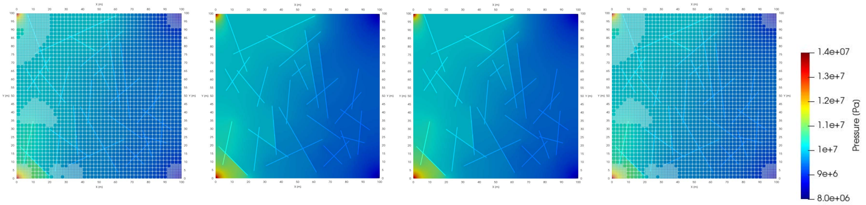

(a) ADM, natural formulation (b) Fine-scale, natural formulation (c) Fine-scale, molar formulation (d) ADM, molar formulation

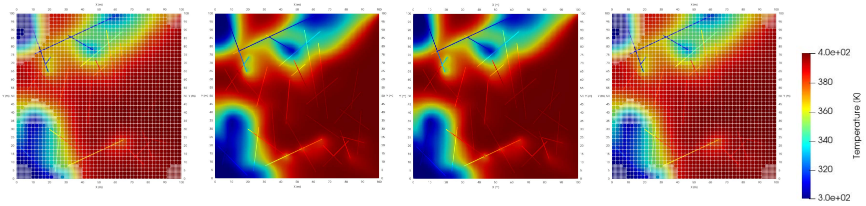

(e) ADM, natural formulation (f) Fine-scale, natural formulation (g) Fine-scale, molar formulation (h) ADM, molar formulation

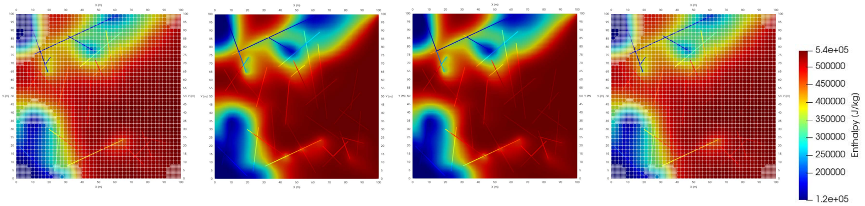

(i) ADM, natural formulation (j) Fine-scale, natural formulation (k) Fine-scale, molar formulation (l) ADM, molar formulation

Figure 7.15: Test case 4: Realization 2. The pressure (top row), temperature (middle row) and the total enthalpy (bottom row) results of the fine-scale and ADM simulations, both for the natural and the molar formulation.

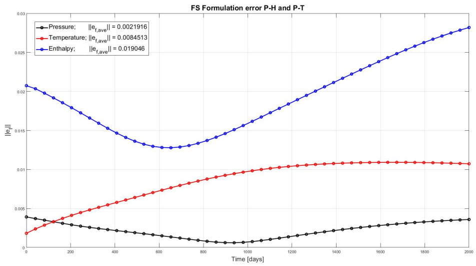

Figure 7.16: Test case 4: Realization 2. The formulation error is calculated as a relative error (in second norm) between the natural formulation and the molar formulation. This error is calculated based on equation (7.7).

TEST CASE 5: GEOTHERMAL FIELD B

In this test case, the geothermal field B with assumption of heterogeneous permeability is considered which is extracted from the SPE10 bottom layer model. Figure 7.11b shows the heterogeneous permeability map. Similar to the previous test case, two realizations are taken into account, one with 15 fractures and one with 30 fractures. Figure 7.12 shows the geometry of the fracture networks.

REALIZATION 1

In the first realization of the geothermal field B, the domain has a network of 15 fractures with mixed conductivities. The results of the multiple runs with both formulations (natural and molar) on fine-scale and ADM are presented in figure 7.17. The relative error indicating the difference between the two formulations is available in figure 7.18.

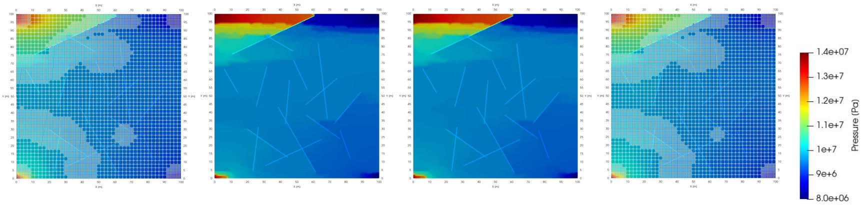

(a) ADM, natural formulation (b) Fine-scale, natural formulation (c) Fine-scale, molar formulation (d) ADM, molar formulation

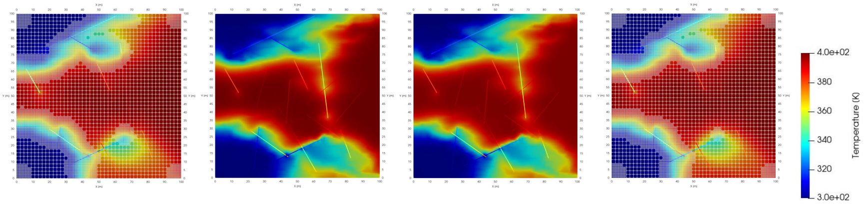

(e) ADM, natural formulation (f) Fine-scale, natural formulation (g) Fine-scale, molar formulation (h) ADM, molar formulation

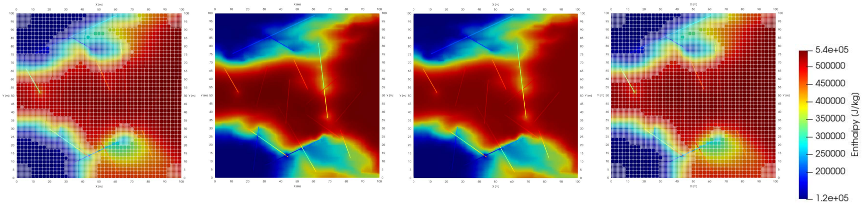

(i) ADM, natural formulation (j) Fine-scale, natural formulation (k) Fine-scale, molar formulation (l) ADM, molar formulation

Figure 7.17: Test case 5: Realization 1. The pressure (top row), temperature (middle row) and the total enthalpy (bottom row) results of the fine-scale and ADM simulations, both for the natural and the molar formulation.

REALIZATION 2

In the second realization of the geothermal field B, the domain consists of 30 fractures (including highly conductive fractures and flow barriers; see figure 7.12b). Figure 7.19 contains the results of the multiple runs with both formulations (natural and molar) on fine-scale and ADM. The relative error indicating the difference between the two formulations can be found in figure 7.20.

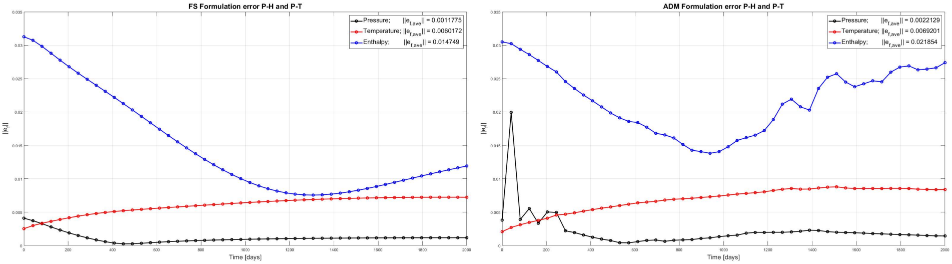

(a) The formulation error for fine-scale

(b) The formulation error for ADM

Figure 7.18: Test case 5: Realization 1. The formulation error is calculated as a relative error (in second norm) between the natural formulation and the molar formulation. This error is calculated separately for the fine-scale and the ADM results and based on the equation (7.7).

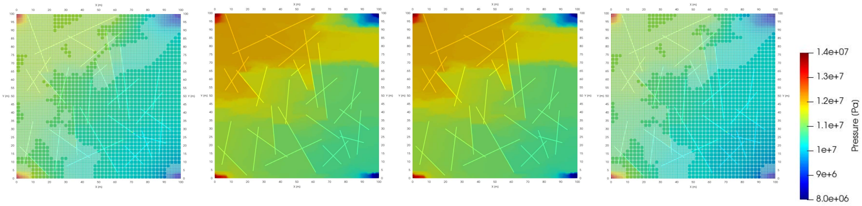

(a) ADM, natural formulation

(b) Fine-scale, natural formulation

(c) Fine-scale, molar formulation

(d) ADM, molar formulation

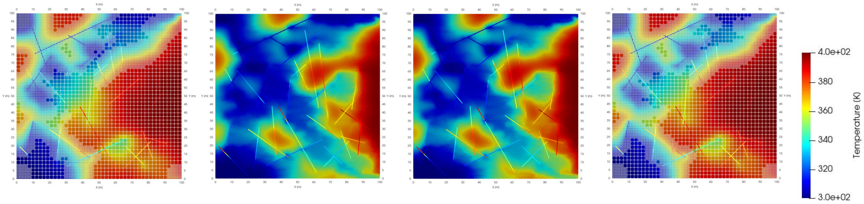

(e) ADM, natural formulation

(f) Fine-scale, natural formulation

(g) Fine-scale, molar formulation

(h) ADM, molar formulation

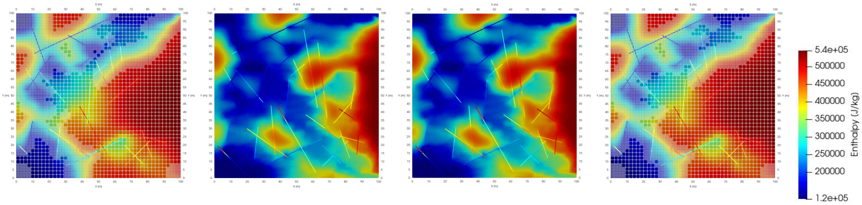

(i) ADM, natural formulation

(j) Fine-scale, natural formulation

(k) Fine-scale, molar formulation

(l) ADM, molar formulation

Figure 7.19: Test case 5: Realization 2. The pressure (top row), temperature (middle row) and the total enthalpy (bottom row) results of the fine-scale and ADM simulations, both for the natural and the molar formulation.

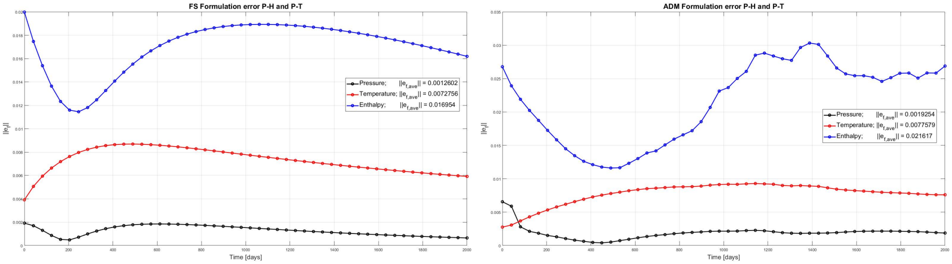

(a) The formulation error for fine-scale

(b) The formulation error for ADM

Figure 7.20: Test case 5: Realization 2. The formulation error is calculated as a relative error (in second norm) between the natural formulation and the molar formulation. This error is calculated separately for the fine-scale and the ADM results and based on the equation (7.7).

7.2.3. MULTIPHASE FLOW IN HIGH-ENTHALPY GEOTHERMAL SYSTEMS USING MOLAR FORMULATION (P-H)

In this subsection with test cases 6-8, the ADM method is assessed for multiphase flow in high-enthalpy fractured geothermal reservoirs using the molar formulation. In test case 6, a 1D domain with input parameters of the geothermal field A is considered. In test case 7 and 8, a 2D and 3D fractured domain is used to assess the ADM results on different tolerances of the ADM grid resolution selection criteria of $\Delta H = \{0.25, 0.5, 1.0, 2.0, 4.0, 8.0\} \times 10^5$ [J/kg]. Table 7.4 lists the input parameters that are mutually used in these two test cases.

TEST CASE 6: 1D HIGH-ENTHALPY SYSTEM (FINE-SCALE)

In this test case, a 1D domain (thus non-fractured) is considered. The rock and fluid properties are taken from the test case 4. The purpose of this test case is the analysis of the multiphase flow in high-enthalpy geothermal systems. However, due to thermodynamical restriction, some input parameters and the initial reservoir conditions are modified for this test case (and the next test case) and are presented in table 7.5.

The simulation results are shown for four different simulation times, i.e.,
$t = \{15, 44, 114, 192\}$[days] in figure 7.21.

The results here are indicative of a correct implementation of the molar formulation for multiphase flow and heat transfer. In order to discuss the physical phenomena observed in multiphase simulations, from the results shown in figure 7.21, those from simulation time $t = 44$[days] is the focused and now highlighted in figure 7.22. Three different regions can be defined in the pressure and enthalpy solutions presented in this figure. Region “A” shows the part of the system in the compressed water region and region “C” shows the system under two-phase conditions. Region “B” marks the transition of the system from two-phase to single-phase conditions. The system, with initial conditions defined in the two-phase region, is still existing under these conditions in region “C” as illustrated by the enthalpy and saturation values. The transition of the system into the single-phase compressed water region is marked by the boundary between regions “C” and “B”. First of all, the transition is indicated by a change in pressure gradient due to the different compressibilities between both phases. Secondly, as steam condenses

Table 7.4: The input parameters mutually used in the test cases 7 and 8.

Property	value
Porosity (ϕ)	0.2
Fracture apertures (a_f)	5.0×10^{-3} [m^{-3}]
Fracture permeability (K_f)	$\{10^{-20}, 10^{-8}\}$ [m^2]
Rock density (ρ_r)	2600 [kg/m^3]
Water liquid compressibility ($c_{w,l}$)	10^{-9} [1/Pa]
Water vapor compressibility ($c_{s,v}$)	10^{-6} [1/Pa]
Rock compressibility (c_r)	10^{-8} [1/Pa]
Water liquid specific heat capacity ($C_{p,w,l}$)	4200 [J/kg/K]
Water vapor specific heat capacity ($C_{p,w,v}$)	8000 [J/kg/K]
Rock specific heat capacity ($C_{p,r}$)	850 [J/kg/K]
Water liquid thermal conductivity ($\Lambda_{w,l}$)	0.6 [W/m/K]
Water vapor thermal conductivity ($\Lambda_{w,v}$)	0.1 [W/m/K]
Rock thermal conductivity (Λ_r)	3.0 [W/m/K]
Initial pressure of the reservoir (p_{init})	5.0×10^6 [Pa]
Initial enthalpy of the reservoir (H_{init})	1.6×10^6 [J/kg]
Injection pressure (p_{inj})	6.0×10^6 [Pa]
Injection enthalpy (H_{inj})	3.0×10^5 [J/kg]
Production pressure (p_{prod})	4.0×10^6 [Pa]
Simulation time [days]	200 [days]

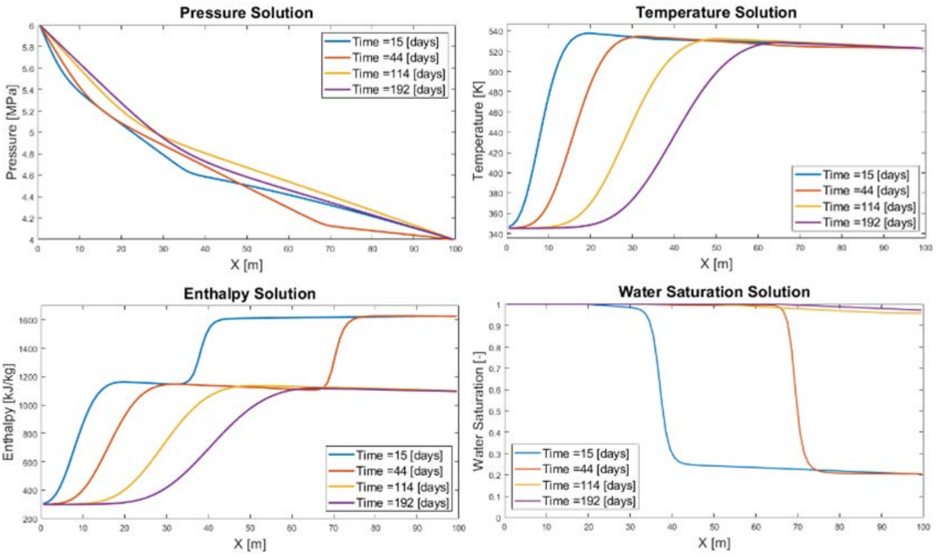

Figure 7.21: Test case 6: The fine-scale results of the multiphase flow in high-enthalpy geothermal system for the 1D domain used in this test case. Pressure, temperature, enthalpy and the saturation of water are plotted for four simulation times of $t = \{15, 44, 114, 192\}$[days].

Table 7.5: The modified input parameters for the test cases 6 and 7.

Property	value
Injection temperature (T_{inj})	345 [K]
Injection pressure (p_{inj})	0.6×10^7 [Pa]
Production pressure (p_{prod})	0.4×10^7 [Pa]
Initial pressure (p_{init})	0.5×10^7 [Pa]
Initial temperature (T_{init})	537 [K]
Initial enthalpy (H_{init})	1.6×10^6 [J/kg]
Initial water saturation ($S_{w,init}$)	0.28 [-]

into the liquid water phase, the enthalpy of the system decreases. This condensation also lowers the reservoir pressure. The latent heat of condensation yields an increase in both enthalpy and temperature when moving from region "*B*" to region "*A*". Note that the water saturation in region "*B*" shows a minor amount of steam being present, and it is only in region "*A*" that the steam phase becomes fully absent. Region "*A*" therefore represents the part of the reservoir in which the system has fully transitioned into the compressed water region, and therefore the cold-water front (shown with dashed red line if figure 7.22) is observed in this region. As the system under two-phase conditions is represented by a single temperature, a temperature gradient is only observed at the location of the cold-water front. Naturally, a second enthalpy gradient is also observed at this location. Note that a slight change in pressure gradient can be observed at the position of the cold-water front due to the differences in the properties of liquid water at different temperatures.

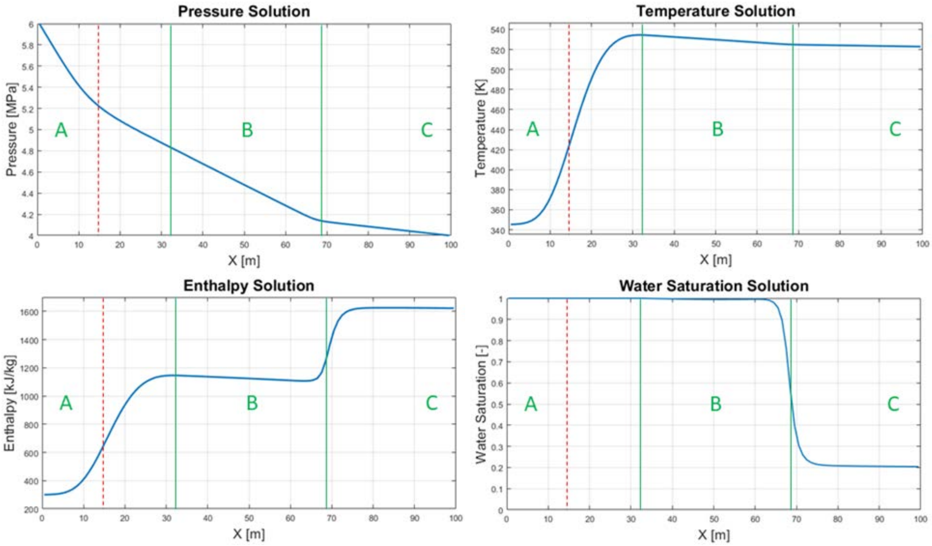

Figure 7.22: Test case 6: The results of simulation at time $t = 44$[days].

7.2.4. TEST CASE 7: 2D HIGH-ENTHALPY FRACTURED TEST CASE (ADM)

In this test case, a 2D domain of 75 [m] × 75 [m] with 30 fractures is considered. A 176 × 176 fine-scale computational grid is imposed on the rock matrix and the fractures are discretized into 815 grids (total of 31791 grids). The permeability of the rock matrix has a range of $K_{m_{min}} = 1.4 \times 10^{-15}$ [m^2] to $K_{m_{max}} = 1.4 \times 10^{-12}$ [m^2]. Fractures are either highly conductive with $K_{f_{max}} = 10^{-8}$ [m^2] or impermeable with $K_{f_{min}} = 10^{-20}$ [m^2]. The fracture network can be seen in figure 7.23a. Two injection wells are located at the bottom and top left corners with injection pressure of $p_{\text{inj}} = 6 \times 10^6$ [Pa] and two production wells are at the bottom and top right corners with pressure of $p_{\text{prod}} = 4 \times 10^6$ Pa. Table 7.4 shows the input parameters of this test case. The simulation time is set for $t = 200$[days] with reports being printed at 100 isochronal intervals.

The ADM simulations make use of two coarsening levels with coarsening ratio of $\gamma = 5$ at each dimension for all the media. The ADM results are obtained for $\Delta H = \{0.25, 0.5, 1.0, 2.0, 4.0, 8.0\} \times 10^5$ [J/kg] tolerances and are compared to fine-scale results.

Figure 7.23 shows the permeability map and the simulation results for fine-scale and the ADM with grid resolution selection tolerance of $\Delta H = \{1.0, 2.0, 4.0\} \times 10^5$ [J/kg]. These results are at simulation time $t = 40$[days]. In the permeability map, the fractures with high conductivity are shown in black color and the flow barriers are shown in white color. The first row below the permeability map contains the pressure results. The saturation of liquid water, the temperature and the total fluid enthalpy distribution in the reservoir at the mentioned simulation time are presented in the rows below the pressure results respectively. For the selected ADM tolerances, the errors are given below each 2D plot.

Figures 7.24 illustrates more details regarding the errors and the percentage of the active grid cells used during the simulation for this test case. Note that the percentage of active grid cells represents the reduction in the number of grid cells that are used to solve the system of equations. For instance, a percentage of 25% means that the size of the linear system is by average 4 times smaller in the ADM run compared with the fine-scale simulation, over the entire simulation time.

7.2.5. TEST CASE 8: 3D HIGH-ENTHALPY FRACTURED TEST CASE (ADM)

For the purpose of this test case, a 3D domain with the extent of 100 [m] × 100 [m] × 40 [m] consisting of 15 fractures with mixed conductivities is designed. The rock matrix is discretized into 54 × 54 × 18 grid cells and 1017 grid cells are imposed on the fracture network (in total 53505 grid cells). The matrix has homogeneous permeability of $K_m = 10^{-14}$ [m^2], but fractures have mix conductivity with $K_{f_{max}} = 10^{-8}$ [m^2] for highly conductive fractures and $K_{f_{min}} = 10^{-20}$ [m^2] for the impermeable ones. Figure 7.25b illustrates the geometry of the fracture network and highlights the fractures with different colors based on their conductivities. Two injection wells exist on the bottom left and the top left boundaries with pressure of $p_{\text{inj}} = 6 \times 10^6$ [Pa]. Similarly, two production wells are located at the bottom right and the top right boundaries with pressure of $p_{\text{prod}} = 4 \times 10^6$ [Pa]. All the wells are vertical and perforate the entire thickness of the reservoir. All the simulations are run for $t = 200$[days]. Similar to the previous test case, the ADM simulations are run for grid resolution selection tolerance of $\Delta H = \{0.25, 0.5, 1.0, 2.0, 4.0\} \times 10^5$ [J/kg]. In the ADM runs, two coarsening levels are used with the coarsening ratio of $\gamma = 3$ at each dimension for all the media. For the sake of visualization aid, figure 7.25a shows how

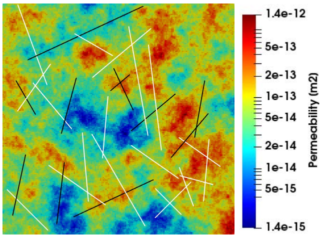

(a) Permeability (b)

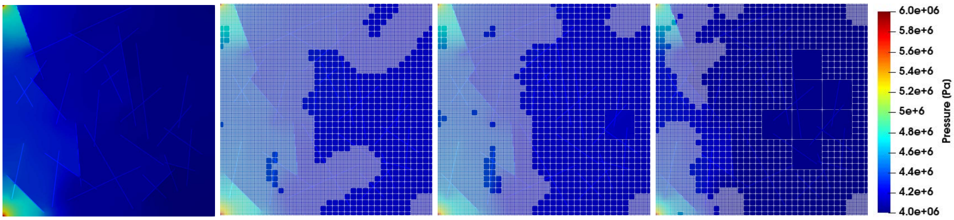

(c) Fine-scale

(d) ADM with $\Delta H = 1.0 \times 10^5$ [J/kg], $e_p = 1.1 \times 10^{-2}$, $AGC = 53\%$

(e) ADM with $\Delta H = 2.0 \times 10^5$ [J/kg], $e_p = 1.2 \times 10^{-2}$, $AGC = 41\%$

(f) ADM with $\Delta H = 4.0 \times 10^5$ [J/kg], $e_p = 1.8 \times 10^{-2}$, $AGC = 16\%$

(g)

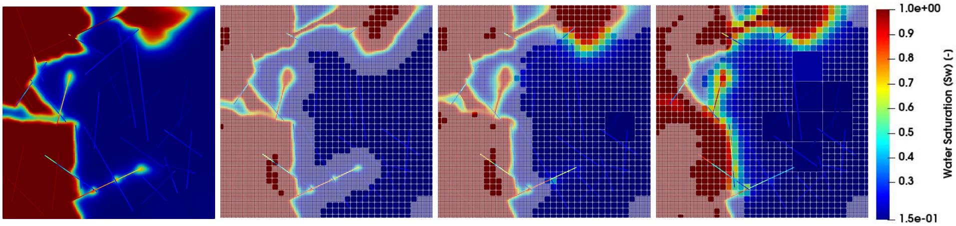

(h) Fine-scale

(i) ADM with $\Delta H = 1.0 \times 10^5$ [J/kg], $e_S = 1.2 \times 10^{-1}$, $AGC = 53\%$

(j) ADM with $\Delta H = 2.0 \times 10^5$ [J/kg], $e_S = 1.4 \times 10^{-1}$, $AGC = 41\%$

(k) ADM with $\Delta H = 4.0 \times 10^5$ [J/kg], $e_S = 1.6 \times 10^{-1}$, $AGC = 16\%$

(l)

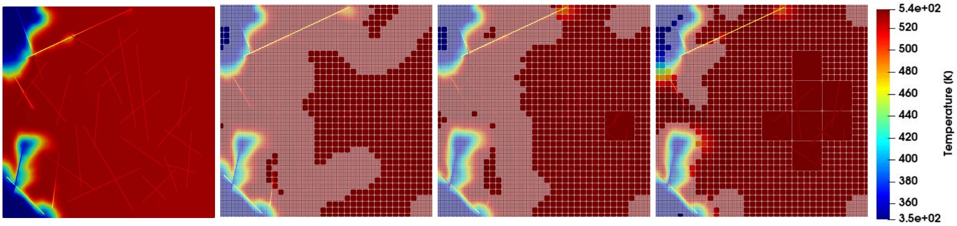

(m) Fine-scale

(n) ADM with $\Delta H = 1.0 \times 10^5$ [J/kg], $e_T = 2.7 \times 10^{-2}$, $AGC = 53\%$

(o) ADM with $\Delta H = 2.0 \times 10^5$ [J/kg], $e_T = 3.5 \times 10^{-2}$, $AGC = 41\%$

(p) ADM with $\Delta H = 4.0 \times 10^5$ [J/kg], $e_T = 3.2 \times 10^{-2}$, $AGC = 16\%$

(q)

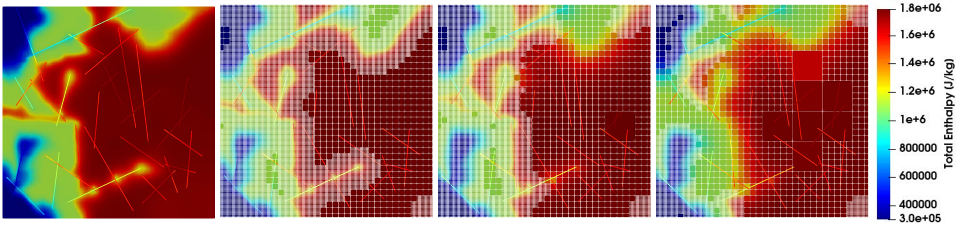

(r) Fine-scale

(s) ADM with $\Delta H = 1.0 \times 10^5$ [J/kg], $e_H = 8.6 \times 10^{-2}$, $AGC = 53\%$

(t) ADM with $\Delta H = 2.0 \times 10^5$ [J/kg], $e_H = 1.0 \times 10^{-1}$, $AGC = 53\%$

(u) ADM with $\Delta H = 4.0 \times 10^5$ [J/kg], $e_H = 1.1 \times 10^{-1}$, $AGC = 53\%$

(v)

Figure 7.23: Test case 7: Fine-scale and ADM results from the tolerances of $\Delta H = \{1.0, 2.0, 4.0\} \times 10^5$ [J/kg]. The top figure shows the permeability map of the reservoir and the fracture networks consisting of highly conductive fractures (in black color) and impermeable ones (in white color). Underneath the permeability map, in descending order, the solutions of pressure, water saturation, temperature and total enthalpy distribution are illustrated.

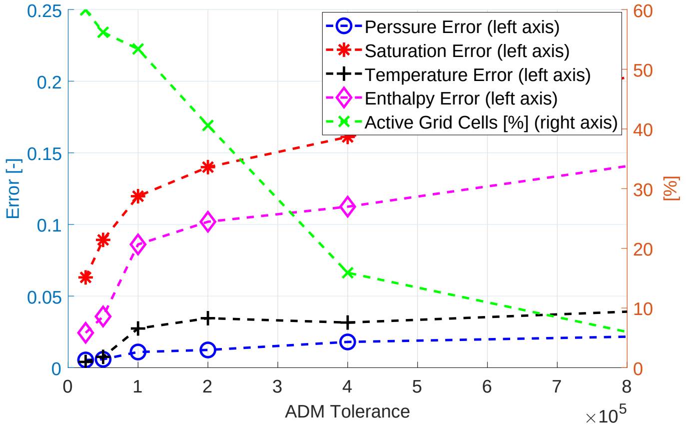

Figure 7.24: Test case 7: ADM errors and the percentage of the active grid cells used for each ADM run. The error for each parameter as well as the percentage of the active grid cells for each ADM run are averaged over the entire simulation.

the ADM grid combines the grids from different resolution in this test case at simulation time $t = 28$[days].

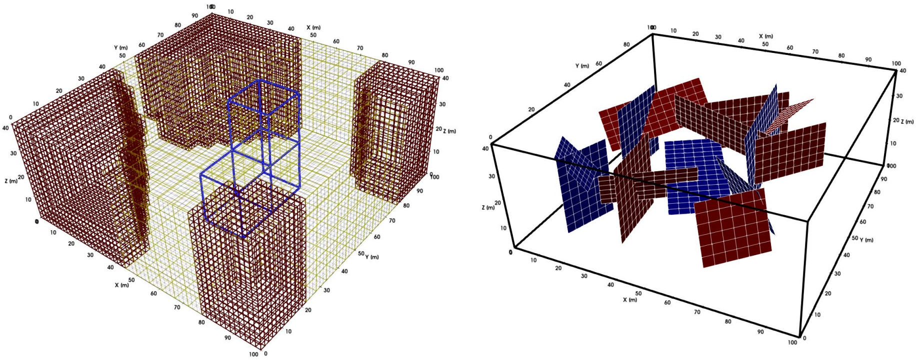

(a) The ADM grid

(b) The fracture network

Figure 7.25: Test case 8: Figure 7.25a provides illustration of the ADM grid at simulation time $t = 28$ [dyas]) for $\Delta H = 0.5 \times 10^5$ [J/kg]. Note that the grid cells near the wells are always kept at the fine-scale resolution. The figure 7.25b visualizes the geometry of the fracture network. The highly conductive fractures ($K_f = 10^{-8}$ [m^2]) are shown in red color and the impermeable ones ($K_f = 10^{-20}$ [m^2]) are colored in blue.

The errors of the ADM runs as well as the percentage of the active grid cells for the test case 8 are presented in figure 7.27. Please note that these values are averaged over the entire simulation time.

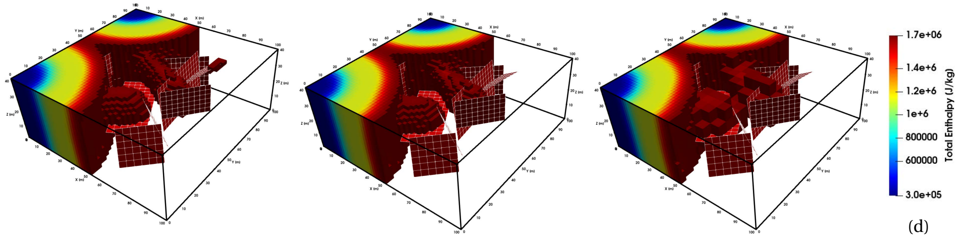

(d)

(a) Fine-scale

(b) ADM with $\Delta H = 1.0 \times 10^5$ [J/kg], $e_H = 2.5 \times 10^{-3}$, $AGC = 53\%$

(c) ADM with $\Delta H = 4.0 \times 10^5$ [J/kg], $e_H = 3.4 \times 10^{-3}$, $AGC = 41\%$

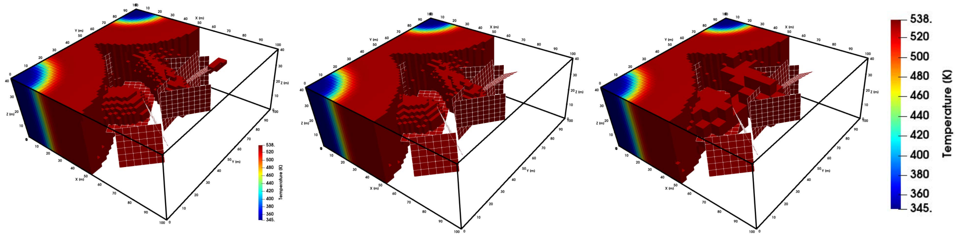

(h)

(e) Fine-scale

(f) ADM with $\Delta H = 1.0 \times 10^5$ [J/kg], $e_H = 1.8 \times 10^{-4}$, $AGC = 53\%$

(g) ADM with $\Delta H = 4.0 \times 10^5$ [J/kg], $e_H = 2.5 \times 10^{-4}$, $AGC = 41\%$

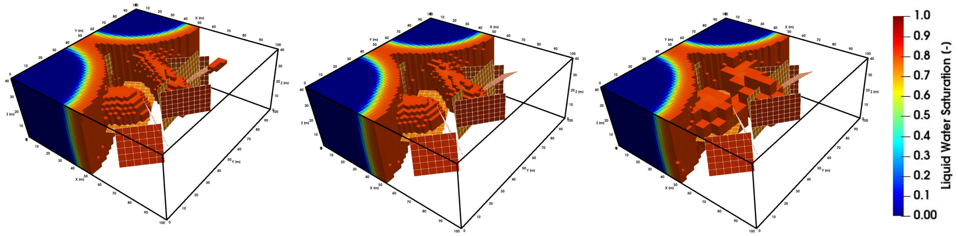

(l)

(i) Fine-scale

(j) ADM with $\Delta H = 1.0 \times 10^5$ [J/kg], $e_S = 1.0 \times 10^{-2}$, $AGC = 53\%$

(k) ADM with $\Delta H = 4.0 \times 10^5$ [J/kg], $e_S = 1.3 \times 10^{-2}$, $AGC = 41\%$

Figure 7.26: Test case 8: Fine-scale and ADM results from the tolerances of $\Delta H = \{1.0, 4.0\} \times 10^5$ [J/kg]. Starting from the top row to the bottom row, the results of total enthalpy, temperature and the saturation of liquid water are presented. Fhe fine-scale results are on the left column and the ADM results are on the middle and the right columns, with their corresponding ADM errors mentioned at the bottom of each plot. Note that for a better visualization, only grids that have a certain range in the solutions are visible.

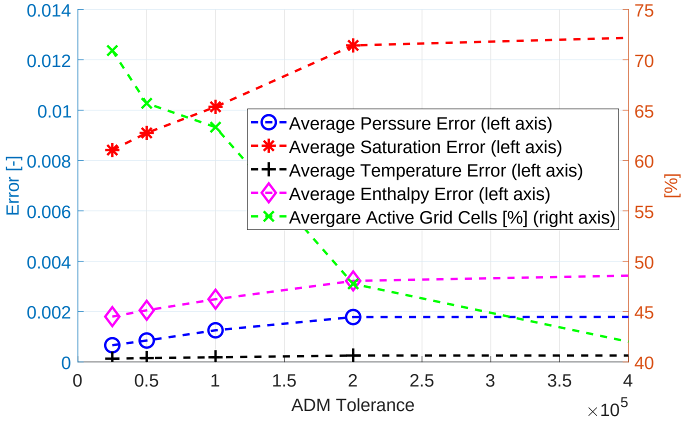

Figure 7.27: Test case 8: ADM errors and the percentage of the active grid cells. The errors provided here and the percentage of the active grid cells are averaged over the entire simulation for each ADM run.

7.3. DISCUSSIONS AND CONCLUSION

7.3.1. SINGLE-PHASE LOW-ENTHALPY SYSTEMS

In this chapter, the ADM method for coupled mass-heat single-phase flow (low-enthalpy) and multiphase flow (high-enthalpy) in fractured geothermal reservoirs was described. The discretized and linearized system of equations was mapped to a dynamically defined multilevel resolution grid (also called as ADM grid) using the ADM prolongation and restriction operators. This multilevel grid resolution provides significant reduction in the size of the fine-scale linear system of equations while keeping the accuracy at a user-defined threshold. This is achieved by employing fine-scale high resolution grid cells only where and when needed (e.g., at the heat front with sharp solution gradient, and near the wells with high velocity fluxes). For fractured models, the pEDFM model (see section 3.3.3) was used to capture the explicit fractures with mixed conductivities. Once the system is solved at the ADM resolution, to obtain an approximated fine-scale solution, the ADM solution is mapped back to fine-scale resolution using the ADM prolongation operator. The resolution of each grid cell in the ADM method is selected via a front tracking technique set by a user-defined threshold. Through the first three test cases (2D and 3D, all fractured), the accuracy and performance of the ADM method especially for low-enthalpy systems using natural formulation (having pressure p and temperature T as the primary unknowns) was assessed by comparing the ADM results with their fine-scale counterparts. The sensitivity of ADM to different grid coarsening criteria was also studied. It is observed that ADM is capable of providing accurate simulations by employing only a fraction of the fine-scale grid cells in the sub-domains where it is needed. Due to the rarefaction of the temperature distribution (highly diffused temperature at the front), more fine-scale grid cells are used at the temperature front depending on the threshold. Additionally, ADM provides an algebraic framework which brings a scalable simulation method for thermal fluid flows. One can expect that by increasing the size of the domain, the percentage of active grid cells used during simulation reduces. Therefore, ADM introduces a promising simulation strategy for real field-scale geothermal reservoir simulations.

7.3.2. NATURAL FORMULATION VS. MOLAR FORMULATION

In addition, for low-enthalpy geothermal systems, comparisons were made between the natural formulation (p-T system) and the molar formulation (having pressure p and the total fluid enthalpy H as the primary unknowns), both for fine-scale and ADM simulations. Various test cases and scenarios were used to compare the results of both formulations. The simulation performance of both primary variable formulations shows the same behavior, independent of the simulation strategy. When cold-water is injected into the reservoir, the temperature at the location of the injection well decreases only due to conduction. It is when the reservoir temperature has decreased to the injection temperature that transport of the cold water through the reservoir starts taking place. When the cold-water front propagates further from the injection well, the effect of the convective flux stabilizes and the number of iterations decreases again. Furthermore, the number of iterations also stabilizes at this point. A heterogeneous permeability distribution greatly affects the transport of cold-water through the reservoir. Similar to the heterogeneous absolute permeability, the different positions of the fractures relative to the position of the cold-water front further increase the erratic behavior of the actual number of iterations required. The fine-scale simulation performance of both primary variable formulations is very similar for the model realizations.

The ADM simulation performance of both primary variable formulations shows similar behavior to the fine-scale simulation performance described above. Furthermore, the performance between the fine-scale and ADM simulation approaches is near identical, with the exception of the third realization of the geothermal field A. Here, the ADM simulation strategy failed to find a solution based on the natural variable formulation. As the ADM strategy was able to effectively find a solution based on the molar formulation, the apparent issue regarding the natural formulation may be related to the increasing mismatch in reservoir enthalpy when using this formulation. The ADM results from the first realization of field A show no issues between the formulations in terms of capability of the ADM method to find a solution. The fine-scale simulation performance of both primary variable formulations is again very similar for the model realizations of the geothermal field B. Due to the heterogeneous permeability field, the required number of iterations to achieve convergence as well as the sensitivity to the size of the time-step is generally higher compared to the geothermal field A. The ADM simulation performance is also similar between both primary variable formulations.

The difference in performance between both formulations using a fine-scale simulation strategy is negligible. The performance itself is largely dependent on the complexity of the problem. These results are similar to those presented in literature [93], despite the added model complexities of a fracture network. Considering the ADM simulation strategy for the geothermal field B, the natural formulation tends to perform slightly better when the model complexity is increased.

7.3.3. MULTIPHASE-PHASE HIGH-ENTHALPY SYSTEMS

At next, the multiphase flow in high-enthalpy geothermal systems using molar formulation was developed for fine-scale and ADM simulations. Through two test cases 6 and 7

(1D non-fractured and 2D fractured), it was shown that the developed method can capture the heat and saturation fronts as well as the transition zone from liquid water to steam. The results presented in the 1D high-enthalpy test case 6 are indicative of a successful implementation of the molar formulation for multiphase flow and heat transfer simulations. In order to discuss the physical phenomena observed in the multiphase simulation, the results from figure 7.21 were presented again in figure 7.22 highlighting the solution at simulation time $t = 44$[days]. In test cases 7 (2D) and 8 (3D), the ADM method and its demonstration of front tracking technique for high-enthalpy fractured media (homogeneous and heterogeneous) using the molar formulation was presented. The ADM performance was assessed by comparing the ADM runs against the fine-scale simulations (as reference solution). The ADM method provides significant computational efficiency by reducing the size of the linear system, while keeping the accuracy at a used-defined level. The ADM error is expectedly higher in presence of increased heterogeneity contrast. ADM performance is significantly dependent on the model complexity. One can conclude that, as the size of the domain increases, the ADM computational gain will be significantly higher.

All the software developments of this dissertation have been carried out in our in-house simulation package DARSim (Delft Advanced Reservoir Simulator) and have been made available open-source at DARSim GitLab repository. As an attempt to deliver the science to the public, various tutorial videos on DARSim have been created by the author and have been published on the ADMIRE YouTube channel.

IV

CONCLUSIONS AND FUTURE WORK

8

CONCLUSIONS AND FUTURE WORK

In the previous chapters various scientific developments during this PhD project were covered. In this chapter, some conclusions are pointed out regarding the various developments and studies done in this dissertation. Moreover, recommendations for possible future work will be presented afterwards.

8.1. CONCLUSIONS

The conducted studies and developments in this work aimed to address the next generation of modeling challenges, solving problems with societal, economic, and environmental impacts in the field of flow in porous media. The demand for technological innovation is one of the main drivers for such work. Accurate modeling of the subsurface flow is crucial for successful field development plans. However, the simulation of fractured porous media especially for real field-scale subsurface domains has proven to be challenging in many aspects. Therefore advanced and scalable numerical schemes are needed that can provide computational efficiency while honoring the accuracy at an acceptable level. Different developments have been made during this PhD project to answer such needs.

8.1.1. PART I

In the introduction chapter 1, the importance of numerical simulations in field of porous media was expressed. The key challenges were highlighted thus emphasizing the necessity of developing advanced scalable numerical methods. Moreover, the efforts done by the scientific community to address the various aspects of those challenges were acknowledged. In addition, new and improved methods were proposed by the author in the mentioned chapter.

In chapter 2, the governing equations and the constitutive correlations for flow in fractured porous media for various flow models were covered in great detail. The thermodynamical relations in geothermal flow models where also discussed.

8.1.2. PART II

In chapter 3, the first section (3.1) included the discretization of the equations. The fine-scale simulation approaches, the coupling strategies for the mass conservation and energy conservation equations, as well as the linearization of the non-linear equations were discussed in the second section of this chapter (3.2). In the last section of this chapter (3.3), different fracture models were covered. First, the embedded discrete fracture model (EDFM) was explained (3.3.1). The EDFM model was evaluated through a simple numerical test by validating its result against the direct numerical simulation (DNS) solution. The EDFM could provide accurate capture of the explicit fractures with high conductivity compared to the rest of the domain. However, it fails to capture the impermeable fractures (or flow barriers). Next, the projection-based EDFM (pEDFM) [46] was described in detail. This method was also validated using a numerical test case and was compared to the DNS (direct numerical simulation) and the EDFM results. The pEDFM can capture the fractures with generic range of conductivities and at the same time provide grid discretization flexibility for the fractures and the rock matrix.

In chapter 4, the development of the pEDFM model for the corner-point grid (CPG) geometry was presented. This development was crucial as real field-scale geological formations cannot be represented by the Cartesian grid geometry, but they are conveniently represented by flexible grids such as the corner-point grid (CPG) geometry. Therefore, the pEDFM model was developed for the CPG geometry to answer the needs for an advanced embedded fracture model to capture the fractures and faults in such subsurface formations. Using various synthetic and geologically-relevant test cases the accuracy and performance of the developed pEDFM model was presented. In these fine-scale simulations with mix-conductivity fractures, it was shown that the pEDFM can accurately capture the physical influence of both highly conductive fractures and flow barriers on the flow patterns. The development of this model can offer great flexibility in the gridding strategies for the real field-scale models, as for many of these models currently, millions of computational grid cells with complex geometrical alignments is imposed to match the positioning of the fractures and faults. The embedded capture of these discontinuities can provide simpler gridding and significant computational gains.

8.1.3. PART III

Up until the end of the previous chapter, the methodologies and the numerical schemes consisted of the simulation strategies in fine-scale resolutions. However, due to the large size of the real field-scale domains, remarkably high-resolution computational grids are usually imposed, resulting in billions of grid cells. Despite the technological advancements in computer hardware and high performance computation, such simulations cannot be run effectively for thousands of realizations using fine-scale simulation strategies. Chapter 5 described the static multilevel multiscale methods for simulation of fluid flow in fractured domains. Using a linear interpolation of the locally computed multiscale basis functions at multiple coarsening levels, an approximated fine-scale solution is obtained. While the multilevel multiscale method reduces the size of the linear system significantly (compared to the fine-scale system), it honors the accuracy and the fine-scale heterogeneity by using the fully coupled basis functions both for the rock matrix and all the explicit fractures. The model described in this chapter employs the multiscale operators that are constructed fully algebraically. The test cases and their results in this chapter demonstrated the model order reduction capabilities of the multilevel multiscale method while showing its accuracy levels.

In chapter 6, the algebraic dynamic multilevel (ADM) method for isothermal fluid flow in fractured porous media was explained. The ADM method [84] combines the dynamic local grid refinement (DLGR) with multilevel multiscale techniques. Using the ADM map, the fine-scale system is mapped to a dynamic multilevel grid resolution. The mapping is occurred by employing the ADM operators that are assembled from the static multilevel multiscale restriction and prolongation operators. These operators are only computed in the beginning of the simulation to increase the computational efficiency. Once the system is solved at this ADM grid resolution, it is mapped back to the fine-scale resolution using the ADM prolongation operator to obtain an approximated solution. The selection of the ADM grid resolution uses a user-defined ADM tolerance for the gradient of the solution at the previous time-step, which serves as a front tracking technique. Therefore, the ADM method uses fine-scale resolution grid cells only when and where needed (e.g., on the transport front), providing a robust and efficient performance while honoring the accuracy at a desired level. Using various 2D and 3D fractured test cases, the performance of the ADM method was assessed by comparing its results to the fine-scale simulations. It was shown that ADM could provide accurate results while using a fraction of the fine-scale grid cells. For large-scale domains, the ADM results in a significant reduction in the size of the linear system, providing an optimal scalability.

Chapter 7 extended the ADM methodology to thermal flow in low-enthalpy and high enthalpy geothermal systems. Regarding the thermodynamical relations, two different formulations exist, the so-called natural formulation with pressure and temperature as the main unknowns, and the so-called molar formulation with pressure and the total fluid enthalpy as the primary unknown.

In the case of the low enthalpy geothermal systems in which the water is assumed to stay in liquid phase (thus a single-phase flow condition), at first, the ADM method was assessed through the first three test cases, where it could be seen that ADM could solve the system with lower number of degrees of freedom (DoF) while keeping the accuracy in a desired level. Moreover, using the next two test cases, a comparison study was made between the two formulation approaches for the fine-scale and the ADM methods. It was shown that the difference between the results of the two formulations was negligible for the low-enthalpy systems.

However, for the high-enthalpy systems where water exists in two phases (liquid and vapor), and mass exchange occurs between the two phases, usage of the molar formulation is preferred as the thermodynamical state of the system is uniquely defined and singularities in the constitutive equations at the critical point are avoided [94]. Through two 2D and 3D fractured test cases, the ADM performance was compared with that of the fine-scale results. The ADM method could decrease the size of the linear system at the cost of accuracy reduction, yet, keeping at a desired level via a user-defined threshold in grid resolution selection. The ADM error was higher in presence of high heterogeneity contrast. Expectedly, the computational efficiency gains of the ADM method increases as the size of the domain becomes larger. The ADM method introduces a promising scalable simulation strategy for the simulation of flow in real field-scale geo-models.

8.2. RECOMMENDATION FOR FUTURE WORK

The methods devised and developed in this work were merely an effort to provide efficient yet accurate scalable simulation strategy for modeling of mass-heat flow in fractured porous media with complex fracture networks and reservoir geometry. While many of the objectives have been fulfilled, the author thinks that various topics and scopes can be considered as future research and development plans. These future developments can potentially enhance the devised methods and shed light on their performance and practicality.

8.2.1. MULTILEVEL MULTISCALE AND ADM METHOD FOR CORNER-POINT GRID GEOMETRY USING THE PEDFM MODEL

The pEDFM model on corner-point grid geometry shows a promising approach to simplification of gridding strategies in geologically relevant models. In parallel, the multilevel multiscale and the ADM methods presented great opportunities for the scalability of the simulation models. Developing the multilevel multiscale and the ADM methods for the corner-point grid geometry using the pEDFM can combine the significant computational gains of these scalable models with the realistic field applicability of the fracture models for real field-scale and geologically relevant fractured domains. Such a development will surely introduce a new horizon for the numerical methods in the field of porous media flow.

8.2.2. CPU BENCHMARKING AND PARALLELIZATION USING GPU

The software developments in this work have been done in an object oriented scientific programming (OOSP) style. The result of these developments is the Delft Advanced Reservoir Simulator (DARSim). The DARSim code is structured with insights to provide better readability and simpler future implementations. However, coding DARSim was carried out in the MATLAB computing environment. There has been no accurate performance comparison study (e.g., CPU time study) on the performance of the devised method compared to the traditional and already-developed techniques. Implementing the DARSim simulator or the devised methods in a compiled programming language (such as C++) would allow a better performance comparison study for the developed methods. Moreover, many computational processes can be done in a parallel manner, such as the computation of multiscale basis functions. Implementation of algorithms for parallelization (e.g., using GPU programming with CUDA) in DARSim could be of significant help towards higher computational efficiency.

8.2.3. DEVISING APPROPRIATE LINEAR SOLVERS FOR ADM

In all the simulation runs of the projects in this work, the linearized set of equations were solved using the MATLAB backslash operator. Studying the employment of other linear solvers such as generalized minimal residual method (GMRES) or biconjugate gradient method (BiCG) could shed light on the reflectivity and performance of various linear solvers in the simulation runs with the ADM method.

REFERENCES

[1] British Petroleum Company. Bp statistical review of world energy. Technical report, British Petroleum Co., 2019.

[2] International Energy Agency. Global energy and co2 emissions in 2020. Technical report, International Energy Agency, 2020.

[3] Agoria. World energy outlook: 5 predictions for the post-covid-19 energy sector. Technical report, Agoria Organization, Belgium, 2021.

[4] J. W. Lund and T. L. Boyd. Direct utilization of geothermal energy 2015 worldwide review. *Geothermics*, 2016.

[5] J. H. Norbeck, M. W. McClure, and R. N. Horne. Field observations at the fenton hill enhanced geothermal system test site support mixed-mechanism stimulation. *Geothermics*, 74:135–149, 2018.

[6] Michael A Celia. Geological storage of captured carbon dioxide as a large-scale carbon mitigation option. *Water Resources Research*, 53(5):3527–3533, 2017.

[7] S. A. Rackley. *Carbon Capture and Storage*. Butterworth-Heinemann, 2017.

[8] J. Gale, N. P. Christensen, A. Cutler, and T. A. Torp. Demonstrating the potential for geological storage of co2: The sleipner and gestco projects. *Environmental Geosciences*, 8(3):160, 2001.

[9] T. A Torp and J. Gale. Demonstrating storage of co2 in geological reservoirs: The sleipner and sacs projects. *Energy*, 29(9):1361 – 1369, 2004. 6th International Conference on Greenhouse Gas Control Technologies.

[10] V. P. Singh, A. Cavanagh, H. Hansen, B. Nazarian, M. Iding, P. S. Ringrose, et al. Reservoir modeling of co2 plume behavior calibrated against monitoring data from sleipner, norway. In *SPE annual technical conference and exhibition*. Society of Petroleum Engineers, 2010.

[11] Jan-Dirk Jansen, Okko H Bosgra, and Paul MJ Van den Hof. Model-based control of multiphase flow in subsurface oil reservoirs. *Journal of Process Control*, 18(9):846–855, 2008.

[12] M. J. OSullivan, K. Pruess, and M. J. Lippmann. State of the art of geothermal reservoir simulation. *Geothermics*, 30(4):395–429, 2001.

[13] G. Axelsson, V. Stefansson, and Y. Xu. Sustainable management of geothermal resources. In *Proceedings of the International Geothermal Conference*, pages 40–48, 2003.

[14] J. Burnell, E. Clearwater, Croucher A., W. Kissling, J. OSullivan, M. OSullivan, and A. Yeh. Future directions in geothermal modelling. In *34rd New Zealand Geothermal Workshop*, pages 19–21, 2012.

[15] J. Burnell, M. OSullivan, J. OSullivan, W. Kissling, A. Croucher, J. Pogacnik, S. Pearson, G. Caldwell, S. Ellis, S. Zarrouk, and M. Climo. Geothermal supermodels: the next generation of integrated geophysical, chemical and flow simulation modelling tools. In *World Geothermal Congress*, pages 19–21, 2015.

[16] Norne field, equinor. https://www.equinor.com/en/what-we-do/norwegian-continental-shelf-platforms/norne.html. Accessed: 2021-02-30.

[17] Statoil makes new oil and gas discovery near norne. https://www.oceannews.com/news/energy/statoil-makes-new-oil-gas-discovery-near-norne. Accessed: 2021-02-30.

[18] K. Bao, K.-A. Lie, O. Møyner, and M. Liu. Fully implicit simulation of polymer flooding with mrst. *Comput. Geosci.*, 21(5-6):1219–1244, 2017.

[19] Riyadh Al-Raoush and Apostolos Papadopoulos. Representative elementary volume analysis of porous media using x-ray computed tomography. *Powder Technology*, 200(1-2):69–77, jun 2010.

[20] Quan Gan and Derek Elsworth. Production optimization in fractured geothermal reservoirs by coupled discrete fracture network modeling. *Geothermics*, 62:131–142, 2016.

[21] Nima Gholizadeh Doonechaly, Reda R Abdel Azim, and Sheik S Rahman. A study of permeability changes due to cold fluid circulation in fractured geothermal reservoirs. *Groundwater*, 54(3):325–335, 2016.

[22] S Salimzadeh, M Grandahl, M Medetbekova, and HM Nick. A novel radial jet drilling stimulation technique for enhancing heat recovery from fractured geothermal reservoirs. *Renewable energy*, 139:395–409, 2019.

[23] Brian Berkowitz. Characterizing flow and transport in fractured geological media: A review. *Advances in water resources*, 25(8-12):861–884, 2002.

[24] Zhi Yang Wong, Roland N. Horne, and Hamdi A. Tchelepi. Sequential implicit nonlinear solver for geothermal simulation. *Journal of Computational Physics*, 368:236 – 253, 2018.

[25] E. Rossi, M. A. Kant, C. Madonna, M. O. Saar, and P. Rudolf von Rohr. The effects of high heating rate and high temperature on the rock strength: Feasibility study of a thermally assisted drilling method. *Rock Mechanics and Rock Engineering*, 2018.

[26] T. T. Garipov, M. Karimi-Fard, and H. A. Tchelepi. Discrete fracture model for coupled flow and geomechanics. *Computational Geosciences*, 20(1):149–160, Feb 2016.

[27] N Gholizadeh Doonechaly, R Abdel Azim, and SS Rahman. Evaluation of recoverable energy potential from enhanced geothermal systems: a sensitivity analysis in a poro-thermo-elastic framework. *Geofluids*, 16(3):384–395, 2016.

[28] F. Morel and J. Morgan. Numerical method for computing equilibriums in aqueous chemical systems. *Environmental Science & Technology*, 6(1):58 – 67, 1972.

[29] A. M. M. Leal, D. A. Kulik, W. R. Smith, and M. O. Saar. An overview of computational methods for chemical equilibrium and kinetic calculations for geochemical and reactive transport modeling. *Pure and Applied Chemistry*, 89(5):597 – 643, 2017.

[30] S Salimzadeh and HM Nick. A coupled model for reactive flow through deformable fractures in enhanced geothermal systems. *Geothermics*, 81:88–100, 2019.

[31] J. Warren and P. Root. The behavior of naturally fractured reservoirs. *SPE J.*, pages 245–255, 1963.

[32] G. Barenblatt, Y Zheltov, and I. Kochina. Basic concepts in the theory of seepage of homogeneous fluids in fissurized rocks. *J. Appl. Math. Mech.*, 5(24):1286–1303, 1983.

[33] H. Kazemi, L.S. Merrill, K.L. Porterfield, and P.R. Zeman. Numerical simulation of water-oil flow in naturally fractured reservoirs. *SPE Journal*, (5719):317–326, December 1996.

[34] P. Dietrich, R. Helmig, M. Sauter, H. Hotzl, J. Kongeter, and G. Teutsch. *Flow and Transport in Fractured Porous Media.* Springer, 2005.

[35] Karimi-Fard, L.J. Durlofsky, and K.Aziz. An efficient discrete-fracture model applicable for general-purpose reservoir simulators. *SPE Journal*, pages 227–236, June 2004.

[36] C. L. Jensen S. H. Lee and M. F. Lough. An efficient finite difference model for flow in a reservoir with multiple length-scale fractures. *SPE ATCE*, October 1999.

[37] S.H. Lee, M.F. Lough, and C.L. Jensen. Hierarchical modeling of flow in naturally fractured formations with multiple length scales. *Water Resource Research*, 37(3):443–455, March 2001.

[38] H. Hajibeygi, D. Karvounis, and P. Jenny. An upstream finite element method for solution of transient transport equation in fractured porous media. *Journal of Computational Physics*, 230:8729–8743, 2012.

[39] L. Li and S. H. Lee. Efficient field-scale simulation of black oil in naturally fractured reservoir through discrete fracture networks and homogenized media. *SPE Reservoir Evaluation & Engineering*, pages 750–758, 2008.

[40] R Ahmed, Michael G Edwards, Sadok Lamine, B A H Huisman, and M Pal. Control-volume distributed multi-point flux approximation coupled with a lower-dimensional fracture model. *J. Comput. Phys.*, 284:462–489, 2015.

[41] D. C. Karvounis. *Simulations of Enhanced Geothermal Systems with an Adaptive Hierarchical Fracture Representation.* PhD thesis, ETH Zurich, 2013.

[42] V. Reichenberger, H. Jakobs, P. Bastian, and Rainer Helmig. A mixed-dimensional finite volume method for two-phase flow in fractured porous media. *Advances in Water Resources*, 29:1020–1036, 2006.

[43] A. Moinfar, A. Varavei, K. Sepehrnoori, and R. T. Johns. Development of an efficient embedded discrete fracture model for 3d compositional reservoir simulation in fractured reservoirs. *SPE J.*, 19:289–303, 2014.

[44] H. Hajibeygi, D. Karvounis, and P. Jenny. A hierarchical fracture model for the iterative multiscale finite volume method. *J. Comput. Phys.*, 230(24):8729–8743, 2011.

[45] M. HosseiniMehr, M. Cusini, C. Vuik, and H. Hajibeygi. Algebraic dynamic multilevel method for embedded discrete fracture model (f-adm). *Journal of Computational Physics*, 373:324–345, 2018.

[46] M. Tene, S. B. M. Bosma, M. S. A. Kobaisi, and H. Hajibeygi. Projection-based embedded discrete fracture model (pedfm). *Adv. Water Resour.*, 105:205 – 216, 2017.

[47] Mousa HosseiniMehr, Cornelis Vuik, and Hadi Hajibeygi. Adaptive dynamic multilevel simulation of fractured geothermal reservoirs. *Journal of Computational Physics: X*, 7:100061, 2020.

[48] Knut-Andreas Lie, Trine S. Mykkeltvedt, and Olav Møyner. A fully implicit weno scheme on stratigraphic and unstructured polyhedral grids. *Computational Geosciences*, 24(2):405–423, 2020.

[49] Jiamin Jiang and Rami M. Younis. Hybrid coupled discrete-fracture/matrix and multicontinuum models for unconventional-reservoir simulation. *SPE Journal*, 21(03):1009–1027, 2016.

[50] David K Ponting. Corner point geometry in reservoir simulation. In *ECMOR I-1st European Conference on the Mathematics of Oil Recovery*, pages cp—-234. European Association of Geoscientists & Engineers, 1989.

[51] Y Ding, P Lemonnier, and Others. Use of corner point geometry in reservoir simulation. In *International Meeting on Petroleum Engineering*. Society of Petroleum Engineers, 1995.

[52] Schlumberger GeoQuest. ECLIPSE reference manual. *Schlumberger, Houston, Texas*, 2014.

[53] Knut-Andreas Lie. *An introduction to reservoir simulation using MATLAB/GNU Octave: User guide for the MATLAB Reservoir Simulation Toolbox (MRST)*. Cambridge University Press, 2019.

[54] L. J. Durlofsky. Upscaling and gridding of fine scale geological models for flow simulation. In *8th International Forum on Reservoir Simulation Iles Borromees, Stresa, Italy*, volume 2024, pages 1–59, 2005.

[55] T. Y. Hou and X.-H. Wu. A multiscale finite element method for elliptic problems in composite materials and porous media. *J. Comput. Phys.*, 134:169–189, 1997.

[56] Y Efendiev, T Hou, and T Strinopoulos. Multiscale simulations of porous media flows in flow-based coordinate system. *Computational Geosciences*, 12(3):257–272, 2008.

[57] Y. Efendiev, S.H. Lee, G. Li, J. Yao, and N. Zhang. Hierarchical multiscale modeling for flows in fractured media using generalized multiscale finite element method. *GEM - International Journal on Geomathematics*, 6(2):141–162, Nov 2015.

[58] P. Jenny, S. H. Lee, and H. A. Tchelepi. Multi-scale finite-volume method for elliptic problems in subsurface flow simulation. *J. Comput. Phys.*, 187:47–67, 2003.

[59] P. Jenny, S. H. Lee, and H. A. Tchelepi. Adaptive fully implicit multi-scale finite-volume method for multi-phase flow and transport in heterogeneous porous media. *J. Comput. Phys.*, 217:627–641, 2006.

[60] H. Hajibeygi, G. Bonfigli, M.A. Hesse, and P. Jenny. Iterative multiscale finite-volume method. *J. Comput. Phys.*, 227:8604–8621, 2008.

[61] Ivan Lunati and Seong H Lee. An operator formulation of the multiscale finite-volume method with correction function. *Multiscale modeling & simulation*, 8(1):96–109, 2009.

[62] Y. Wang, H. Hajibeygi, and H. A. Tchelepi. Monotone multiscale finite volume method. *Comput. Geosci.*, pages 1–16, 2015.

[63] O. Møyner and K-A. Lie. A multiscale restriction-smoothed basis method for high contrast porous media represented on unstructured grids. *J. Comput. Phys.*, 304:46 – 71, 2016.

[64] M.J. Berger and J. Oliger. Adaptive mesh refinement for hyperbolic partial differential equations. *J. Comput. Phys.*, 53:484–512, 1984.

[65] D.K. Han, C.Z. Yan, and L.T. Peng. A more flexible approach of dynamic local grid refinement for reservoir modeling. *SPE 16014, SPE Symposium on Reservoir Simulation, 1-4 February, San Antonio, Texas, USA, 1987*, 1987.

[66] G.H. Schmidt and F.J. Jacobs. Adaptive local grid refinement and multi-grid in numerical reservoir simulation. *J. Comput. Phys.*, 77:140–165, 1988.

[67] W.A. Mulder and R.H.J. Gmelig Meyling. Numerical simulation of two-phase flow using locally refined grids in three space dimensions. *SPE 21230, SPE Advanced Technology Series*, 1:36–41, 1991.

[68] M.B. Biterge and T. Ertekin. Development and testing of a static/dynamic local grid-refinement technique. *J. Petrol. Technol.*, 44:487–495, 1992.

[69] M. Edwards and M. A. Christie. Dynamically adaptive godunov schemes with renormalization in reservoir simulation. In *SPE Symposium on Reservoir Simulation*. Society of Petroleum Engineers, 1993.

[70] M.G. Edwards. A higher-order godunov scheme coupled with dynamical local grid refinement for flow in a porous medium. *Comput. Methods Appl. Mech Eng.*, 131:287–308, 1996.

[71] Z.E. Heinemann, G. Gerken, and G. von Hantelmann. Using local grid refinement in a multiple-application reservoir simulator. *in: SPE Reservoir Simulation Symposium, 15-18 November, San Francisco, California, USA, 1983, SPE paper 12255*, 1983.

[72] B. Faigle, R. Helmig, I. Aavatsmark, and B. Flemisch. Efficient multiphysics modelling with adaptive grid refinement using a mpfa method. *Computat. Geosci.*, 18:625–636, 2014.

[73] J. B. Bell, M. J. Lijewski, G. S. H. Pau, and A. S. Almgren. A parallel second-order adaptive mesh algorithm for incompressible flow in porous media. *Philos. T. Roy. Soc. A*, 367:4633–4654, 2009.

[74] G. S. H. Pau, J. B. Bell, A. S. Almgren, K.M. Fagnan, and M. J. Lijewski. An adaptive mesh refinement algorithm for compressible two-phase flow in porous media. *Computat. Geosci.*, 16:577–592, 2012.

[75] Michael G Edwards. A higher-order godunov scheme coupled with dynamic local grid refinement for flow in a porous medium. *Computer Methods in applied mechanics and engineering*, 131(3-4):287–308, 1996.

[76] P. H. Sammon. Dynamic grid refinement and amalgamation for compositional simulation. *in: SPE Reservoir Simulation Symposium, 21-23 February, The Woodlands, Texas, USA, 2003, SPE paper 79683,*, pages 1–11, 2003.

[77] H. Hajibeygi and P. Jenny. Adaptive iterative multiscale finite volume method. *J. Comput. Phys.*, 230(3):628–643, 2011.

[78] I. Lunati, S. Lee, and M. Tyagi. An iterative multiscale finite volume algorithm converging to exact solution. *J. of Comp. Phys.*, 230(5):1849–1864, 2011.

[79] Y. Wang, H. Hajibeygi, and H. A. Tchelepi. Algebraic multiscale linear solver for heterogeneous elliptic problems. *J. Comput. Phys.*, 259:284–303, 2014.

[80] M. Tene, H. Hajibeygi, Y. Wang, and H.A. Tchelepi. Compressible algebraic multiscale solver (cams). *Proceedings of the 14th European Conference on the Mathematics of Oil Recovery (ECMOR), Catania, Sicily, Italy*, 2014.

[81] M. Tene, M. S. Al Kobaisi, and H. Hajibeygi. Algebraic multiscale method for flow in heterogeneous porous media with embedded discrete fractures (f-ams). *J. of Comput. Phys.*, 321:819 – 845, 2016.

[82] R. Kunze, I. Lunati, and S. H. Lee. A multilevel multiscale finite-volume method. *J. Comput. Phys.*, 225:502–520, 2013.

[83] Mousa HosseiniMehr. Multilevel multiscale method for embedded discrete fracture modeling approach (f-mmsfv), 2016.

[84] M. Cusini, C. van Kruijsdijk, and H. Hajibeygi. Algebraic dynamic multilevel (adm) method for fully implicit simulations of multiphase flow in porous media. *J. Comput. Phys.*, 314:60 – 79, 2016.

[85] M. Cusini, B. Fryer, C. van Kruijsdijk, and H. Hajibeygi. Algebraic dynamic multilevel method for compositional flow in heterogeneous porous media. *J. Comput. Phys.*, 354:593 – 612, 2018.

[86] D. W. Peaceman. Interpretation of well-block pressures in numerical reservoir simulation. *SPE J.*, 18 (3):183–194, 1978.

[87] Charles R Faust and James W Mercer. Geothermal reservoir simulation: 1. mathematical models for liquid-and vapor-dominated hydrothermal systems. *Water resources research*, 15(1):23–30, 1979.

[88] Zhi Yang Wong, Roland N Horne, and Hamdi A Tchelepi. Sequential implicit nonlinear solver for geothermal simulation. *Journal of Computational Physics*, 368:236–253, 2018.

[89] PK Nag. *Engineering thermodynamics.* Tata McGraw-Hill Education, 2013.

[90] Keith H Coats et al. An equation of state compositional model. *Society of Petroleum Engineers Journal*, 20(05):363–376, 1980.

[91] Water pressure-temperature phase diagram. `https://www2.dawsoncollege.qc.ca/dbaril/NYA/Handout/Phase_Diagram/water_phase_diagram.jpg`. Accessed: 2021-03-10.

[92] Water pressure-temperature phase diagram. `https://demonstrations.wolfram.com/PressureEnthalpyDiagramForWater/`. Accessed: 2021-03-10.

[93] Zhi Yang Wong, Roland Horne, and Denis Voskov. Comparison of nonlinear formulations for geothermal reservoir simulations. In *41 st Workshop on Geothermal Reservoir Engineering.. https://pangea. stanford. edu/ERE/db/GeoConf/papers/SGW/2016/Wong. pdf*, 2016.

[94] Steven E Ingebritsen, Ward E Sanford, and Christopher E Neuzil. *Groundwater in geologic processes.* Cambridge University Press, 2006.

[95] Philip Fletcher. *Chemical thermodynamics for earth scientists.* 1993.

[96] K. H. Coats. Geothermal Reservoir Modelling. In *SPE Annual Fall Technical Conference and Exhibition*, 1977.

[97] Charles R Faust and James W Mercer. *Finite-difference Model of Two Dimensional, Single-, and Two-phase Heat Transport in a Porous Medium: Version I*, volume 77. US Department of the Interior, Geological Survey, 1977.

[98] Noriaki Watanabe, Takuma Kikuchi, Takuya Ishibashi, and Noriyoshi Tsuchiya. ν-x-type relative permeability curves for steam-water two-phase flows in fractured geothermal reservoirs. *Geothermics*, 65:269–279, 2017.

[99] Donald A Nield, Adrian Bejan, et al. *Convection in porous media*, volume 3. Springer, 2006.

[100] K. Aziz and A. Settari. *Petroleum Reservoir Simulation.* Blitzprint Ltd., Calgary, Alberta, 2002.

[101] I. M. Cheshire, J. R. Appleyard, and D. Banks. An efficient fully implicit simulator. *in: Proceedings of the European Offshore Petroleum Conference and Exhibition, London, United Kingdom, 1980, SPE paper 179-1980-MS.*, 1980.

[102] H. Cao. *Development of Techniques for General Purpose Simulation.* Phd thesis, Stanford University, USA, 2002.

[103] H. Hajibeygi and H. A. Tchelepi. Compositional multiscale finite-volume formulation. *SPE Journal*, 19(2):316–326, 2014.

[104] K.H. Coats, W.D. George Chieh Chu, and B.E. Marcum. Three-dimensional simulation of steamflooding. *SPE J.*, 14(6):573–592, 1974.

[105] S. H. Lee, C. Wolfsteiner, and H. A. Tchelepi. Multiscale finite-volume formulation for multiphase flow in porous media: black oil formulation of compressible, three-phase flow with gravity. *Comput. Geosci.*, 12(3):351–366, 2008.

[106] O. Møyner and K.A. Lie. A multiscale restriction-smoothed basis method for compressible black-oil models. *SPE J.*, 2016.

[107] O. Møyner and H. A. Tchelepi. A multiscale restriction-smoothed basis method for compositional models. In *SPE Reservoir Simulation Conference, 20-22 February, Montgomery, Texas, USA*, 2017.

[108] A. Moncorgé, H.A. Tchelepi, and P. Jenny. Modified sequential fully implicit scheme for compositional flow simulation. *Journal of Computational Physics*, 337:98 – 115, 2017.

[109] A. Moncorgé, H.A. Tchelepi, and P. Jenny. Sequential fully implicit formulation for compositional simulation using natural variables. *Journal of Computational Physics*, 371:690 – 711, 2018.

[110] R. Younis. *Advances in Modern Computational Methods for Nonlinear Problems; A Generic Efficient Automatic Differentiation Framework, and Nonlinear Solvers That Converge All The Time.* Phd thesis, Stanford University, USA, 2009.

[111] S. H. Lee, C. L. Jensen, and M. F. Lough. Efficient finite-difference model for flow in a reservoir with multiple length-scale fractures. *SPE J.*, 3(5):268–275, 2000.

[112] S B M Bosma, H Hajibeygi, M Tene, H A Tchelepi, and Others. Multiscale Finite Volume Method for Discrete Fracture Modeling with Unstructured Grids. *SPE Reservoir Simulation Conference*, 351:145–164, 2017.

[113] H.; Hellevang B.; Riis F.; Johansen W.; Eigestad, G.; Dahle and E. Øian. Geological modeling and simulation of co2 injection in the johansen formation. *Computational Geosciences*, 13(1):435–450, 2009.

[114] Arts R. Brouwer G. et al. Peters, L. Results of the brugge benchmark study for flooding optimization and history matching. *SPE Reservoir Evaluation and Engineering*, 294–295:391–405, 2010.

[115] Hetland M. Verlo, S. B. Development of a field case with real production and 4d data from the norne field as a benchmark case for future reservoir simulation model testing. msc thesis. *Norwegian University of Science and Technology, Trondheim, Norway*, 2008.

[116] Open porous media (opm). `http://opm-project.org`. Accessed: 2020-10-30.

[117] Y. Efendiev, V. Ginting, T. Hou, and R. Ewing. Accurate multiscale finite element methods for two-phase flow simulations. *J. Comput. Phys.*, 220:155–174, 2006.

[118] Y. Efendiev and T. Y. Hou. *Multiscale Finite Element Methods: Theory and Applications.* Springer, 2009.

[119] K.H. Coats. A note on impes and some impes-based simulation models. *SPE J.*, 5(3):245–251, 2000.

[120] M Cusini. *Dynamic Multilevel Methods for Simulation of Multiphase Flow in Heterogeneous Porous Media.* PhD thesis, 2019.

[121] H. Zhou and H. A. Tchelepi. Operator based multiscale method for compressible flow. *SPE J.*, 13:267–273, 2008.

[122] I. Lunati and P. Jenny. Multiscale finite-volume method for density-driven flow in porous media. *Comput. Geosci.*, 12(3):337–350, 2008.

[123] J. M. Nordbotten and P. E. Bjøstad. On the relationship between the multiscale finit volume method and domain decomposition preconditioners. *Comput. Geosci.*, 13(3):367–376, 2008.

[124] H. Hajibeygi, M.A. Hesse, G. Bonfigli, and P. Jenny. Iterative multiscale finite volume method. *CMWR XII, San Francisco, USA*, 2008.

[125] M. Tene, Y. Wang, and H. Hajibeygi. Adaptive algebraic multiscale solver for compressible flow in heterogeneous porous media. *J. Comput. Phys.*, 300:679–694, 2015.

[126] S. Shah, O. Møyner, M. Tene, K-A. Lie, and H. Hajibeygi. The multiscale restriction smoothed basis method for fractured porous media (f-msrsb). *J. Comput. Phys.*, 318:36 – 57, 2016.

[127] S. Bosma, H. Hajibeygi, M. Tene, and H. A. Tchelepi. Multiscale finite volume method for discrete fracture modeling on unstructured grids (ms-dfm). *J. Comput. Phys.*, 351:145 – 164, 2017.

[128] N. Castelletto, H. Hajibeygi, and H. A. Tchelepi. Multiscale finite-element method for linear elastic geomechanics. *J. Comput. Phys.*, 331:337 – 356, 2017.

[129] I.V. Sokolova and H. Hajibeygi. Multiscale finite volume method for finite-volume-based poromechanics simulations. In *ECMOR XVI - 16th European Conference on the Mathematics of Oil Recovery*, 2018.

[130] A. Kozlova, Z. Li, J. R. Natvig, S. Watanabe, Y. Zhou, K. Bratvedt, and S. H. Lee. A real-field multiscale black-oil reservoir simulator. *SPE J.*, 21(06), 2016.

[131] K.-A. Lie, O. Møyner, J. R. Natvig, A. Kozlova, K. Bratvedt, S. Watanabe, and Z. Li. Successful application of multiscale methods in a real reservoir simulator environment. *Comput. Geosci.*, 21(5-6):981–998, December 2017.

[132] D. Cortinovis and P. Jenny. Iterative galerkin-enriched multiscale finite-volume method. *J. Comput. Phys.*, 277:248–267, 2014.

[133] Abdulrahman M. Manea, Jason Sewall, and Hamdi A. Tchelepi. Parallel multiscale linear solver for highly detailed reservoir models. *SPE J.*, 21(06), 2016.

[134] D. Cortinovis and P. Jenny. Zonal multiscale finite-volume framework. *J. Comput. Phys.*, 337:84 – 97, 2017.

[135] J. Fu, H. A. Tchelepi, and J. Caers. A multiscale adjoint method to compute sensitivity coefficients for flow in heterogeneous porous media. *Adv. Water Resour.*, 33(6):698 – 709, 2010.

[136] S. Krogstad, V. L. Hauge, and A. Gulbransen. Adjoint multiscale mixed finite elements. *SPE J.*, 16(01):162–171, 2011.

[137] R. Moraes, J. R.P. Rodrigues, H. Hajibeygi, and J. D. Jansen. Multiscale gradient computation for flow in heterogeneous porous media. *J. Comput. Phys.*, 336:644 – 663, 2017.

[138] R. Moraes, R. M. Fonseca, M. Helici, A. W. Heemink, and J.D. Jansen. Improving the computational efficiency of approximate gradients using a multiscale reservoir simulation framework. In *SPE Reservoir Simulation Conference, 20-22 February, Montgomery, Texas, USA*, 2017.

[139] R. Moraes, H. Hajibeygi, and J.D. Jansen. A multiscale method for data assimilation. In *ECMOR XVI - 16th European Conference on the Mathematics of Oil Recovery*, 2018.

[140] Yixuan Wang, Hadi Hajibeygi, and Hamdi A. Tchelepi. Algebraic multiscale solver for flow in heterogeneous porous media. *Journal of Computational Physics*, 259:284 – 303, 2014.

[141] I. Aavatsmark. An introduction to multipoint flux approximations for quadrilateral grids. *Comput. Geosci.*, 6:405–432, 2002.

[142] Hadi Hajibeygi, Manuela Bastidas Olivares, Mousa HosseiniMehr, Sorin Pop, and Mary Wheeler. A benchmark study of the multiscale and homogenization methods for fully implicit multiphase flow simulations. *Advances in Water Resources*, 143:103674, 2020.

[143] P.M. Boerrigter, A.H. de Zwart, D.W. van Batenburg, M. Bosch, and J.C. Vink. Application of dynamic gridding techniques to IOR/EOR-processes. *in: SPE Reservoir Simulation Symposium, 21-23 February, The Woodlands, Texas, USA, 2011, SPE paper 141711*, 2011.

[144] H. Hajibeygi, S. H. Lee, and I. Lunati. Accurate and efficient simulation of multiphase flow in a heterogeneous reservoir by using error estimate and control in the multiscale finite-volume framework. *SPE Journal*, 17(4):1071–1083, 2012.

[145] E Weinan. *Principles of multiscale modeling*. Cambridge University Press, 2011.

[146] J. Aarnes and T. Y. Hou. Multiscale domain decomposition methods for elliptic problems with high aspect ratios. *Acta Math. Appl.*, 18(1):63–76, 2002.

[147] Eric T. Chung, Yalchin Efendiev, and Chak Shing Lee. Mixed generalized multiscale finite element methods and applications. *Multiscale Modeling & Simulation*, 13(1):338—-366, 2015.

[148] E Weinan and Xing Y Yue. Heterogenous multiscale method for locally self-similar problems. *Communications in Mathematical Sciences*, 2(1):137–144, 2004.

[149] Assyr Abdulle, E Weinan, Björn Engquist, and Eric Vanden-Eijnden. The heterogeneous multiscale method. *Acta Numerica*, 21:1–87, 2012.

[150] E Weinan, Bjorn Engquist, Xiantao Li, Weiqing Ren, and Eric Vanden-Eijnden. Heterogeneous multiscale methods: a review. *Communications in computational physics*, 2(3):367–450, 2007.

[151] Grégoire Allaire. Homogenization and two-scale convergence. *SIAM Journal on Mathematical Analysis*, 23(6):1482–1518, 1992.

[152] A. Abdulle and W. E. Finite difference heterogeneous multi-scale method for homogenization problems. *J. Comput. Phys.*, 191(1):18–39, 2003.

[153] Todd Arbogast and Hailong Xiao. A multiscale mortar mixed space based on homogenization for heterogeneous elliptic problems. *SIAM Journal on Numerical Analysis*, 51(1):377–399, 2013.

[154] Yerlan Amanbek, Gurpreet Singh, Mary F Wheeler, and Hans van Duijn. Adaptive numerical homogenization for upscaling single phase flow and transport. *Journal of Computational Physics*, 387:117–133, 2019.

[155] Gurpreet Singh, Wingtat Leung, and Mary F Wheeler. Multiscale methods for model order reduction of non-linear multiphase flow problems. *Computational Geosciences*, 23(2):305–323, 2019.

[156] M. Cusini, R. Gielisse, H. Groot, C. van Kruijsdijk, and H. Hajibeygi. Incomplete mixing in porous media: Todd-longstaff upscaling approach versus a dynamic local grid refinement method. *Computational Geosciences*, 2018.

[157] Ulrich Hornung. *Homogenization and Porous Media*, volume 6. Springer Science & Business Media, 1997.

[158] C.J. van Duijn, H. Eichel, R. Helmig, and I.S. Pop. Effective equations for two-phase flow in porous media: the effect of trapping at the micro-scale. *Transport in Porous Media*, 9:411—428, 2007.

[159] Manuela Bastidas, Carina Bringedal, Sorin Pop, and Florin Radu. Adaptive numerical homogenization of non-linear diffusion problems. *arXiv preprint arXiv:1904.10665*, 2019.

[160] Assyr Abdulle and Achim Nonnenmacher. A short and versatile finite element multiscale code for homogenization problems. *Computer Methods in Applied Mechanics and Engineering*, 198:2839–2859, 2009.

[161] Adam Szymkiewicz, Rainer Helmig, and Hartmut Kuhnke. Two-phase flow in heterogeneous porous media with non-wetting phase trapping. *Transport in Porous Media*, 86:27—47, 2011.

[162] Patrick Henning, Mario Ohlberger, and Ben Schweizer. Adaptive heterogeneous multiscale methods for immiscible two-phase flow in porous media. *Computational Geosciences*, 19(1):99—114, 2015.

[163] M. A. Christie and M. J. Blunt. Tenth SPE comparative solution project: A comparison of upscaling techniques. *SPE 72469*, 4:308 – 317, 2001.

[164] Arjan Marelis. A benchmark study for dynamic multilevel multiscale simulation of heat production from fractured geothermal reservoirs, 2020.

Curriculum Vitæ

S.Mousa HosseiniMehr

5 May 1987	Born in Ahvaz, Iran

Education

2001 - 2005	**National Organization for Development of Exceptional Talents (NODET), Iran** Highschool Diploma in Mathematics and Physics
2005 - 2010	**Sharif University of Technology, Tehran, Iran** Faculty of Chemical and Petroleum Engineering Bachelor of Science in Petroleum Engineering
2014 - 2016	**Delft University of Technology, Delft, the Netherlands** Faculty of Civil Engineering and Geosciences (CEG) Master of Science in Applied Earth Sciences
2017 - 2021	**Delft University of Technology, Delft, the Netherlands** Delft Institute of Applied Mathematics (DIAM) Faculty of Electrical Eng., Mathematics and Computer Science (EEMCS) Ph.D. in Computational Mathematics and Numerical Analysis

Work experience and Internships

Jun 2010 - Aug 2010	**South Pars Gas Refinery, Asaluyeh, Iran** *Reservoir Engineer Intern*
Sep 2010 - Mar 2014	**Tuition Center for Pre-University Students, Tehran, Iran** *Tutor in Mathematics and Physics*
Sep 2015 - Nov 2016	**Delft University of Technology, Delft, the Netherlands** *Teaching and Lab Assistant in Courses:* Rock Fluid Physics, 2015-2016 Field Development Plan (FDP), 2016-2017
Nov 2016 - Aug 2017	**Delft University of Technology, Delft, the Netherlands** Department Geoscience and Engineering *Research Assistant*
Sep 2015 - Nov 2016	**Delft University of Technology, Delft, the Netherlands** *Teaching and Lab Assistant in Courses:* Rock Fluid Physics, 2017-2018 Matlab Programming, 2018-2019 Reservoir Simulation, 2017-2018-2019 Forward and Inverse Geo-modeling, 2019-2020-2021 Numerical Methods for Subsurface Simulation, 2019-2020-2021 Scientific Computing, 2019-2020-2021
Aug 2021 - Nov 2021	**Schlumberger, Abingdon, United Kingdom** *Software Engineer Intern*

Extracurricular Activities

SIAM:

2017-2018	Secretary and Vice President of the SIAM student chapter Delft

Latin Dance:

2017-2018	Giving Dance Workshops at TU Delft and Leiden University
2017-2019	Event Organizing Assistant at SoSalsa
2018-2019	Chairman of S.D.A. Leidance

Football:

2017-2018	Player at the Krylov Tigers, the Football Team of the Numerical Analysis Department

SCIENTIFIC CONTRIBUTIONS

JOURNAL PAPERS

5. M. HosseiniMehr, C. Vuik and H. Hajibeygi, Comparative study of dynamic multilevel simulation of fractured geothermal reservoirs, *In preparation, to be Submitted to journal of Geothermics.*

4. M. HosseiniMehr, J.P.P. Tomala, C. Vuik, M. Al Kobaisi and H. Hajibeygi, Projection-based embedded discrete fracture model (pEDFM) for flow and heat transfer in real-field geological formations with corner-point grid geometries, *Submitted to journal of Advances in Water Resources* (2021).

3. M. HosseiniMehr, C. Vuik and H. Hajibeygi, Dynamic Multilevel Simulation of Fractured Geothermal Reservoirs, *Journal of Computational Physics: X* (2020) 7, 100061.

2. H. Hajibeygi, M.B. Olivares, M. HosseiniMehr, I. Pop and M. Wheeler, A benchmark study of the multiscale and homogenization methods for fully implicit multiphase flow simulations with adaptive dynamic mesh (ADM), *Advances in Water Resources* (2020) 143, 103674.

1. M. HosseiniMehr, M. Cusini, C. Vuik and H. Hajibeygi, Algebraic dynamic multilevel method for embedded discrete fracture model (F-ADM), *Journal of Computational Physics* 373 (2018) 324-345.

CONFERENCE PAPERS

5. M. HosseiniMehr, J.P.P. Tomala, C. Vuik and H. Hajibeygi, Projection-based Embedded Discrete Fracture Model (pEDFM) on Corner-point Grid Geometry for Subsurface Flow and Geothermal Modeling, *ECMOR XVII-17th European Conference on the Mathematics of Oil Recovery* (2020).

4. D. Ris, M. HosseiniMehr and H. Hajibeygi, Geologically Relevant Framework for Adaptive Fractured Reservoir Modeling, *EAGE Annual Conference and Exhibition* (2020) 1-4.

3. M. HosseiniMehr, M. Al Kobaisi, C. Vuik and H. Hajibeygi, Dynamic Multilevel Multiscale Simulation of Naturally Fractured Reservoirs with Generic Fracture-Matrix Conductivity Contrasts, *SPE Reservoir Characterization and Simulation Conference and Exhibition* (2019).

2. M. HosseiniMehr, R. Arbarim, M. Cusini, C. Vuik and H. Hajibeygi, Algebraic Dynamic Multilevel Method for Fractured Geothermal Reservoir Simulation, *SPE Reservoir Simulation Conference* (2019).

1. M. HosseiniMehr, R. Arbarim, M. Cusini, C. Vuik and H. Hajibeygi, Algebraic Dynamic Multilevel Method for Single-phase Flow in Heterogeneous Geothermal Reservoirs, *ECMOR XVI-16th European Conference on the Mathematics of Oil Recovery* (2018).

EVENTS AND TALKS

14. **14/09/2020:** Talk at the *ECMOR XVII* 2020 *Conference* Online.

13. **31/08/2020:** Talk at the *InterPore* 2020 *conference*, Online.

12. **05/03/2020:** Talk at the *SFB* 1313 *Status Seminar* 2020 in Gultstein, Germany.

11. **03/10/2019:** Talk at the *European Numerical Mathematics and Advanced Applications Conference* 2019 in Egmond aan Zee, the Netherlands.

10. **10/05/2019:** Talk at the *InterPore* 2019 *conference* in Valencia, Spain.

9. **21/03/2019:** Talk at the *SFB* 1313 *Status Seminar* 2019 in Blaubeuren, Germany.

8. **04/10/2018:** Poster Presentation at the *Woudschoten* 2018 *Conference* in Zeist, The Netherlands.

7. **20/09/2018:** Talk at the *Annual Meeting of European SIAM Chapters (*2018*)* in Berlin, Germany.

6. **06/09/2018:** Talk at the *ECMOR XVI* 2018 *Conference* in Barcelona, Spain.

5. **07/06/2018:** Talk at the *Computational Methods in Water Resources (CMWR) XXIII* 2018 *Conference* in Saint-Malo, France.

4. **30/05/2018:** Talk at the *Multigrid and Multilevel Methods Workshop Day by The SIAM Student Chapter at TU Delft* in Delft, the Netherlands.

3. **11/04/2018:** Participation at the *The Computational Mathematics Aspects of Porous Media, and Fluid Flow Seminar* at Lorentz Center, in Leiden, The Netherlands.

2. **05/10/2017:** Poster Presentation at the *Woudschoten* 2017 *Conference* in Zeist, The Netherlands.

1. **08/05/2017:** Poster Presentation at the *InterPore* 2017 *conference* in Rotterdam, The Netherlands.

ACKNOWLEDGEMENTS

This four-years journey with all the adventures around it would not have been possible without the help, support and contribution of many around me. Here, as little as it may seem, I would like to express my appreciation towards these amazing people.

First, I would like to thank my promotors, **Dr. Hadi Hajibeygi** and **Prof. Cornelis (Kees) Vuik** for giving me such a great opportunity to start my PhD and work on this project. Dear Hadi, your enthusiasm, motivation and energy have always been a great driver for my progress, allowing me to believe in my potentials. The amount of time you have spent days and nights to help me find answers to my questions, to provide novel ideas, and to improve the quality of my work towards almost perfection is beyond anyone's guess. This does not only apply to the four years of this PhD, but also goes back to my MSc studies. What an adventure we have been through. There is no way I can ever thank you enough for all the supports you have provided me with. Dear Kees, next to Hadi, you have also always guided me via fruitful discussions at many moments with a smile on your face despite your busy schedule as the head of the numerical analysis department and many other responsibilities. Your feedback and suggestions made my work much easier.

My gratitude goes also to **prof. Jan Dirk Jansen**, **Prof. Bert Sluys**, **Prof. Yalchin Efendiev**, **Prof. Sebastian Geiger**, and **Dr. Mohammed Al Kobaisi** for being part of my PhD committee, and **Prof. Bill Rossen** as the reserve member. Another thank you goes to Jan Dirk and Bill who gave me various feedback and suggestions on the improvement of my dissertation. Moreover, I would like to thank **Prof. Hamdi Tchelepi** for being in the committee of my Go/No-Go assessment in the first year, and **Dr. Denis Voskov** for the discussions we have had during various meetings and seminars. Hamdi and Dennis, with your social engagements, the ECMOR conference in Barcelona was of a much nicer experience for me.

I would also like to express my special gratitude to **Jonathan Morris** for giving me the opportunity to have my internship as a high-performance computing software engineer at Schlumberger. Even though this internship was carried out remotely, I really enjoyed it and I learned a great deal during its three-months duration.

Special thanks to my colleagues from the departments of applied mathematics and numerical analysis. **Roel**, **Jochen**, **Prajakta**, **Vandana** and **Marieke**, we have had lots of nice discussions and happy moments as office mates. Many times I had questions either related to my PhD or my personal life, and you always gave nice feedback and suggestions. Such nice moments. I wish this pandemic had not shortened the duration of our office moments. **Gabriela**, our trips to Saint-Malo in France for the CMWR conference and to Barcelona for the ECMOR conference (with the rest of the group) were great adventures. So many lovely memories we have had. **Alice**, your cakes and many different dishes you made for us were always a great reason to have lovely lunch and coffee breaks. Together with you, Roel, Gabriela, Prajakta and **Xiaoshan**, we were the fancy lunch group of the department. I will never forget the tastes of the dishes. **Merel**, **Mo** and **Anne**, we have had the opportunity to go to dance events together at various occasions, such nice memories. Moreover, thank you Merel, Roel and Jochen for being nice companions in the SIAM Student Chapter, organizing workshops, movie nights, chess tournaments and so on. Also, **Reinaldo** and **Baljaa**, thank you for helping me during the teaching assistantship of the Scientific Computing course. Furthermore, playing in a football team together with Reinaldo, **Luis**, Roel, Mo, and many others, and also playing table tennis with Baljaa, Luis and **Jiao**, all were amazing moments which deserve their own gratitude.

Next, I would like to thank my colleagues at the department of geoscience and engineering. Thank you DARSim members, **Matei**, **Matteo**, **Fanxiang**, **Kishan**, **Sara**, **Yuhang** and **Johno**, for all the valuable discussions during our weekly meetings. Moreover, thank you **Rhadityo**, **Daan**, **Janio** and **Arjan** for contributing to different parts of this dissertation during your MSc theses. I am also thankful to **Mohsen**, **Mark**, **Nikita**, **Swej** and **Kiarash** for various events and drinks we have had together during these years.

Of course one of the very life-changing experiences I had in my time at university, was to learn Latin dances at university events and the SoSalsa dance society. Thank you **Jan** and **Vivian** for the salsa dance classes, **Jeroen** and **Regina** for all the Rueda dance session, and **Daniel** for the bachata workshops and the bachata performances. Thank you my SoMiembros (no typo, it is correct!) teammates, **Dawn**, **Rebecca** and **Caithlin** for all the amazing adventures we had in organizing SoSalsa events. Also more thanks towards **Didi**, **Chad**, **Dylan**, **Jeannete**, **Juliette** and many others at SoSalsa for all the nice time we have had together. Thank you **Remko** for all the time we spent together, going to various dance events especially to Leiden. Speaking of Leiden, I got to know more lovely people after joining the Leidance group. Thank you **Johnathan** and **Jura** for all the salsa and bachata classes and parties. Our relationship was not just about dancing, but also photo shoots and dinners made it richer. Thank you **Casper**, **Riccardo** and **Emrah** for the kizomba classes and workshops. Thank you **Robin**, **Nikki**, **Annemarijn** and **Zander** for being in the Leidance board with me, organizing various unforgettable events for our members. Also my special thanks to **Andy**, **Devi**, **Jeanne**, **Lisanne**, **Loes**, **Thomas**, **Beaudine** and **Linde** for all the times we spent together organizing various drinks and dinners and going to dance events; after all we made the “Dine and Dance” group. I need to thank you **Maarten**, **Amir**, **Carlijne**, **Michael**, **Manon**, **Paloma**, **Josca** and **Sabine** for many discussions we have had, all the activities and lovely dances.

During these years, I have been lucky to have a close group of friends. We call it the “Gang”. Dear **Matei**, **Alina**, **Fardin**, **Mohsen**, **Leonoor**, **Cantika** and **Mihai**, I am always thankful for all the time we spent together, and countless activities we have had together. Alina, you are very sociable, approachable and open-hearted. The trips we had together to France, Germany and Gran Canaria (some with Matei and some with Fardin) were among the best trips in my memories. All the talks and discussions (some deep philosophy and some just jokes and laughter) were wonderful. I should not disregard all the amazing time we had together dancing Ballroom. Matei, you have been always helpful, rational and patient with all the helps I have needed and I am thankful for that. Fardin, we know each other from the first day in Delft. So much time we have spent together, it makes me feel I know you from my childhood. I am thankful of all the great time we had and all the things we arranged together. Mohsen, I am also thankful of all the nice things we have done together. Leonoor, Cantika and Mihai, thank you for all the things we did together. Alina, Matei and Mihai, you helped me with moving many times and I am very thankful for that. And dear my Gang friends, I hope we continue seeing each other even though we are not in the same city or country anymore. I hope we keep in touch and when we all grow old, we look back in time and say cheers to all the happy memories.

At the beginning of this book, I mentioned how blessed I have been to have met my girlfriend during my dance life. And yes, this has also been an iconic life changing moment of my life. Dear **Nora**, since the day I met you, the beautiful smile on your face pierced deep through my heart. I am so lucky to have met you and started another chapter of my life with you. I enjoyed all the beautiful dances I have had with you each second. The beautiful bachata song Como El Agua is always in my heart because of you. All the lovely adventures we did, trips in the Netherlands, to Germany, Belgium and especially Switzerland, were all amazing. Four out of the last twelve months staying at your parents in Switzerland was a great experience. You made me love sledging and have a different sense for cheese. Your love is a great driver in my life and I am so looking forward to the future and where life next brings us to. I am greatly thankful for your patience and support during the final phase of my PhD.

I would also like to thank my uncle **Ebi** and his wife **Barbara**. Dear Ebi and Barbara, I will never forget the help and support you gave me at various occasions during my stay in the Netherlands so far, especially when I first arrived at Schiphol airport and you drove all the way from Germany and brought me back to your place. And many other times I traveled to Germany and you were always welcoming.

Last but certainly not least, I would also like to thank my brother **Mojtaba** and my parents, **Ahmad** and **Vajiheh**. Mojtaba, we have spent so much time together talking about various aspects of my professional and personal life. You coming to Germany for MSc studies, made it possible to be closer and meet more. Dear my parents, the moral and financial supports you have given me to make it possible for me to move to another country, more than 5 thousand kilometers away, cannot be described with words. During all these years, you have always made sacrifices to make sure I have a better life and become more. All my past, current and future accomplishments are the direct results of your invaluable time and efforts. I could not have achieved anything without your support. Dedicating this thesis to you is just a small step in showing my appreciation.

S.Mousa HosseiniMehr
Delft, November 18, 2021

About the author

Mousa HosseiniMehr was born on May 5th, 1987, in Ahvaz, Iran. He earned his BSc in Petroleum Engineering at Sharif Univeristy of Technology in Tehran. He then moved to the Netherlands to pursue an MSc in Applied Earth Sciences at TU Delft. After being a research assistant for a year, he started his PhD at the department of Applied Mathematics at TU Delft specializing in scalable simulation models. Joining Schlumberger as an HPC software engineer, he brought his academic skills into industry and learned new ones.

Besides his professional life, Mousa is a passionate salsa and bachata dancer. His dance life extends not only to social dancing, but also to giving workshops and performing on various dance shows. In addition to dancing, hiking and table tennis are his other hobbies. Being sociable and outgoing, he is always open to meet and socialize with new people.

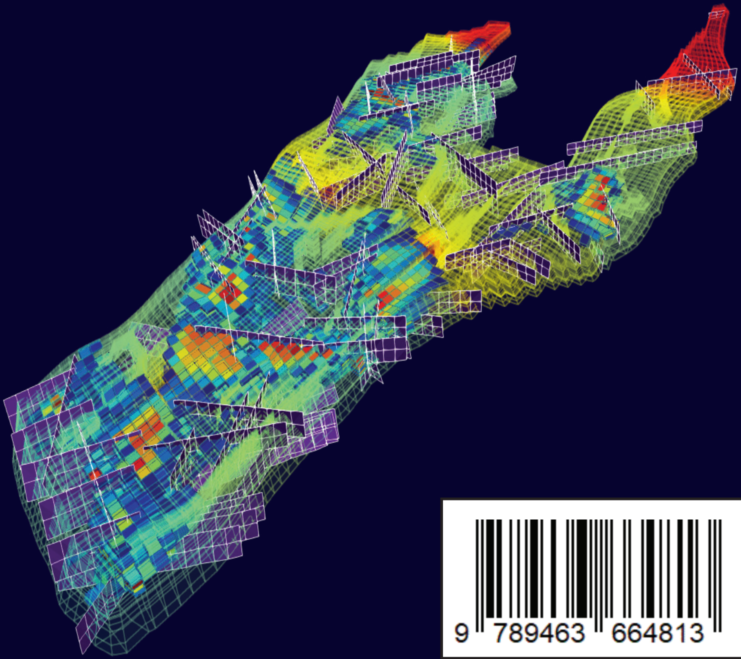

TU Delft

9 789463 664813